Deriving function from complex linked equilibria: systems chemistry with self-assembled *p*-sulfonatocalix[*n*]arenes in aqueous solution

by

Allison J. Selinger
B.Sc., Queen's University, 2017

A Dissertation Submitted in Partial Fulfillment
of the Requirements for the Degree of

DOCTOR OF PHILOSOPHY

in the Department of Chemistry

University of Victoria

We acknowledge and respect the Lək̓ʷəŋən (Songhees and Xʷsepsəm/ Esquimalt) Peoples on whose territory the university stands, and the Lək̓ʷəŋən and W̱SÁNEĆ Peoples whose historical relationships with the land continue to this day.

Supervisory Committee

Deriving function from complex linked equilibria: systems chemistry with self-assembled *p*-sulfonatocalix[*n*]arenes in aqueous solution

by

Allison J. Selinger
B.Sc., Queen's University, 2017

Supervisory Committee

Dr. Fraser Hof, Department of Chemistry
Supervisor

Dr. Cornelia Bohne, Department of Chemistry
Departmental Member

Dr. Raad Nashmi, Department of Biology
Outside Member

Abstract

Building systems of increasing complexity can give rise to emergent properties that are otherwise unobtainable. The design and development of macrocyclic-based systems that function in aqueous solution has many applications in detection, delivery and reversal of biologically relevant molecules. This dissertation focuses on synthetic analogs of the macrocyclic host *p*-sulfonatocalix[*n*]arene, as key building blocks in the creation of self-assembled complex systems, covering applications in therapeutic design and differential sensing in aqueous solution. Chapter 1 sets the stage for this work, introducing current synthetic and systems strategies employed in biorelevant host-based sensing.

An advanced property addressed in this dissertation is the ability to achieve pan-selectivity — binding well across a whole class of target analytes while maintaining good selectivity against other chemically similar analytes. Synthesizing a host that selectively binds a target analyte can be an inefficient and arduous task. In Chapter 2, I report on the templated synthesis of new bivalent hosts, **Super-sCx4** and **Super-sCx5**, as pan-selective binders of neuromuscular blocking agent's (NMBA's). Synthesis was achieved using a bisquaternary amine NMBA template, self-assembling two highly anionic *p*-sulfonatocalix[*n*]arene building blocks for covalent linkage. These bivalent anionic hosts bind by engaging both quaternary amines present on a variety of NMBA's, making them potential candidates for host-based NMBA drug reversal. We report low μM binding to alkyl, steroidal, curarine and benzylisoquinoline NMBA's, with selectivity over endogenous monovalent hydrophobic amines.

Another advanced property addressed in this dissertation is the ability to produce useful sensing outputs for a variety of analytes, without programming specific molecular recognition events. Differentiation of analytes by supramolecular sensors is typically achieved through sensor arrays, relying on pattern recognition responses from a large panel of isolated sensors. The differentiation of highly similar analytes poses an ongoing challenge. In Chapter 3, I explore a new one-pot systems chemistry approach to differential sensing in biological solutions. This systems approach relies on a network of three cross-assembling DimerDye *p*-sulfonatocalix[*n*]arene sensors, containing different integrated fluorophores. This robust approach exploits complex interconnected host•host and

host•analyte equilibria, producing emergent supramolecular and photophysical responses unique to each analyte. We apply this inherently information-rich systems approach to the discrimination of closely related serum albumin proteins and protein mixtures, without relying on targeted recognition elements. We show that a single adaptive sensing solution provides better analyte discrimination than an analogous sensor array.

Macrocyclic host-based sensors are often limited to detecting a single class of interacting analytes because they tend to bind molecules with similar properties. In Chapter 4, I address this challenge, reporting a mixed host system that detects analytes from many different classes, including cationic, neutral, and anionic. We show that co-assembling two different macrocyclic scaffolds, DimerDye *p*-sulfonatocalix[4]arenes and cucurbit[*n*]urils ($n = 7$ and 8), effectively increases the scope of analyte binding interactions and sensor outputs. This simple strategy exploits cross-reactive noncovalent host•host interactions through a synthetically integrated reporter dye. Emergent photophysical responses are produced by analyte interactions to either host. We demonstrate the advantages of mixed host co-assembled sensors in an array-based platform, differentiating a range of illicit drugs and common adulterating substances. The potential of this approach is further applied in profiling real-world multi-component illicit street drug samples.

Table of Contents

List of Tables

List of Figures

List of Schemes

Abbreviations

β-CD	*β*-cyclodextrin
ΔG	Gibbs free energy
ΔH	enthalpy
ΔS	entropy
^{13}C NMR	carbon nuclear magnetic resonance
^{1}H NMR	proton nuclear magnetic resonance
6-MAM	6-monoacetylmorphine
A	amphetamine
Abs	absorbance
ACh	acetylcholine
$AdNH_3^+$	amantadine
ANPP	4-anilino-N-phenethyl-piperidine
ATCC	American type culture collection
ATR	attenuated total reflection
a.u.	arbitrary units
BC	berberine chloride
BSA	bovine serum albumin
BODIPY	4,4-difuloro-4-bora-3a,4a-diaza-*s*-indacene
BzCl	benzoyl chloride
CB[*n*]	cucurbit[*n*]uril
CBD	cannabidiol
Ch	choline
CHCA	α-cyano-4-hydroxycinnamic acid
COSY	correlated spectroscopy
D	diffusion coefficient
D1	relaxation delay time
D20	saturation time
D29	spin lock time
DAP	2,7-diazapyrene
DD	DimerDye
DEPT	distortionless enhancement by polarization transfer
DMSO	dimethylsulfoxide
DOSY	diffusion-ordered spectroscopy
EC_{50}	half maximal effective concentration
EMEM	Eagle's minimal essential medium
ES+	positive electrospray
ESI	electrospray ionization
FBS	fetal bovine serum
FID	free induction decay
Fl	fluorescence
FRET	Förster resonance energy transfer
FTIR	fourier transform infrared
G	field gradient strength
GDA	guest displacement assay

GRAVY	grand average of hydropathy
HEK-293	human embryonic kidney 293 cell line
Hep-G2	human hepatoblastoma cell line
HMTA	hexamethylenetetramine
HOMO	highest occupied molecular orbital
HPLC	high performance liquid chromatography
HRMS	high resolution mass spectrometry
HSA	human serum albumin
I_0	NMR signal intensity at a gradient strength of zero
IC_{90}	90% inhibition concentration
IDA	indicator displacement assay
IR	infrared
ITC	isothermal titration calorimetry
J	coupling constant
K	lysine
k_B	Boltzmann constant
K_d	equilibrium dissociation constant
$K_{d,app}$	apparent dissociation constant
LCG	lucigenin
LC-MS	liquid chromatography mass spectrometry
LDA	linear discriminant analysis
LOD	limit of detection
LUMO	lowest occupied molecular orbital
M	monoisotopic mass
m.p.	melting point
MA	methamphetamine
MALDI-TOF	matrix assisted laser desorption ionization-time of flight
MDA	methylenedioxyamphetamine
MDAP	N,N’-dimethyl-2,7-diazapyrenium diiodide
MDMA	3,4-methylenedioxymethamphetamine
MeOH	methanol
MS	mass spectrometry
MSA	mouse serum albumin
nAChR	nicotinic acetylcholine receptor
NBD	nitrobenzoxadiazole
NMBA	neuromuscular blocking agent
NMR	nuclear magnetic resonance
P1	null pulse length
PC	principal component
PCA	principal component analysis
PCT	photoinduced charge transfer
PET	photoinduced electron transfer
PSA	porcine serum albumin
PS-MS	paper spray-mass spectrometry
PTFE	polytetrafluorethylene
QDa	quadrupole dalton

R	arginine
R2	coefficient of determination
RFE	recursive feature elimination
RG	receiver gain
r_H	hydrodynamic radius
RSA	rat serum albumin
SA	serum albumin
sCx	*p*-sulfonatocalix[*n*]arene
SSA	sheep serum albumin
STD	saturation transfer difference
SVM	support vector machine
T	temperature
T1	longitudinal relaxation time
THC	tetrahydrocannabinol
TX-100	triton X-100 detergent
UPLC-MS	ultra performance liquid chromatography mass spectrometry
UV-Vis	ultraviolet-visible spectroscopy
W	tryptophan
WP[6]	water-soluble carboxylatopillar[6]arene
Y	tyrosine

Acknowledgments

I’d like to extend my utmost appreciation to my supervisor Dr. Fraser Hof. Throughout my degree you’ve helped me grow into a better scientist, writer and presenter, and for that I’m grateful. I’d also like to thank my committee members Dr. Cornelia Bohne and Dr. Raad Nashmi. A special thank you to Cornelia for her attentive insight into my research, helpful discussions and experimental suggestions that improved my work. I’d also like to thank my undergraduate supervisor Dr. Donal Macartney for sparking my interest in research and supramolecular chemistry. Without that experience I wouldn’t have pursued graduate studies.

Thank you to all the facilities managers who have helped throughout my degree. Your expertise and guidance extended my knowledge, advanced my skillset and produced some interesting results along the way. I’d like to thank Chris Barr for training me on DOSY and establishing STD NMR parameters with me (it was rather exciting when it first worked). Thank you to Dr. Ori Granot and Dr. Tyler Trefz for acquiring the HRMS data presented in this dissertation. Thank you to Rebecca Hof (Centre for Advanced Materials and Related Technology) and Charmaine Wetherell (Health Core) for maintaining well-run facilities, that I used throughout my degree. I’d also like to thank all the collaborators who have contributed to this dissertation; Anat Yanai and Inanc Birol (Canada’s Michael Smith Genome Sciences Centre, Vancouver, Canada) for cell viability studies; Dr. Frank Biedermann and Dr. Joana Krämer (Institute of Nanotechnology, Karlsruhe Institute of Technology, Karlsruhe, Germany) for collaborative work on mixed host sensors; Dr. Dennis Hore and Eric Poarch (Canadian Institute For Substance Use Research, Victoria, Canada) for providing the opportunity to work with samples from Substance, the Vancouver Island Drug Checking Project; and Angela Jackson (UVic-Genome BC Proteomics Centre, Victoria, Canada) for expert assistance on MALDI-TOF MS.

I’d like to thank all current and past Hof group members who contributed to an enjoyable work environment, along with Bohne group members for pepping up our joint group meetings. Thank you to Dr. Meagan Beatty for training me when I first started and passing along DimerDyes. I’d also like to thank all the undergraduate students I had the opportunity to work with, particularly Natalie Cavallin and Cara Gallo, for your positivity and hard work. Thank you to my lab mates, Chelsea Wilson and Dr. Zoey Warmerdam. All the coffee breaks, walks and scientific discussions provided constant outlets of comic relief and comradery throughout my degree. As conference travel companions you made the most memorable and enjoyable times of my degree.

Lastly, thank you to all my friends and family for your support. Thank you to my best friend and biggest cheerleader Andrew Rinald, for being there for me throughout it all. Last and most important, thank you to my parents, Aloysius and Susan, and my brother, Bruce, for your endless love and support. To my parents, thank you for instilling in me the value of hard work and the persistence to always strive for better. I couldn’t have done this without you both.

Dedication

To my parents.

Chapter 1: Achieving function from equilibrating systems – designing macrocyclic host-based systems as supramolecular sensing tools

1.1 Introduction

Supramolecular systems are fundamental to life. Molecules coming together on the molecular, meso- and nanoscale to achieve function are critical in biological processes. Although biology readily achieves this through the evolution of complicated systems, the design and development of synthetic systems represents an ongoing frontier in science.[1] In the field of systems chemistry, molecular interactions and chemical complexity are exploited to generate emergent properties, where a system takes on new characteristics beyond the sum of its individual parts.[2] Through the lens of "life" this can be viewed as self-assembled systems that exist in transient dissipative states and supramolecular chemically fuelled processes that require the input of energy. In systems chemistry, chemical complexity can also be introduced through the construction of self-organizing "networks", containing multiple building blocks, simultaneously interacting within a web of interconnected equilibria. As synthetic supramolecular systems become more elaborate, chemists get closer to mimicking the complex systems that govern biology.[2]

One subfield of supramolecular chemistry involves the construction of synthetic organic macrocyclic concave "host" molecules with motifs that recognize and bind targeted "guest" analytes. The molecular recognition of host•guest complexes is driven by supramolecular processes that occur beyond the molecule.[3] Such systems that function in water, buffer and biofluids have many applications in the detection, delivery, and reversal of biologically relevant compounds.[4-8] In particular, the development of host-based sensors that function under biological conditions are valuable tools in areas of diagnostics, theranostics and biochemical research.[4]

This review Chapter provides an introductory perspective on designing water-soluble macrocyclic hosts-based systems for applications in sensing. Here we focus on host-based systems that operate at an equilibrium position, that can be shifted upon the addition of a new binding partner. First, we briefly introduce the basic concepts to consider in the design of host-based systems. Then we highlight illustrative examples of macrocyclic supramolecular sensing, incorporating strategies and lessons in systems chemistry. Throughout this Chapter we build in both chemical and systems complexity. We end on multi-component systems as a current evolving strategy to obtaining emergent information-rich outputs that surpass the performance of conventional pairwise host-based systems involving isolated sensing elements. These recent developments in complex host-based sensing systems represent the forefront of the field, shifting towards more challenging sensing tasks of distinguishing multiple analytes within complex mixtures.

1.2 Key considerations in designing host-based systems

Reversible interactions make up the foundation of self-assembled supramolecular systems. A molecular recognition event occurs when molecular building blocks reversibly come together, as driven and guided by intermolecular noncovalent interactions, dynamic covalent bonds and the hydrophobic effect (Figure 1.1). Combined, weak noncovalent interactions, including electrostatics (ion-ion, ion-dipole, ion-induced dipole and dipole-dipole), cation-π, π-π, hydrogen-bonding and dispersive interactions (van der Waals or London dispersion forces), can have a strong influence on molecular recognition (Figure 1.1a).[9] Dynamic covalent bonds can also be applied in self-assembled systems to reversibly favour the most thermodynamically stable species. Many types of dynamic covalent bonds exist.[10, 11] Here we highlight a few biologically relevant examples, such as imine, hydrazone and disulfide formation (Figure 1.1b). Later we will explore some examples of dynamic covalent bonds used within sensing systems. Lastly, the hydrophobic effect also plays an important role in molecular recognition in water.[12] To date, several evolving theories and models of the hydrophobic effect have been reported.[12-20] Although not strictly defined as a noncovalent interaction, water can aid in the self-assembly of molecular building blocks. Within a system, water is in constant motion, where interfacial water (surrounding the host and guest molecules) and inner host cavity water experience reduced degrees of freedom and hydrogen bond formation. Upon host•guest complexation, enthalpy (ΔH) and/or entropy (ΔS) can contribute favourably to Gibbs free energy (ΔG) of binding. A decrease of interfacial surface area and host cavity desolvation can induce an overall release of water into bulk solution, where it experiences increased degrees of freedom and

H-bond formation (~3.6 per molecule) (Figure 1.1c).[12] To various extents, the contributions from noncovalent interactions, hydrophobic effect and/or dynamic covalent bonds, can achieve molecular recognition of targeted guest analytes.

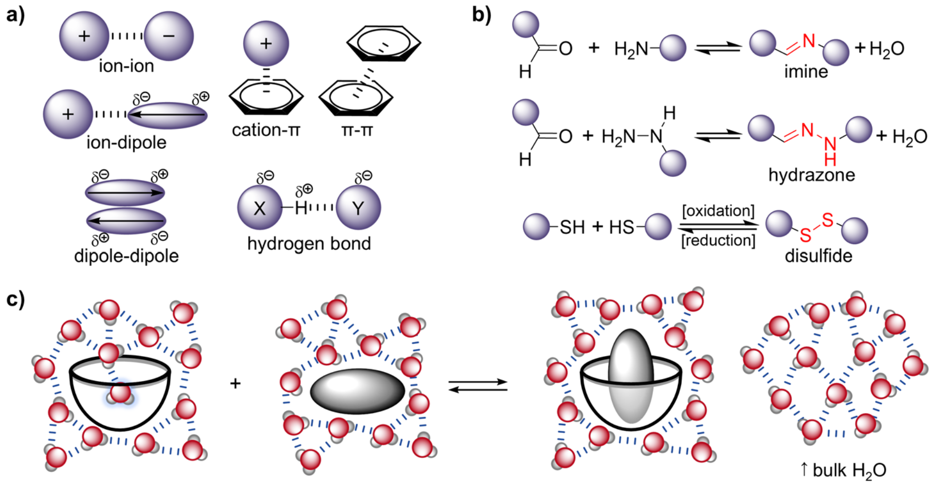

Figure 1.1. Supramolecular self-assembly is driven by reversible processes including **a)** noncovalent interactions, **b)** dynamic covalent bonds and **c)** the hydrophobic effect.

Host rigidity and host•guest shape complementarity play key roles in driving self-assemblies. A variety of host scaffolds offer different advantages and disadvantages in systems design (Figure 1.2). Overall, host receptors must contain some form of rigidity to prevent hydrophobic collapse and provide beneficial preorganization. Deeper cavities can introduce more surface area interactions by further extending the hydrophobic pocket, while maintaining scaffold rigidity. This can improve both enthalpic and entropic contributions to the hydrophobic effect.[21, 22] The construction of wider host cavities can accommodate larger guests but often introduces more flexibility, consequently creating less preorganization and resulting in weaker binding affinities.[23] Guest binding properties can be further tuned through the incorporation of polar and non-polar functional groups inside and outside the host cavity.[24] Polar groups on the upper or lower rim of a host (e.g. carbonyl portals or polyethylene glycol tails) can be used to favour hydration, assisting in water solubility and binding of hydrophobic guests with interacting polar head groups. Functional groups that are anionic (e.g. sulfonate, carboxylate and phosphonate) or cationic (e.g. ammonium, guanidinium and pyridinium) are often incorporated, favouring binding to oppositely charged guest molecules. Alternatively, host cavities containing inwardly directed polar groups can assist in hydrogen bonding and electrostatic interactions within the cavity, binding hydrophilic polar guests in aqueous conditions.[25] Throughout this Chapter, different host scaffolds and their characteristic binding properties will be introduced as examples of sensing systems arise.

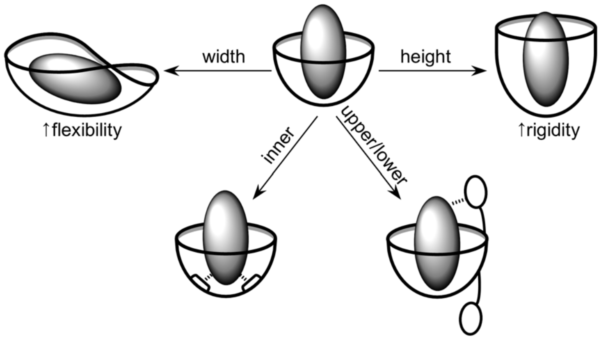

Figure 1.2. Macrocyclic host scaffolds can be tuned to control conformation, binding interactions, and introduce new properties.

Molecular recognition is driven by the formation of the most thermodynamically stable species when molecules with complementary structures come together. Traditional supramolecular systems are under thermodynamic control and exist at a stable energy minimum. In its simplest molecular form, this is a 1:1 host•guest complex. Thermodynamically stable systems can increase in complexity through the incorporation of multiple interacting host and guest components, to form a network of simultaneous reversible interactions within a single solution. Although the thermodynamically stable collection of species will be favoured, it is important to remember that self-assembly is not a static event but a reversible process of exchanging components. Le Châtelier's principle applies to all equilibrating systems, even those with multiple reversibly interacting components. Alterations in extrinsic factors, like relative component concentrations, solvent, polarity, pH and additive co-solutes or mediators, can be used to shift the equilibrium position of a system.[26] The selection of a buffer or addition of salts can also impact the binding affinity of a system, where buffers and salts can competitively bind to the host cavity.[27, 28] In instances where the ionic strength of a solution is altered, electrostatic screening effects on charged hosts and guests also play a role, diminishing Coulombic interactions.[27] Overall, adaptation of a system in response to external or internal factors can impact molecular recognition and the strength of association. This provokes careful consideration of the complete composition and design of host•guest systems, particularly under biologically relevant conditions or in biological media where higher salt content is required and additional competitive species are present.

In this Chapter we will focus on specific examples of macrocyclic host-based sensing systems that operate in aqueous solution and harness some aspects of chemical or systems complexity. Comprehensive reviews are available covering the broader topics of complexity in systems chemistry,[2, 29] supramolecular analytical chemistry, and macrocyclic host•guest molecular recognition in water.[30, 31] Here we explore select examples that introduce lessons in the design of macrocyclic host-based sensors, the effect of solvent conditions, use of additional system components and benefits that arise from increased systems complexity. To illustrate these mechanisms, we focus mainly on a family of hosts called calix[*n*]arenes and to a lesser extent the family called cucurbit[*n*]urils, as they are the main building blocks used within this dissertation.

1.2 Pairwise sensing of biologically relevant molecules

Supramolecular hosts are transformed into optical chemosensors through noncovalent or synthetic incorporation of an environmentally sensitive dye (Figure 1.3). Dye structures that form noncovalent interactions with hosts are selected to encourage self-assembly. This can be attained through intermolecular self-assembly of a dye present in solution (Figure 1.3a), or intramolecular self-assembly of a dye covalently tethered to the host (Figure 1.3b). Alternatively, environmentally sensitive dyes can be covalently integrated into the host scaffold, eliminating the need for noncovalent dye complexation (Figure 1.3c). Each of these frameworks relies on analyte binding induced changes to the microenvironment of the dye, producing monitorable colourimetric and/or fluorescent responses.

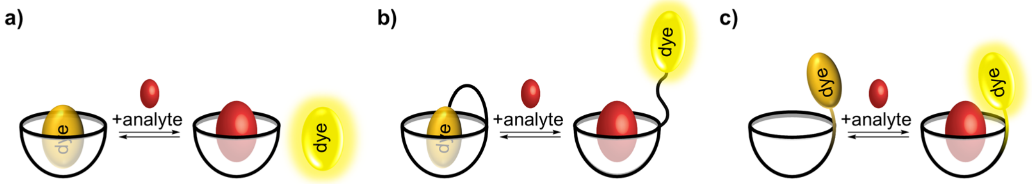

Figure 1.3. Supramolecular hosts are transformed into optical sensors through self-assembly or covalent incorporation of a reporter dye. Analyte detection can occur through **a)** intermolecular competitive displacement of a host•dye complex, **b)** intramolecular competitive displacement of a synthetically tethered dye, or **c)** direct detection from a covalently integrated environmentally sensitive dye.

Photoinduced electron transfer (PET) is the most common photophysical mechanism employed in host-based sensing systems. An example of PET applied in this dissertation is the quenched complex of the fluorescent dye lucigenin (**LCG**) inside the anionic host *p*-sulfonatocalix[4]arene (**sCx4**). This is explained by a static quenching process in which host•dye complexation results in the highest occupied molecular orbital (HOMO) of the host being proximal to the dye, which has a lower energy HOMO (Figure 1.4a). The phenolic units comprising **sCx4** make it electron rich, acting as a good electron donor. After excitation, the host undergoes a full electron transfer to the partly vacant HOMO of the excited dye, quenching the excited state (Figure 1.4a).[32-34] This mechanism allows for competitive analyte displacement that produces a turn-on fluorescence response from free dye.

Assemblies that induce dye aggregation can be designed such that disruption from guest binding alters absorbance and emission properties. An example adapted in this dissertation is the self-assembled formation of homodimer dye aggregates. Synthetic integration of the solvatochromic styryl dye, Brooker's Merocyanine (compound **1.1**), into **sCx4**, produces DimerDye **DD1Cx4** (Figure 1.4b). In aqueous solution two copies of this anionic host self-assemble into a homodimer, **DD1Cx4$_2$**, with the hydrophobic cationic dye pendant arm binding inside the hydrophobic pocket of another copy. Dimer-induced stacking of the two fluorophores results in blue shifted absorbance and quenched emission, relative to the analyte-bound monomer (Figure 1.4b). These features are characteristic of H-aggregates, explained by excited state face-to-face interactions of the two fluorophores. The stacked dye arrangement allows for transition to a higher energy excited state, producing a larger energy gap and blue shift in absorbance.[35] This higher energy excited state can then undergo internal conversion to lower energy excited states, thereby suppressing radiative pathways and quenching emission.[35]

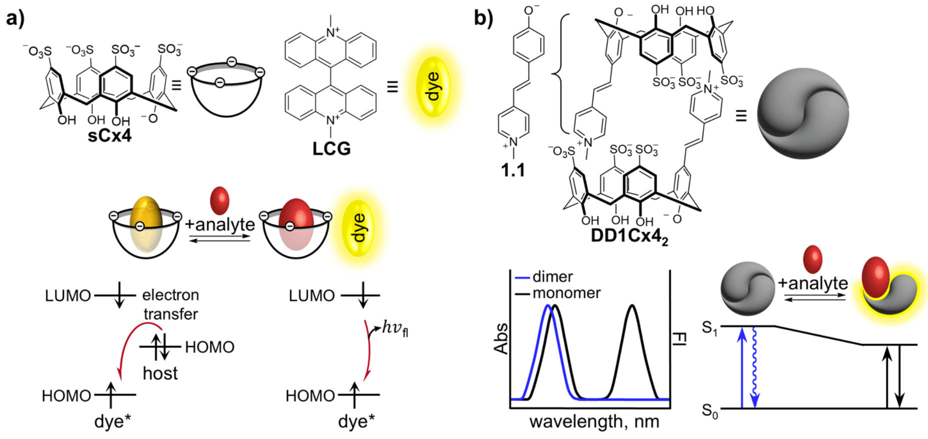

Figure 1.4. Turn-on fluorescence detection mechanisms applied in this dissertation include PET and H-aggregate dimers. **a)** The complexed host•dye reporter pair **sCx4•LCG** undergoes static PET quenching. In the presence of an analyte, competitive displacement of the dye produces a turn-on fluorescence response. **b)** DimerDye sensor **DD1Cx4** integrates merocyanine dye, compound **1.1**, into the host scaffold. In aqueous solution a homodimer forms, stacking two integrated dyes face-to-face resulting in blue shifted absorbance and quenched emission. Disassembly-driven sensing produces turn-on fluorescence detection of analytes.

Several other photophysical mechanisms can be used to probe host•guest binding events. Host•dye complexes that display enhanced fluorescence can occur when flexible dyes are confined inside a host cavity. This binding-induced restriction of rotational and vibrational freedom disfavours non-radiative decay pathways, enhancing emission. Host•dye complexation can also enhance emission by shielding diffusional dynamic quenching events that can occur within complex media.[36] Many macrocyclic sensing systems have also utilized charge transfer mechanisms through complexation events that alter the dipole electron-withdrawing or accepting character of a dye. This is generally seen in self-assembled systems with electron-deficient dyes next to electron rich aromatic hosts, inducing spectral shifts in the same direction for both absorbance and fluorescence, as well as changes in molar absorptivity.[34, 37] To a lesser extent Förster resonance energy transfer (FRET) is also applied in host•guest systems, requiring a pair of fluorophores with overlap of the donor emission and acceptor excitation spectra. FRET-mediated energy transfer from the donor to the acceptor is influenced by the spatial distance between the fluorophores, extent of spectral overlap and dipole orientations.[38]

In addition to the variety of different photophysical mechanisms that can be used to probe host•guest binding, there are also distinct molecular and supramolecular arrangements by which a host-based system can achieve sensing. The following sections include examples in which different supramolecular mechanisms are applied to host-based sensing in aqueous conditions.

Noncovalent binding of a dye to a host is a facile entry to host-based sensing. This conventional technique, known as an indicator displacement assay (IDA), relies on reversible binding of an indicator dye to the host scaffold. Upon addition of a competitive guest analyte, the indicator is displaced producing a monitorable response (Figure 1.3a).[39-41] IDAs operate best under conditions where the host•guest affinity product is approximately equal to the host•dye affinity product, where affinity product is the host•analyte or host•dye equilibrium binding constant (*K*) times the respective assay concentration.[42] This method is easily applied by mixing different known indicators with different host receptors, tailoring concentrations as needed.[36] Further adaptations include the guest displacement assay (GDA), where the guest analyte is first bound to the host and then subsequently displaced by an indicator dye, proving more suitable for insoluble or weaker binding guests.[43]

IDAs can be used in biological applications where interferants (e.g. salts, buffer ions and metabolites) remain constant. An earlier example from Nau and co-workers paired the electron-rich anionic host **sCx4**, with the cationic reporter dye **LCG** (Figure 1.5a), as a label-free method for continuous real-time enzyme assay monitoring (Figure 1.5b).[42] In this example a stronger host•dye binding constant is favourable, as it allows for lower host•dye concentrations to be used relative to the detected enzyme substrate and product. The hydrolysis of the neurotransmitter acetylcholine (**ACh**) to choline (**Ch**) produces the same “on” response, attributed to similar binding affinities. However, the oxidation of **Ch** to enzyme product betaine (compound **1.2**) results in an “off” response from weaker binding affinity (Figure 1.5b). Through a domino enzyme-coupled supramolecular tandem assay, absolute concentrations of **Ch** followed by **ACh** are determined. The success of this assay relies on a difference in enzyme substrate versus product affinity by a factor of 10 or more.

Recent IDA applications show the use of **sCx4•LCG** in increasingly complex biologically relevant systems, quantifying guest transport through liposome membrane channels,[44, 45] and transmembrane permeation.[46] Liposomes are formed containing the pre-assembled host•dye reporter pair **sCx4•LCG** inside, unable to permeate the membrane barrier (Figure 1.5c). The crossing of cationic peptide, protamine, via ion channels is monitored by competitive displacement of the host•dye complex inside the liposome, providing real-time fluorescence monitoring and kinetics of translocation (Figure 1.5c).[44, 45] A reported variation to this approach applies a pH gradient across the lipid bilayer to aid in controlling detected interior analyte concentrations, improving sensitivity.[46]

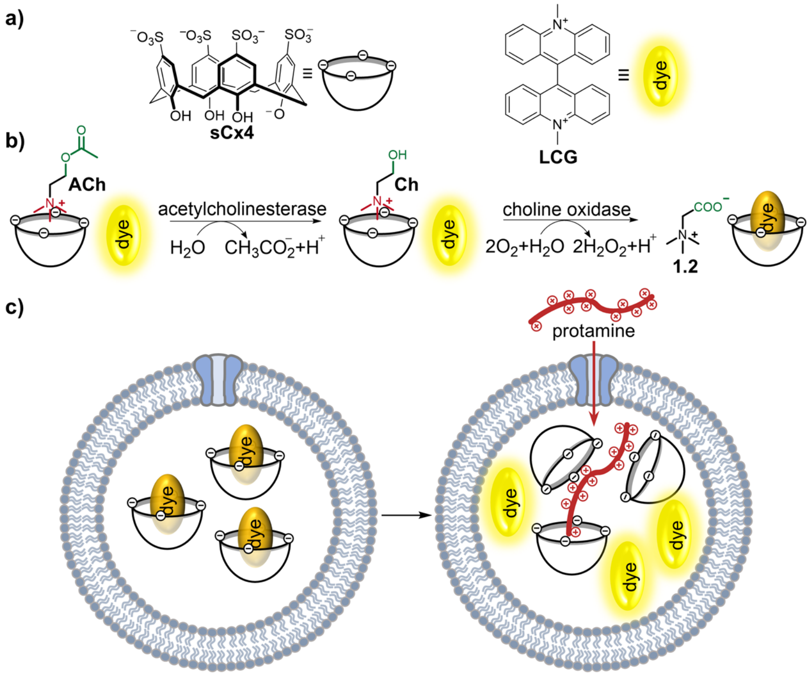

Figure 1.5. IDAs provide a facile label free method for biological tandem assay monitoring. **a)** Chemical structures of host•dye reporter pair **sCx4** and **LCG**. **b)** Choline oxidase followed by acetylcholineseterase enzyme kinetic activity is monitored through a domino turn-off response, as the bound substrates **Ch** and **ACh** are converted to the weaker binding product **1.2**. **c)** Peptide migration into liposomes is monitored through competitive binding of the cationic peptide protamine to **sCx4**, displacing **LCG** and inducing a turn-on fluorescence response.

Despite their ease of design, IDAs can be less effective in the presence of competitive interferants. IDAs are suitable in instances where relative concentrations of interferants do not change over the course of an experiment and the absolute change in signal is high. Although not always commented on, the presence of higher salt concentrations in biological assays and matrix effects among different biological samples can diminish the signal response and reproducibility in IDA experiments. This is a result of the free (unbound) dye being more susceptible to dynamic quenching events with salts and co-solutes in solution, decreasing the amplitude of response. Salts can also act as competitive interferants binding to host cavities and portals, blocking desired host•dye and host•guest complexation events, consequently weakening apparent binding constants. The use of IDAs in biological imaging assays of tissue or whole cells is further complicated by unbound dye being present everywhere in solution.

Synthetically incorporating a dye into a host scaffold is beneficial in cases where dynamic quenching and competition significantly influence apparent binding constants. Commonly used design strategies include the use of a covalently flexible dye tether, allowing intramolecular host•dye complexation or direct integration of an environmentally sensitive dye into the host scaffold (Figure 1.3bc). Although both these methods can be synthetically taxing, often requiring multi-step syntheses, they can help mitigate competitive salt effects as well as dye dilution effects in competitive biological solutions.

Covalently tethering a dye to a host at an optimal distance provides beneficial preorganization and prevents dye dilution. Intramolecular complexation via a flexible tether has been shown to produce increased intramolecular affinity in comparison to an equivalent intermolecular assembly, susceptible to diffusion and competitive binding.[47] The benefits of intramolecular tethered sensors are illustrated by a recent example from Biedermann and co-workers, who compared the conjugated host-linker-dye compounds, cucurbit[7]uril-hexathylene glycol-berberine (**1.3**) and cucurbit[7]uril-tetraethylene glycol-berberine (**1.4**), to an equivalent noncovalent IDA of cucurbit[7]uril (**CB7**) and berberine chloride (**BC**) (Figure 1.6).[48] The barrel-shaped host **CB7** consists of glycoluril units bridged by methylene pairs, forming a rigid hydrophobic cavity, lined with neutral polar carbonyl groups. Complexation of the cationic dye **BC** inside **CB7** induces confinement enhanced photostability, increasing fluorescence.[49] At 100 mM NaCl, complete disruption of the intermolecular **CB7•BC** complex occurs. This is a result of known cationic salts binding cucurbit[*n*]uril carbonyl portals,[50-52] blocking desired binding events (Figure 1.6a). In comparison, intramolecular self-assembly of the conjugated cationic **BC** dye in **1.3** and **1.4**, provides pre-organization and further repels cationic salt binding, functioning in the presence of ~10^6-fold excess NaCl (Figure 1.6a). This tethered intramolecular assembly allows for the detection of Parkinson’s drug amantadine (**AdNH$_3^+$**) in solutions of human urine and saliva at medically relevant concentrations (Figure 1.6b).[48] Conjugated cucurbit[*n*]uril cationic dye sensors have been further explored in complex media with examples of cellular imaging in live and fixed HT22 neurons, where sensor conjugation alleviates dye dilution effects within cell-based applications.[53]

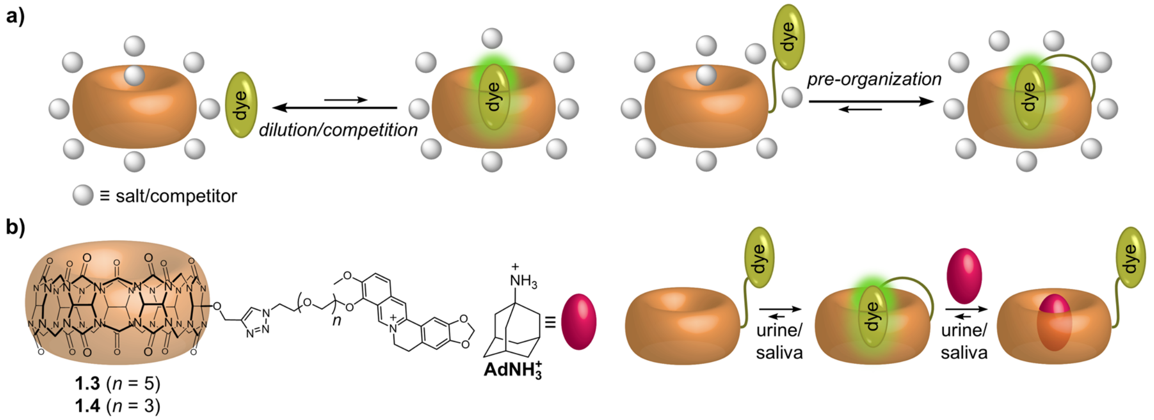

Figure 1.6. Covalently tethered host-linker-dye conjugates help mitigate salt effects. **a)** High concentrations of salts present in biofluids can competitively bind host portals. Synthetic host-linker-dye conjugates provide pre-organization, reducing competitive salt effects. **b)** Chemical structures of unimolecular host-linker-dye conjugates **1.3** and **1.4**, covalently tether **BC** dye to the host **CB7** via a hydrophilic flexible ethylene glycol linker. Chemical structure of target Parkinson’s drug **AdNH$_3^+$**. Intramolecular self-assembled sensing detects **AdNH$_3^+$** in saline solution, urine and saliva.

Salt tolerant sensing motifs can be achieved through directly integrating a dye into the host scaffold. The aforementioned DimerDye, **DD1Cx4** integrates Brooker’s Merocyanine, compound **1.1** into the host scaffold, forming a nonemissive homodimer **DD1Cx4$_2$** in aqueous solution (Figure 1.7).[54] This dimerization motif persists in the presence of salts, likely due to cationic salt screening effects, decreasing repulsion and facilitating the self-assembly of the like-charged anionic hosts.[55] Disassembly driven turn-on fluorescence detection of cationic hydrophobic analytes is maintained in the presence of co-solutes, buffers, metal ions and cofactors, functioning in biologically relevant media. The biological application potential of this system was illustrated by a real-time enzyme assay, monitoring the conversion of 21-mer histone tail peptide **H3K4** to **H3K4me$_3$** by methyltransferase PRDM9 (Figure 1.7). Disassembly-driven turn-on sensing of **H3K4me$_3$** is achieved through binding of the cationic hydrophobic methylated lysine residue, outcompeting homodimerization.

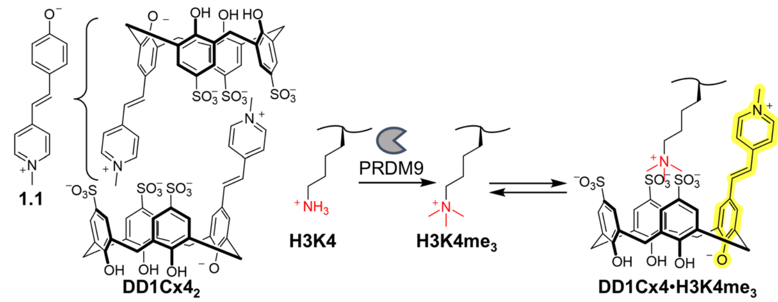

Figure 1.7. DimerDye disassembly-driven turn-on sensing functions in biological enzyme assay conditions. Lysine methyltransferase PRDM9 converts the 21-mer histone tail peptide **H3K4** to **H3K4me$_3$**, monitored by turn-on fluorescence detection of **DD1Cx4**.

Mechanical bonds can be used to further protect sensor function in complex media. In one study, the host•dye reporter pair, cucurbit[8]uril (**CB8**) and di-alkylated 2,7-diazapyrene (**DAP**), were embedded within a rotaxane structure (**1.5**) (Figure 1.8).[56] The attachment of β-cyclodextrin (***β*-CD**) stoppers on either end of the rotaxane prevent disassembly of the threaded **CB8•DAP** complex, while the polyethylene glycol linkages to **DAP** aid in water solubility (Figure 1.8). This elaborate interlocked construction only allows binding to select small molecules capable of forming a ternary complex with **CB8•DAP**, minimizing media interference and inhibiting host•dye dilution effects. Binding of the electron-rich aromatic biomarker tryptophan (**W**), produces decreased emission through charge transfer to the electron-deficient aromatic dye **DAP**.[56] Through a rotaxane protection strategy, binding of amino acid biomarker **W** in human blood serum and urine was achieved, operating at physiologically relevant concentrations associated with cardio-vascular and neurodegenerative diseases.

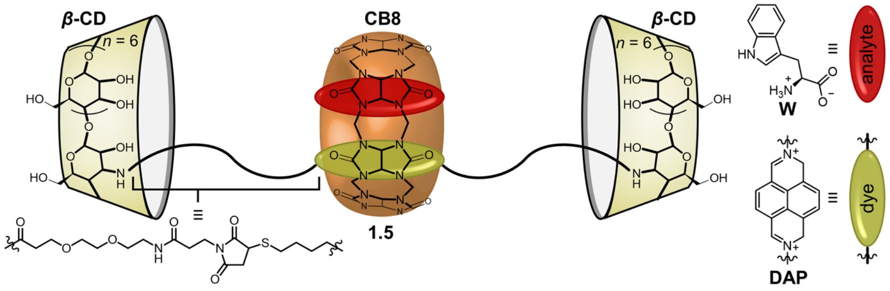

Figure 1.8. Rotaxane structure **1.5** protects the mechanically interlocked host•dye reporter pair **CB8•DAP** with ***β*-CD** stoppers, producing a decreased emission response upon **W** binding in human blood serum and urine.

Selective detection of larger biomacromolecules by host-based sensors is challenging due to the increased number of similar binding sites. For example, larger peptides can contain multiple amino acid residues known to form binding interactions with macrocyclic hosts. In cases where sensing of a single peptide or protein occurs in isolation this does not pose a problem. However, this becomes more challenging in complex mixtures where selectivity is desired for one peptide over another, sharing the same known amino acid binders within its sequence.

Heteromultivalent host co-assemblies can enable selective sensing of larger biotargets. A more recent multi-macrocyclic adaptation to IDAs, reported by Guo and co-workers, introduces a method of self-adaptable detection through multiple peptide biotarget binding interactions.[57] In this example, co-assembly of an amphiphilic ***β*-CD** host (**1.6**) and an amphiphilic calix[5]arene host (**1.7**) form heteromultivalent vesicle aggregates, with many copies of the hosts coating the outer surface (Figure 1.9). This approach addresses multi-modal binding and site mismatching through recognition of the amino acids tyrosine (**Y**) with host **1.6** and lysine (**K**) with host **1.7**, using **LCG** as a noncovalent indicator for competitive binding to **1.7**. The dynamic self-assembly of the vesicle itself allows for surface mobility of the co-assembled hosts, providing self-adaptable detection of model peptides containing **Y** and **K** amino acid residues at different positions. The affinity-enhancing effects of multivalency are sufficient to allow binding and detection under competitive aqueous conditions,[58] while significantly enhancing selectivity towards peptides rich in **Y** and **K** amino acids. Although this work operates on the premise of a conventional IDA, it represents a large jump in systems complexity, incorporating known molecular recognition events with larger dynamic aggregated self-assemblies.

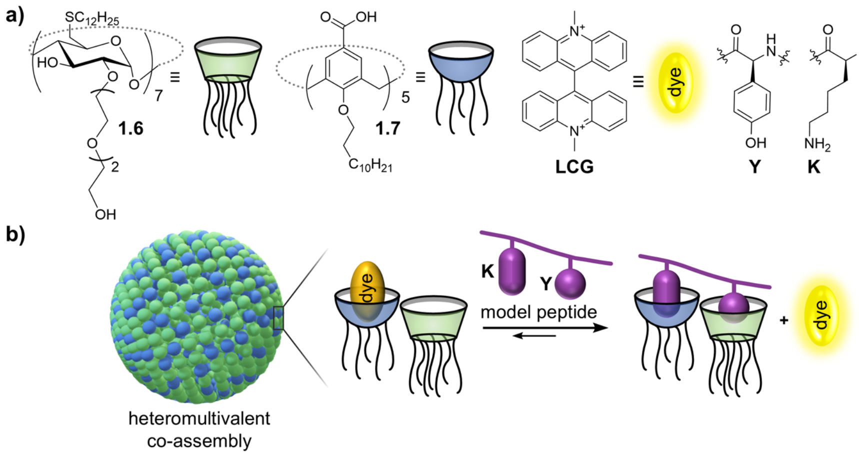

Figure 1.9. Co-assembly of amphiphilic hosts **1.6** and **1.7** form heteromultivalent vesicles for heterotopic detection of **Y** and **K** containing peptides. **a)** Chemical structures of amphiphilic host **1.6**, amphiphilic host **1.7**, indicator dye **LCG**, and amino acid residues **Y** and **K**. **b)** Co-assembly of amphiphilic hosts form heteromultivalent supramolecular vesicles. Binding of **LCG** to host **1.7**, transforms the co-assembled heteromultivalent vesicles into an IDA. The mobile self-assembled nature of the system allows for flexible heterotopic binding with enhanced affinity towards peptides rich in **Y** and **K** amino acids.

1.3 Strategies in cross-reactive differential sensing

Host-based systems are inherently selective towards a given type of analyte. Examples introduced thus far have incorporated pairwise scenarios where a single analyte is targeted for binding. Here, the distinction between specificity and selectivity is important. In the context of sensing systems, we define specificity as the detection of a single analyte by a single sensor, responding only to that analyte. This is based around the "lock-and-key" principle established by Emil Fischer, where the asymmetric properties of an enzyme binding pocket induce specific binding to one substrate.[59] Specific sensors are most valuable in cases where a single target needs to be identified within a complex mixture (e.g. antibodies). Conversely, we define selectivity as the ability to bind multiple structurally similar analytes to varying degrees. Unlike protein binding pockets, which evolved to have specificity, macrocyclic hosts contain a high level of symmetry and are therefore selective by nature. In the context of host-based systems, most macrocyclic hosts are good at binding certain classes of analytes but fall short when it comes to the specific binding of a single target molecule amongst structurally similar binding partners. This inherent selectivity (and corresponding lack of specificity) is advantageous in differential sensing platforms.

Selective cross-reactive receptors are powerful tools in differential sensing schemes. Often referred to as "chemical nose", cross-reactive sensors use signal response patterns as a fingerprint to identify many different entities. Relying on cross-reactive selectivity, chemical nose sensors surpass the limitations enforced by lock-and-key specific detection (i.e. *n* receptors are needed for *n* analytes). This is likened to the mammalian olfactory system,[60] where the human nose can detect and discriminate over 10^{12} different olfactory stimuli, despite containing only approximately 400 olfactory receptors.[61, 62] The key to applying this approach in differential host-based sensing is obtaining reproducible unique response patterns for a variety of analytes, through fast stable equilibria varying in affinity. While signal processing in the human brain is complex, the signal processing for chemical nose sensors can be relatively straightforward. Through chemometric statistical analysis methods, multiple numerical absorbance and/or fluorescence responses from host•dye reporter pairs can be used as a fingerprint pattern to differentiate and identify analytes (Figure 1.10). The true power in this approach lies within the ability to differentiate more analytes than the number of sensors required.

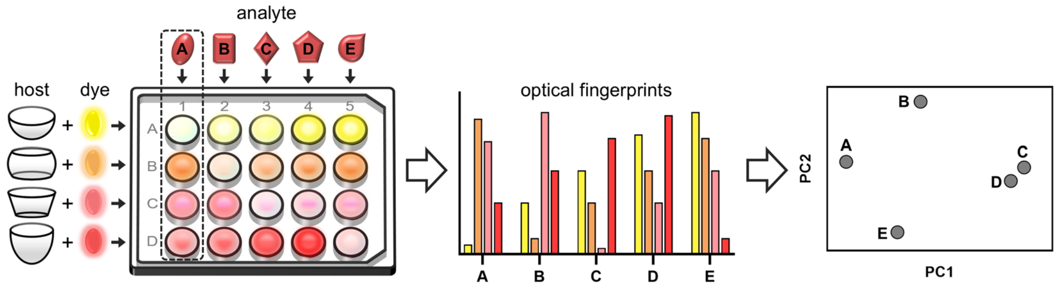

Figure 1.10. An array of host•dye reporter pairs can discriminate multiple guest analytes through chemometric analysis.

Differential sensing analysis is performed using multivariate statistical methods such as principal component analysis (PCA) and linear discriminant analysis (LDA). The aim of both techniques is to reduce large data sets – in this case multiple absorbance and fluorescence wavelength observations from the same or different sensing units – down to two- or three-dimensional space for visualization. PCA applies an unsupervised approach to retain the greatest variance while simplifying a complex dataset,[63] whereas LDA applies a supervised approach to identify classes (in this case target analytes) and maximize the distance between them.[64] Anslyn and co-workers have provided a helpful review describing the many factors involved in refining and improving differentiation plots.[65] More recently, machine learning algorithms like support vector machine (SVM),[66] and iterative recursive feature elimination (RFE)[66-69] are being applied as supervised techniques to aid in both regression and classification to identifying the most informative responses within an array, eliminate over-fitting data and build calibration models.[70, 71]

Pattern-recognition based sensing is easily applied to the differentiation of small molecules. During my first year as a graduate student, I contributed as second author on a project led by Dr. Meagan Beatty, detecting and differentiating hydrophobic cationic illicit drugs in buffer and saliva.[72] This work expanded on the previously mentioned DimerDye sensors, applying a parallel synthesis approach to develop an array of sixteen DimerDye analogs, varying the integrated merocyanine dye. Parallel testing of turn-on fluorescence responses narrowed down the array to five hit DimerDye sensors; containing *N*-methylpyridinium (**DD1Cx4** and **DD8Cx4**), indolinium (**DD4Cx4**), bipyridinium (**DD12Cx4**) and *N*-phenylpyridinium (**DD13Cx4**) pendant arms (Figure 1.11a). This assortment of integrated dyes introduces both photophysical diversity, covering a range of absorbance and emission wavelengths, as well as structural diversity, varying affinities towards detected analytes. Each of these sensors operates through disassembly driven turn-on fluorescence, detecting cationic hydrophobic drugs, nicotine, cocaine, and 3,4-methylenedioxymethamphetamine (**MDMA**) in both buffer and saliva within relevant low µM concentrations found after ingestion. Deployed in an array, PCA and LDA analysis of isolated DimerDye responses successfully differentiates between active illicit drugs and closely related metabolites within classes of amphetamines (Figure 1.11b), anesthetics (Figure 1.11c) and opioids (Figure 1.11d).

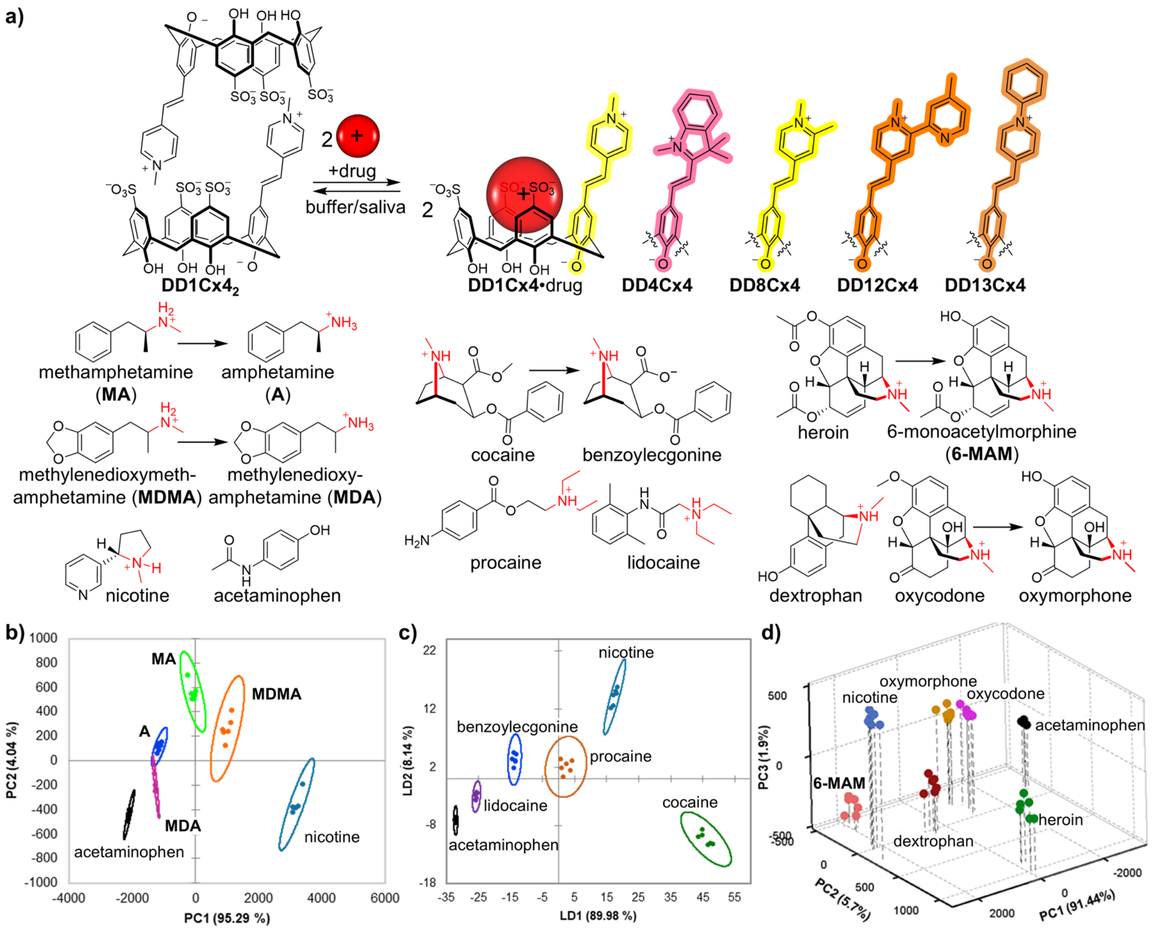

Figure 1.11. An array of five DimerDye sensors distinguishes between different members and classes of illicit cationic drugs. **a)** An array of five DimerDye sensors (**DD1Cx4**, **DD4Cx4**, **DD8Cx4**, **DD12Cx4** and **DD13Cx4**) operate by a disassembly driven turn-on fluorescence sensing mechanism, detecting hydrophobic cationic drugs in buffer and saliva. Chemical structures of tested hydrophobic cationic drugs and their metabolites. Red indicates binding motifs. PCA and LDA analysis of an array of five DimerDyes distinguishes between **b)** amphetamines **c)** anesthetics and **d)** opioids. Adapted with permission from *J. Am. Chem. Soc.* 2019, 141, 42, 16763–16771. Copyright 2019 American Chemical Society.

Beyond data refinement, differential sensing falls short when analyte affinities for a set of hosts are too similar. Overlapping analyte clusters in differential plots are often an indication that sensor array response patterns are not unique among a given panel of analytes. Overlap of analyte confidence ellipses can also occur when sensing responses have high deviation within a set of replicates, relative to the amplitude of response. One strategy to overcome this is the incorporation of more hosts in an array that reinforce observed patterns, decreasing noise within clustered replicates. Alternatively, building sensor arrays that incorporate hosts with different binding properties, or different photophysical response mechanisms, can have a greater impact on multivariate analysis and improve analyte discrimination.

Incorporating different modes of analyte interactions can aid in differential sensing. This is demonstrated by reported dual site upper- and lower-rim functionalized pillar[5]arene host **1.8**, that combines noncovalent host•guest recognition with two reactive dynamic covalent fluorophore handles (Figure 1.12).[73] This design strategy provides an alternative approach to a panel of host•dye self-assembled sensors. Instead, seven neurotransmitters are differentiated by a singular host through different modes of interaction, prompting different fluorescence response patterns. The pillar[5]arene's electron-rich host cavity contributes electrostatic noncovalent binding to the hydrophobic cationic neurotransmitter **ACh** (Figure 1.12b). Appended fluorophores on host **1.8** provide emission wavelength variables, corresponding to the chemical reactivity of the two attached dynamic covalent handles. Boric acid-naphthalimide allows for condensation reactions with catechol-containing neurotransmitters (dopamine, epinephrine and norepinephrine), while aldehyde-coumarin undergoes Schiff base condensation reactions with monoamine containing neurotransmitters (dopamine, norepinephrine, serotonin, glutamate, and histamine) (Figure 1.12b). This design strategy provides rapid access to detection and maintains function in cerebrospinal fluids. Two photon long wavelength excitation of the napthlaimide and coumarin fluorophores enabled PCA neurotransmitter differentiation within live neurons, and three-dimensional imaging of neurotransmitters in brain tissue, from the hippocampus Alzheimer's disease region of a mouse.

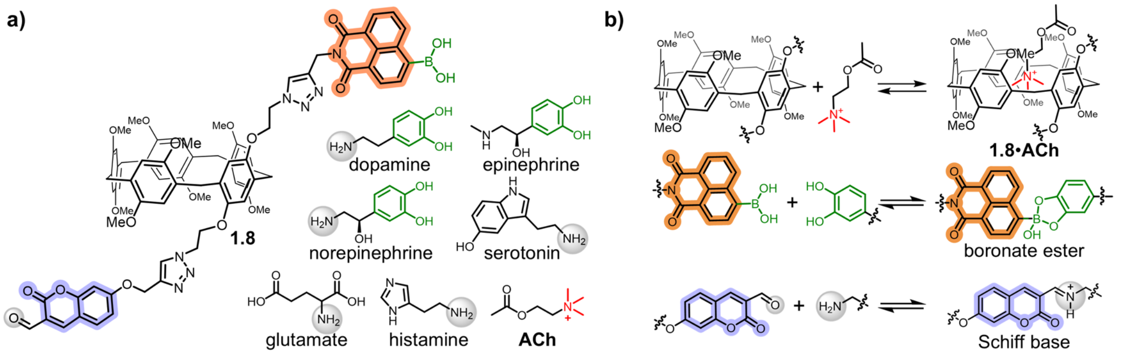

Figure 1.12. Dual reactive host sensor **1.8** provides multimodal detection and differentiation of neurotransmitters in live neurons. **a)** Chemical structure of host **1.8** and differentiated neurotransmitters. The incorporated naphthalimide and coumarin fluorophores on host **1.8** are indicated by orange and purple highlights respectively. Reactive boric acid and catechol handles are show in green. Reactive aldehyde and primary amine handles are shown as grey circles. **ACh** quaternary amine binding motif is shown in red. **b)** Neurotransmitter detection by host **1.8** occurs through noncovalent self-assembly with cationic quaternary amines, and dynamic covalent reactions with catechol and primary amines.

Extending this concept further, sensor arrays that incorporate a range of binding interactions and photophysical mechanisms provide more diverse differential response patterns. In one example a library of six **CB7**-fluorophore conjugated hosts (**1.9** to **1.14**) were applied to the detection and differentiation of twelve different model proteins (Figure 1.13).[74] In this system the **CB7** cavity pan-selectively binds protein surface amino acid residues phenylalanine, tryptophan and tyrosine, with the conjugated dye providing additional secondary surface binding interactions. Diversity of response within this array arises from topological dye•protein interactions, inducing different photophysical response mechanisms. This includes binding induced steric hindrance of the conjugated cyanine dyes in hosts **1.10** and **1.11** resulting in enhanced emission (Figure 1.13b), as well as **1.11** absorbance/emission shifts resulting from instances of induced dye polarity and decreased emission from dye aggregate formation. Hydrophobic binding interactions of conjugated silicon rhodamine in **1.14** results in ground state deactivated spirolactone formation (Figure 1.13b). Decreased emission responses from conjugated coumarin in **1.9**, 4,4-difluoro-4-bora-3a,4a-diaza-*s*-indacene (**BODIPY**) in **1.12** and tetramethyl rhodamine in **1.13** are likely a result of amino acid static quenching events, as well as local pH effects on **1.9**. This sensitivity to a range of topological features linked to different photophysical responses was exploited in the differentiation of protein conformational changes, identifying native, misfolded, oligomeric and fibrillar protein states. Notably, this approach was able to distinguish amyloid-β folded aggregates associated with Alzheimer's disease.

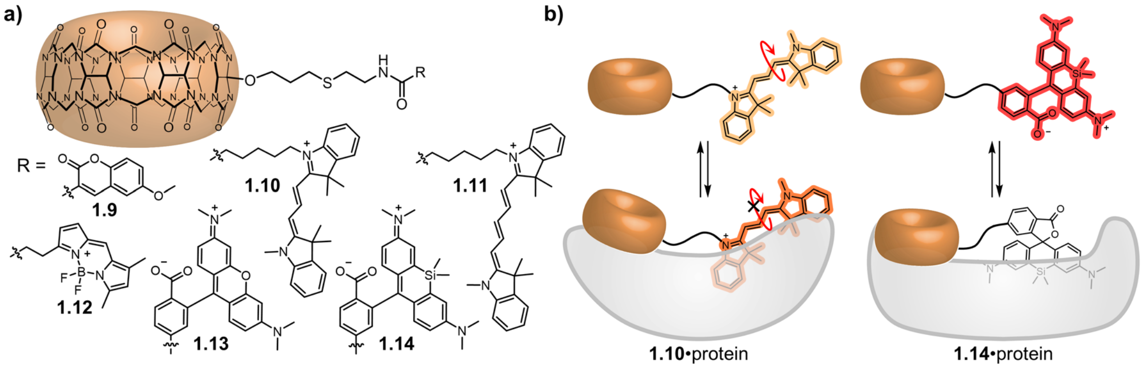

Figure 1.13. A diverse array of conjugated **CB7**-fluorophores provides different mechanisms for probing protein surfaces, identifying a range of proteins and conformational folded states. **a)** Chemical structures of an array of **CB7**-fluorophore conjugates, **1.9** to **1.14**. **b)** Sensing scheme illustrations of enhanced emission of **CB7**-cyanine host **1.10** through protein induced restricted rotation and decreased emission of **CB7**-silicon rhodamine host **1.14** from spirolactone formation in hydrophobic protein environments.

So far, cross-reactive sensor arrays consisting of isolated host•dye reporter pairs or conjugated host sensors have proven effective at discriminating individual target analytes. In these examples solution complexity has progressed towards sensors that maintain function in biorelevant conditions, containing higher salt content and other competitive species. More recent examples in literature have demonstrated that incorporating diversity through a range of recognition properties and photophysical outputs can enhance differenital applications from biologically important small molecules, to larger peptides and proteins. Despite these advances, distinguishing highly similar analytes and complex mixtures of analytes is an ongoing challenge within the field. As application difficulty increases, more information-rich sensing outputs are required.

1.4 Expanding differential sensing through increased systems complexity

Systems chemistry is a powerful tool at the forefront of adaptive information-rich sensing. In complex systems, adaptive behaviour arises through self-organized networks of multiple interconnected equilibria. Information-rich outputs are produced from induced shifts in the overall networked equilibria, and emergent properties can arise that are otherwise unobtainable from the isolated system components.[75] Earlier work by Anslyn[76] and Severin[77] applied systems chemistry in sensing, showing that a single mixture of multiple interacting receptors and indicators can differentiate analytes through unique networked equilibria. The recent application of systems chemistry in macrocyclic host-based sensing has switched perspectives from isolated pairwise molecular recognition events, towards building more complex systems. A simple way to increase complexity is through a co-complexation agent, an additional component (e.g. metal ion or salt) that interacts with sensor building blocks, promoting the formation of additional complexes and/or binding geometries in equilibrium. Complexity can also be introduced by increasing the number of interacting building blocks (e.g. multiple dynamic covalent building blocks, multiple interacting hosts and/or dyes in a single solution), this can be further extended into multicomponent systems that form higher order complexation events.

Co-complexation agents in host-based sensing systems can modulate multiple binding geometries, enhancing sensing outputs for differentiation. In one example the known adverse effects of cationic salt interactions binding cucurbit[*n*]uril carbonyl portals was exploited as a method of introducing adaptive sensing (Figure 1.14).[78] The unimolecular host-linker-dye conjugate **1.15** tethers a polarity responsive dye, nitrobenzoxadiazole (**NBD**), to **CB7**. This synthetic design encourages co-complexation interactions with cationic salts (M^{n+}), facilitated by the conjugation of a neutral weak binding dye, **NBD** (as apposed to the previously introduced cationic dye conjugates **1.3** and **1.4** that repelled cationic salts). Host **1.15** forms an equilibrium of multiple analyte binding geometries modulated by secondary salt interactions (Figure 1.14b). These salt interactions induce distinctive spectral shifts in absorbance and emission, contributing to a unique analyte fingerprint. Through alterations in fixed salt concentration and salt type, PCA differentiation of 14 bioorganic analytes (Figure 1.14a) in buffer and biofluids (human urine, deproteinized human serum, artificial saliva and artificial synthetic urine) was achieved.

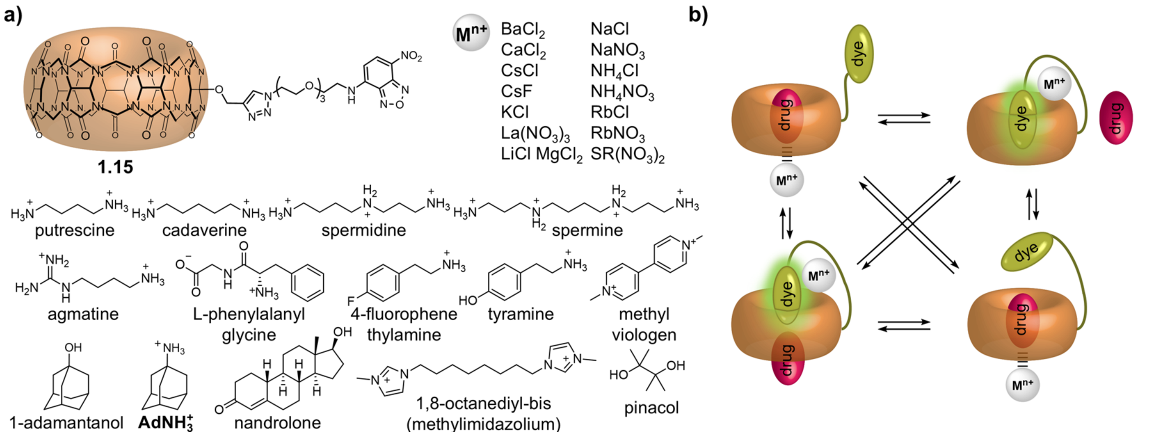

Figure 1.14. Salts can be used as binding modulators, providing adaptive differential sensing of biorelevant compounds. **a)** Chemical structures of the unimolecular dye conjugated host **1.15**, biorelevant analytes for differentiation and modulating salts (M^{n+}). **b)** Salt-induced analyte binding effects can cause displacement of the dye or induce different modes of binding in equilibrium, creating unique analyte sensing outputs.

Combining dynamic combinatorial libraries and multi-component noncovalent networks introduces a new method of *in situ* host formation and differential sensing. Waters and co-workers described an "imprint-and-report" dynamic combinatorial library, in which exchangeable dithiol building blocks form template-driven macrocycles, for indicator displacement differential sensing (Figure 1.15).[79] First the formation of disulfide containing macrocycles is templated by a guest (analyte or dye), amplifying a mixture of thermodynamically favoured hosts at increased concentrations relative to an untemplated system. Key to the operation of this approach is complete disulfide oxidation, "imprinting" the formed macrocycles that inhibit building block re-equilibration. Subsequent addition of a secondary guest (dye or analyte) provides a unique signal based on a network of noncovalent interactions with the mixture of imprinted macrocycles (Figure 1.15bc). Applied in an array, combinations of 3-5 dynamic combinatorial libraries (incorporating different macrocycle building blocks (**1.16**, **1.17** and **1.18**), dyes (**LCG**, **1.19** to **1.22**), and analytes (methylated states of histone peptides) discriminate all post translational modifications on arginine (**R**) and lysine (**K**) residues of histone peptides **H3R8me**$_x$ and **K9me**$_y$ respectively. This dynamic combinatorial and noncovalent systems approach negates the requirements of host synthesis optimization, purification and characterization, achieving analyte differentiation through a complex network of equilibria. Further advancements of "imprint-and-report" dynamic combinatorial libraries have been applied to the differentiation of trimethylamine N-oxide dietary metabolites and precursors,[80] as well as per- and polyfluoroalkyl contaminant mixtures in water.[81]

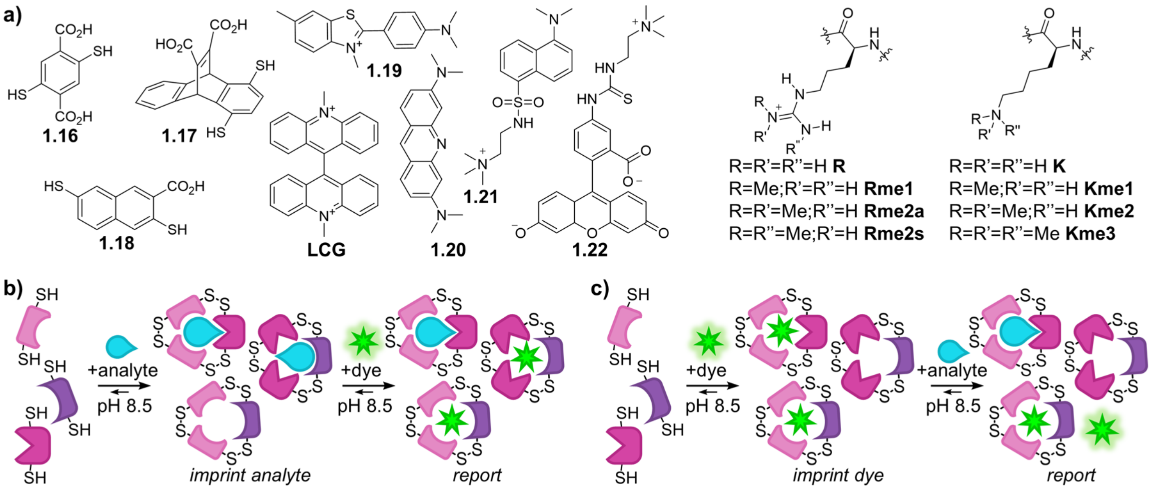

Figure 1.15. Dynamic combinatorial libraries are combined in an "imprint-and-report" sensor array, differentiating methylation states of **R** and **K** containing peptides. **a)** Chemical structures of exchangeable building blocks (**1.16**, **1.17** and **1.18**), fluorescent dyes (**LCG**, **1.19**, **1.20**, **1.21** and **1.22**) and methylation states of arginine and lysine containing histone peptides **H3R8me$_x$** and **K9me$_y$**. **b)** Dynamic combinatorial library components are imprinted by an analyte and then competitively displaced by a reporter fluorophore. **c)** Dynamic combinatorial library components are imprinted by a fluorophore and then competitively displaced by an analyte.

Highly similar biomacromolecules pose a challenge in differential sensing. Identifying small variations between biomacromolecules with conserved sequences and relative charge (e.g. differences in 3D folding and orientation) is a nontrivial task, often requiring techniques like crystallography and multi-dimensional NMR spectroscopy. In host-based sensing, detection of highly similar biomacromolecules is limited by the similarity between molecular recognition events, engaging closely related binding motifs present on the surface of biomacromolecules (e.g. anionic hosts binding cationic **K** and/or **R** amino acid residues). When slight differences in biomacromolecules do not strongly influence host binding events, differential sensing becomes more challenging. Systems chemistry approaches that introduce multiple interacting components, in equilibrium with each other and with multiple analyte surface features, can overcome these limitations. Through their combined output the effects of many relatively small differences can be detected.

Multi-complexation systems can distinguish identical biomacromolecule sequences that have adopted different folded structures. Work presented by Hooley and coworkers demonstrated that an array of sensing systems differentiated noncanonical folded DNA motifs by increasing the number of competing equilibria.[70, 82, 83] In this approach, cationic styryl pyridinium dyes (compounds **1.26** to **1.29**) act as the primary sensing motif, mimicking known oligonucleotide ligands that directly bind DNA through aromatic nucleotide π-π stacking and phosphate backbone ionic interactions. The addition of cationic deep cavitand hosts (**1.23** to **1.25**) can interact with the dye, DNA, or both, in a mixture of competing binary and ternary fluorescent complexes (Figure 1.16b). In one report a 16-element sensor array (4 styryl pyridinium dyes × 3 cavitand hosts and 4 isolated dyes) was applied to the differentiation of 18 different nonclassical DNA motifs (DNA G-quadruplexes with bulges and vacancies, Hoogsteen triplexes, hairpin and i-motifs).[70] This large data set illustrates an example where hand-selecting array responses for multivariate analysis becomes challenging. Fluorescence array outputs analyzed by an SVM-RFE training algorithm followed by PCA, not only allowed for successful challenging differentiation but also classification of unknown DNA folded motif samples. Most notably, differentiation is not possible with a traditional sensor array consisting of a set of DNA binding dyes. This demonstrates an increase in information obtained from additional competing equilibria, through hosts that don't bind DNA directly, but compete with DNA for dye binding. The performance of this system-based sensor exceeds that of the related dye-based sensor array.

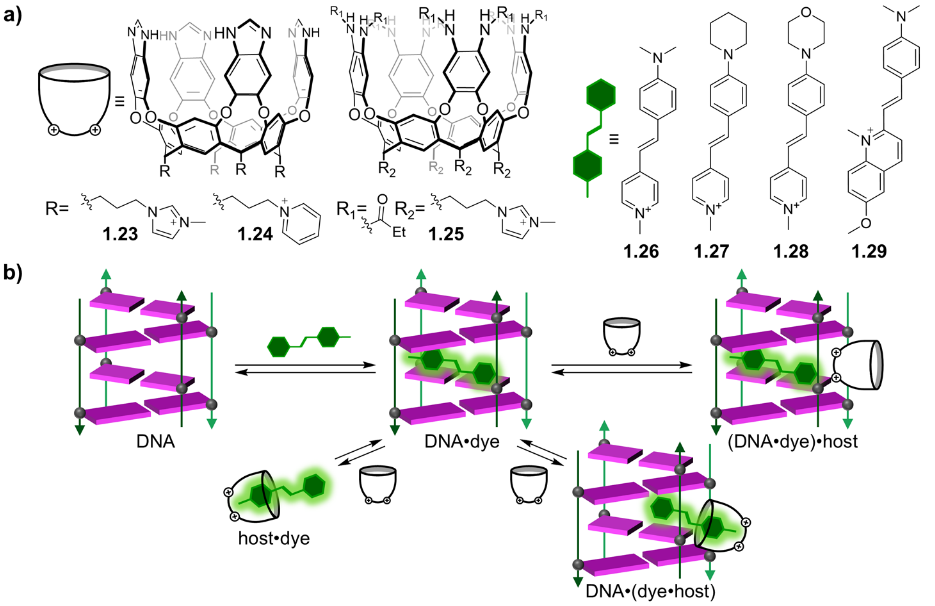

Figure 1.16. An array of cationic deep cavitand hosts and styryl pyridinium dyes discriminate highly similar noncanonical DNA folded motifs. **a)** Chemical structures of cavitand hosts (**1.23** to **1.25**) and reporter styryl pyridinium dyes (**1.26** to **1.29**). **b)** Schematic illustration of the multiple binary and ternary complex equilibria between DNA i-motif, host, and reporter dye leading to differential sensing of folded DNA.

Adjustments in building block combinations, component ratios and environment are a facile way to provide a level of complexity that enhances differential sensing while requiring a relatively small number of sensor building blocks. Work presented by Guo and coworkers reports on the straightforward construction of tunable sensor array libraries that involve heteromultivalent self-assemblies.[84] Co-assembly of calixarene (**1.30** to **1.37**) and cyclodextrin (**1.7**) amphiphilic hosts leads to the formation of self-assembled vesicle aggregates that vary in recognition ability (Figure 1.17a). The dynamic noncovalent self-assembly of vesicles allows for the generation of several different co-assembled sensors whose binding properties are modified simply by varying their relative concentrations. Fluorescent dyes were selected for known binding interactions with cationic calixarene hosts (**1.30** to **1.33**) that induces fluorescence quenching (dyes **1.38** and **1.41**) and fluorescence enhancement (dyes **1.39**, **1.40** and **1.42**), as well as binding to anionic calixarene hosts (**1.34** to **1.37**) that induce fluorescence quenching (**LCG**). This work incorporates a multitude of sensor arrays with different host co-assemblies, outlined dye combinations, component ratios and solution pH; fixing one of these variable within each array (Figure 1.17b). Through this array library strategy, thirteen model proteins and their mixtures were differentiated using LDA analysis. Array-based sensing was further applied to the differentiation of honeys from different floral origins, brands and adulterated mixtures representing more complex sample compositions (containing sugars, enzymes, amino acids, vitamins, minerals and aromatic compounds). The discrimination ability of these senor arrays arises from the different intertwined host•dye, host•analyte, and dye•analyte affinities within the system, as well as the nonlinear relationship between signal response and concentration. This work represents a very robust path to quickly and easily obtaining information-rich libraries that can be extended to many building blocks and targets. Further development of heteromultivalent amphiphilic co-assemblies have been applied in recognition and discrimination of normal, cancerous and cross-contaminated cell lines.[85]

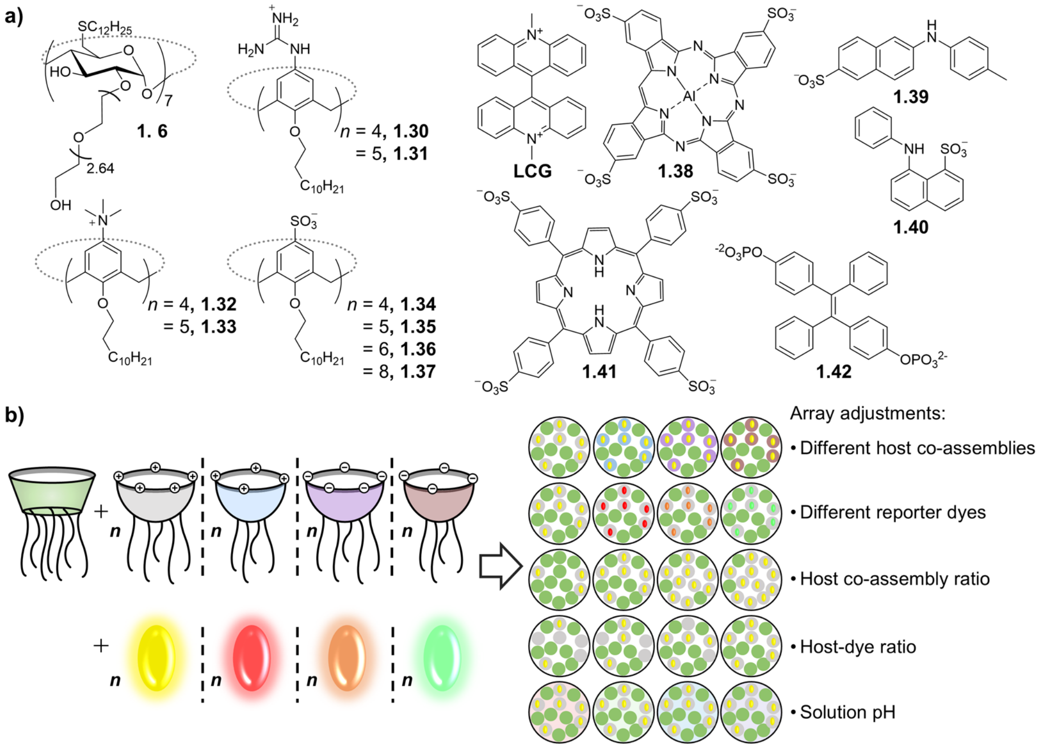

Figure 1.17. Muli-complexation sensing systems provide a robust and facile method for building differential sensor arrays. **a)** Chemical structures of amphiphilic hosts (**1.7**, **1.30** to **1.37**) and reporter dye (**LCG**, and **1.38** to **1.42**) building blocks explored in the construction of multiplexing sensor arrays. **b)** Schematic representation of different host co-assemblies, reporter dye combinations, ratios and environmental pH conditions used to differentiate model proteins.

Overall, the recent application of systems chemistry represents a paradigm shift in the field towards increasingly complex, information-rich sensing. The development of multi-component macrocyclic systems has led to more advanced sensing functions, with rapid access to information-rich outputs. Through increased complexity, differential sensing outcomes can be reached that are otherwise unachievable by conventional isolated host•dye sensor arrays. This development in complex systems has begun to shift supramolecular host-based sensing towards larger information-rich data sets, akin to those seen in bioinformatics. This will stimulate further advancement and implementation of machine learning algorithms and supervised differential analysis techniques, as host-based sensing systems continue to grow in both complexity and capability.

Summary of dissertation

This dissertation presents strategies for developing functional supramolecular systems of increasing complexity in aqueous solution. The goal of this dissertation is to explore and expand on system-oriented approaches that can be used to improve host synthesis and develop more powerful sensing tools. The host **sCx4** is the parent structure used throughout this dissertation, as it is an excellent candidate for biological applications.[86, 87] The sulfonated upper rim imparts water solubility, with the hydrophobic cavity forming favourable complexes with nonpolar cationic guests in aqueous solution. Synthetic modifications are readily achieved, tuning molecular recognition events and introducing new functionalities.[88] In this dissertation I create novel hosts with applications in drug reversal (Chapter 2) and sensing of challenging analytes (Chapters 3 and 4). The degree of complexity builds from Chapter to Chapter, aiming to provide conceptually new methods that can be readily applied by others in the field. To demonstrate the benefit and value of multi-interacting systems, each Chapter makes direct comparisons to previously reported reductionist approaches.

In Chapter 2, I use a target drug to template the synthesis of novel bivalent hosts in aqueous solution as new potential drug reversal agents. This work illustrates how noncovalent self-assembly and dynamic covalent chemistry in aqueous solution can be used as a tool to obtain more synthetically challenging host structures. We show that templated synthesis in aqueous solution not only produces pan-selective hosts, binding target drugs that share a common pharmacophore to the template, but it also ensures strong binding affinity under biologically relevant conditions.

In Chapter 3, I introduce an adaptive network of hosts as a new systems-oriented approach to differential sensing. This work builds on the concepts of multi-component host systems that were introduced in Section 1.4. We show that combining multiple hosts with different integrated fluorophores into a single sensing solution forms a network of interconnected equilibria. This network is primed to shift in distinct ways when an analyte is introduced, with the overall shifts in multiple linked equilibria providing a unique information-rich photophysical fingerprint. We show that the adaptive network out-performs analogous traditional sensor arrays by distinguishing highly similar serum albumin proteins and by profiling complex protein tissue extracts.

In Chapter 4, I further advance host-based sensing systems by co-assembling hosts from different families, achieving an increase in the scope of analytes that can be detected. By co-assembling two different host types via an integrated environmentally sensitive fluorophore, we create a system that can detect analyte binding interactions to either host. We show that mixed host co-assembled sensors can distinguish a range of hydrophobic, cationic and neutral drugs. We further challenge the system and introduce complexity by applying mixed host sensors to multi-component illicit street drug samples.

Chapter 2: Template-directed synthesis of bivalent, broad-spectrum hosts for neuromuscular blocking agents

This work was adapted from a previously published paper.

Allison J. Selinger, Natalie A. Cavallin, Anat Yanai, Inanc Birol and Fraser Hof
Angew. Chem. Int. Ed., **2022**, 61, e202113235.

AJS and FH conceptualized the idea. AJS was lead on investigation, formal analysis and methodology development. AJS designed, optimized and characterized the synthesis of the novel calix[5]arene precursor compounds **2.13**, **2.14**, **sCx5-CHO**, along with the novel bivalent water-soluble hosts **Super-sCx4** and **Super-sCx5** and the control monofunctionalized hosts **sCx4-CH$_2$NHNH$_2$** and **sCx5-CH$_2$NHNH$_2$**. AJS supervised NAC in preliminary IDA binding experiments, while the final reported IDA results were completed by AJS. Mechanistic studies that included DOSY NMR, molecular modeling, ^{1}H NMR titrations, and ITC were designed, conducted, and analyzed by AJS. AY led the cell viability assay experiments supervised by IB, in collaboration with Canada's Michael Smith Genome Sciences Centre, Vancouver, Canada. AJS wrote the original draft of the paper. AJS and FH contributed to reviewing and editing the paper.

2.1 Foreword

The work presented in this Chapter began through a serendipitous discovery. The original intent of this dissertation was to develop new sensing systems. While attempting to synthesize a new monovalent hydrazone-linked calixarene sensor, I noticed a small amount of bivalent hydrazone-linked host had formed in an NMR-tube scale experiment. This opened the door to the possibility of synthesizing bivalent water-soluble hosts. The synthesis of several different kinds of bivalent sulfonate calixarene hosts had been previously attempted in the Hof group and repeatedly failed, due to the mutual repulsion encountered when trying to link two highly anionic building blocks. To overcome this challenge, I applied a templated synthesis approach. Motivated by the rising application of synthetic hosts as drug reversal therapeutics, we selected a bisquaternary amine neuromuscular blocking agent (NMBA) as both a template for synthesis and a target analyte for further binding studies. We wanted to show that this template strategy can produce new hosts that operate in biologically relevant conditions, with pan-selective affinity towards drugs that share the same key binding motifs. This Chapter demonstrates the power of equilibrating systems, relying on dynamic covalent interactions and self-assembly to achieve a previously unobtainable host with therapeutic potential.

2.2 Introduction

Neuromuscular blocking agent's (NMBA's) are frequently administered in clinical practice during anesthesia. NMBA's block the action of acetylcholine (**ACh**) by binding nicotinic acetylcholine receptors (nAChR) at the postsynaptic endplate of the neuromuscular junction.[89] A variety of structurally diverse NMBA's are used in clinical practice to meet different pharmacological needs.[90] Although NMBA's vary in structure, they adhere to a pharmacophore model having two alkyl ammonium ions separated by ~14 Å in their lowest energy conformation.[91] After surgery, NMBA reversal is needed to facilitate patient recovery.

While NMBA's are bivalent, all reported supramolecular reversal agents contain a single macrocyclic binding motif.[7, 8] Supramolecular reversal agents administered by intravenous injection bind free NMBA's in the blood, lowering the concentration of NMBA's at the neuromuscular junction and reversing effects.[92] Several NMBA reversal agents have been developed from macrocyclic hosts, including cyclodextrins, cucurbit[*n*]urils and pillar[*n*]arenes (Figure 2.1 and Figure 2.82).[7, 8] These hosts operate via an inclusion binding mode that is inherently limited by the size of the host cavity and the fit of the NMBA (**Table 2.23**). Sugammadex, a *γ*-cyclodextrin host that is approved for clinical use in over 50 countries, reverses steroidal NMBA's vecuronium and rocuronium.[93] However, its cavity is too small to achieve reversal of wider curarine and benzylisoquinoline NMBA's, and it is similarly inactive towards the thinner NMBA suxamethonium.[94] Likewise, pillar[5]arene is too small to form a threaded complex with steroidal NMBA's, but thioether carboxylate decafunctionalized pillar[5]arene can form a nesting complex with rocuronium.[95] Water-soluble carboxylatopillar[6]arene (WP[6]) strongly binds the thinner NMBA suxamethonium,[96] and sulfated Pillar[6]MaxQ strongly binds steroidal NMBA's.[97] Calabadion 2, an acyclic cucurbituril analog, has broader binding preferences, reversing steroidal and benzylisoquinoline NMBA's, vecuronium, rocuronium and cisatracurium; binding to suxamethonium has not been reported.[98]

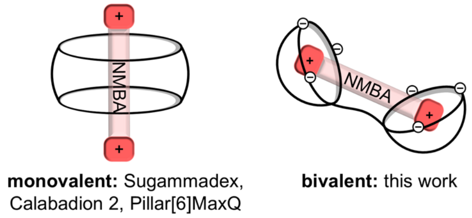

Figure 2.1. Supramolecular reversal agents reported to date contain a single binding site. We propose a reversal agent with dual binding sites separated by a flexible linker.

To complement a family of molecules with diverse biscationic structures but a common geometrically defined pharmacophore, we chose a conceptually new approach: building bivalent hosts using two promiscuous, but carefully spaced binding pockets (Figure 2.1 and Figure 2.2). We selected *p*-sulfonatocalix[*n*]arenes, **sCx4** and **sCx5**, as their anionic upper rims and dynamic bowl like cavities are known to bind many kinds of cationic moieties.[99]

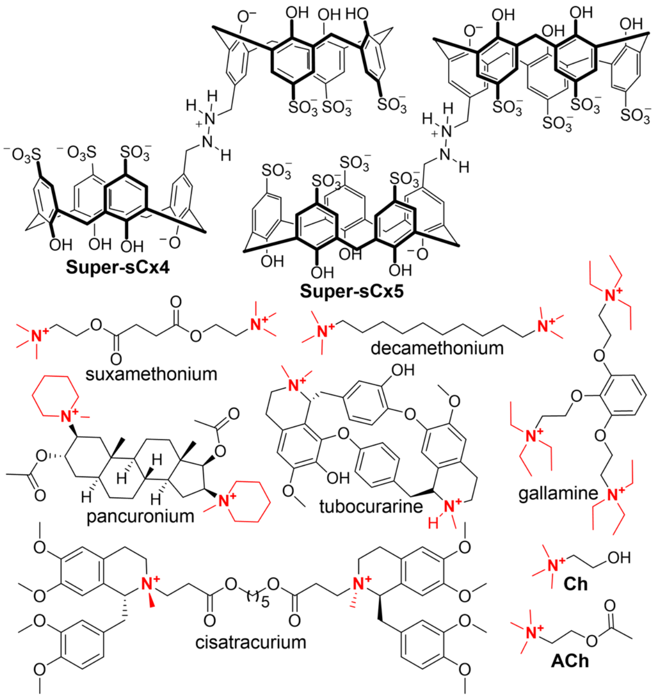

Figure 2.2. Chemical structures of bivalent calixarene hosts, NMBA's and cholines.

2.3 Results and discussion

Templated synthesis with the NMBA decamethonium was effective at creating a new water-soluble bivalent host. Simple models predicted that a very short linker would be needed between two *p*-sulfonatocalix[*n*]arene building blocks. However, we repeatedly found that late-stage covalent coupling was hampered by the mutual repulsion between two highly anionic calixarenes. To overcome this barrier, monofunctionalized **sCx4-CHO** and decamethonium were mixed in a 2:1 ratio in aqueous solution (Figure 2.3a). *In situ* ^{1}H NMR showed upfield shifting of the decamethonium methyl peaks, indicating complexation (Figure 2.3bii). One-dimensional diffusion-ordered spectroscopy (1D DOSY) NMR on the uncomplexed calixarene **sCx4-CHO** has a reported hydrodynamic radius of 7.4 ± 0.3 Å,[72] which we found increased to 11.7 ± 0.3 Å upon complexation with decamethonium, supporting the formation of a self-assembled 2:1 complex under the reaction conditions (Table 2.1 and Figure 2.65). Addition of hydrazine formed compound **2.1**, a complex system with two reversible imine bonds and calixarenes engaged on either end of the templating NMBA. Reductive amination locks the structure, forming the bivalent host **Super-sCx4** (Figure 2.3a). Continuous NMBA complexation throughout the reaction is observed by further upfield-shifted methyl peaks in the final crude reaction mix (Figure 2.3biii). Ultraperformance liquid chromatography mass spectrometry (UPLC-MS) of the crude reaction identified the bivalent host **Super-sCx4** as the major product with minor formation of monovalent **sCx4-CH$_2$NHNH$_2$** (Figure 2.3c). **Super-sCx4** was isolated in a 50% yield after preparative high performance liquid chromatography (HPLC) purification.

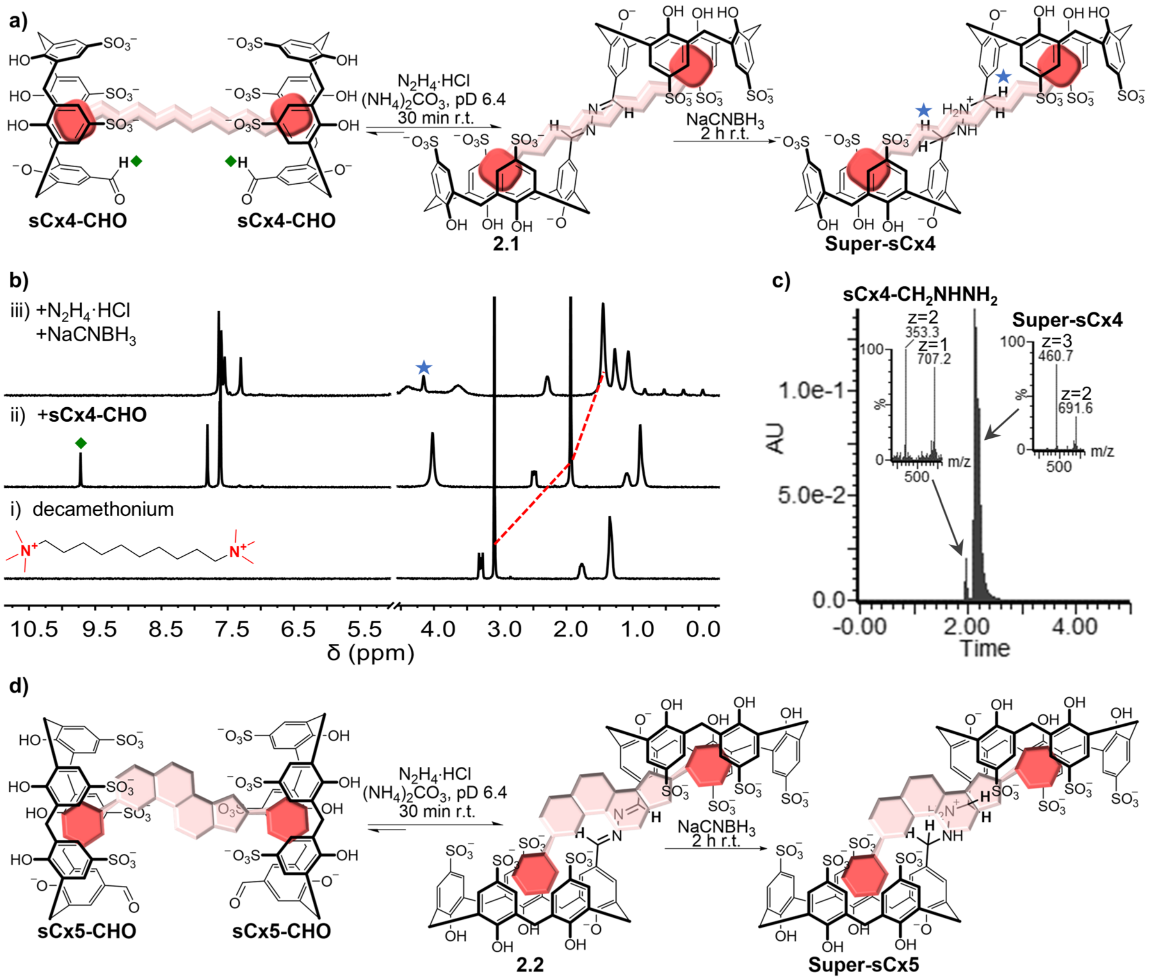

Figure 2.3. NMBA templated synthesis forms bivalent calixarene hosts with a flexible hydrazine linker. **a)** Synthetic scheme of **Super-sCx4** templated by decamethonium in $(NH_4)_2CO_3$ (50 mM, pD 6.4) in D_2O. **b)** ^1H NMR spectrum of i) decamethonium (5 mM), ii) followed by the addition of 2 eq **sCx4-CHO** (10 mM), aldehyde indicated by green diamond, and iii) the final crude after completed reductive amination (hydrazine linkage indicated by blue star). Red dotted line shows encapsulation of decamethonium methyl groups throughout the reaction. **c)** UPLC-MS (ES-) of the final crude shows major product formation of bivalent **Super-sCx4** and minor formation of monovalent **sCx4-CH₂NHNH₂**. **d)** Synthetic scheme of **Super-sCx5** templated by pancuronium in $(NH_4)_2CO_3$ (50 mM, pD 6.4) in D_2O.

We also developed a templated bivalent *p*-sulfonatocalix[5]arene analog (Figure 2.3d). Novel building block **sCx5-CHO** was synthesized in six steps by site-specific functionalization of the calix[5]arene scaffold (see Section 2.5.2). Initial templation attempts with **sCx5-CHO** and decamethonium showed a folded conformation was adopted by decamethonium inside the larger **sCx5-CHO** cavity, forming a 1:1 complex (Figure 2.30) and preventing the success of the templated synthesis. The steroidal NMBA pancuronium was selected as a more rigid template, as it has been shown to form a 2:1 complex with similarly sized cucurbit[7]uril.[100] Monofunctionalized **sCx5-CHO** and pancuronium were equilibrated in a 2:1 ratio in aqueous solution. Upfield shifts of the quaternary amine methyl groups were observed by *in situ* ^{1}H NMR reaction monitoring (Figure 2.31). 1D DOSY NMR of this complex supports the formation of a 2:1 self-assembly, 11 ± 1 Å in size (Table 2.1 and Figure 2.70). The addition of hydrazine formed compound **2.2**, followed by reductive amination obtaining bivalent **Super-sCx5**, isolated in a 25% yield after HPLC purification. A slightly larger hydrodynamic radius of 12.6 ± 0.2 Å for isolated **Super-sCx5** was determined (Table 2.1 and Figure 2.72).

Templation by NMBA's is essential to the formation of each bivalent host. Control reactions without NMBA templates produced little or no detectable bivalent products by UPLC-MS, instead resulting in the formation of monovalent **sCx4-CH$_2$NHNH$_2$**, **sCx5-CH$_2$NHNH$_2$**, and other reduced monovalent calixarenes (Figure 2.29 and Figure 2.32).

A wide variety of NMBA's form 1:1 complexes with the new bivalent hosts. Suxamethonium was selected for detailed 1D DOSY investigation as it displayed distinguishable sharp peaks in ^{1}H NMR when complexed with either **Super-sCx4** or **Super-sCx5.** The hydrodynamic radii of suxamethonium complexes with hosts **Super-sCx4** (11.2 ± 0.6 Å) and **Super-sCx5** (12.4 ± 0.6 Å) were similar to the values for the respective isolated Super-sCx hosts (Table 2.1, Figure 2.68 and Figure 2.73).

Table 2.1. Diffusion coefficients and hydrodynamic radii determined by 1D DOSY.

Compounds	D (10^{-10} m^2/s)	r$_H$ (Å)
sCx4-CHO[72]	3.29 ± 0.02	7.4 ± 0.3
sCx4-CHO•decamethonium[a]	2.16 ± 0.05	11.7 ± 0.3
sCx4-CH$_2$NHNH$_2$[b]	2.77 ± 0.05	9.1 ± 0.2
Super-sCx4[b]	2.22 ± 0.02	11.4 ± 0.1
Super-sCx4•suxamethonium[b]	2.3 ± 0.1	11.2 ± 0.6
sCx5-CHO[b]	2.79 ± 0.03	9.0 ± 0.1
sCx5-CHO•pancuronium[b]	2.2 ± 0.2	11 ± 1
sCx5-CH$_2$NHNH$_2$[b]	2.7 ± 0.1	9.5 ± 0.5
Super-sCx5[b]	2.00 ± 0.03	12.6 ± 0.2
Super-sCx5•suxamethonium[b]	2.04 ± 0.09	12.4 ± 0.6

[a]Samples in $(NH_4)_2CO_3$ (50 mM, pD 6.4) in D_2O (500 MHz, 297 K). [b]Samples in NaH_2PO_4/Na_2HPO_4 (50 mM, pD 7.4) in D_2O (500 MHz, 297 K).

The 1:1 complexation demonstrated by DOSY is further supported by molecular modeling. Conformational searches were carried out on complexes of each bivalent Super-sCx host with a panel of structurally diverse NMBA's (decamethonium, suxamethonium, gallamine, pancuronium, tubocurarine and cisatracurium). In all cases, the most stable energy-minimized structures involved the two quaternary amines from the NMBA's being engaged within the two pockets of the bivalent hosts (Figure 2.74 to Figure 2.77).

Six-point ^{1}H NMR titrations of NMBA's demonstrate qualitatively that matching of bivalent guests with bivalent hosts is required for strong 1:1 binding. The upfield shifts of NMBA methyl groups were monitored upon addition of hosts into NMBA's, with all titrations exhibiting fast exchange on the NMR time scale (see Section 2.5.6). Titrations of bivalent hosts **Super-sCx4** and **Super-sCx5** into NMBA's displayed strong binding, resulting in saturation of chemical shift perturbation at 1.0 to 1.5 equivalents. Titrations with monovalent control hosts **sCx4-CH$_2$NHNH$_2$** and **sCx5-CH$_2$NHNH$_2$** did not display saturation at $\leq$3 equivalents, demonstrating that the monovalent control compounds form weaker complexes with higher stoichiometries. Similarly, titrations of the bivalent **Super-sCx4** and **Super-sCx5** hosts into cholines (**Ch** and **ACh**) showed weaker unsaturated binding.

The new hosts exhibit pan-selective NMBA binding with selectivity over cholines and other hydrophobic amines. We used an indicator displacement assay (IDA), with lucigenin (**LCG**) to determine equilibrium dissociation constant (K_d) values. Competitive titrations of NMBA's into the pre-formed Super-sCx•**LCG** complexes were conducted, with displacement of **LCG** resulting in increased fluorescence (Figure 2.4).[42] **Super-sCx4** exhibited stronger binding to the thinner NMBA's, suxamethonium (71 ± 8 μM) and decamethonium (63 ± 9 μM), with selectivity over **ACh** (Table 2.2). **Super-sCx5** exhibited strong broad-specturm binding to all NMBA's tested (2-18 μM) and selectivity over **ACh** (Table 2.2). Notably the larger *p*-sulfonatocalix[5]arene cavity offered strong binding to both the thinner NMBA suxamethonium (14 ± 3 μM) and the bulkier NMBA cisatracurium (6 ± 3 μM). Other natural monovalent hydrophobic amines and basic drugs (nicotine, acetaminophen, carnatine, phosphocholine and hexylamine) were tested and all displayed weak or no binding (0.7 to >10 mM) (see Section 2.5.5 and Table 2.3).

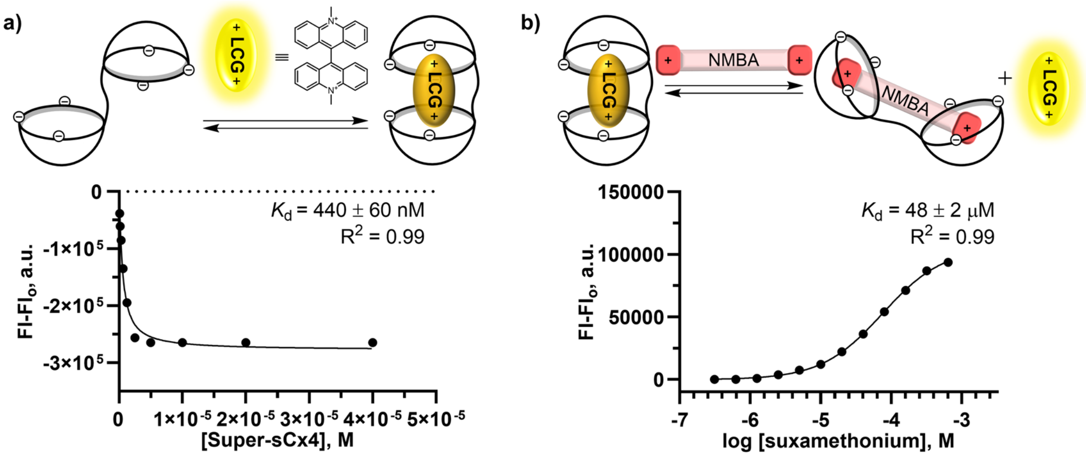

Figure 2.4. IDA determines binding affinity of NMBA's to bivalent Super-sCx hosts. **a)** Direct binding titration of **Super-sCx4** (up to 40 μM) into **LCG** (0.25 μM). **b)** Competitive displacement titration of suxamethonium (up to 640 μM) into **Super-sCx4** (5 μM) and **LCG** (0.25 μM). Error bars were plotted for each duplicate but are not visible in cases where the error is smaller than the plotted point. Solutions in NaH_2PO_4/Na_2HPO_4 (10 mM, pH 7.4) in H_2O, $\lambda_{em} = 485$ nm ($\lambda_{ex} = 369$ nm).

Table 2.2. IDA determined equilibrium dissociation constants of Super-sCx hosts and their selectivity for NMBA's over **ACh**.

Guest	**Super-sCx4** K_d (M)[a]	Selectivity over **ACh** (fold)	**Super-sCx5** K_d (M)[a]	Selectivity over **ACh** (fold)
LCG	$(6 \pm 2) \times 10^{-7}$	-	$(3 \pm 1) \times 10^{-7}$	-
Ch	$>1.0 \times 10^{-2}$	-	$>1.0 \times 10^{-2}$	-
ACh	$>1.0 \times 10^{-2}$	-	$>1.0 \times 10^{-2}$	-
Decamethonium	$(6.3 \pm 0.9) \times 10^{-5}$	>160	$(1.8 \pm 0.4) \times 10^{-5}$	>550
Suxamethonium	$(7.1 \pm 0.8) \times 10^{-5}$	>140	$(1.4 \pm 0.3) \times 10^{-5}$	>720
Gallamine	$(8 \pm 6) \times 10^{-6}$[b]	>1000[b]	$(2 \pm 2) \times 10^{-6}$[b]	>4000[b]
Pancuronium	$(1.0 \pm 0.2) \times 10^{-5}$	>960	$(1.4 \pm 0.3) \times 10^{-5}$	>700
Tubocurarine	$(2 \pm 1) \times 10^{-4}$	>50	$(1.8 \pm 0.8) \times 10^{-5}$	>570
Cisatracurium	$(2.0 \pm 0.4) \times 10^{-4}$	>51	$(6 \pm 3) \times 10^{-6}$[b]	>2000[b]

[a] All solutions in NaH_2PO_4/Na_2HPO_4 (10 mM, pH 7.4) in H_2O. Dissociation constants were determined from fluorescence IDA titrations assuming 1:1 stoichiometry, values reported are the average of six measurements with propagated standard error, where 1:1 binding was supported by molecular modeling of NMBA's with Super-sCx hosts. For exemplary binding curves and residuals see Section 2.5.5. [b] Certain structurally complex NMBA's showed titration profiles that prove a non-1:1 stoichiometry. The apparent K_d values arising from 1:1 fits are provided, but must be considered only as rough approximations of potency for binding.

Isothermal titration calorimetry (ITC) experiments with suxamethonium reveal how *p*-sulfonatocalix[4]arene and *p*-sulfonatocalix[5]arene-based hosts have different enthalpic (ΔH) and entropic (ΔS) driving forces, as expected for macrocycles of different sizes (see Section 2.5.9). In both bivalent and monovalent hosts enthalpy dominates complexation (Figure 2.5), as is also observed (for example) for such diverse comparitors as Suggamadex or Pillar[6]MaxQ binding rocuronium.[92, 97] Notably, bivalent **Super-sCx4** and monovalent **sCx4-CHO** bind suxamethonium with almost identical enthaplies to each other, while the preorganization of **Super-sCx4** provides a benefit in the form of >30 kJ/mol more favourable entropy of binding (Figure 2.5). Super-sCx potencies measured by this gold-standard method were very high (<150 nM), likely due to the use of a different buffer, temperature and the absence of competing dye molecules.

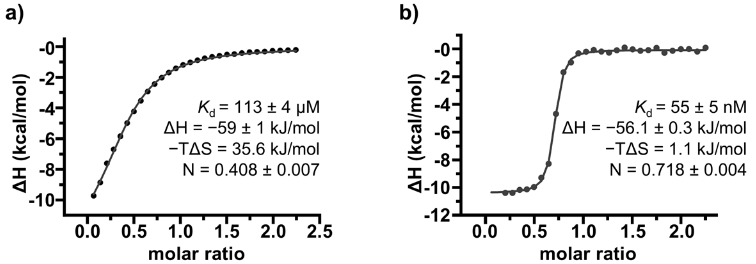

Figure 2.5. Direct ITC titrations of **a)** suxamethonium (7 mM) into **sCx4-CHO** (7 μM) and **b)** suxamethonium (200 μM) into **Super-sCx4** (20 μM). All samples in NaH_2PO_4/Na_2HPO_4 (50 mM, pH 7.4) in H_2O at 30°C.

Sulfonated calixarenes have demonstrated *in vivo* activity in several models of intoxication and have favourable toxicity profiles. **sCx4** itself is biocompatible, with low *in vivo* toxicity (100 mg/kg in mice) making it an excellent candidate for the development of novel supramolecular drug reversal agents.[101] We did *in vitro* cell viability assays of bivalent hosts **Super-sCx4** and **Super-sCx5** and found no measurable toxicity up to tested concentrations of 250 μM in human hepatoblastoma (HepG2) and human embryonic kidney 293 (HEK293) cell lines (Figure 2.80 and Figure 2.81).

2.4 Conclusion

This work provides a new approach to developing reversal agents, using the target as a template to build synthetically challenging hosts in aqueous solution. While several examples of upper-rim-linked bivalent calixarenes exist,[102-108] making covalent connections between highly anionic building blocks is especially challenging. Templation has been widely used to overcome such synthetic challenges, from small ion templation of macrocycles,[109, 110] to larger complex architectures like nanorings,[111] nanorods,[112] molecular knots,[113] and polymers.[114] More recently, templation has been applied to dynamic combinatorial chemistry, by forming mixtures of synthetic building blocks that favour linkage around a desired template.[10, 115, 116]

In some sense, a pharmacophore model is a useful message of promiscuity. It teaches us that many drugs presenting related functional groups in a similar 3D arrangement can be active against the same target. When paired with a promiscuous host macrocycle, the use of a single template during synthesis can provide bivalent hosts that have broad-spectrum activity and yet retain useful selectivity (e.g. over monovalent competitors). While it seems that only certain NMBA's are suitable for a given templation reaction, the bivalent hosts in this work, once synthesized, have good affinity for NMBA's and weak affinity for the neurotransmitter **ACh**. *p*-Sulfonatocalix[*n*]arenes are known for forming intrinsically weak (~mM) complexes with a large variety of cationic guests in salty water.[99] Until now, this has limited their biological applications to those that involve targeted analytes that exist at relatively high *in vivo* concentrations.[117] Although the affinities that arise from this approach are inferior to other NMBA reversal agents, the selectivities over cholines are excellent (Table 2.23), and the broad-spectrum activities are also unique, suggesting this approach might have some advantages over the current state of the art in reversal agents.

2.5 Supplementary information

2.5.1 General materials and methods

2.5.1a Materials

The following compounds were used as purchased. Suxamethonium chloride (>98%), decamethonium bromide (>98%), phosphocholine chloride calcium salt tetrahydrate (>98%), and 4-sulfocalix[4]arene hydrate (**sCx4**) were purchased from Tokyo Chemical Industry. Choline chloride (**Ch**, >98%) and (S)-(-)-nicotine (99%) were purchased from Alfa Aesar. Tubocurarine chloride (98%), cisatracurium besylate (88%), pancuronium bromide (97%) and gallamine triethiodide (95%) were purchased from Toronto Research Chemicals. Acetylcholine chloride (**ACh**, >98%), (±)-carnitine hydrochloride (>98%), hydrazine hydrochloride, sodium cyanoborhydride and lucigenin (**LCG**) were purchased form Sigma Aldrich.

Hexylamine (>99%) was purchased from Sigma Aldrich and converted to water soluble hexylamine hydrochloride prior to use in IDA experiments. Hexylamine (200 μL, 1.51 mmol) was reacted on ice with a 4.0 M HCl solution (3.78 mL, 15.1 mmol) purchased from Sigma Aldrich. Residual solvent was removed by rotary evaporation affording the white powder hexylamine hydrochloride.

2.5.1b General NMR spectroscopy methods

Deuterated solvents were purchased from Sigma Aldrich. Reactions monitored *in situ* were prepared using ammonium carbonate ($(NH_4)_2CO_3$, 50 mM, pD 6.4) in D_2O, pD was adjusted using 1 M DCl. Ammonium carbonate was selected due to its lack of interference in ^1H NMR and compatibility with UPLC-MS. Adjusting the pD to 6.4 favoured the formation of hydrazone in the initial condensation reaction. ^1H NMR titrations were performed in NaH_2PO_4/Na_2PO_4 (50 mM, pD 7.4) in D_2O, prepared using sodium phosphate monobasic and sodium phosphate dibasic in D_2O, the pD was adjusted with 1 M NaOD/DCl and determined using a pH meter.[118]

^1H, ^{13}C, and 1D DOSY were recorded on a Bruker Avance Neo 500 MHz spectrometer or 300 MHz spectrometer as specified. ^1H and ^{13}C NMR spectra were processed using MestReNova by Mestrelab Research S.L. 1D DOSY experiments were pre-processed using TopSpin and diffusion coefficients were analyzed using Bruker Dynamics Center.

2.5.1c General UPLC-MS and HPLC methods

Reactions were monitored and final host purity was verified using a Waters UPLC-MS equipped with UV-Vis and QDa detector. All samples were filtered through a 13 mm syringe filter with a 0.45 µm polytetrafluorethylene (PTFE) membrane then injected onto an Aquity UPLC BEH C18 1.7 µm (21 mm × 50 mm) column. A gradient of 90% H_2O (0.4% CH_2O_2)/10% CH_3CN (0.4% CH_2O_2) to 30% H_2O (0.4% CH_2O_2)/70% CH_3CN (0.4% CH_2O_2) over 5 min at 0.5 mL/min flow was used for all traces. Reaction mixtures were directly purified on a Teledyne ACCQPrep HP150 HPLC system with UV detection at 280 nm. A Phenomenex Luna C18, 250 mm × 22 mm, 5 µm preparative column or a Teledyne Redi Sep C18, 150 mm × 20 mm, 5 µm were used for purification. The column and gradient methods are as specified for each synthetic protocol.

2.5.1d General HRMS, m.p. and IR methods

Accurate mass spectra of pure novel compounds were obtained by electrospray ionization (ESI) using a Thermo Scientific™ Exactive™ Plus Orbitrap Ultimate 3000 liquid chromatography mass spectrometry (LC-MS) system. The eluent used was a 50:50 mix of Milli-Q™ water and Optima™ acetonitrile. Melting points (m.p.) were determined using a Gallenkamp melting point apparatus. Infrared (IR) spectra were collected using a Perkin Elmer 1000 Fourier transform infrared (FTIR) spectrometer. IR data are reported as frequency of absorption (cm^{-1}) intensity; s = strong, m = medium, w = weak, br = broad.

2.5.2 Synthesis

Calix[4]arene synthetic precursors were synthesized using adapted protocols reported for compounds **2.4**,[119] **2.5**,[120] **2.6**,[120] **2.7**,[54] **2.8**,[54] and **sCx4-CHO**.[54]

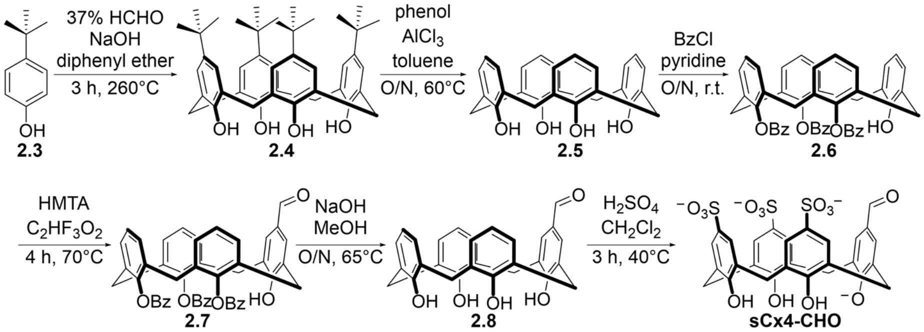

Scheme 2.1. Synthetic route of previously reported **sCx4-CHO**.[54, 119, 120]

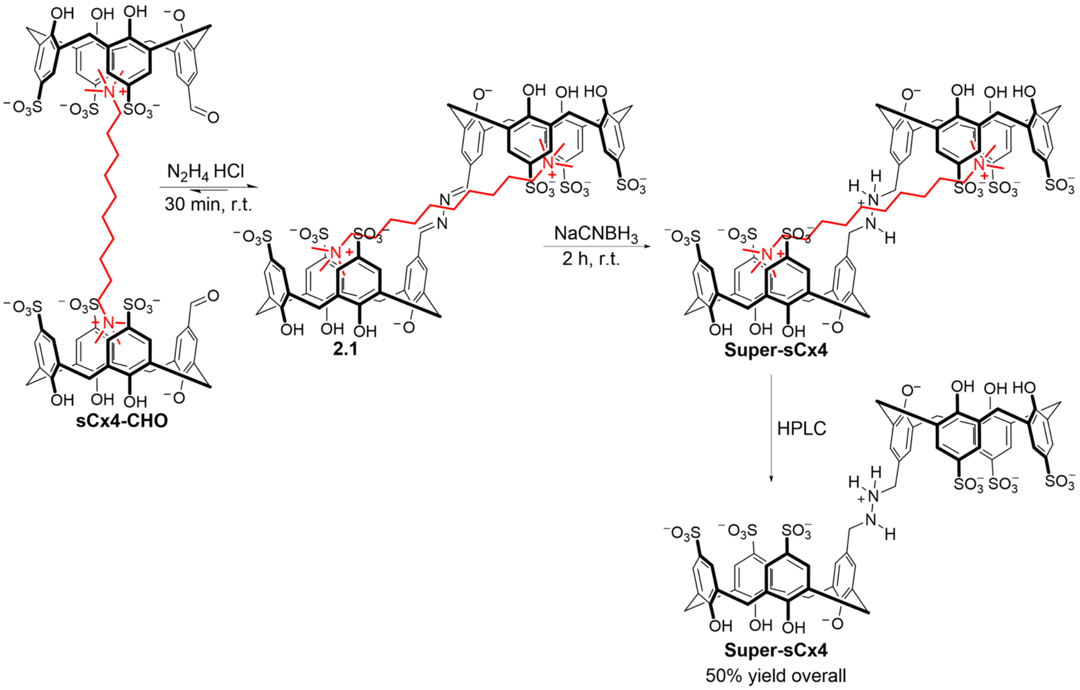

Scheme 2.2. Synthesis of novel **Super-sCx4**.

Super-sCx4 – templated reaction. sCx4-CHO (30 mg, 0.043 mmol, final concentration = 10 mM) and decamethonium bromide (9 mg, 0.022 mmol, final concentration = 5 mM) were dissolved in ammonium carbonate in D_2O (4.34 mL, 50 mM, pD 6.4). The starting material was equilibrated for 15 min at room temperature with stirring. The dissolved starting material formed a clear colourless solution. ^{1}H NMR of the starting material was taken to verify decamethonium complexation. Hydrazine hydrochloride (0.024 mmol, 24 μL of 1 M solution in D_2O) was added and stirred at room temperature for 30 min. Upon hydrazine hydrochloride addition the reaction formed an orange precipitate. Sodium cyanoborohydride (0.43 mmol, 27 mg) was added, and stirred at room temperature for 2 h. Upon sodium cyanoborohydride addition the reaction formed a clear colourless solution. UPLC-MS verified the formation of bivalent **Super-sCx4** as the major product (Figure 2.28). The reaction mixture was directly purified by HPLC using a gradient of 90% H_2O (0.1% $C_2HF_3O_2$)/10% CH_3CN (0.1% $C_2HF_3O_2$) to 68% H_2O (0.1% $C_2HF_3O_2$)/32% CH_3CN (0.1% $C_2HF_3O_2$) over 17 min on a Phenomenex Luna C18, 250 mm × 22 mm, 5 μm preparative column. Fractions were collected, immediately flash frozen and lyophilized to yield a white fluffy solid (15 mg, 50%). m.p. decomposed >250°C; ^{1}H NMR (300 MHz, D_2O): δ (ppm) 7.63 (s, 4H), 7.61 (s, 4H), 7.51 (s, 4H), 7.00 (s, 4H), 4.02 (d, J = 10.9 Hz, 16H), 3.75 (s, 4H); ^{13}C NMR (126 MHz, d_6-DMSO): δ (ppm) 151.6, 150.2, 149.4, 139.5, 139.1, 130.1, 128.1, 127.5, 127.2, 127.0, 126.6, 126.5, 126.4, 126.0, 51.0, 30.9, 30.6; FTIR: 3243 (br), 1594 (w), 1454 (w), 1136 (m), 1111 (m), 1037 (s), 625 (s), 551 (s) cm^{-1}; HRMS (ESI): *m/z* calculated for $C_{58}H_{52}N_2O_{26}S_6^{5-}$ 275.82265 $[M\text{-}5H]^{5-}$; found 275.81569.

Super-sCx4 – control untemplated reaction. The control reaction was carried out exactly as above but omitting decamethonium bromide. The dissolved starting material formed a clear colourless solution. Upon hydrazine hydrochloride addition the reaction formed a clear light-yellow solution. Upon sodium cyanoborohydride addition the reaction formed a clear colourless solution. UPLC-MS verified that bivalent **Super-sCx4** was not synthesized in the absence of the decamethonium template. A mixture of the monovalent hydrazone and reduced starting material sCx4-CH_3 (**2.16**) were formed (Figure 2.29).

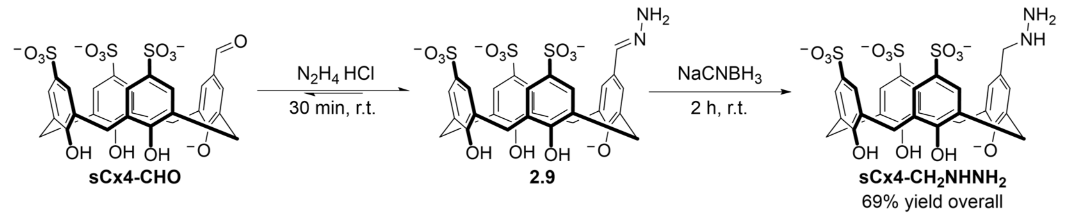

Scheme 2.3. Synthesis of novel **sCx4-CH₂NHNH₂**.

sCx4-CH₂NHNH₂. sCx4-CHO (50 mg, 0.072 mmol, final concentration = 30 mM) was dissolved in ammonium carbonate in D_2O (2.41 mL, 50 mM, pD 6.4), forming a colourless solution. Hydrazine hydrochloride (0.22 mmol, 217 µL of 1 M solution in D_2O) was added. Upon addition the solution turned yellow. The reaction was stirred at room temperature for 30 min, forming a yellow precipitate. Sodium cyanoborohydride (0.72 mmol, 45 mg) was added, and stirred at room temperature for 2 h, forming a white cloudy solution. A minimal amount of water was added to dissolve the precipitate (~2 mL). The crude reaction mixture was directly purified by HPLC using a gradient of 90% H_2O (0.1% $C_2HF_3O_2$)/10% CH_3CN (0.1% $C_2HF_3O_2$) to 65% H_2O (0.1% $C_2HF_3O_2$)/35% CH_3CN (0.1% $C_2HF_3O_2$) over 17 min on a Phenomenex Luna C18, 250 mm × 22 mm, 5 µm preparative column. The fractions were collected, immediately flash frozen and lyophilized, yielding a fluffy white product (35 mg, 69%). m.p. decomposed >250°C; ^{1}H NMR (500 MHz, D_2O): δ (ppm) 7.81 (s, 2H), 7.68 (d, *J* = 2.2Hz, 2H), 7.63 (s, 2H), 6.88 (s, 2H), 4.24-3.88 (m, 10H); ^{13}C NMR (126 MHz, d_6-DMSO): δ (ppm) 151.6, 150.2, 149.4, 139.5, 139.1, 130.1, 128.1, 127.5, 127.2, 127.0, 126.6, 126.5, 126.4, 126.0, 51.0, 30.9, 30.6; FTIR: 3200 (br), 1609 (w), 1460 (w), 1156 (s), 1040 (s), 626 (s), 557 (m) cm^{-1}; HRMS (ESI): *m/z* calculated for $C_{29}H_{28}N_2O_{13}S_3^{3-}$ 235.02512 $[M\text{-}3H]^{3-}$; found 235.01876.

Calix[5]arene compound **2.11** was provided by Prof. Dong-Sheng Guo and Juan-Juan Li, Nankai University Tianjin, synthesized from compound **2.3** following previously reported procedures.[121, 122] Compound **2.12** was synthesized following the reported protocol.[104]

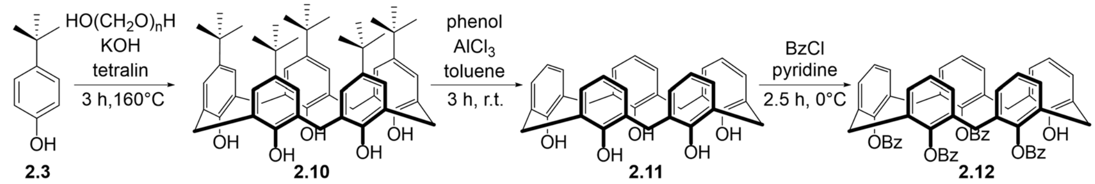

Scheme 2.4. Synthetic route of previously reported compound **2.12**.[104, 121, 122]

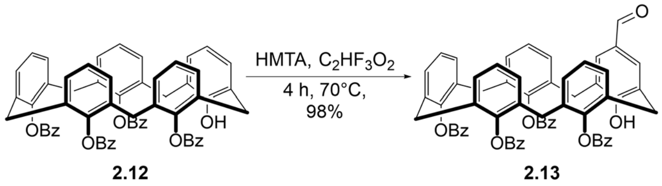

Scheme 2.5. Synthesis of novel compound **2.13**.

4Bz-Cx5-CHO (2.13). 4Bz-Cx5 (**2.12**) (500 mg, 0.52 mmol) was dissolved in trifluoroacetic acid (5 mL) and hexamethylenetetramine (665 mg, 4.75 mmol) was added. The solution was heated for 4 h at 70°C forming a clear pink solution. Water was added to the reaction forming a white precipitate. The precipitate was then dissolved upon addition of dichloromethane and the layers were separated. The water layer was back extracted twice with fresh dichloromethane. The combined organic layers were washed twice with water, then twice with brine and dried over Na_2SO_4. The filtered organic layer was concentrated to dryness on a rotary evaporator resulting in light yellow crystals (500 mg, 98% yield). This product was carried forward to debenzoylation after partial characterization, due to poor ionization in HRMS and multiple conformations resulting in intractable NMR spectra. ^{1}H NMR (500 MHz, $CDCl_3$): δ (ppm) 9.91 (s, 1H), 8.39−5.99 (m, 34H), 4.23−3.11 (m, 10H).

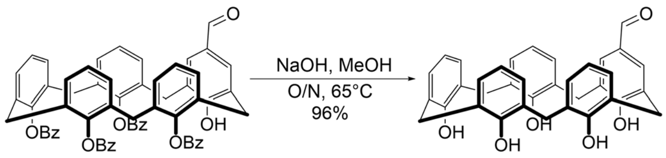

2.13 **2.14**

Scheme 2.6. Synthesis of novel compound **2.14**.

Cx5-CHO (2.14). 4Bz-Cx5-CHO (**2.13**) (500 mg, 0.51 mmol) and sodium hydroxide pellets (410 mg, 10.2 mmol) were dissolved in methanol (20 mL). The reaction was heated at reflux overnight forming a clear orange-brown solution. The mixture was quenched with cold 1 M HCl, forming a white precipitate. The precipitate was collected by vacuum filtration then purified using a silica plug (~10 g). The crude was dissolved in minimal dichloromethane and wet loaded. The plug was run with a starting eluent of CH_2Cl_2 with a gradient to CH_2Cl_2 + 5% MeOH, affording a solid white product. (275 mg, yield 96%). m.p. decomposed >250°C; ^{1}H NMR (300 MHz, $CDCl_3$): δ (ppm) 9.35 (s, 1H), 9.17 (s, 1H), 8.37 (s, 2H), 8.23 (s, 2H), 6.77-6.99 (m, 10H), 6.37 (t, J = 7.7 Hz, 2H), 6.35 (t, J = 7.7 Hz, 2H), 3.38 (br, 10H); ^{13}C NMR (126 MHz, $CDCl_3$): δ (ppm) 191.0, 156.0, 150.0, 149.9, 131.4, 130.6, 129.7, 129.4 (2×), 129.4, 127.8, 127.0, 126.8, 126.6, 125.8, 122.1, 121.8, 31.4, 31.3, 31.3; FTIR: 3249 (br), 1686 (m), 1596 (m), 1446 (m), 753 (s) cm^{-1}; HRMS (ESI): *m/z* calculated for $C_{36}H_{30}O_6^-$ 557.20424 [*M*-H]$^{1-}$; found 557.19679.

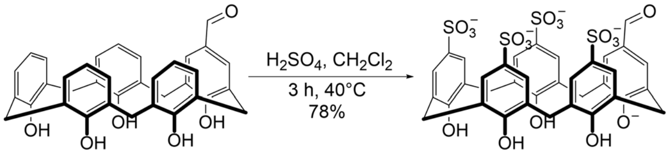

2.14

sCx5-CHO

Scheme 2.7. Synthesis of novel **sCx5-CHO**.

sCx5-CHO. Cx5-CHO (**2.14**) (100 mg, 0.18 mmol) was dissolved in minimal dichloromethane (2 mL). Concentrated sulfuric acid (192 µL, 3.6 mmol) was added and the reaction was heated at reflux for 3 h. An insoluble pink-purple residue formed on the sides of the reaction vial. Dichloromethane was decanted from the reaction. The residue was rinsed with fresh dichloromethane and decanted again. The solid residue was then suspended in ethyl acetate (~4 mL) by sonication and transferred into a 50 mL falcon tube. Suspension in ethyl acetate was repeated two more times to completely remove all residue from the reaction vial (~12 mL total). The suspension was diluted with cold diethyl ether (0°C, ~30 mL) forming a grey precipitate. The suspension was centrifuged into a pellet (10 min, 4°C, 3400 rpm) and the supernatant was decanted. The pellet was resuspended in cold diethyl ether (0°C, ~30 mL) with sonication, repeating the centrifugation and decanting process. The pellet was left to air dry overnight then purified by HPLC. A gradient of 90% H_2O (0.1% $C_2HF_3O_2$)/10% CH_3CN (0.1% $C_2HF_3O_2$) to 77% H_2O (0.1% $C_2HF_3O_2$)/23% CH_3CN (0.1% $C_2HF_3O_2$) over 12 min was used on a Teledyne Redi Sep C18, 150 mm × 20 mm, 5 µm preparative column. Fractions were concentrated by rotary evaporator then lyophilized, affording a white fluffy powder (122 mg, 78%). m.p. decomposed >250°C; ^1H NMR (300 MHz, D_2O): δ (ppm) 9.62 (s, 1H), 7.70 (s, 2H), 7.64 (d, J = 2.4 Hz, 2H), 7.60 – 7.57 (m, 2H), 7.56 (d, J = 2.4 Hz, 1H), 3.92 (br, 10H); ^{13}C NMR (126 MHz, D_2O): δ (ppm) 195.5, 158.2, 153.8, 153.7, 135.7 (2×), 132.1, 129.7, 129.7, 129.6, 129.6, 129.5, 129.3, 127.1, 127.1, 127.0, 126.9, 31.4, 31.4, 31.1; FTIR: 3282 (br), 1664 (w), 1111 (s), 1035 (s), 620 (m), 554 (m) cm^{-1}; HRMS (ESI): *m/z* calculated for $C_{36}H_{30}O_{18}S_4^{3-}$ 291.67717 $[M\text{-}3H]^{3-}$; found 291.66999.

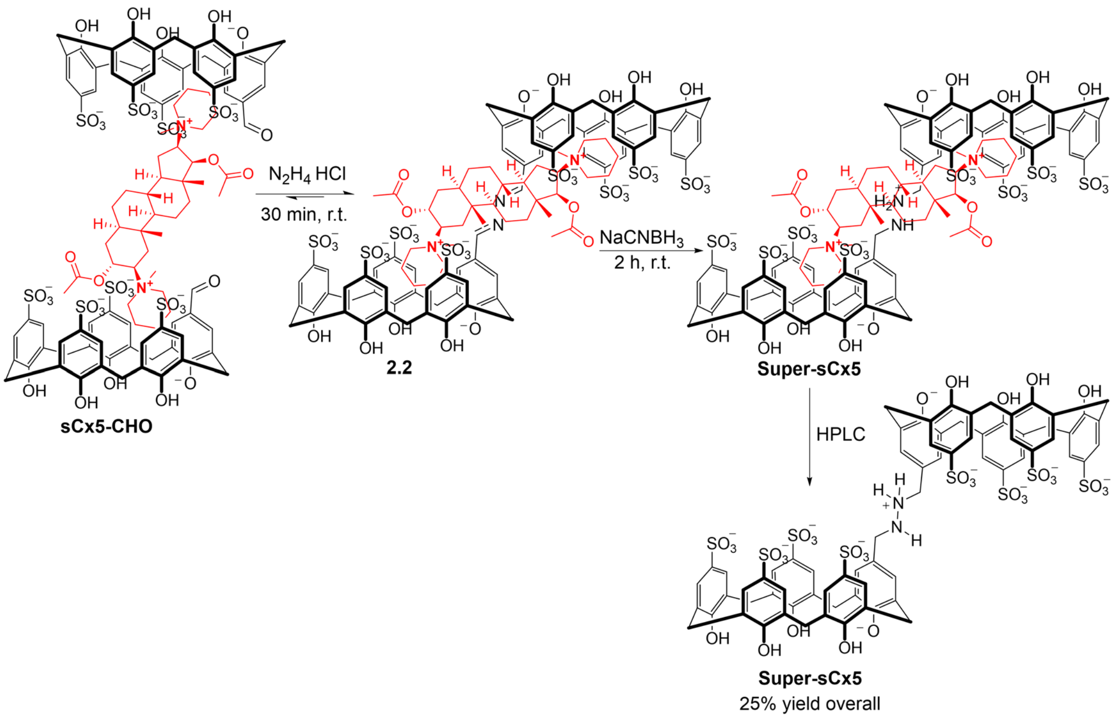

Scheme 2.8. Synthesis of novel **Super-sCx5**.

Super-sCx5 – templated reaction. sCx5-CHO (30 mg, 0.034, final concentration = 10 mM) and pancuronium bromide (12.6 mg, 0.017 mmol, final concentration = 5 mM) were dissolved in ammonium carbonate in D_2O (3.43 mL, 50 mM, pD 6.4). The starting material was equilibrated for 15 min at room temperature with stirring. The dissolved starting material formed a clear colourless solution. ^1H NMR of the starting material was taken to verify pancuronium complexation. Hydrazine hydrochloride (0.019 mmol, 19 µL of 1 M solution in D_2O) was added and stirred at room temperature for 30 min. Upon hydrazine hydrochloride addition the reaction formed an orange solution. Sodium cyanoborohydride (0.34 mmol, 22 mg) was added, and stirred at room temperature for 2 h. Upon sodium cyanoborohydride addition the reaction formed a clear colourless solution. UPLC-MS verified the formation of bivalent **Super-sCx5** as the major product (Figure 2.31). The reaction mixture was directly purified by HPLC using a gradient of 90% H_2O (0.1% $C_2HF_3O_2$)/10% CH_3CN (0.1% $C_2HF_3O_2$) to 68% H_2O (0.1% $C_2HF_3O_2$)/32% CH_3CN (0.1% $C_2HF_3O_2$) over 17 min on a Phenomenex Luna C18, 250 mm × 22 mm, 5 µm preparative column. The fractions were collected, immediately flash frozen and lyophilized to yield a white fluffy solid (6 mg, 25%). m.p. decomposed >250°C; ^1H NMR (500 MHz, D_2O): δ

7.64-7.56 (m, 16H), 7.10 (s, 4H), 3.97 (s, 4H), 3.90 (s, 12H), 3.85 (s, 8H); ^{13}C NMR (126 MHz, *d*$_6$-DMSO): δ 152.2, 152.1, 151.4, 138.7, 138.4, 130.1, 128.4, 127.6, 127.4, 127.4, 127.2, 126.6 (×2), 126.5, 126.3, 124.8, 51.4, 31.5, 31.0, 30.8; FTIR: 3344 (br), 1594 (w), 1474 (w), 1139 (m), 1113 (s), 1038 (s), 622 (m), 558 (m) cm^{-1}; HRMS (ESI): *m/z* calculated for $C_{72}H_{64}N_2O_{34}S_8^{6-}$ 291.68510 [*M*-6H]$^{6-}$; found 291.67723.

Super-sCx5 – control untemplated reaction. The control reaction was carried out exactly as above but omitting pancuronium bromide. The dissolved starting material formed a clear colourless solution. Upon hydrazine hydrochloride addition the reaction formed a clear light-yellow solution. Upon sodium cyanoborohydride addition the reaction formed a clear colourless solution. UPLC-MS verified that bivalent **Super-sCx5** was not synthesized in the absence of the template pancuronium. A mixture of the monovalent hydrazone and reduced starting material sCx5-CH$_3$ (**2.17**) were formed (Figure 2.32).

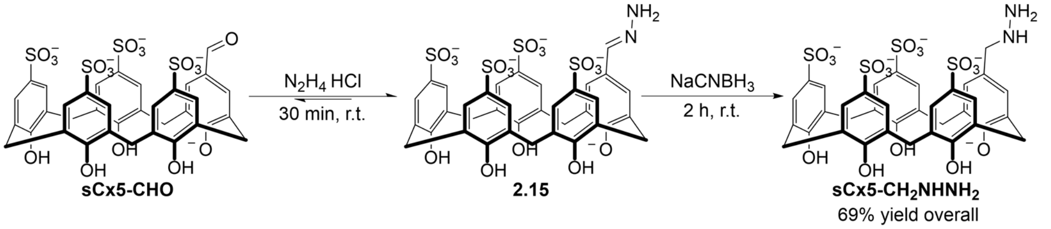

Scheme 2.9. Synthesis of novel **sCx5-CH$_2$NHNH$_2$**.

sCx5-CH$_2$NHNH$_2$. sCx5-CHO (50 mg, 0.057 mmol, final concentration = 30 mM) was dissolved in ammonium carbonate in D_2O (1.91 mL, 50 mM, pD 6.4), forming a colourless solution. Hydrazine hydrochloride (0.17 mmol, 171 µL of 1 M solution in D_2O) was added. Upon addition the solution turned yellow. The reaction was stirred at room temperature for 30 min. Sodium cyanoborohydride (0.57 mmol, 36 mg) was added, and stirred at room temperature for 2 h, forming a colourless solution. The crude reaction mixture was directly purified by HPLC using a gradient of 90% H_2O (0.1% $C_2HF_3O_2$)/10% CH_3CN (0.1% $C_2HF_3O_2$) to 65% H_2O (0.1% $C_2HF_3O_2$)/35% CH_3CN (0.1% $C_2HF_3O_2$) over 17 min on a Phenomenex Luna C18, 250 mm × 22 mm, 5 µm preparative column. The fractions were collected, immediately flash frozen and lyophilized, yielding a fluffy white product (28 mg, 69%). m.p. decomposed >250°C; ^{1}H NMR (500 MHz, D_2O): δ (ppm) 7.73 (d, *J* = 2.3

Hz, 2H), 7.63 (d, *J* = 2.3 Hz, 2H), 7.59 (d, *J* = 2.3 Hz, 2H), 7.53 (d, *J* = 2.3 Hz, 2H), 7.01 (s, 2H), 3.99 (s, 2H), 3.96 (s, 6H), 3.90 (s, 2H). ^{13}C NMR (126 MHz, *d*$_6$-DMSO): δ (ppm) 152.2, 151.9, 151.3, 139.0, 138.7, 128.2, 127.5, 127.3, 127.3, 127.0, 126.9, 126.8, 126.4, 126.3, 54.0, 31.1, 30.9, 30.5; FTIR: 3320 (br), 1593 (w), 1473 (w), 1139 (m), 1112 (s), 1037 (s), 623 (m), 558 (m) cm^{-1}. HRMS (ESI): *m/z* calculated for $C_{36}H_{34}N_2O_{17}S_4^{3-}$ 297.02468 [*M*-3H]$^{3-}$; found 297.01746.

2.5.3 Characterization data – ^{1}H, ^{13}C, DEPT-135 NMR and UPLC-MS

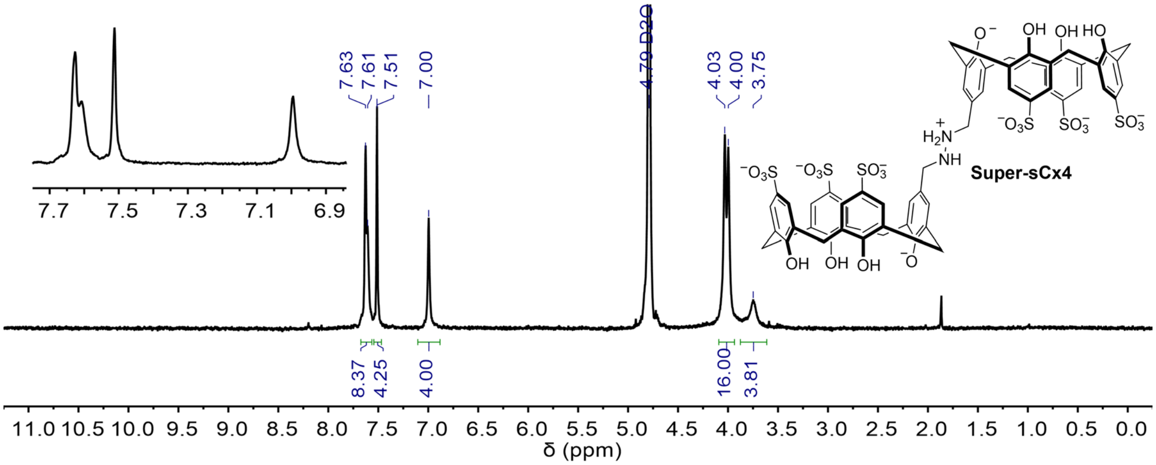

Figure 2.6. ^{1}H NMR spectrum of novel bivalent **Super-sCx4** (300 MHz, 300 K, in D_2O).

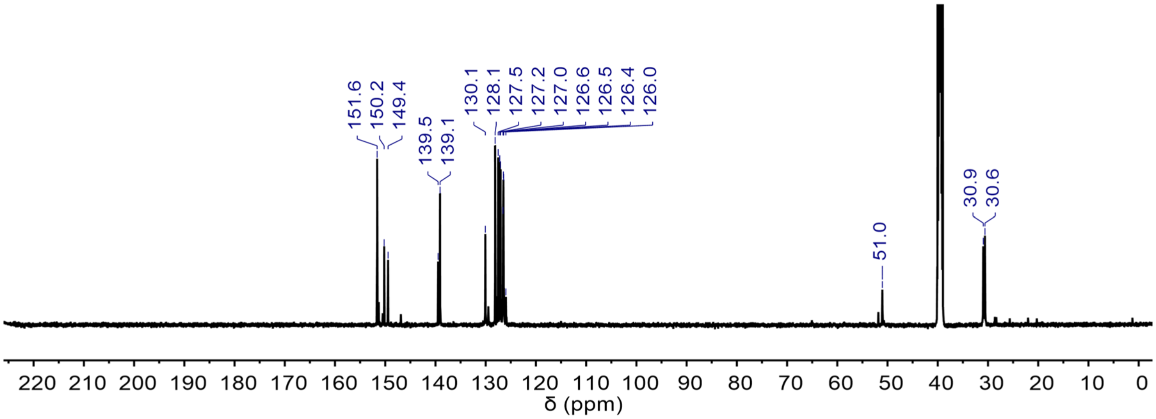

Figure 2.7. ^{13}C NMR spectrum of novel bivalent **Super-sCx4** (125 MHz, 298 K, in *d*$_6$-DMSO).

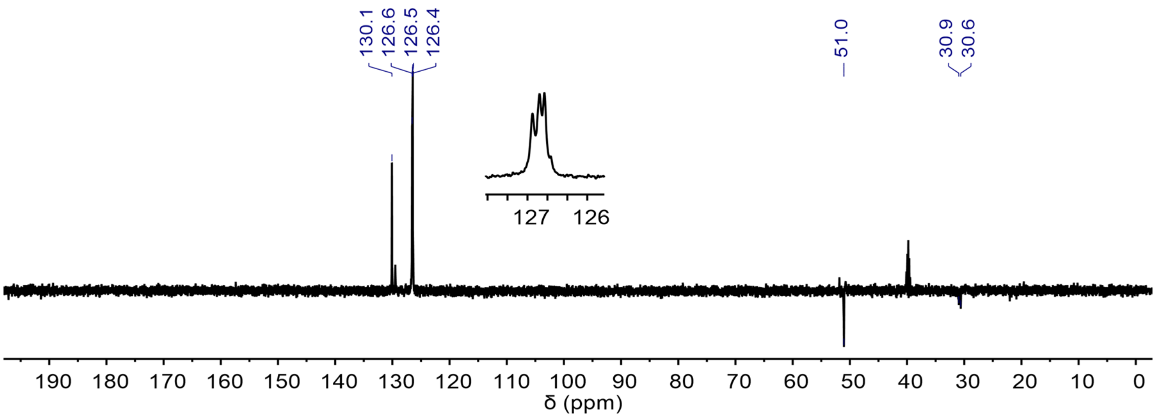

Figure 2.8. DEPT-135 NMR spectrum of novel bivalent **Super-sCx4** (125 MHz, 298 K, in d_6-DMSO).

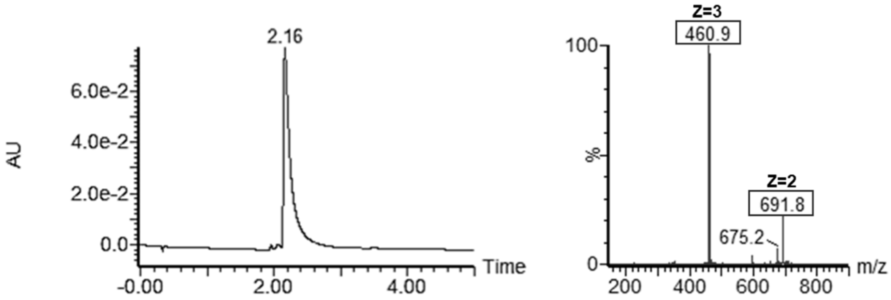

Figure 2.9. UPLC-MS (ES-) trace of novel bivalent **Super-sCx4** after preparative HPLC purification. Left = UV diode array detected chromatogram (190:400 nm). Right = negative ion mode ESI mass spectrum of the eluted peak.

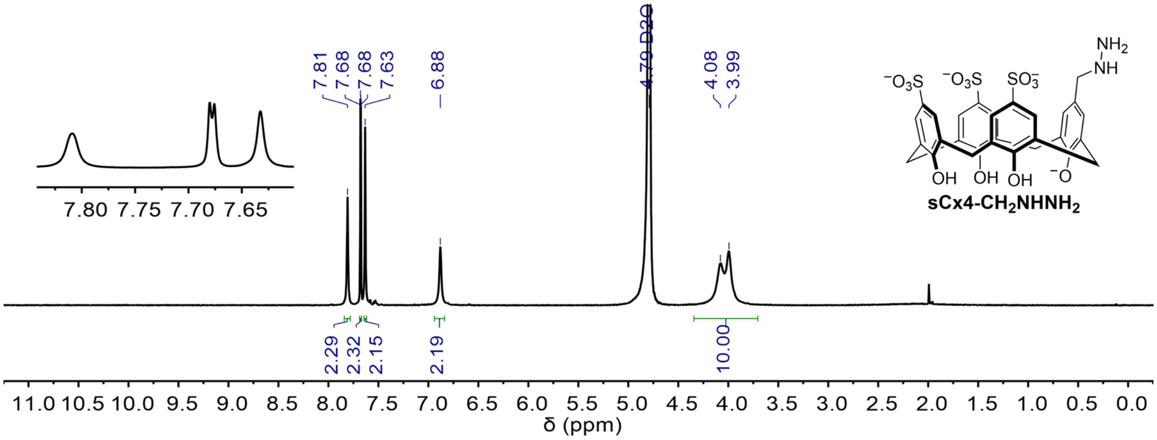

Figure 2.10. ^{1}H NMR spectrum of novel monovalent **sCx4-CH$_2$NHNH$_2$** (500 MHz, 298 K, in D2O).

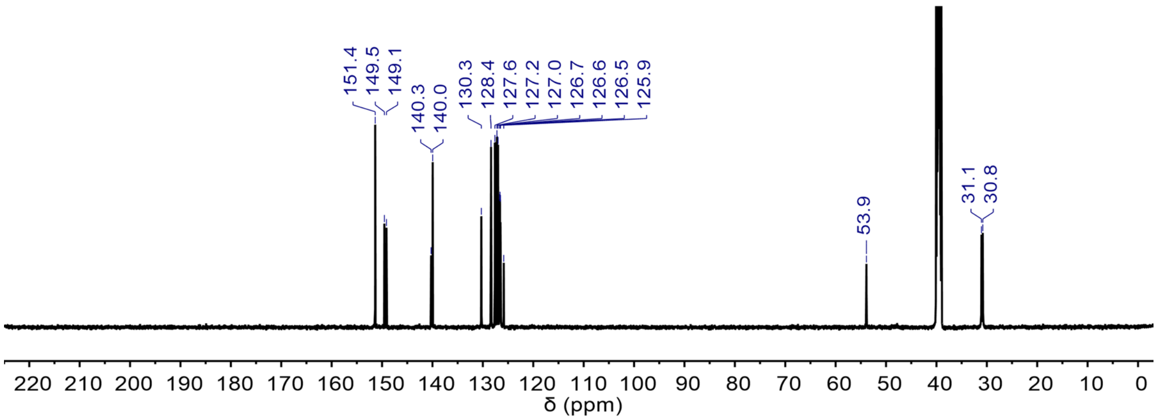

Figure 2.11. ^{13}C NMR spectrum of novel monovalent **sCx4-CH$_2$NHNH$_2$** (125 MHz, 298 K, in *d$_6$*-DMSO).

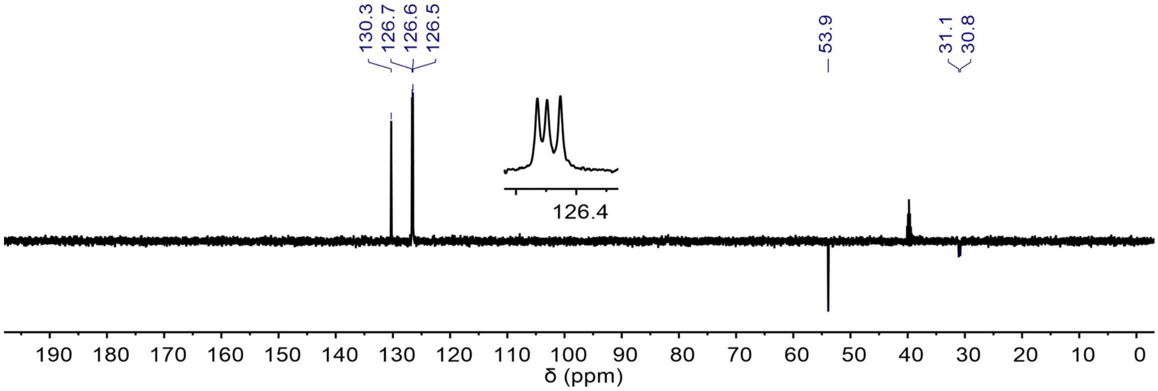

Figure 2.12. DEPT-135 NMR spectrum of novel monovalent **sCx4-CH$_2$NHNH$_2$** (125 MHz, 298 K, in *d$_6$*-DMSO).

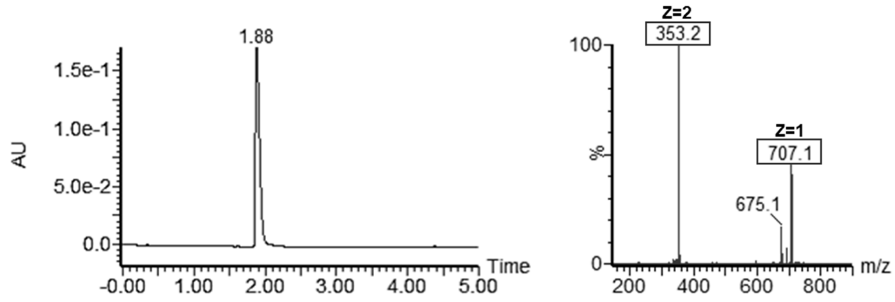

Figure 2.13. UPLC-MS (ES-) trace of novel monovalent **sCx4-CH$_2$NHNH$_2$** after preparative HPLC purification. Left = UV diode array detected chromatogram (190:400 nm). Right = negative ion mode ESI mass spectrum of the eluted peak.

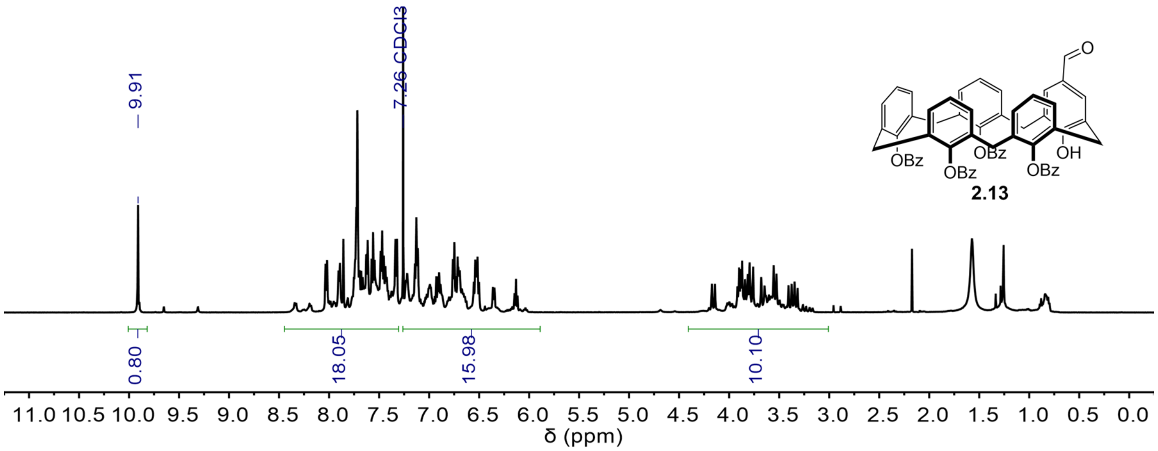

Figure 2.14. ^{1}H NMR spectrum of novel compound **2.13** (500 MHz, 298 K, in $CDCl_3$). This compound was carried forward without full characterization due to the intractable NMR spectra.

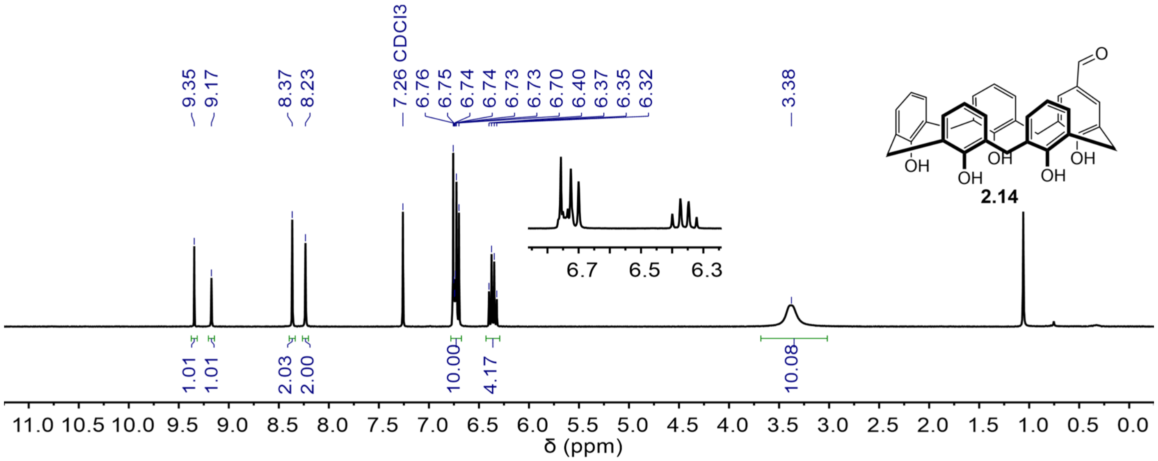

Figure 2.15. ^{1}H NMR spectrum of novel compound **2.14** (300 MHz, 300 K, in $CDCl_3$).

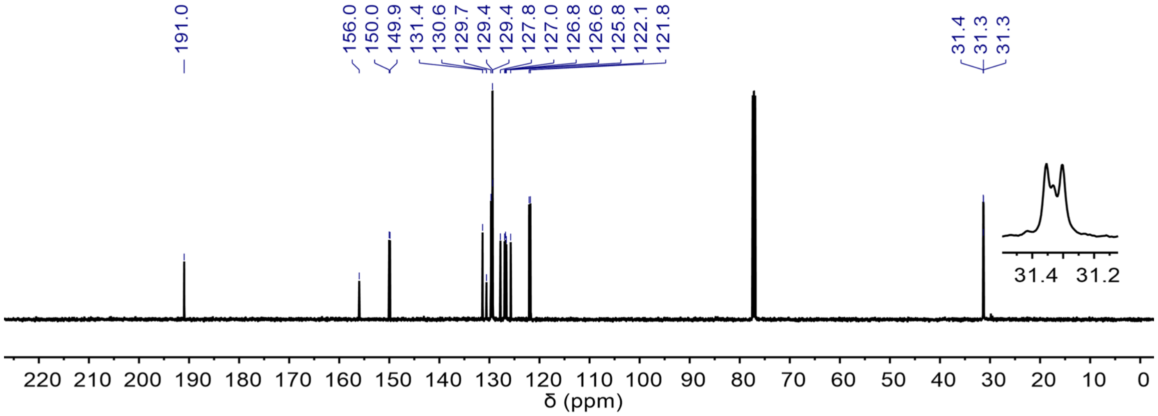

Figure 2.16. ^{13}C NMR spectrum of novel compound **2.14** (125 MHz, 298 K, in $CDCl_3$).

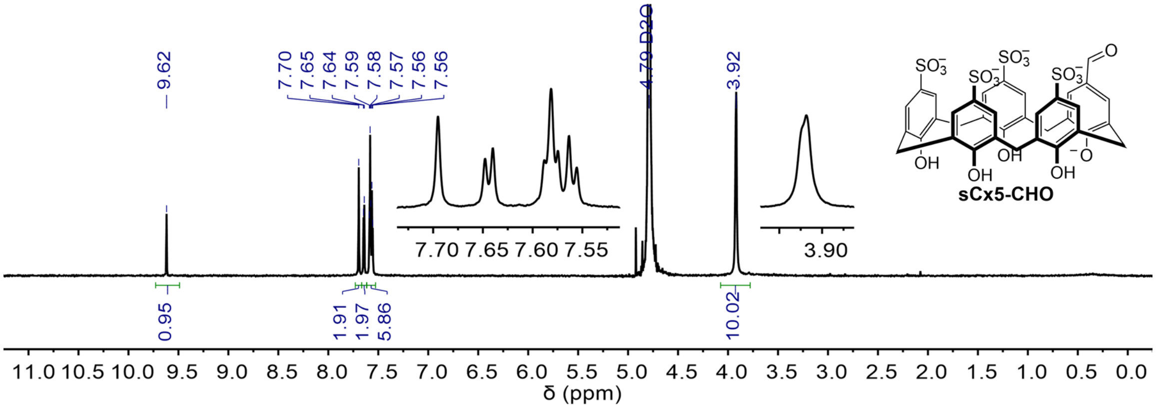

Figure 2.17. ^{1}H NMR spectrum of novel **sCx5-CHO** (300 MHz, 300 K, in D_2O).

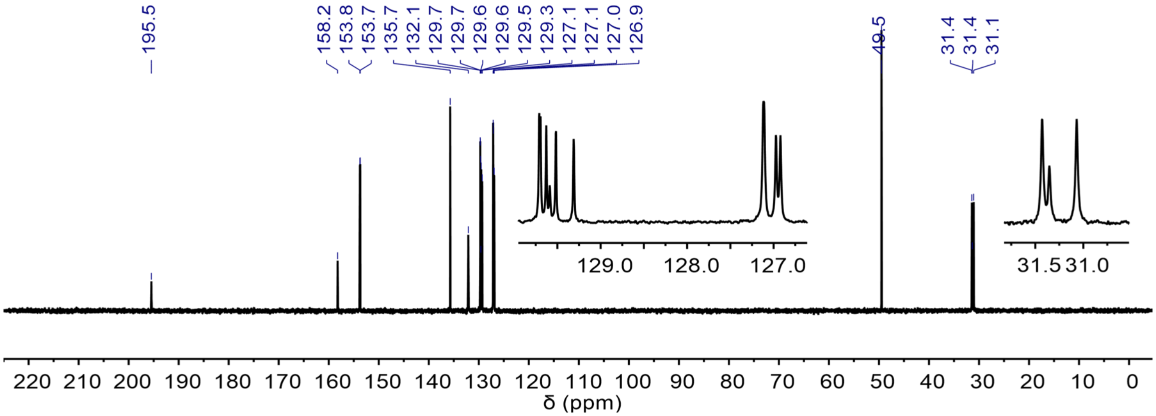

Figure 2.18. ^{13}C NMR spectrum of novel **sCx5-CHO** (125 MHz, 298 K, in D_2O) calibrated with an external reference (5% MeOH in D_2O, 49.5 ppm).

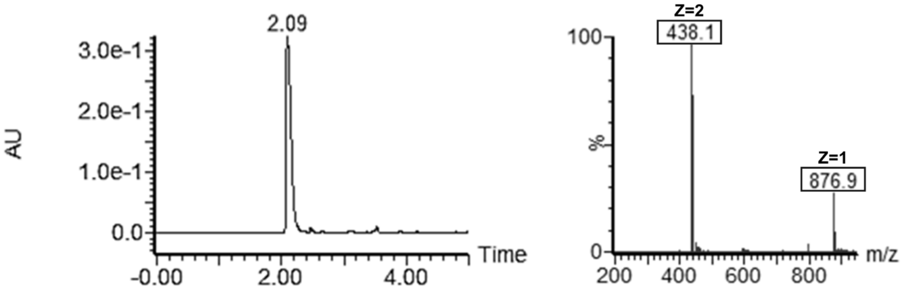

Figure 2.19. UPLC-MS (ES-) trace of novel **sCx5-CHO** after preparative HPLC purification. Left = UV diode array detected chromatogram (190:400 nm). Right = negative ion mode ESI mass spectrum of the eluted peak.

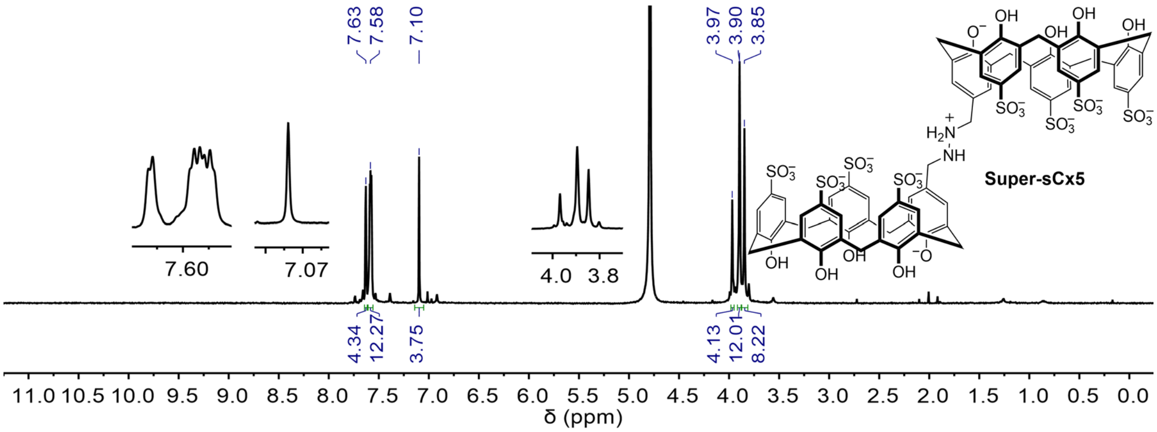

Figure 2.20. ^{1}H NMR spectrum of novel bivalent **Super-sCx5** (500 MHz, 298 K, in D_2O).

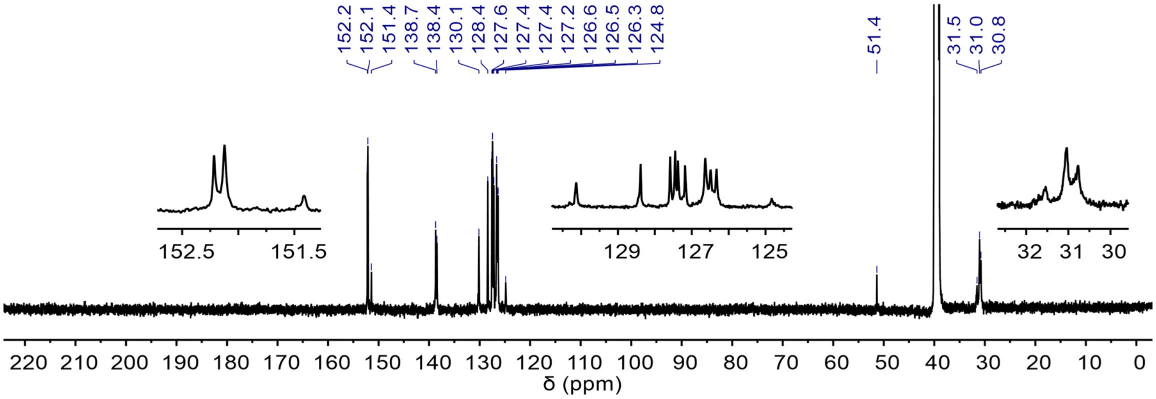

Figure 2.21. ^{13}C NMR spectrum of novel bivalent **Super-sCx5** (125 MHz, 298 K, in d_6-DMSO).

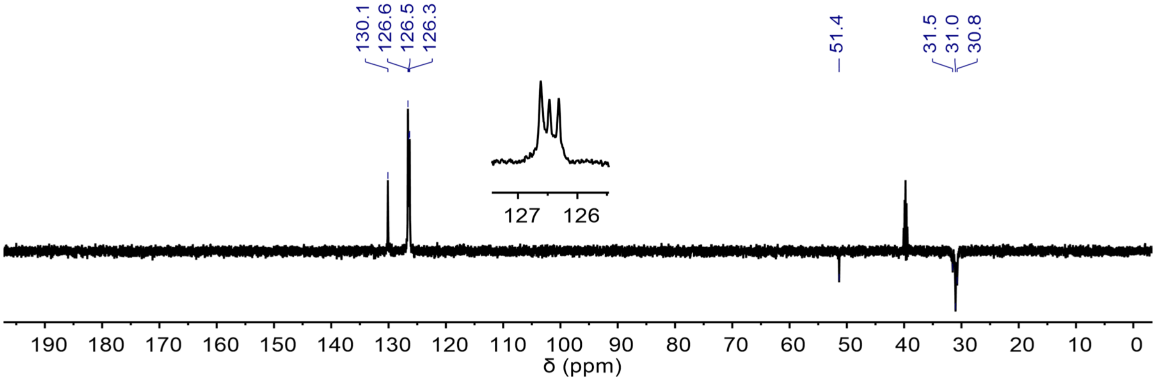

Figure 2.22. DEPT-135 NMR spectrum of novel bivalent **Super-sCx5** (125 MHz, 298 K, in d_6-DMSO).

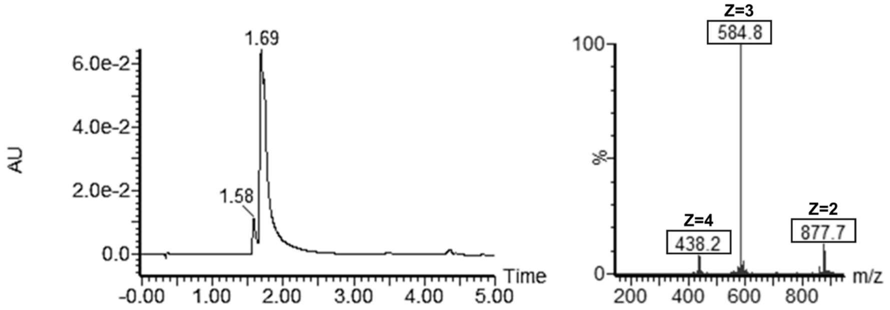

Figure 2.23. UPLC-MS (ES-) trace of novel bivalent **Super-sCx5** after preparative HPLC purification. Left = UV diode array detected chromatogram (190:400 nm). Right = negative ion mode ESI mass spectrum of the eluted peak.

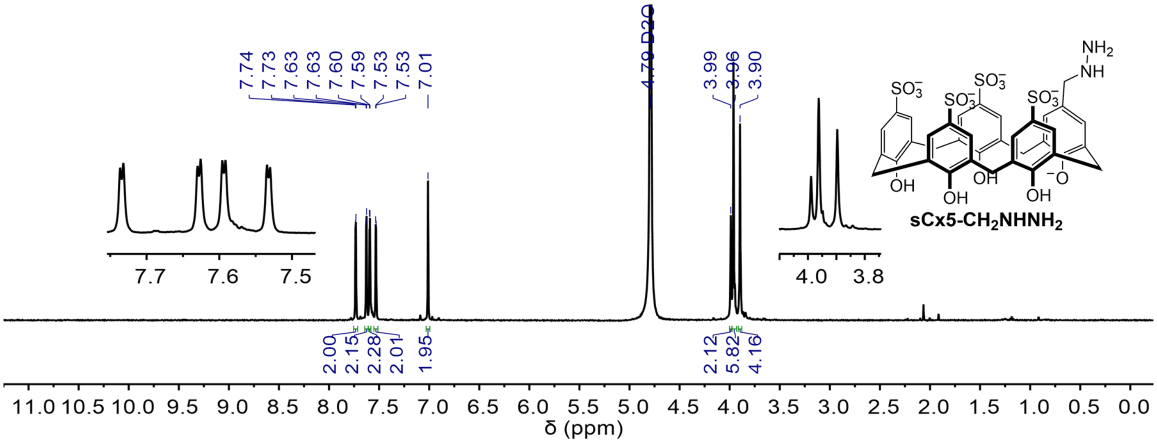

Figure 2.24. ^{1}H NMR spectrum of novel monovalent **sCx5-CH$_2$NHNH$_2$** (500 MHz, 298 K, in D$_2$O).

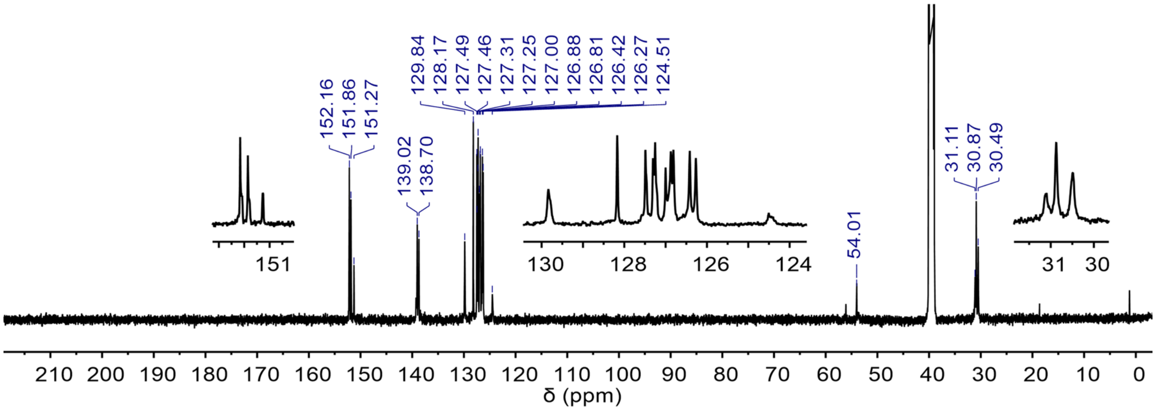

Figure 2.25. ^{13}C NMR spectrum of novel monovalent **sCx5-CH$_2$NHNH$_2$** (125 MHz, 298 K, in d_6-DMSO).

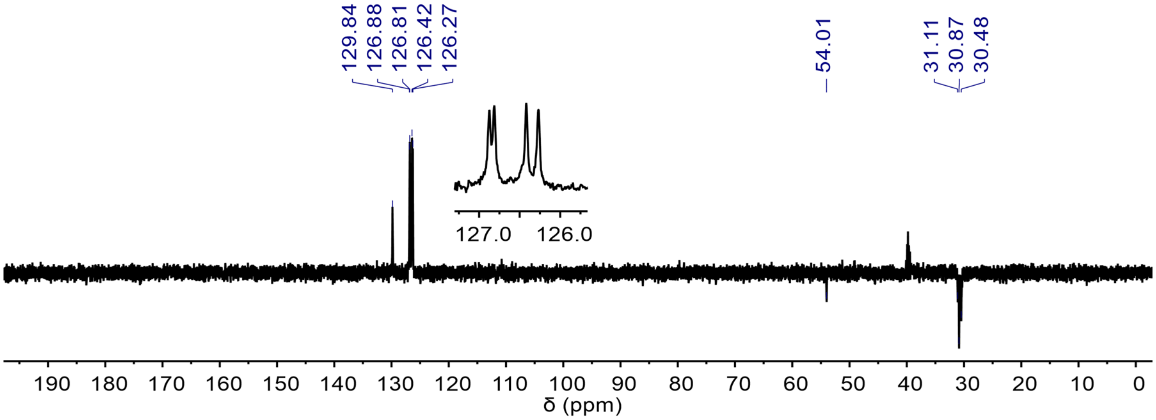

Figure 2.26. DEPT-135 NMR spectrum of novel monovalent **sCx5-CH$_2$NHNH$_2$** (125 MHz, 298 K, in d_6-DMSO).

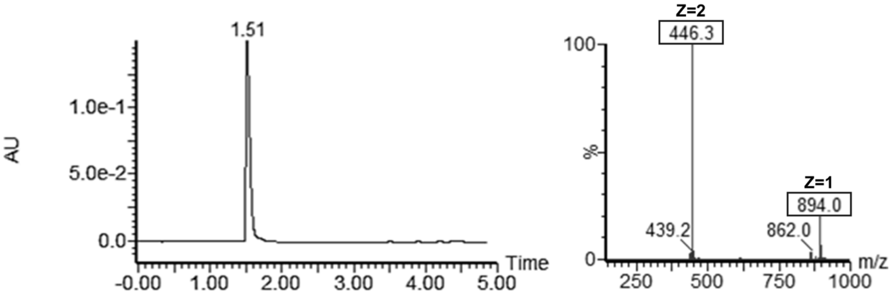

Figure 2.27. UPLC-MS (ES-) trace of novel monovalent **sCx5-CH$_2$NHNH$_2$** after preparative HPLC purification. Left = UV diode array detected chromatogram (190:400 nm). Right = negative ion mode ESI mass spectrum of the eluted peak.

2.5.4 *In situ* reaction monitoring by ^{1}H NMR and UPLC-MS

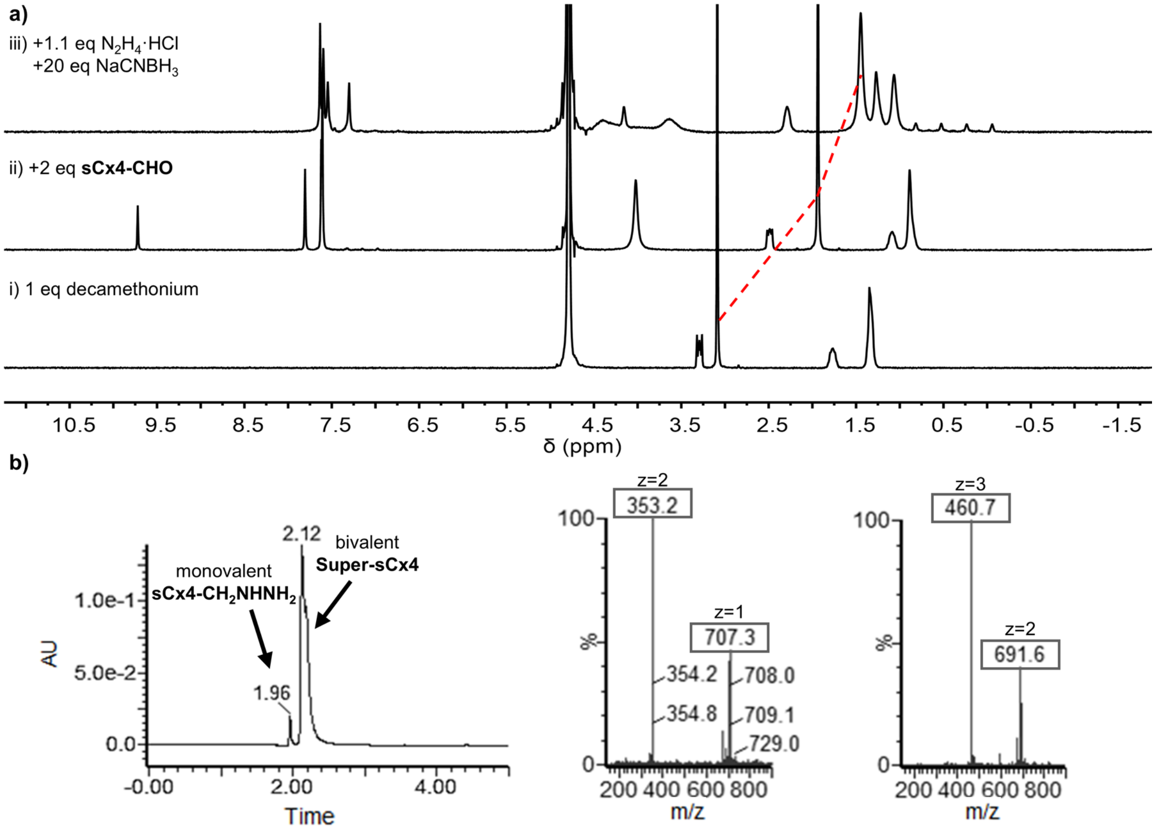

Figure 2.28. Bivalent **Super-sCx4** host synthesis is templated by the NMBA decamethonium. **a)** ^{1}H NMR of i) decamethonium bromide (5 mM), ii) after addition of **sCx4-CHO** (10 mM), and iii) crude reaction mixture after condensation and reductive amination. Red dashed line illustrates the upfield-shifted decamethonium methyl peak, indicating complexation inside the calix[4]arene cavity. Reaction in $(NH_4)_2CO_3$ (50 mM, pD 6.4) in D_2O (300 MHz, 298 K). **b)** UPLC-MS (ES-) of the crude templated reaction shows minor formation of monovalent **sCx4-CH$_2$NHNH$_2$** (1.96 min peak, left MS trace) and major product formation of bivalent **Super-sCx4** (2.12 min peak, right MS trace).

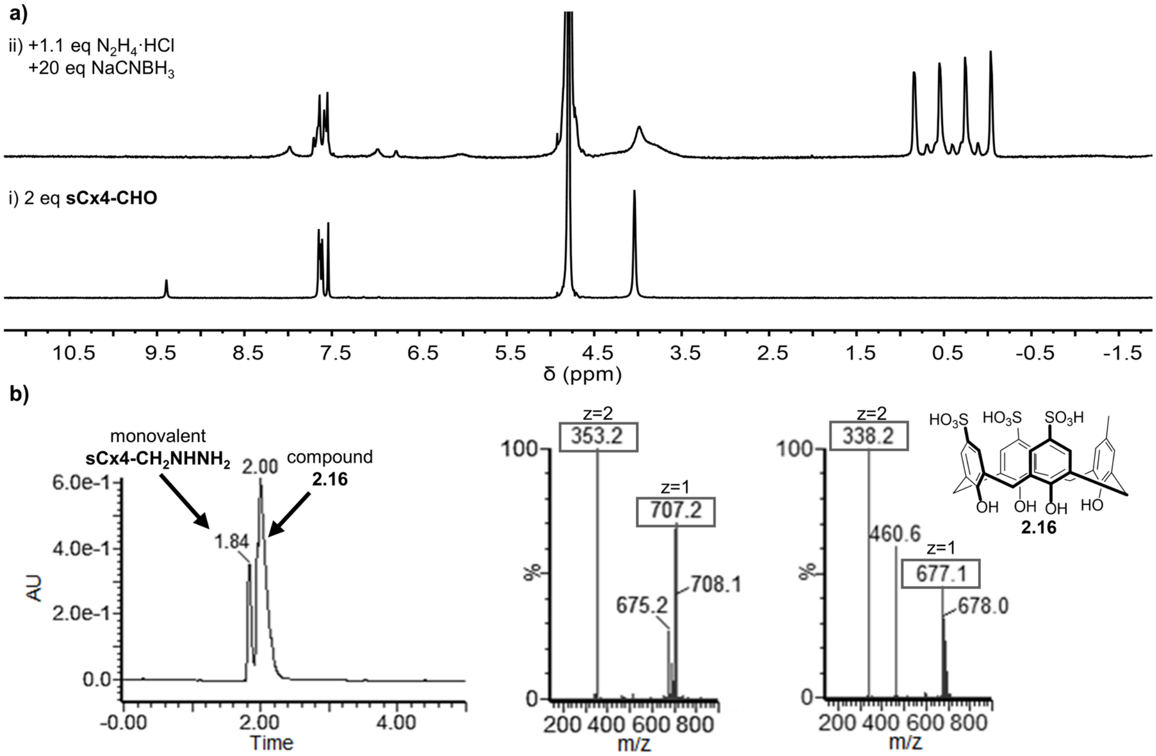

Figure 2.29. The untemplated control reaction does not form a bivalent host. **a)** ^{1}H NMR of i) **sCx4-CHO** (10 mM), and ii) crude reaction mixture after condensation and reductive amination. Reaction in $(NH_4)_2CO_3$ (50 mM, pD 6.4) in D_2O (300 MHz, 298 K). **b)** UPLC-MS (ES-) of the crude untemplated control reaction shows formation of monovalent **sCx4-CH$_2$NHNH$_2$** (1.84 min peak, left MS trace) and reduced starting material sCx4-CH$_3$ (**2.16**) (2.00 min peak, right MS trace).

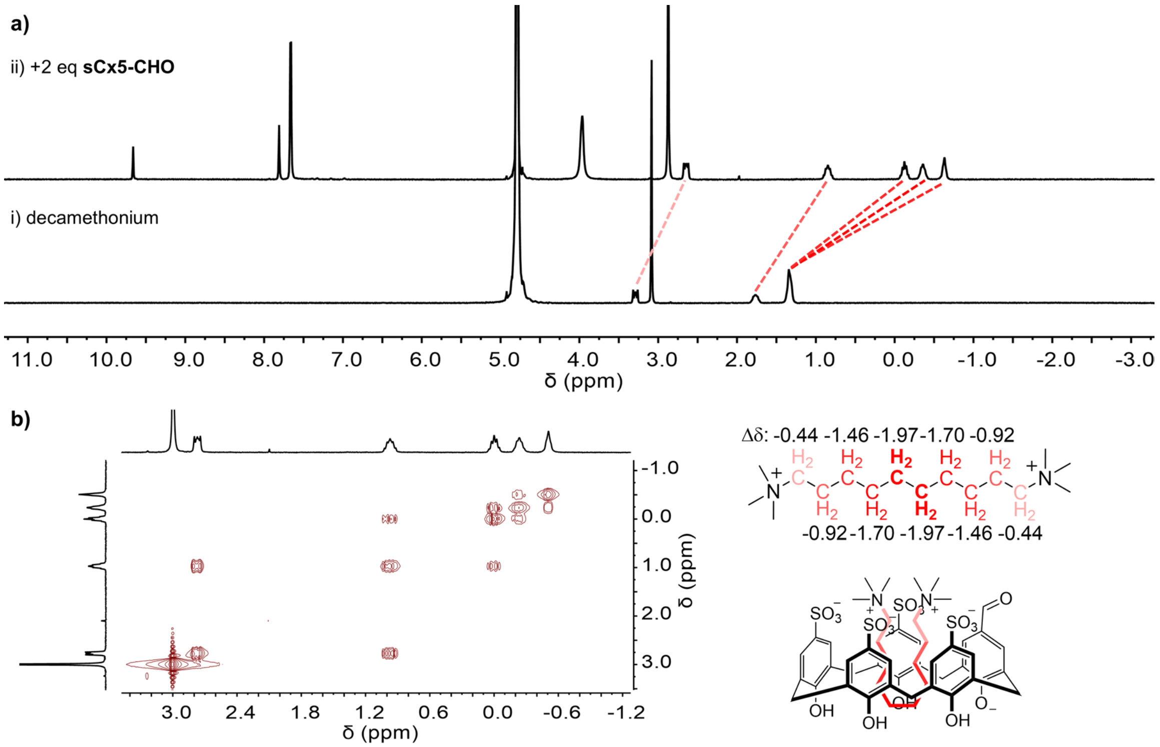

Figure 2.30. Decamethonium is not suitable for bivalent calix[5]arene host templation. **a)** ^{1}H NMR of i) decamethonium bromide (5 mM) and ii) addition of 2 eq **sCx5-CHO** (10 mM). Red dashed lines illustrate upfield chemical shifts of decamethonium methylene peaks. **b)** COSY and change in chemical shifts (Δδ) of decamethonium methylene peaks indicate decamethonium assumes a folded conformation inside the binding pocket of **sCx5-CHO**. Spectra collected in $(NH_4)_2CO_3$ (50 mM, pD 6.4) in D_2O (300 MHz, 298 K).

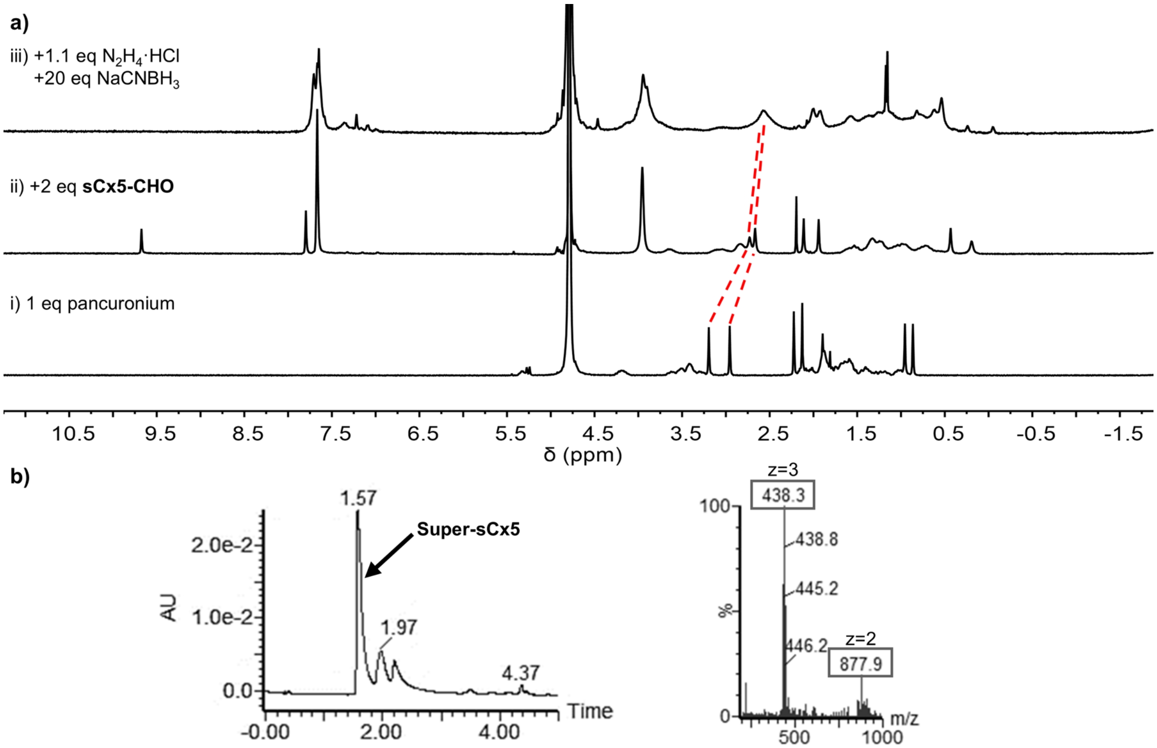

Figure 2.31. Bivalent **Super-sCx5** host synthesis is templated by the rigid NMBA pancuronium. **a)** ^{1}H NMR of i) pancuronium bromide (5 mM), ii) after addition of **sCx5-CHO** (10 mM), and iii) the crude reaction mixture after condensation and reductive amination. Red dashed lines illustrate upfield-shifted quaternary amine methyl peaks, indicating complexation inside the calix[5]arene cavity. Reaction in $(NH_4)_2CO_3$ (50 mM, pD 6.4) in D_2O (300 MHz, 298 K). **b)** UPLC-MS (ES-) of the crude templated reaction shows formation of bivalent **Super-sCx5** (1.57 min peak, right MS trace) as the major product.

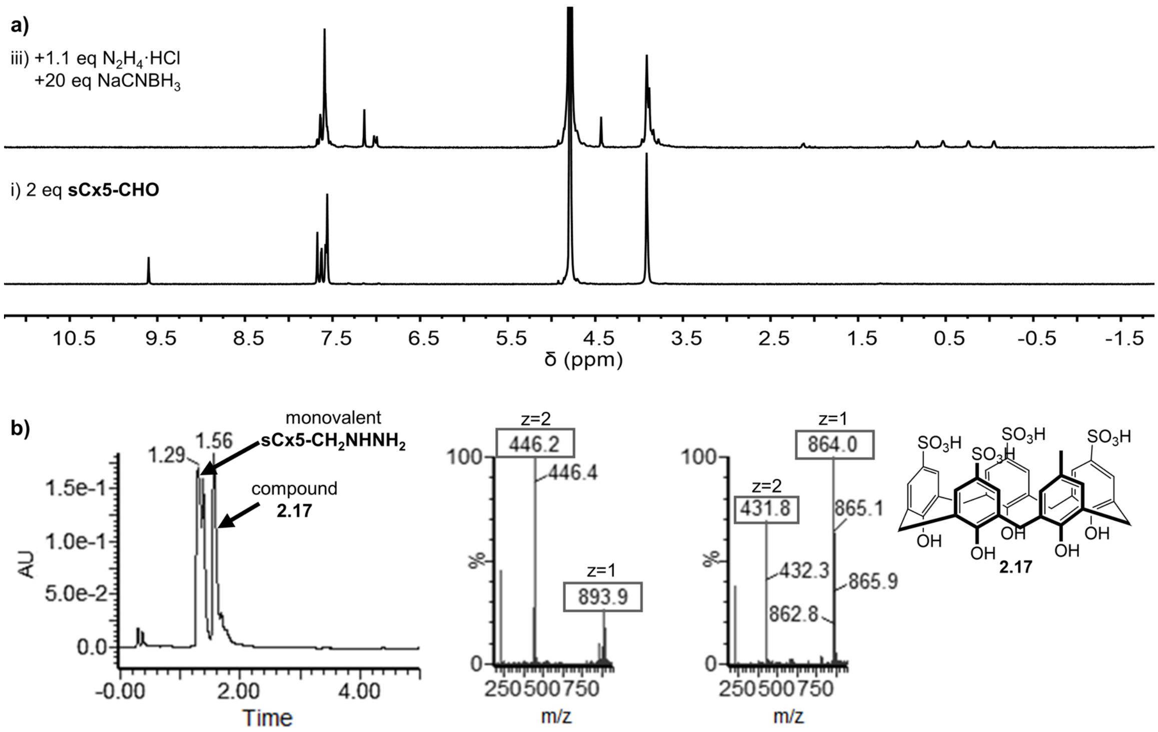

Figure 2.32. The untemplated control reaction does not form a bivalent host. **a)** ^{1}H NMR of i) **sCx5-CHO** (10 mM), and ii) the crude reaction mixture after condensation and reductive amination. Reaction in $(NH_4)_2CO_3$ (50 mM, pD 6.4) in D_2O (300 MHz, 298 K). **b)** UPLC-MS (ES-) of the crude untemplated control reaction shows formation of monovalent **sCx5-CH$_2$NHNH$_2$** (1.29 min peak, left MS trace) and reduced staring material sCx5-CH$_3$ (**2.17**) (1.56 min peak, right MS trace).

2.5.5 Indicator displacement assays

Direct and competitive titrations were done in NUNC black-walled, optical bottom 96-well plates. **LCG** was used as the indicator in all titrations and stock concentrations were determined by $\varepsilon_{410nm} = 8900\ M^{-1}cm^{-1}$. Direct titration solutions were composed of 0.25 μM **LCG** and varying concentrations of host (0-40 μM) in Na_2HPO_4/NaH_2PO_4 (10 mM, pH 7.4), made in Milli-Q™ ultrapure water. Competitive titration solutions were composed of 0.25 μM **LCG**, 5 μM host and varying concentrations of guest (0-10 mM), in Na_2HPO_4/NaH_2PO_4 (10 mM, pH 7.4), made in Milli-Q™ ultrapure water. Each well had a final volume of 100 μL. All fluorescence readings were collected on a BioTek Cytation-5, λ_{em} 485 nm (λ_{ex} 369 nm). Experiments were done in duplicate, performed on three different days using new stock solutions for each guest, totaling six replicates per guest.

A blank containing only the **LCG** dye and no host (Fl_o) was subtracted from each duplicate experiment. The data for each of the duplicates was plotted producing a K_d with standard error. The average K_d values of the three sets of duplicates was reported along with the propagated standard error for each host•guest interaction.

Direct host•**LCG** affinities were determined by plotting the fluorescence ($Fl-Fl_o$, a.u.) as a function of host concentration. The data was fit in GraphPad Prism using the following direct one site binding equation:

$$Y = A \times \frac{(D_{\boldsymbol{LCG}} + x + K_{d\,\boldsymbol{LCG}}) - \sqrt{(D_{\boldsymbol{LCG}} + x + K_{d\,\boldsymbol{LCG}})^2 - (4D_{\boldsymbol{LCG}}x)}}{2D_{\boldsymbol{LCG}}}$$

Where, A = amplitude of change in fluorescence ($Fl-Fl_o$)
$D_{\boldsymbol{LCG}}$ = concentration of **LCG**
x = amount titrated
$K_{d\,\boldsymbol{LCG}}$ = dissociation constant of **LCG**

Direct host•**LCG** fitting was constrained by the constant concentration of dye (0.25 μM). The graphs were plotted with standard deviation, along with a second plot of x residuals. All graphs met a criterion of $R^2 > 0.95$. The 90% inhibition concentration (IC_{90}) point from the direct titration was selected as the host concentrations used in competitive guest titrations, determined to be 5 μM for both **Super-sCx4** and **Super-sCx5**.

Competitive host•guest affinities were determined by plotting the logarithm of guest concentration and the fluorescence response from **LCG** displacement (Fl-Fl$_o$, a.u.). The data was analyzed in GraphPad Prism using the following competitive one site binding equation:

$$logEC_{50} = log\left(10^{logK_{d\,guest} * \left(1+\frac{D_{\boldsymbol{LCG}}}{K_{d\,\boldsymbol{LCG}}}\right)}\right)$$

Where, $K_{d\,\boldsymbol{LCG}}$ = dissociation constant of **LCG**
$D_{\boldsymbol{LCG}}$ = concentration of **LCG**
$K_{d\,guest}$ = dissociation constant of the guest of interest

Competitive host•guest fitting was constrained by the determined direct host•**LCG** dissociation constant ($K_{d\,\mathbf{LCG}}$) and the concentration of **LCG** (0.25 μM). This model fits $K_{d\,guest}$ directly and does not report the half maximal effective concentration (EC_{50}). This analysis assumes a 1:1 host•guest reversible binding interaction at equilibrium. Data was entered as logarithms of concentration and graphed on a linear axis with standard deviation. A second plot of x residuals were determined. All graphs met a criterion of $R^2 > 0.95$. In cases of weak binding where a clear inflection point of the curve was not observed and change in Fl-Fl$_o$ was <5000 a.u. (up to 10 mM concentrations tested) a cut off $K_d > 1.0 \times 10^{-2}$ M was assigned, a line of best fit and residuals were not plotted.

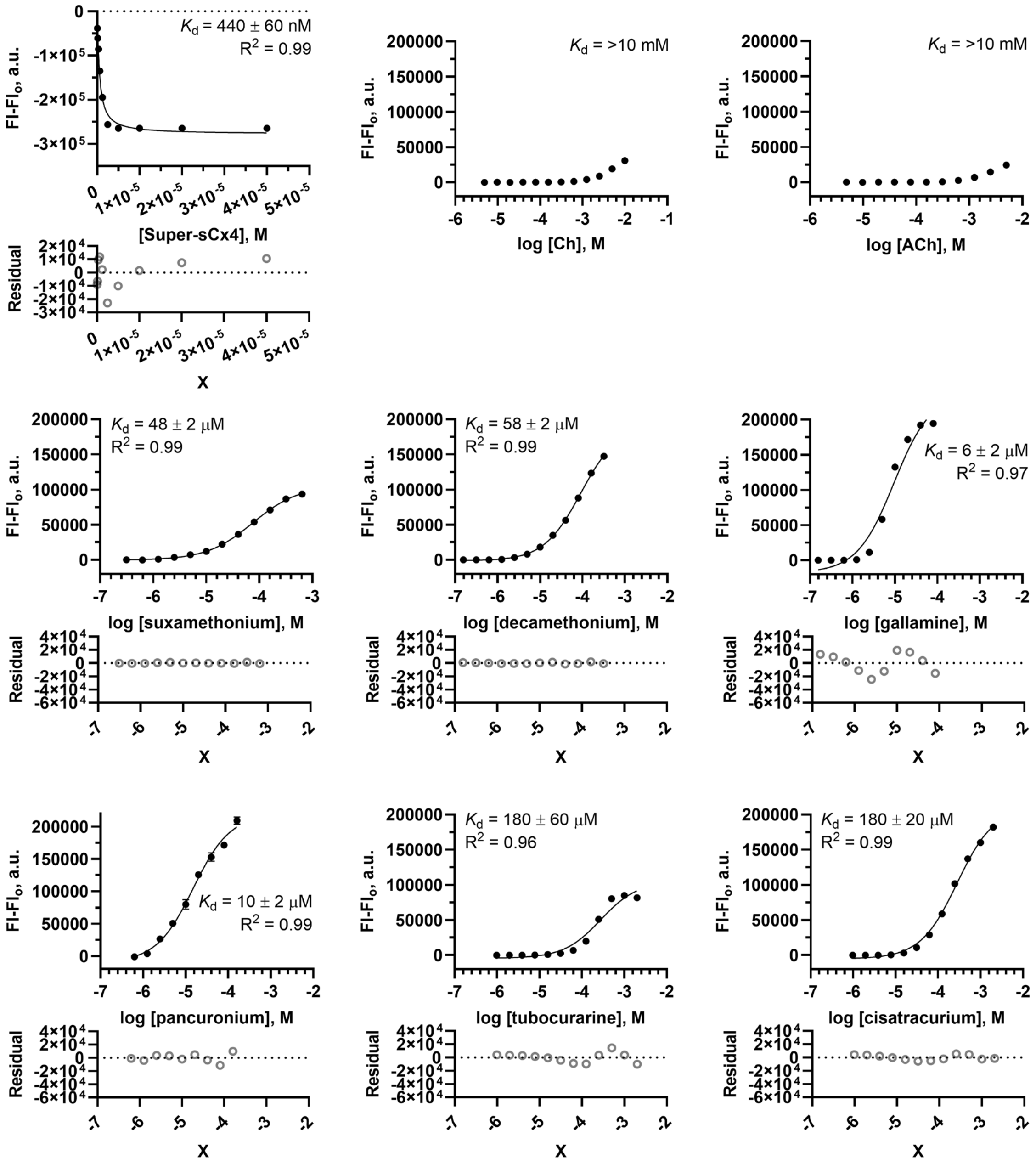

Figure 2.33. Exemplary duplicate data from direct titrations of **Super-sCx4** into **LCG**, and competitive titrations of NMBA's and cholines into **Super-sCx4•LCG**. Error bars were plotted for each duplicate but are not visible in cases where the error is smaller than the plotted point.

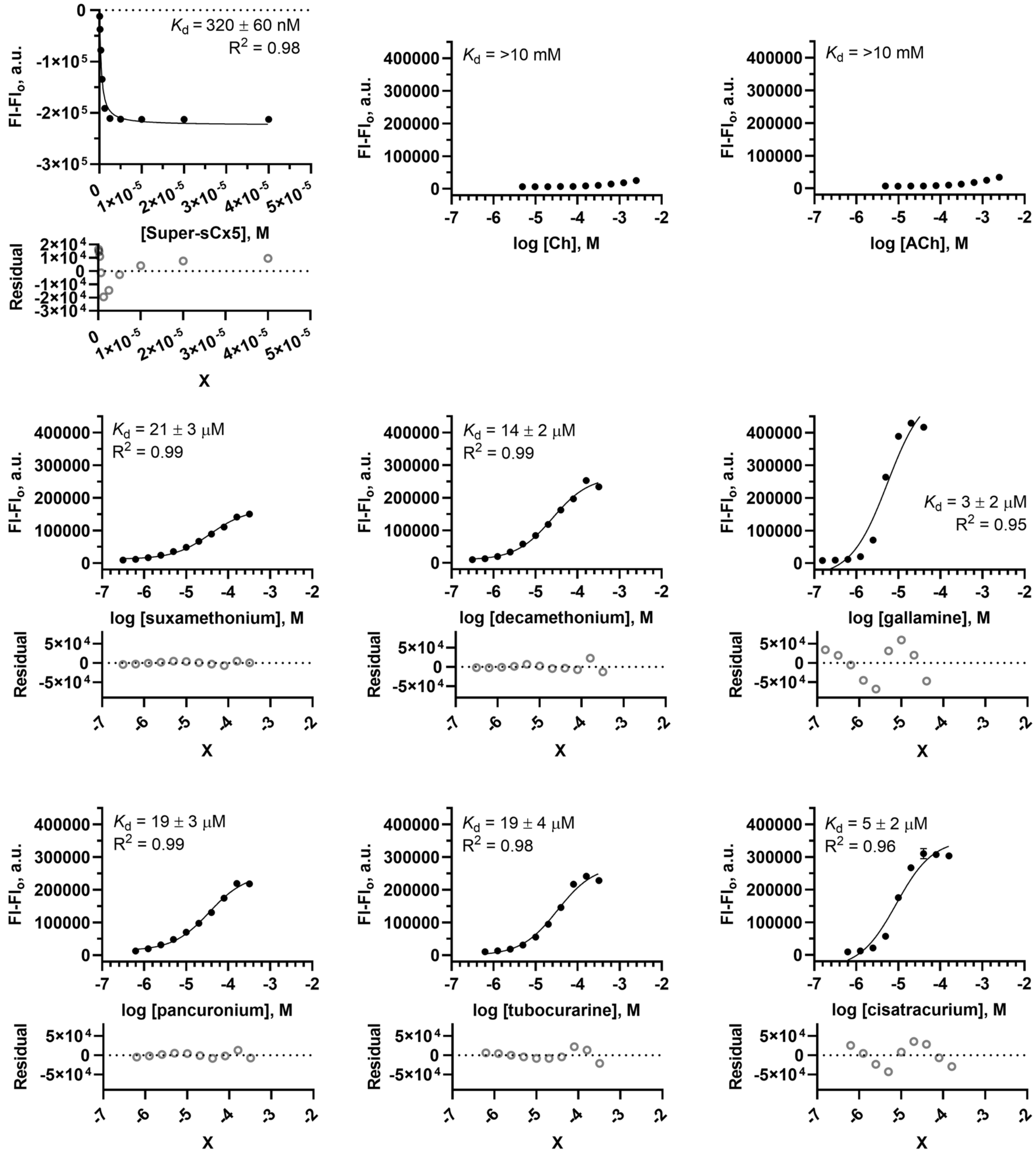

Figure 2.34. Exemplary duplicate data from direct titrations of **Super-sCx5** into **LCG**, and competitive titrations of NMBA's and cholines into **Super-sCx5•LCG**. Error bars were plotted for each duplicate but are not visible in cases where the error is smaller than the plotted point.

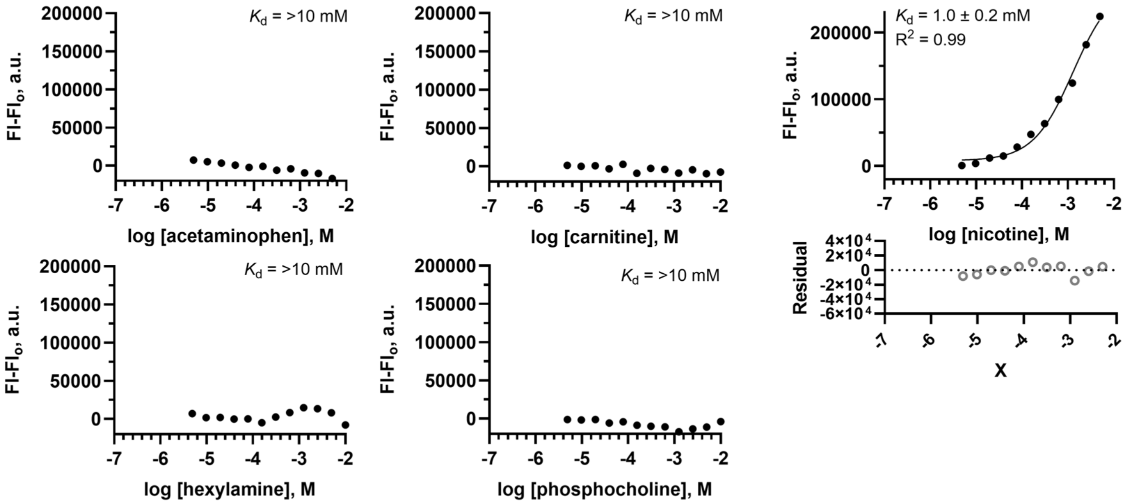

Figure 2.35. Exemplary duplicate data from competitive titrations of other hydrophobic amines into **Super-sCx4•LCG**. Error bars were plotted for each duplicate but are not visible in cases where the error is smaller than the plotted point.

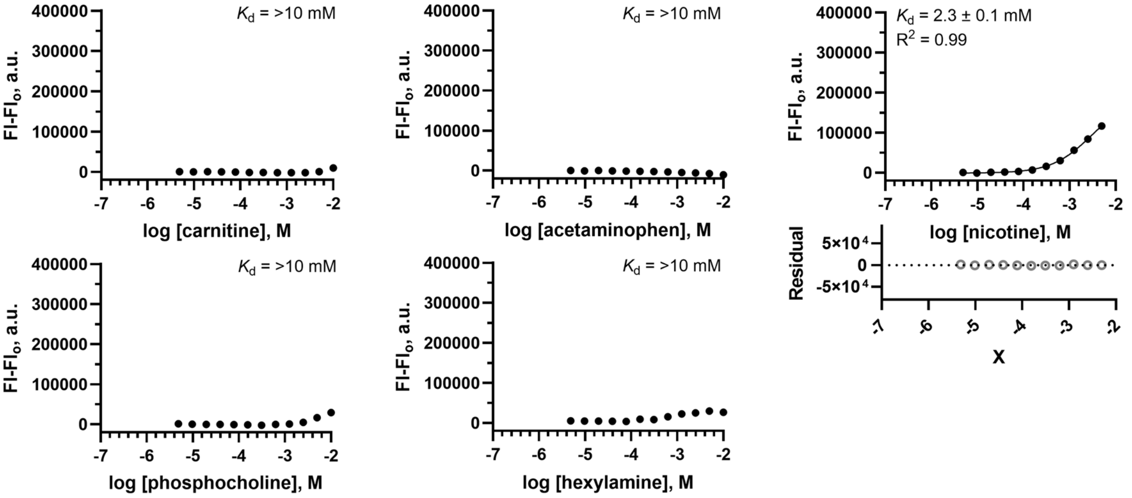

Figure 2.36. Exemplary duplicate data from competitive titrations of other hydrophobic amines into **Super-sCx5•LCG**. Error bars were plotted for each duplicate but are not visible in cases where the error is smaller than the plotted point.

Table 2.3. IDA determined equilibrium dissociation constants of Super-sCx hosts with other hydrophobic amines.

Guest	**Super-sCx4** K_d (M)^a	**Super-sCx5** K_d (M)^a
Nicotine	$(7 \pm 1) \times 10^{-4}$	$(1.7 \pm 0.1) \times 10^{-3}$
Acetaminophen	$>1.0 \times 10^{-2}$	$>1.0 \times 10^{-2}$
Carnitine	$>1.0 \times 10^{-2}$	$>1.0 \times 10^{-2}$
Phosphocholine	$>1.0 \times 10^{-2}$	$>1.0 \times 10^{-2}$
Hexylamine	$>1.0 \times 10^{-2}$	$>1.0 \times 10^{-2}$

^{a}All studies in NaH_2PO_4/Na_2HPO_4 (10 mM, pH 7.4) in H_2O. Dissociation constants were determined from fluorescence IDA titrations assuming 1:1 stoichiometry, values reported are the average of six measurements with propagated standard error.

2.5.6 ^{1}H NMR titrations

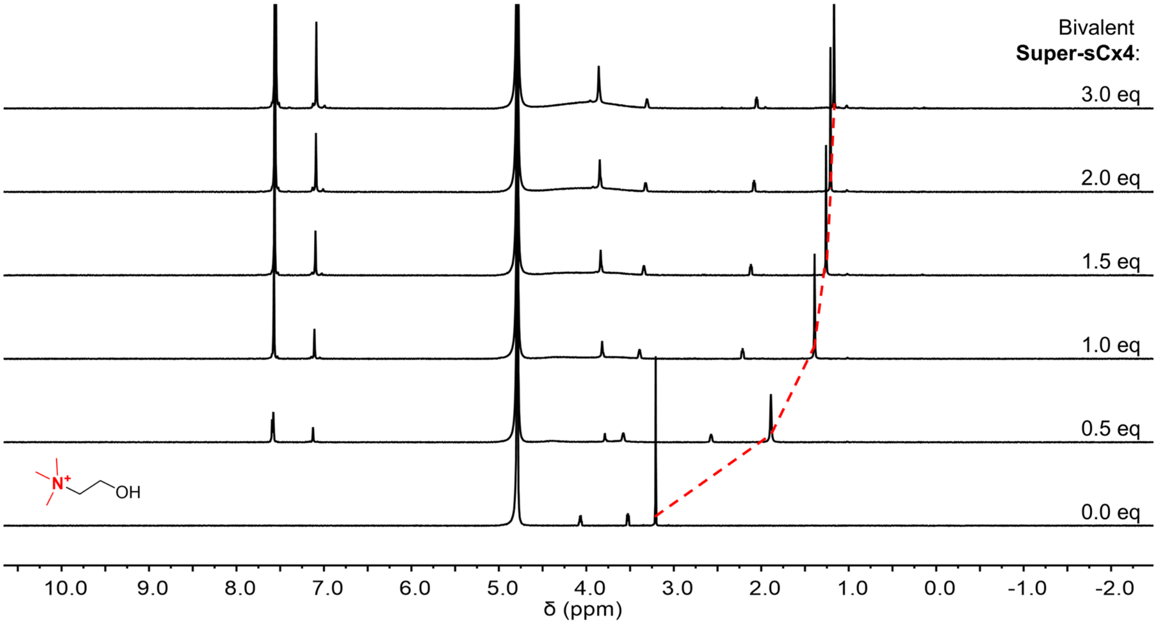

Figure 2.37. ^{1}H NMR titration of bivalent **Super-sCx4** (4 mM) into **Ch** (800 µM). Red dashed line indicates binding of methyl groups. All solutions were in NaH_2PO_4/Na_2HPO_4 (50 mM, pD 7.4) in D_2O (500 MHz, 297 K).

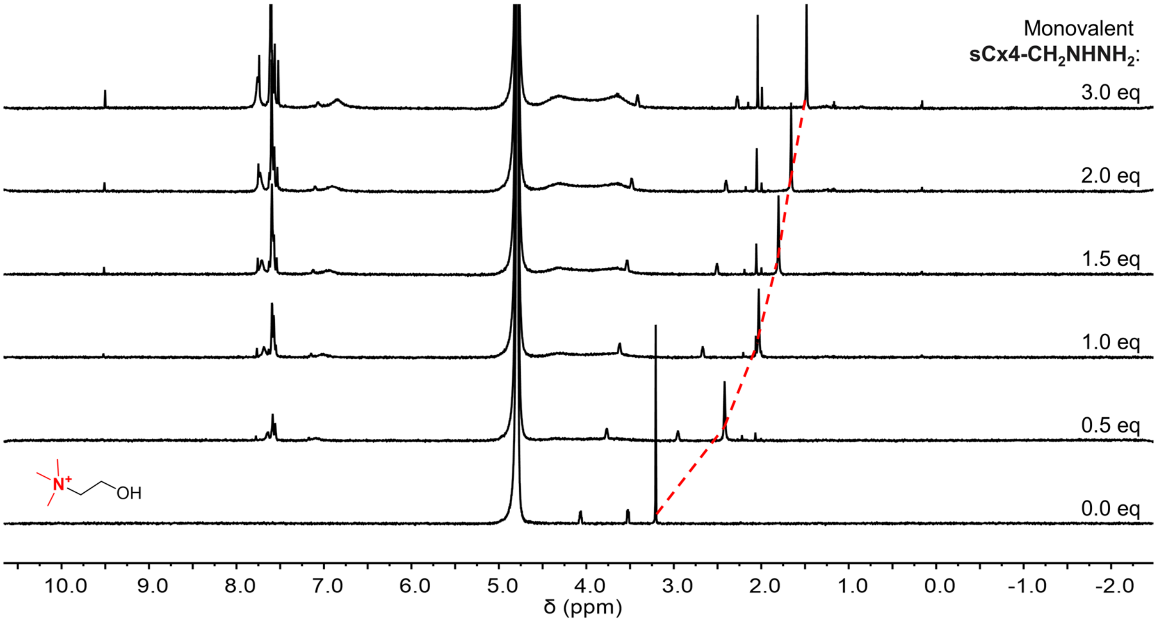

Figure 2.38. ^{1}H NMR titration of monovalent **sCx4-CH$_2$NHNH$_2$** (4 mM) into **Ch** (800 µM). Red dashed line indicates binding of methyl groups. All solutions were in NaH_2PO_4/Na_2HPO_4 (50 mM, pD 7.4) in D_2O (500 MHz, 297 K).

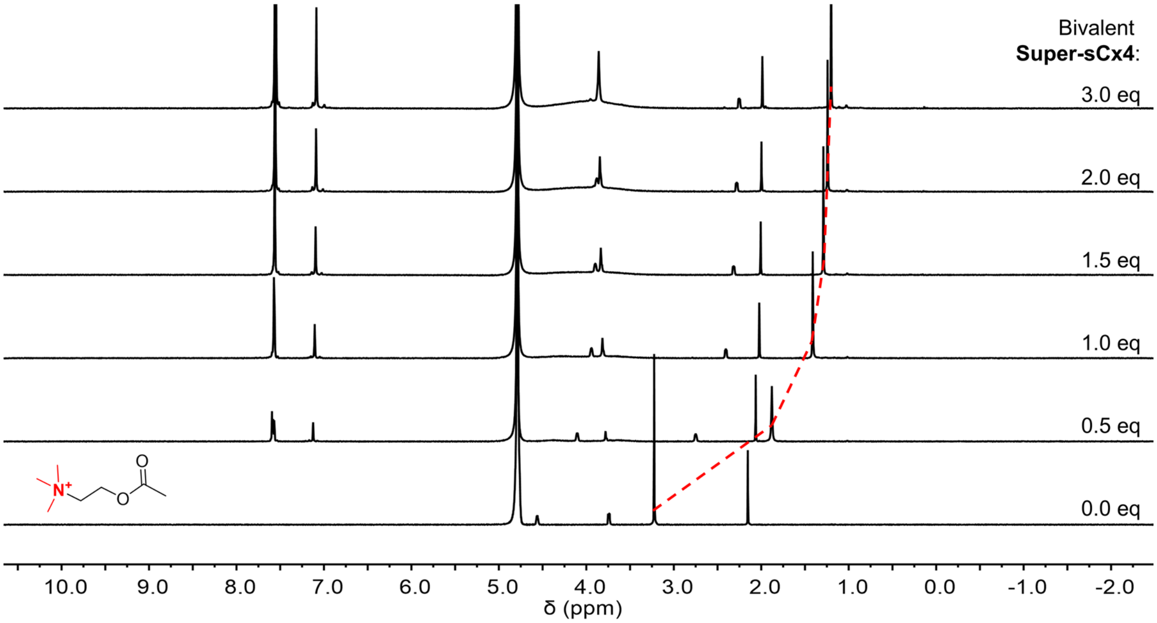

Figure 2.39. ^{1}H NMR titration of bivalent **Super-sCx4** (4 mM) into **ACh** (800 µM). Red dashed line indicates binding of methyl groups. All solutions were in NaH_2PO_4/Na_2HPO_4 (50 mM, pD 7.4) in D_2O (500 MHz, 297 K).

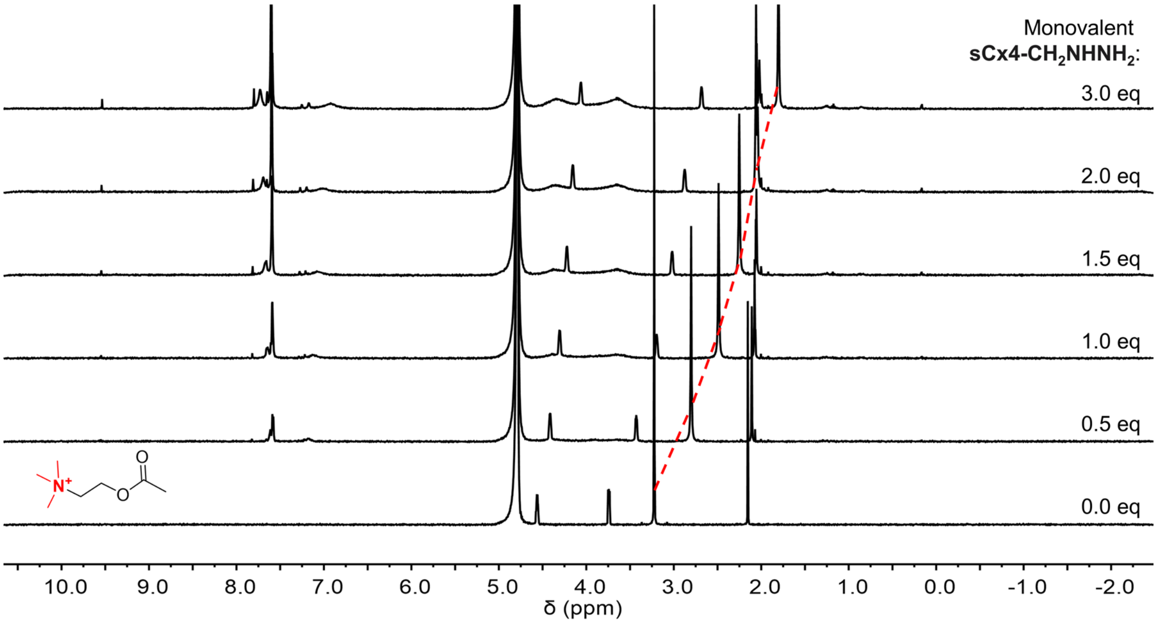

Figure 2.40. ^{1}H NMR titration of monovalent **sCx4-CH$_2$NHNH$_2$** (4 mM) into **ACh** (800 µM). Red dashed line indicates binding of methyl groups. All solutions were in NaH_2PO_4/Na_2HPO_4 (50 mM, pD 7.4) in D_2O (500 MHz, 297 K).

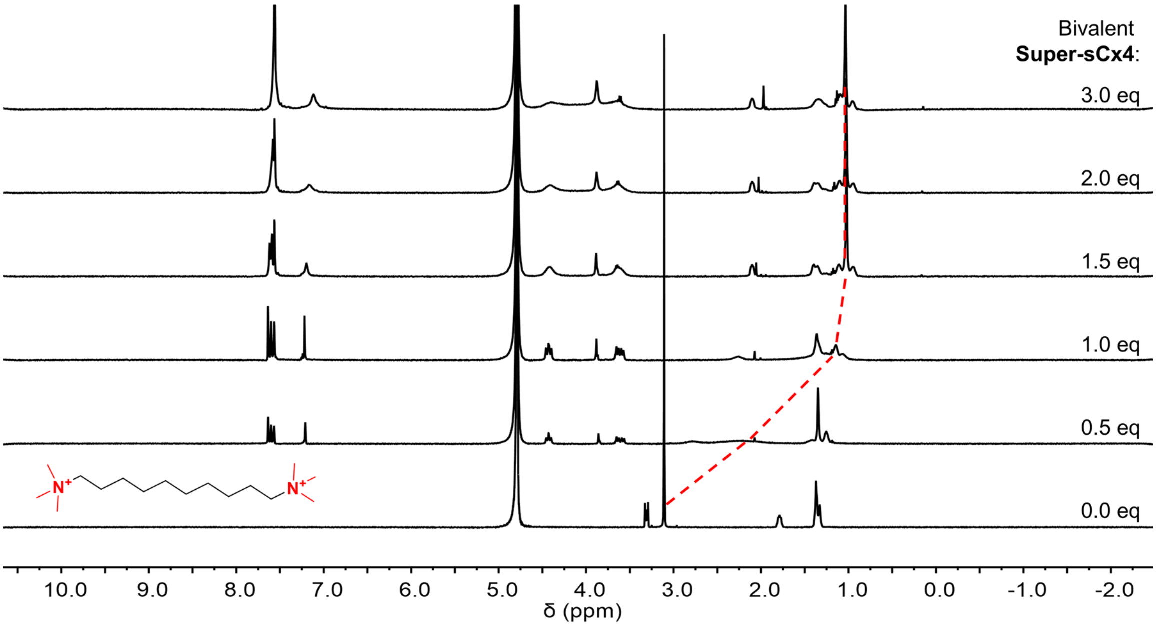

Figure 2.41. ^{1}H NMR titration of bivalent **Super-sCx4** (4 mM) into decamethonium (800 µM). Red dashed line indicates binding of methyl groups. All solutions were in NaH_2PO_4/Na_2HPO_4 (50 mM, pD 7.4) in D_2O (500 MHz, 297 K).

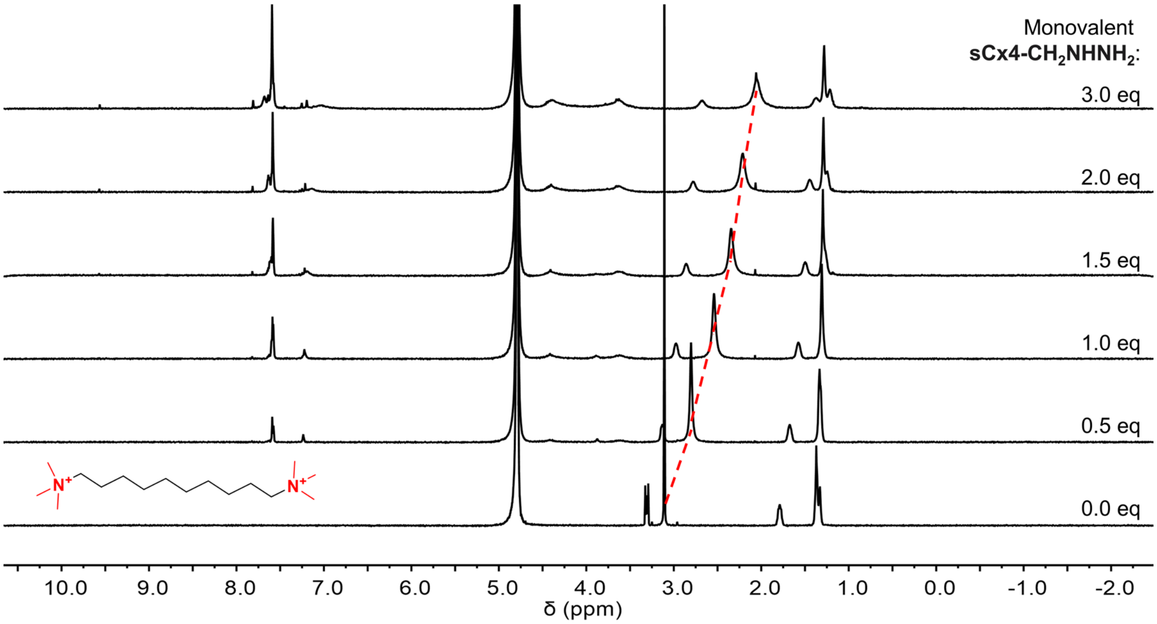

Figure 2.42. ^{1}H NMR titration of monovalent **sCx4-CH$_2$NHNH$_2$** (4 mM) into decamethonium (800 µM). Red dashed line indicates binding of methyl groups. All solutions were in NaH_2PO_4/Na_2HPO_4 (50 mM, pD 7.4) in D_2O (500 MHz, 297 K).

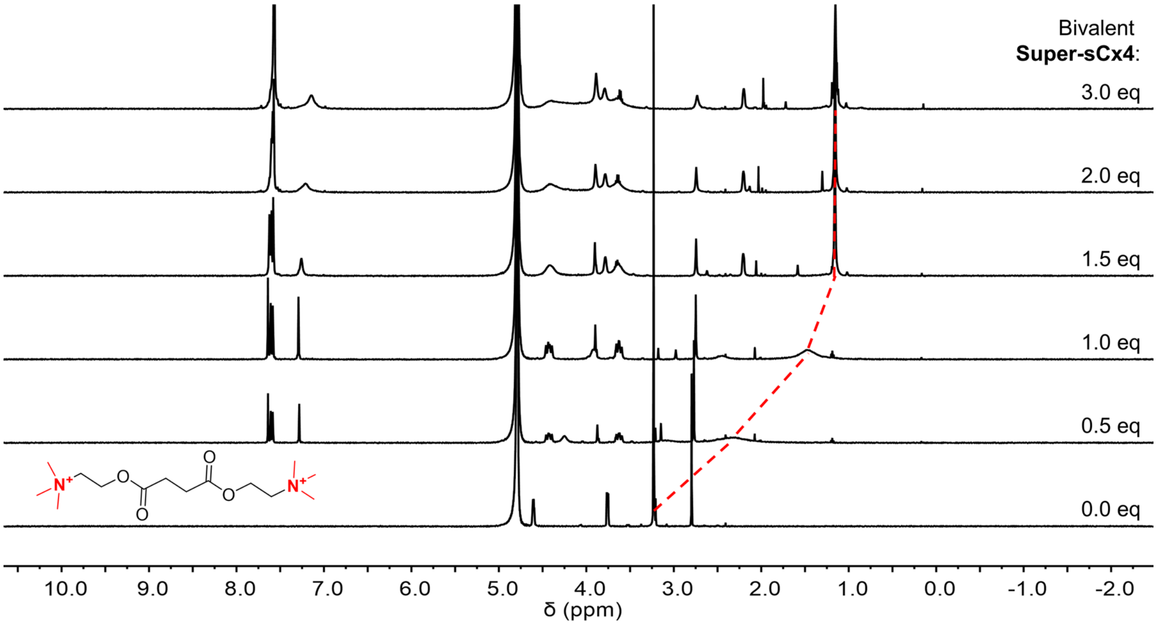

Figure 2.43. ^{1}H NMR titration of bivalent **Super-sCx4** (4 mM) into suxamethonium (800 μM). Red dashed line indicates binding of methyl groups. All solutions were in NaH_2PO_4/Na_2HPO_4 (50 mM, pD 7.4) in D_2O (500 MHz, 297 K).

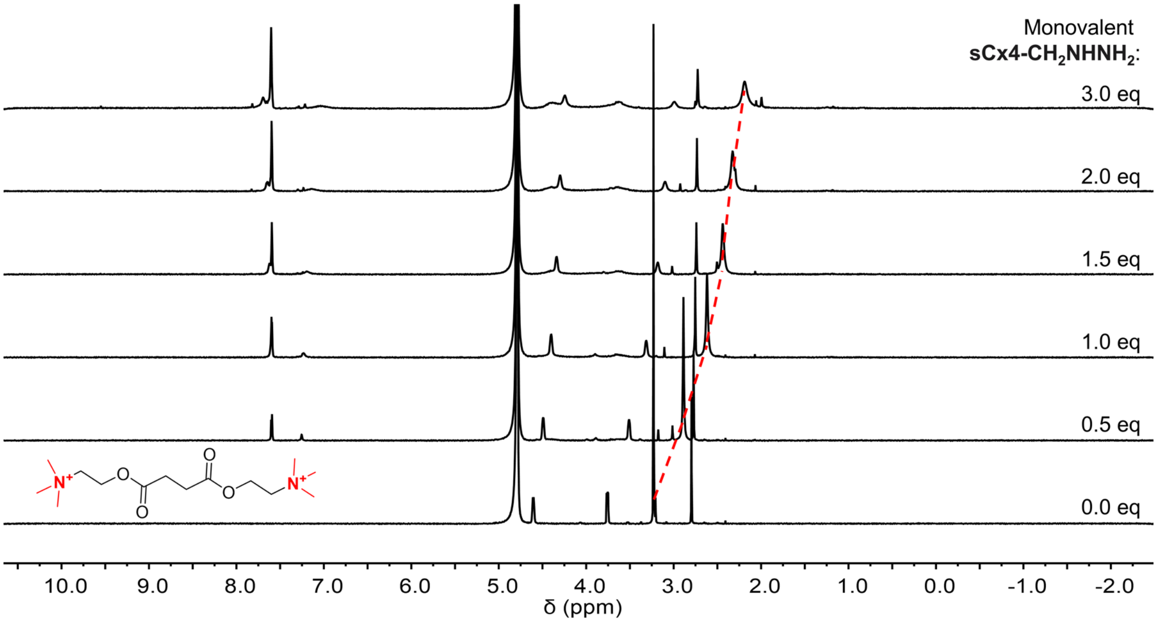

Figure 2.44. ^{1}H NMR titration of monovalent **sCx4-CH$_2$NHNH$_2$** (4 mM) into suxamethonium (800 μM). Red dashed line indicates binding of methyl groups. All solutions were in NaH_2PO_4/Na_2HPO_4 (50 mM, pD 7.4) in D_2O (500 MHz, 297 K).

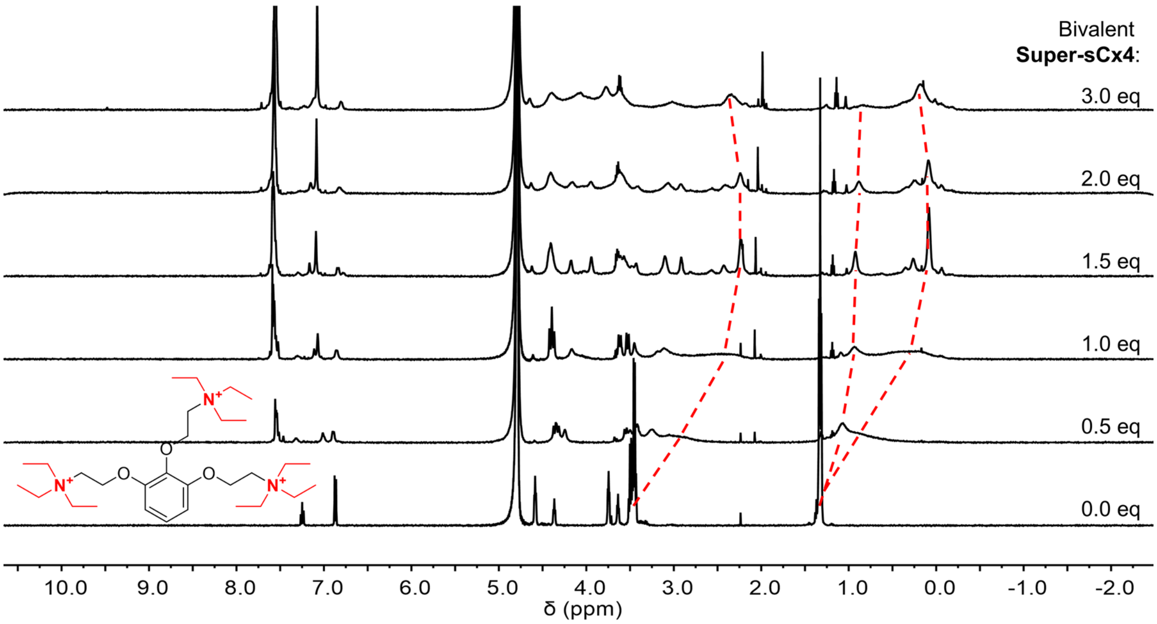

Figure 2.45. ^{1}H NMR titration of bivalent **Super-sCx4** (4 mM) into gallamine (800 μM). Red dashed lines indicate binding of ethyl and methyl groups. All solutions were in NaH_2PO_4/Na_2HPO_4 (50 mM, pD 7.4) in D_2O (500 MHz, 297 K).

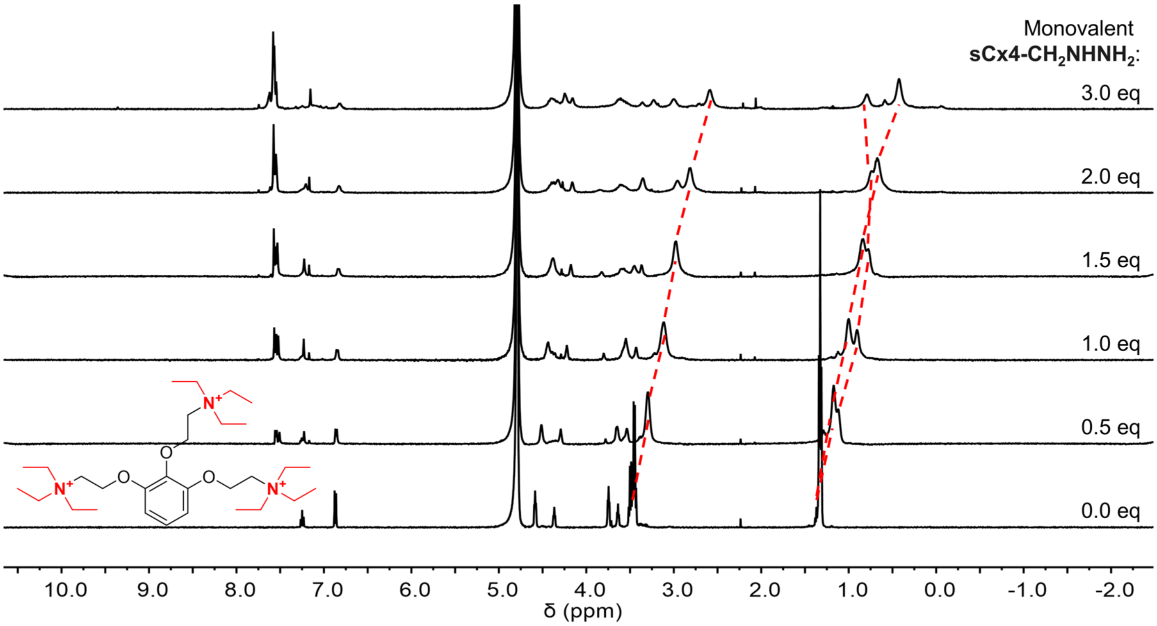

Figure 2.46. ^{1}H NMR titration of monovalent **sCx4-CH$_2$NHNH$_2$** (4 mM) into gallamine (800 μM). Red dashed lines indicate the binding of ethyl and methyl groups. All solutions were in NaH_2PO_4/Na_2HPO_4 (50 mM, pD 7.4) in D_2O (500 MHz, 297 K).

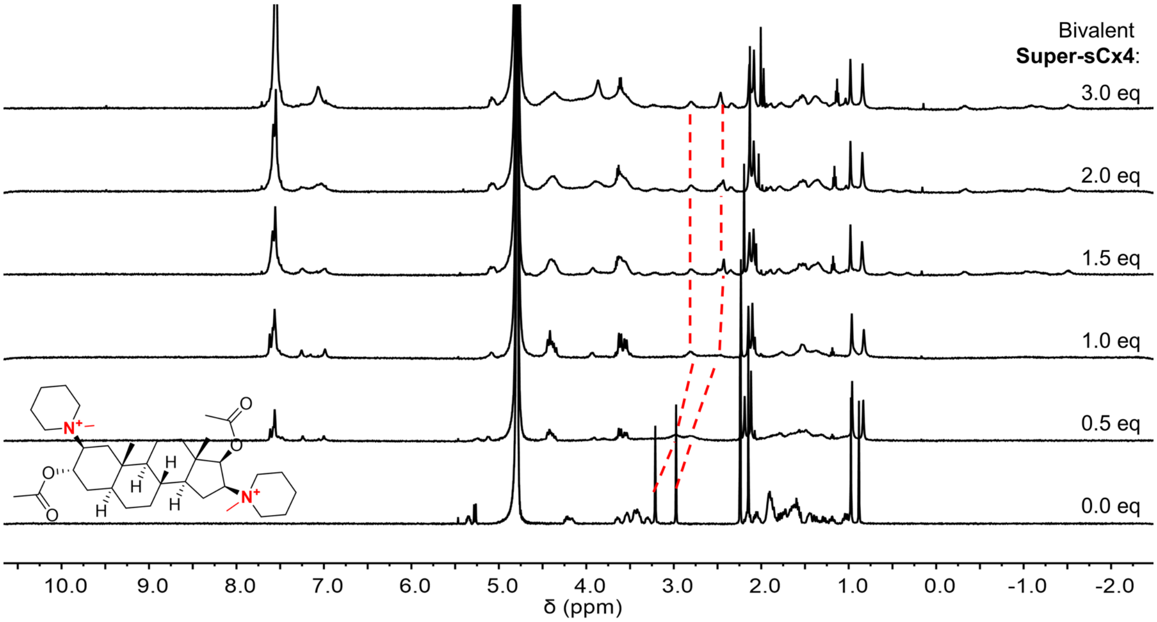

Figure 2.47. ^{1}H NMR titration of bivalent **Super-sCx4** (4 mM) into pancuronium (800 µM). Red dashed lines indicate binding of methyl groups. All solutions were in NaH_2PO_4/Na_2HPO_4 (50 mM, pD 7.4) in D_2O (500 MHz, 297 K).

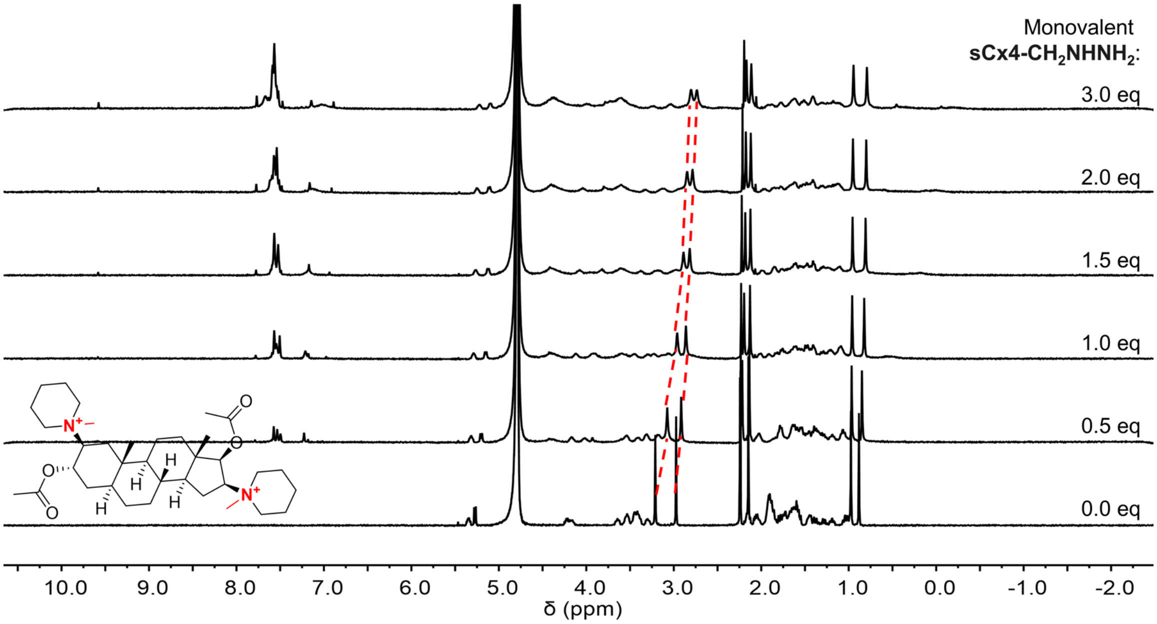

Figure 2.48. ^{1}H NMR titration of monovalent **sCx4-CH$_2$NHNH$_2$** (4 mM) into pancuronium (800 µM). Red dashed lines indicate binding of methyl groups. All solutions were in NaH_2PO_4/Na_2HPO_4 (50 mM, pD 7.4) in D_2O (500 MHz, 297 K).

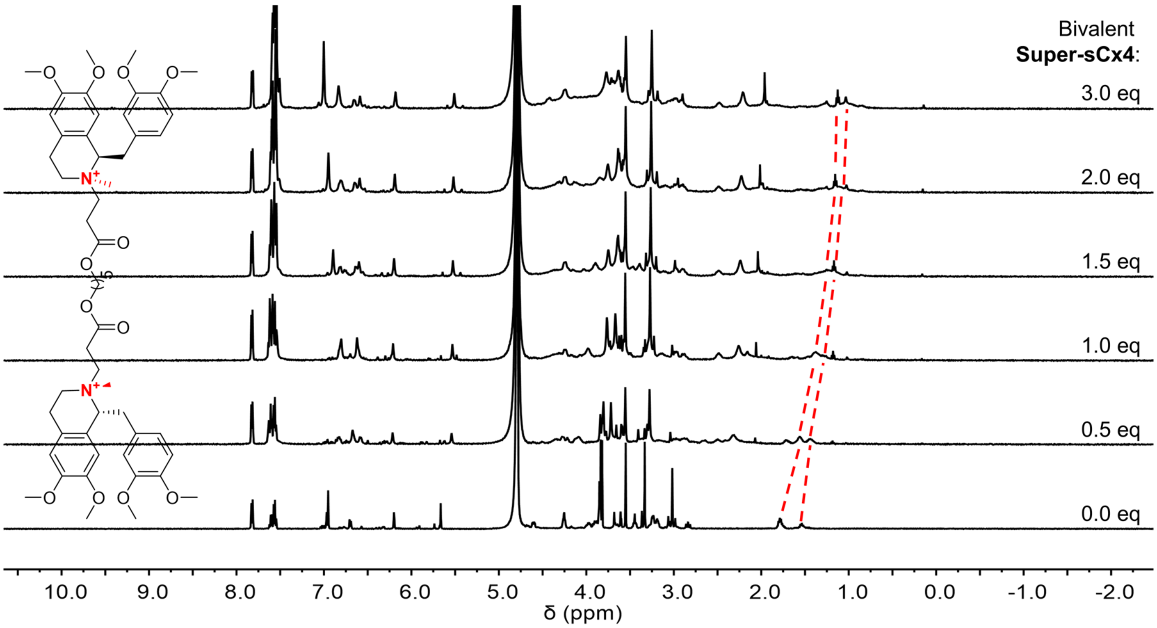

Figure 2.49. ^{1}H NMR titration of bivalent **Super-sCx4** (4 mM) into cisatracurium (800 µM). Red dashed lines indicate the binding of methyl groups. All solutions were in NaH_2PO_4/Na_2HPO_4 (50 mM, pD 7.4) in D_2O (500 MHz, 297 K).

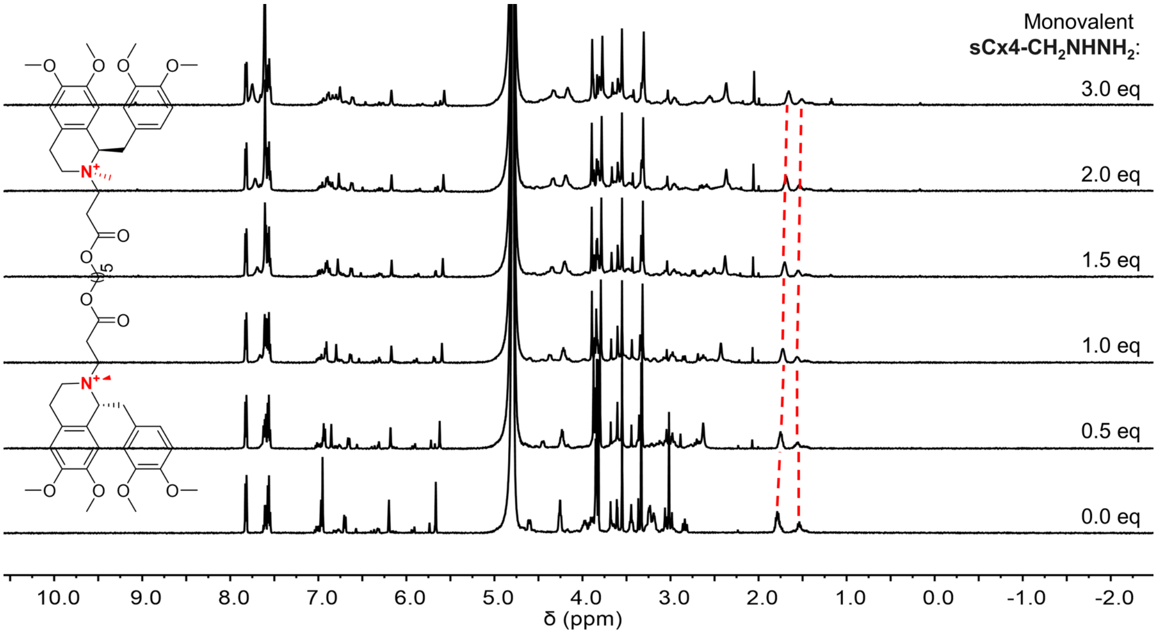

Figure 2.50. ^{1}H NMR titration of monovalent **sCx4-CH$_2$NHNH$_2$** (4 mM) into cisatracurium (800 µM). Red dashed lines indicate the binding of methyl groups. All solutions were in NaH_2PO_4/Na_2HPO_4 (50 mM, pD 7.4) in D_2O (500 MHz, 297 K).

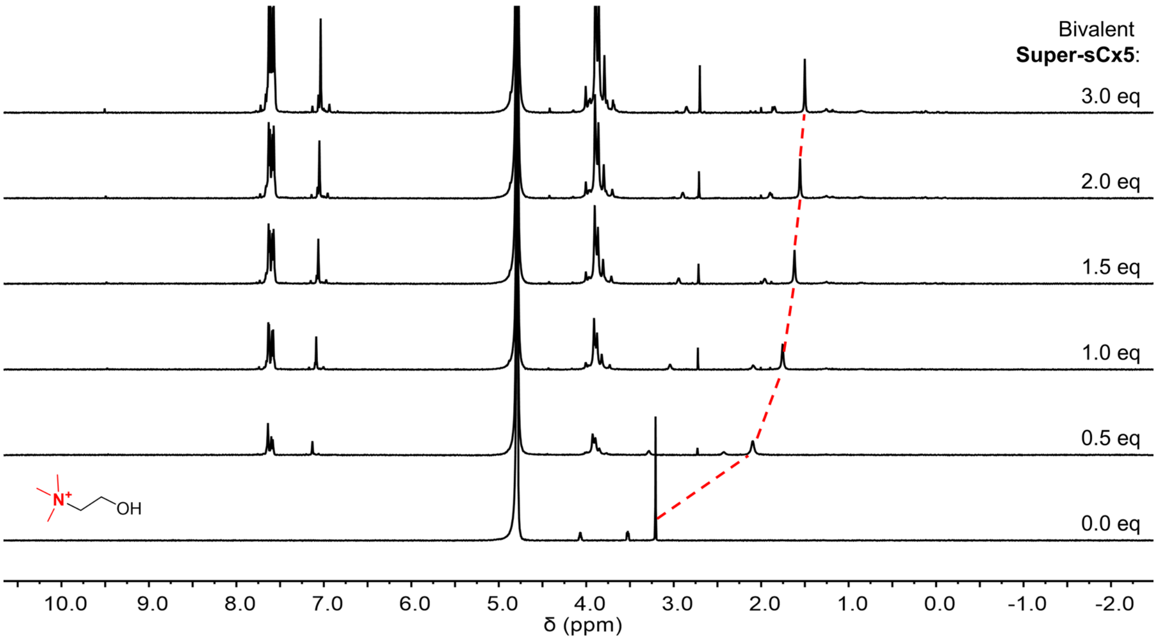

Figure 2.51. ^{1}H NMR titration of bivalent **Super-sCx5** (4 mM) into **Ch** (800 µM). Red dashed line indicates binding of methyl groups. All solutions were in NaH_2PO_4/Na_2HPO_4 (50 mM, pD 7.4) in D_2O (500 MHz, 297 K).

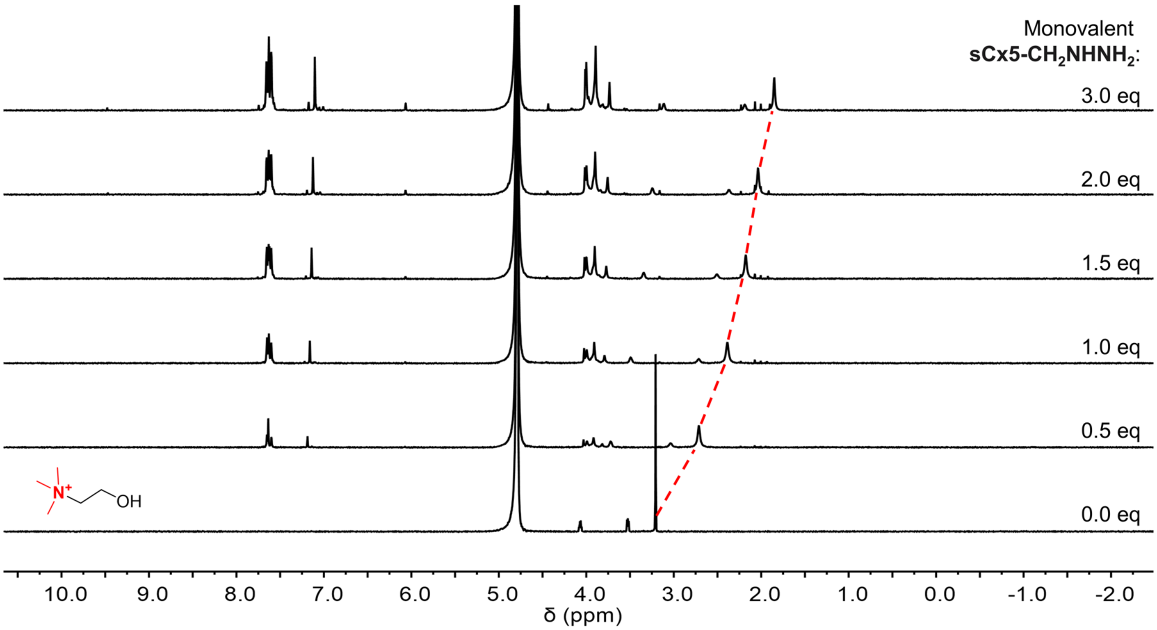

Figure 2.52. ^{1}H NMR titration of monovalent **sCx5-CH$_2$NHNH$_2$** (4 mM) into **Ch** (800 µM). Red dashed line indicates binding of methyl groups. All solutions were in NaH_2PO_4/Na_2HPO_4 (50 mM, pD 7.4) in D_2O (500 MHz, 297 K).

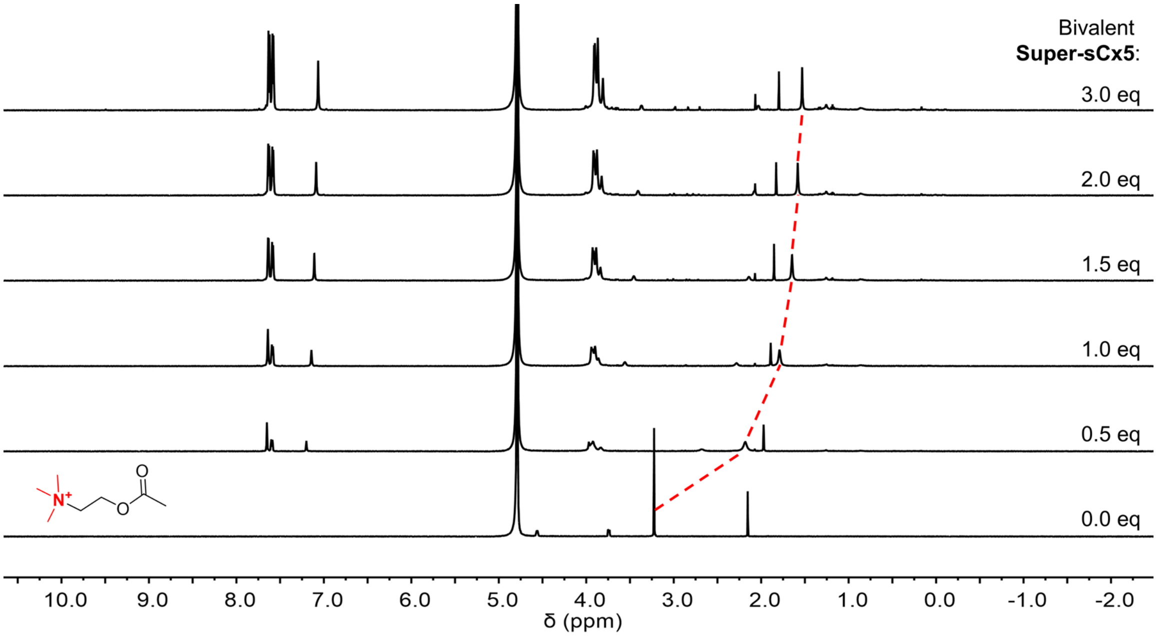

Figure 2.53. ^{1}H NMR titration of bivalent **Super-sCx5** (4 mM) into **ACh** (800 µM). Red dashed line indicates binding of methyl groups. All solutions were in NaH_2PO_4/Na_2HPO_4 (50 mM, pD 7.4) in D_2O (500 MHz, 297 K).

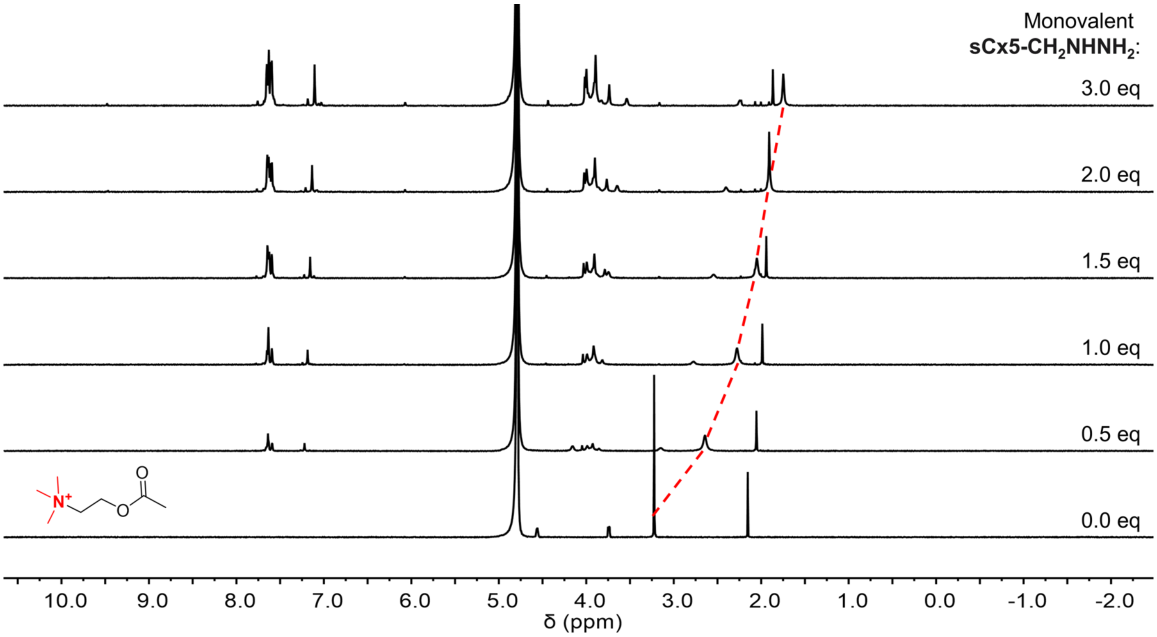

Figure 2.54. ^{1}H NMR titration of monovalent **sCx5-CH_2NHNH_2** (4 mM) into **ACh** (800 µM). Red dashed line indicates binding of methyl groups. All solutions were in NaH_2PO_4/Na_2HPO_4 (50 mM, pD 7.4) in D_2O (500 MHz, 297 K).

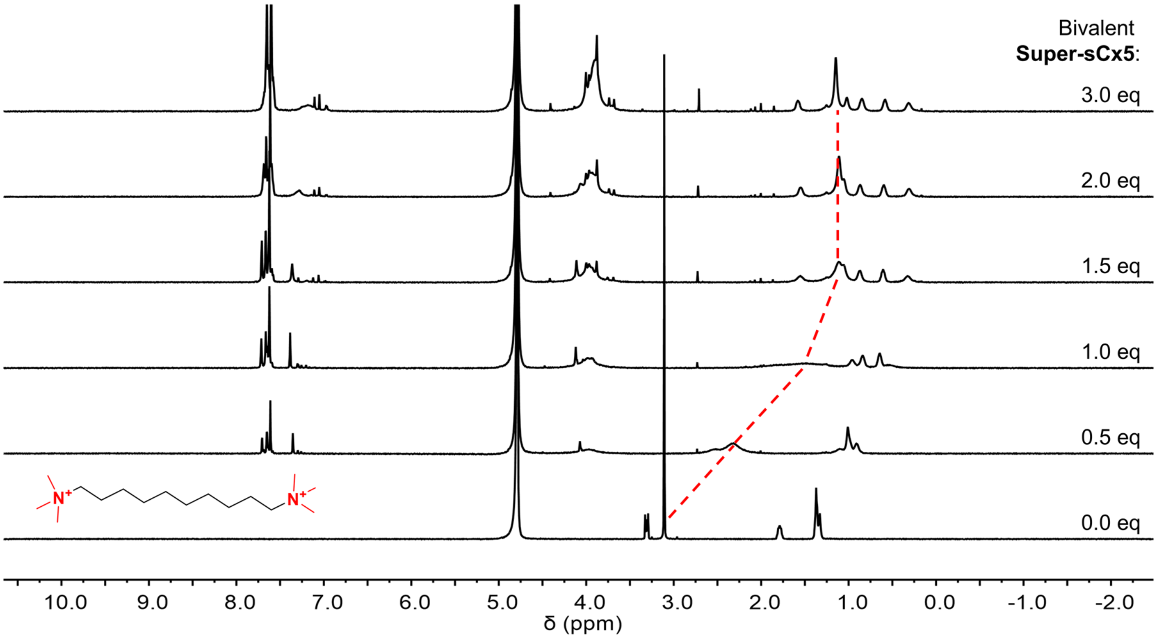

Figure 2.55. ^{1}H NMR titration of bivalent **Super-sCx5** (4 mM) into decamethonium (800 μM). Red dashed line indicates binding of methyl groups. All solutions were in NaH_2PO_4/Na_2HPO_4 (50 mM, pD 7.4) in D_2O (500 MHz, 297 K).

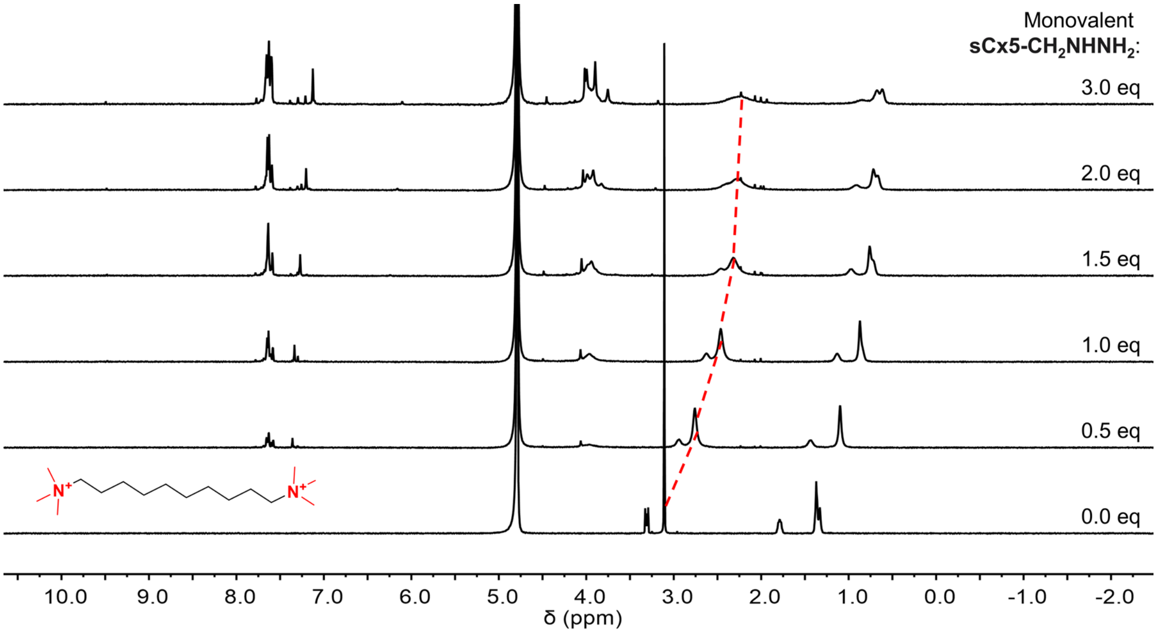

Figure 2.56. ^{1}H NMR titration of monovalent **sCx5-CH$_2$NHNH$_2$** (4 mM) into decamethonium (800 μM). Red dashed line indicates binding of methyl groups. All solutions were in NaH_2PO_4/Na_2HPO_4 (50 mM, pD 7.4) in D_2O (500 MHz, 297 K).

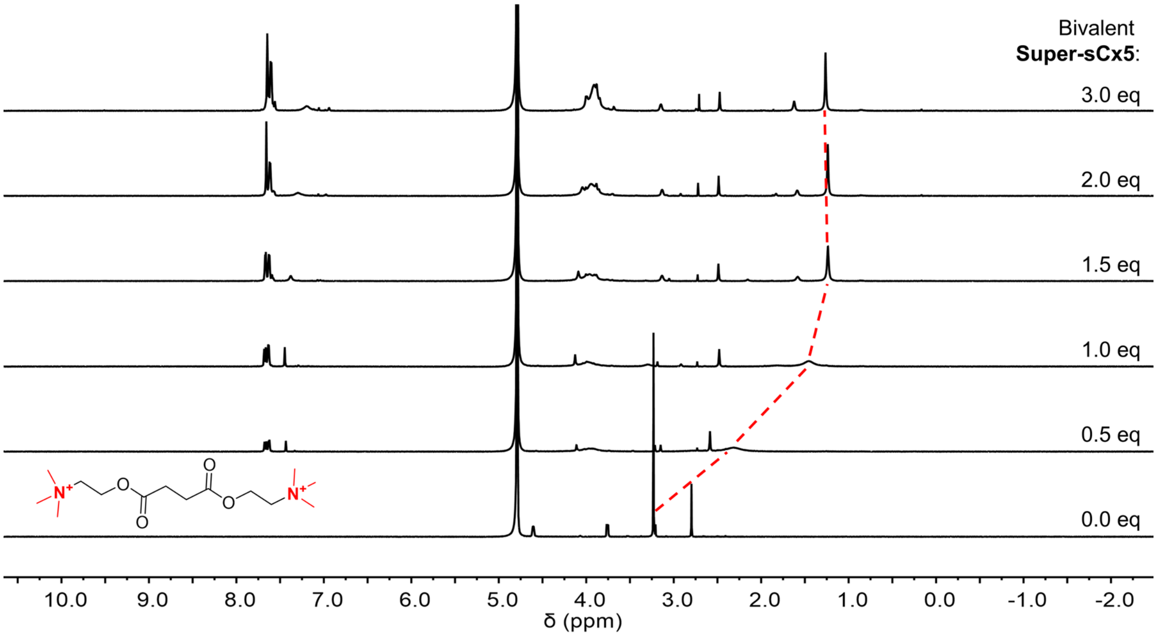

Figure 2.57. ^{1}H NMR titration of bivalent **Super-sCx5** (4 mM) into suxamethonium (800 µM). Red dashed line indicates binding of methyl groups. All solutions were in NaH_2PO_4/Na_2HPO_4 (50 mM, pD 7.4) in D_2O (500 MHz, 297 K).

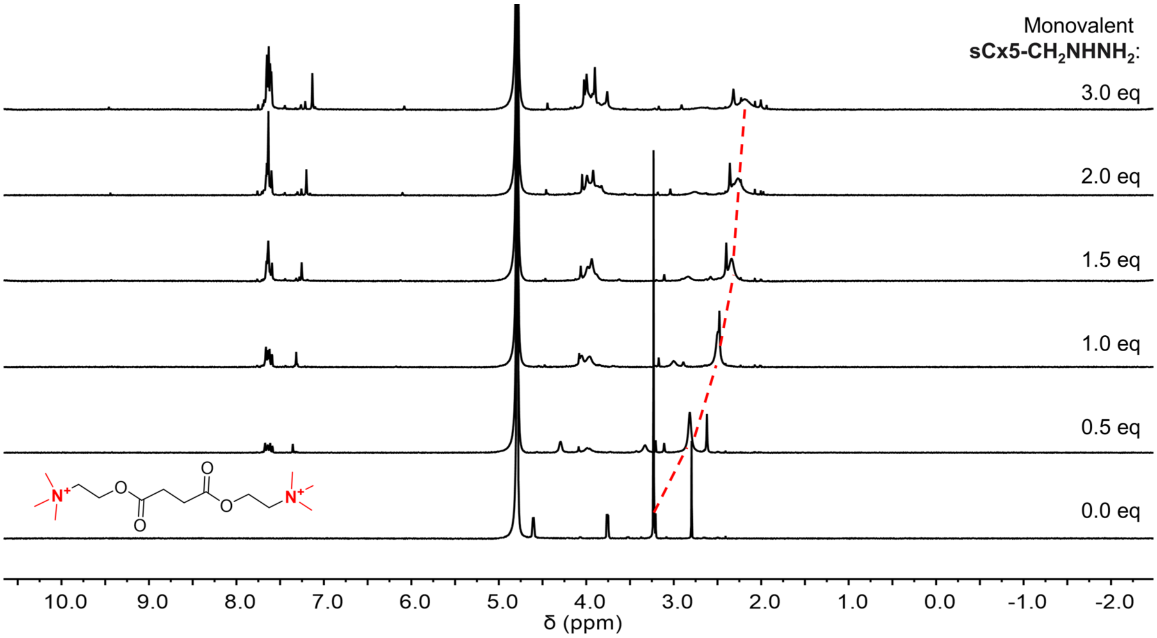

Figure 2.58. ^{1}H NMR titration of monovalent **sCx5-CH$_2$NHNH$_2$** (4 mM) into suxamethonium (800 µM). Red dashed line indicates binding of methyl groups. All solutions were in NaH_2PO_4/Na_2HPO_4 (50 mM, pD 7.4) in D_2O (500 MHz, 297 K).

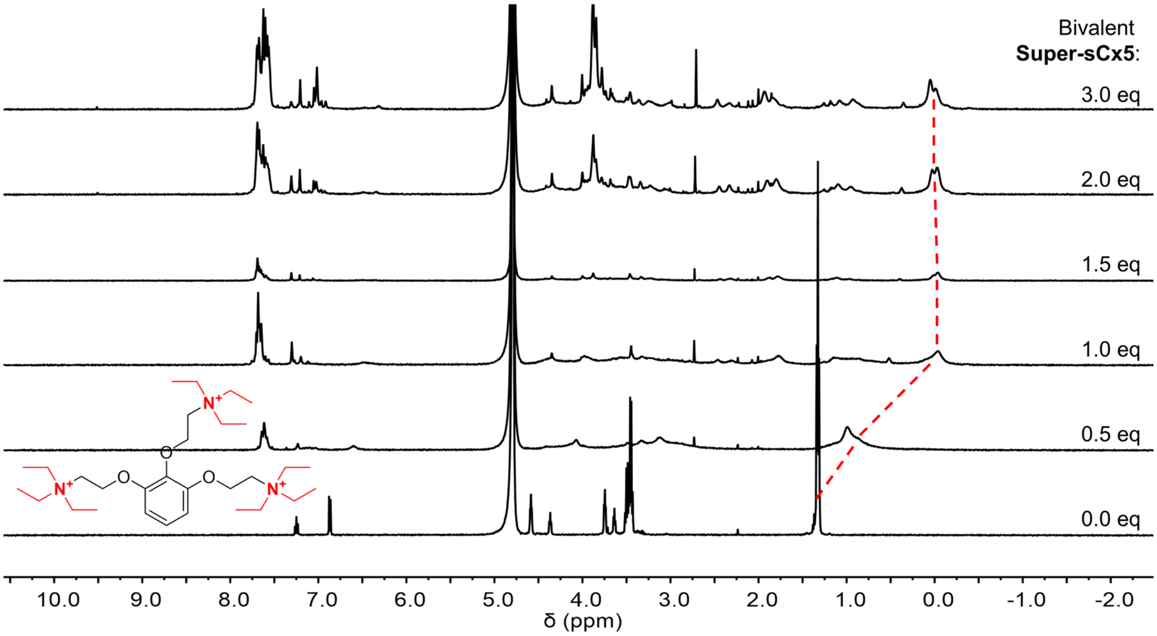

Figure 2.59. ^{1}H NMR titration of bivalent **Super-sCx5** (4 mM) into gallamine (800 µM). Red dashed line indicates binding of ethyl and methyl groups. All solutions were in NaH_2PO_4/Na_2HPO_4 (50 mM, pD 7.4) in D_2O (500 MHz, 297 K).

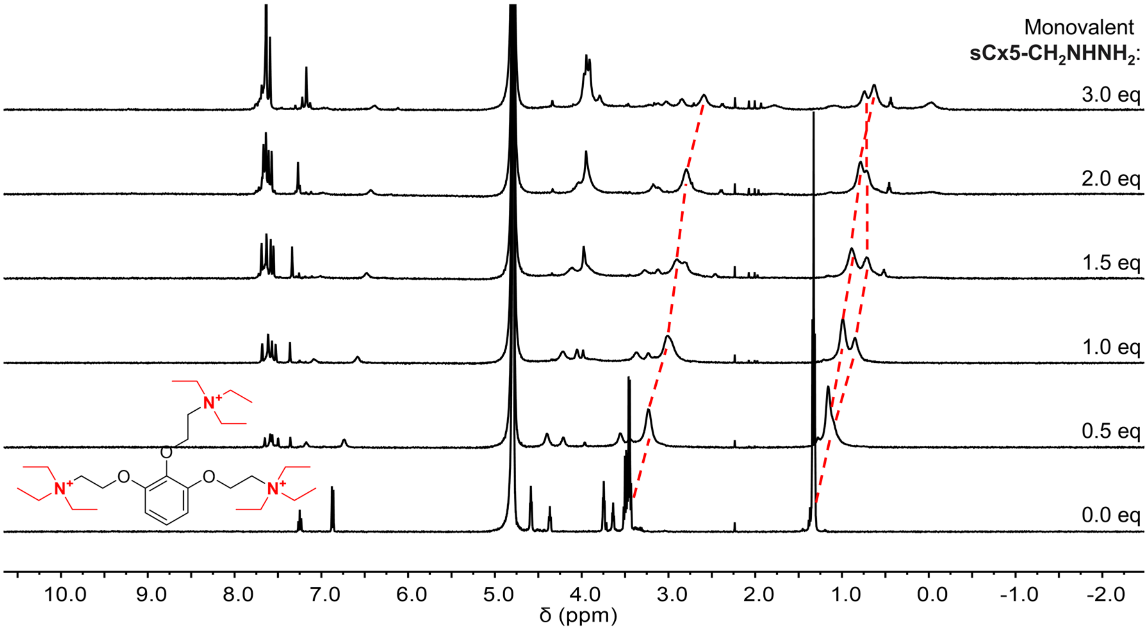

Figure 2.60. ^{1}H NMR titration of monovalent **sCx5-CH$_2$NHNH$_2$** (4 mM) into gallamine (800 µM). Red dashed lines indicate binding of ethyl and methyl groups. All solutions were in NaH_2PO_4/Na_2HPO_4 (50 mM, pD 7.4) in D_2O (500 MHz, 297 K).

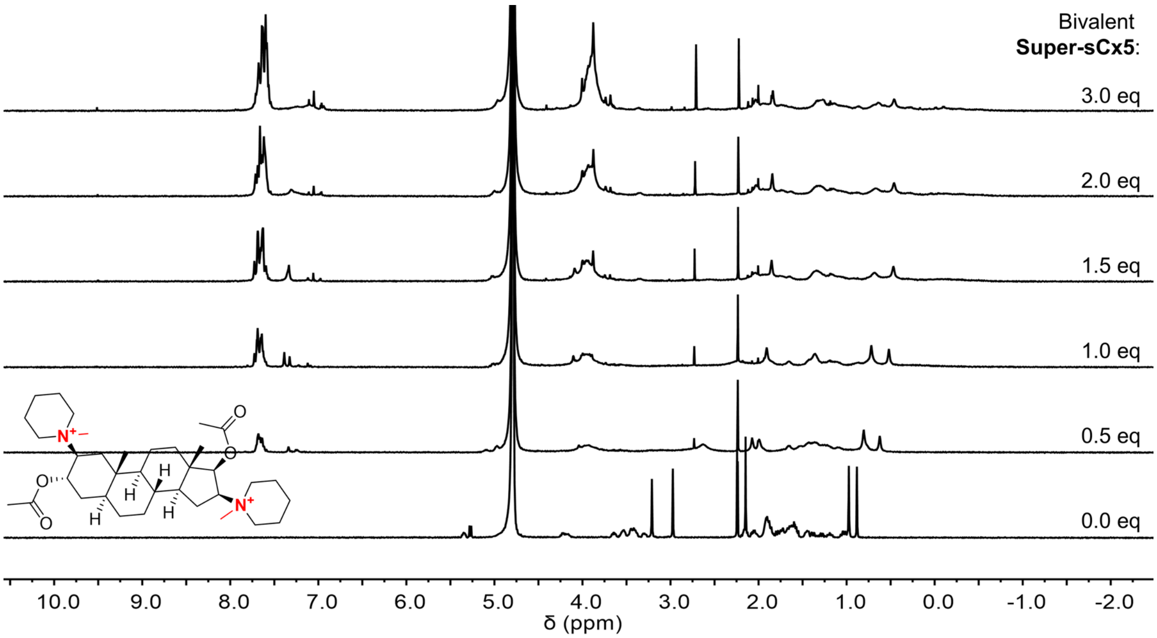

Figure 2.61. ^{1}H NMR titration of bivalent **Super-sCx5** (4 mM) into pancuronium (800 µM). Migration of quaternary amine methyl groups were not distinguishable. All solutions were in NaH_2PO_4/Na_2HPO_4 (50 mM, pD 7.4) in D_2O (500 MHz, 297 K).

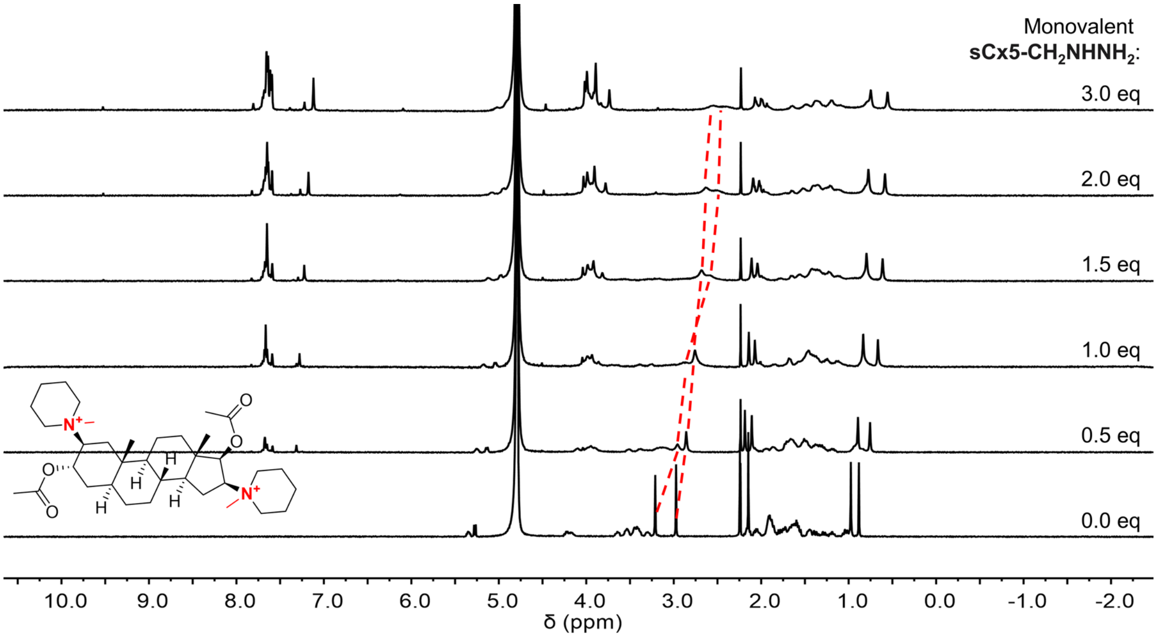

Figure 2.62. ^{1}H NMR titration of monovalent **sCx5-CH$_2$NHNH$_2$** (4 mM) into pancuronium (800 µM). Red dashed lines indicate binding of methyl groups. All solutions were in NaH_2PO_4/Na_2HPO_4 (50 mM, pD 7.4) in D_2O (500 MHz, 297 K).

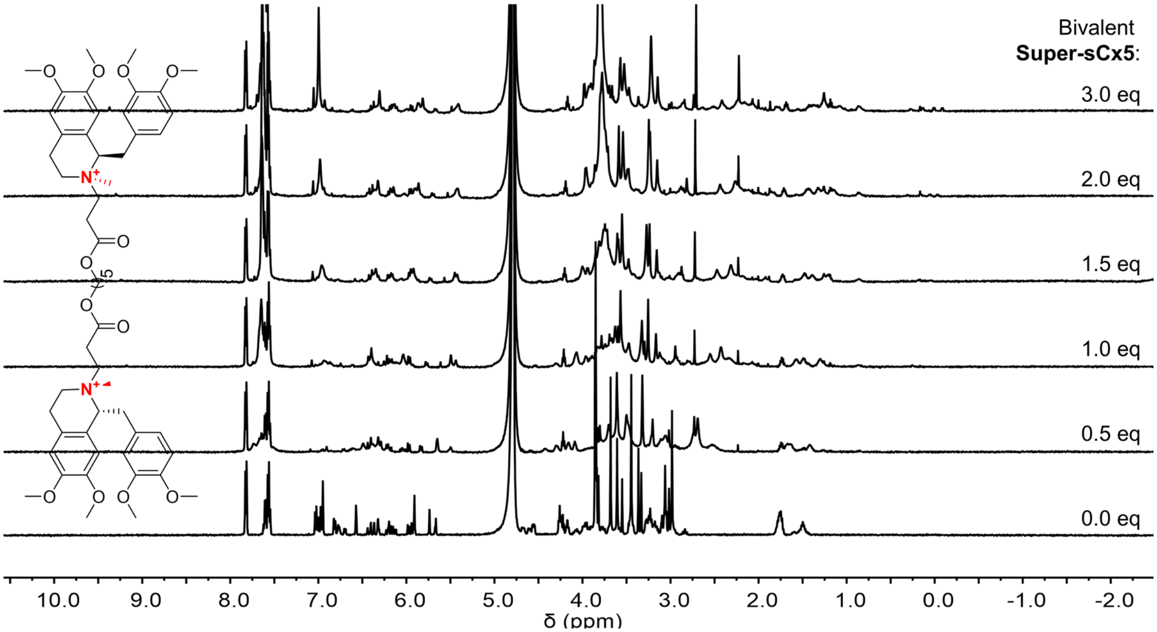

Figure 2.63. ^{1}H NMR titration of bivalent **Super-sCx5** (4 mM) into cisatracurium (800 µM). Migration of quaternary amine methyl groups were not distinguishable. All solutions were in NaH_2PO_4/Na_2HPO_4 (50 mM, pD 7.4) in D_2O (500 MHz, 297 K).

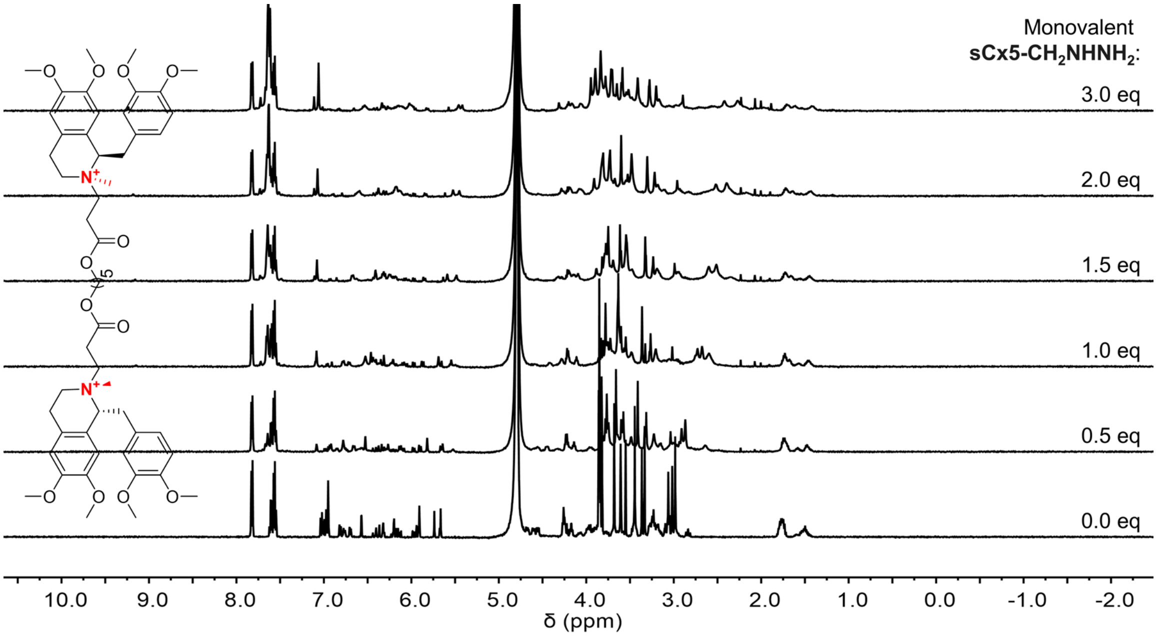

Figure 2.64. ^{1}H NMR titration of monovalent **sCx5-CH$_2$NHNH$_2$** (4 mM) into cisatracurium (800 µM). Migration of quaternary amine methyl groups were not distinguishable. All solutions were in NaH_2PO_4/Na_2HPO_4 (50 mM, pD 7.4) in D_2O (500 MHz, 297 K).

*Note: ^{1}H NMR titrations were not completed for tubocurarine due to solubility issues at the concentrations required for NMR.

2.5.7 Diffusion-ordered spectroscopy

For each DOSY experiment the 90° pulse was determined, the longitudinal relaxation time (T1) was estimated, the diffusion time Δ (d20) was optimized and the diffusion gradient length δ (p30) was set. The 90° pulse was determined by measuring the null pulse length (P1) at 360° and dividing by four using a zg pulse sequence. The T1 longitudinal relaxation time was estimated through an inversion recovery pulse sequence, t1ir1d. The relaxation delay time (D1) for each DOSY experiment was set to be 5× the estimated T1. For each DOSY experiment, the diffusion time Δ was determined by finding a 90-95% intensity difference between the first and last spectra in the power array. The diffusion gradient length δ was set to 2500 μs (maximum for the probe) and the diffusion time Δ was initially set to 0.1 ms, then increased if needed to achieve 90-95% peak intensity difference between the first and last power array spectra. A stimulated echo with bipolar gradient pulses and 1 spoiler gradient (stebpgp1s1d) pulse sequence was used for all DOSY experiments with a free induction decay (FID) size of 32 and a field gradient of 2% to 95%. DOSY data was pre-processed and phased in TopSpin. The diffusion coefficients were calculated using Bruker Dynamic Center. Peak integrals were defined and plotted as a function of the field gradient (G). The data was fit using the following diffusion fit function with a variable gradient strength and 95% confidence level to determine the diffusion coefficient:

$$f(x) = I_o exp^{\left(-\gamma^2 G^2 \delta^2 \left(\Delta - \frac{\delta}{3}\right) D\right)}$$

Where, I_o = NMR signal intensity at a gradient strength of zero
γ = gyromagnetic ratio of observed nuclei
G = field gradient strength (variable)
δ = length of the diffusion gradient
Δ = diffusion time
D = diffusion coefficient

The data was plotted as a function of the field gradient strength (G) with a residuals plot. For each DOSY experiment the average diffusion coefficient was calculated with standard error. The Stokes-Einstein equation was used to calculate the hydrodynamic radius (r_H) assuming the molecule or complex is spherical in shape.

$$r_H = \frac{k_B T}{6\pi\eta D}$$

Where, k_B = Boltzmann constant
T = temperature, 297 ± 1 K,
η = viscosity of water, 8.94 x 10^{-4} ± 2.78 x 10^{-5} Pa·s[123]
D = diffusion coefficien

Table 2.4. Parameters used in diffusion analysis of templated starting material **sCx4-CHO** and decamethonium (2:1).

Parameter	Used value
γ	26752 rad/(s*Gauss)
δ	0.0025000 s
Δ	0.13990 s

Table 2.5. Dynamics Center calculated diffusion coefficient outputs from defined integrals of the templated starting material **sCx4-CHO** and decamethonium (2:1).

Peak name	F2 (ppm)	D (m^2/s)	error
1	9.66	2.21×10^{-10}	7×10^{-13}
2	7.56	2.20×10^{-10}	2×10^{-13}
3	3.97	2.18×10^{-10}	1×10^{-12}
4	1.97	2.12×10^{-10}	1×10^{-13}
5	0.81	2.11×10^{-10}	1×10^{-13}

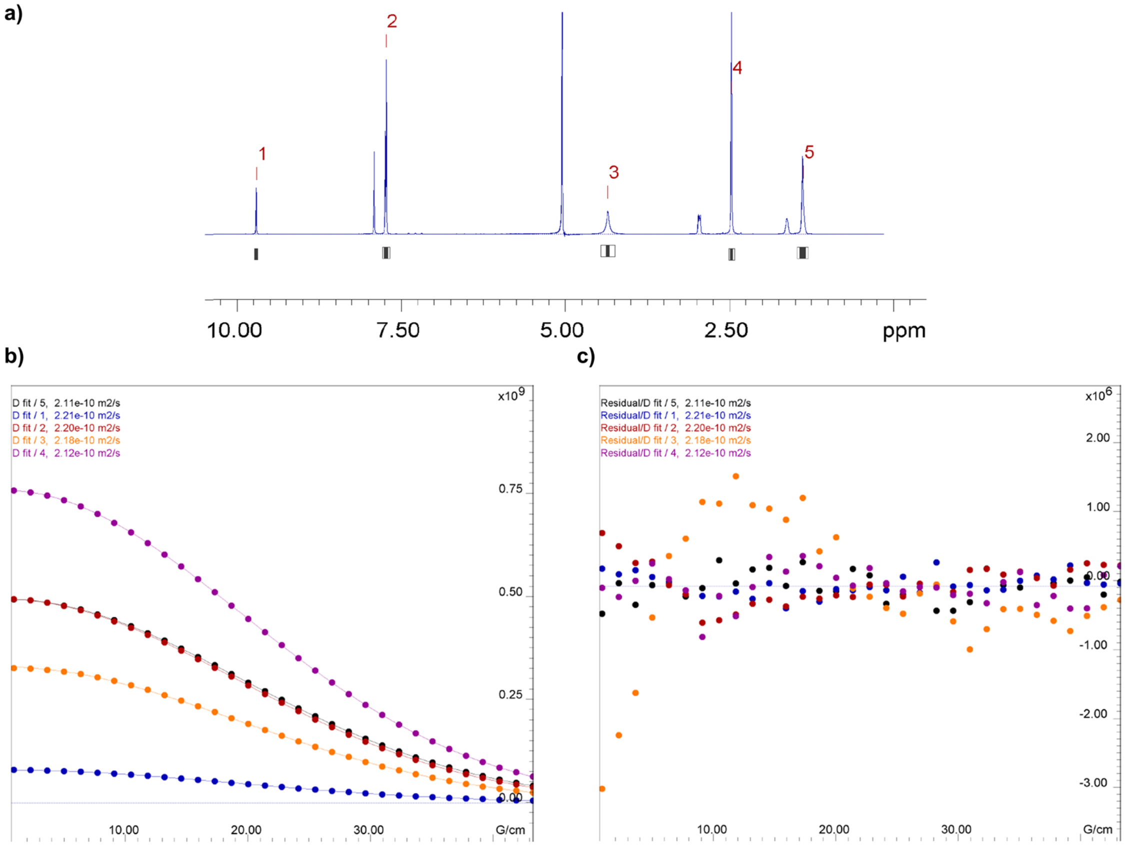

Figure 2.65. a) ^{1}H NMR of templated starting material **sCx4-CHO** (10 mM) and decamethonium (5 mM). Peak area integrals highlighted in grey were used to calculate sample diffusion coefficients. **b)** 1D DOSY plots of each selected integral, and **c)** the corresponding 1D residuals plot. Solution was in $(NH_4)_2CO_3$ (50 mM, pD 6.4) in D_2O (500 MHz, 297 K).

Table 2.6. Parameters used in diffusion analysis of bivalent **Super-sCx4**.

Parameter	Used value
γ	26752 rad/(s*Gauss)
δ	0.0025000 s
Δ	0.13990 s

Table 2.7. Dynamics Center calculated diffusion coefficient outputs from defined integrals for bivalent **Super-sCx4**.

Peak name	F2 (ppm)	D (m^2/s)	error
1	7.47	2.24×10^{-10}	4×10^{-13}
2	6.99	2.20×10^{-10}	4×10^{-13}
3	3.78	2.21×10^{-10}	7×10^{-13}

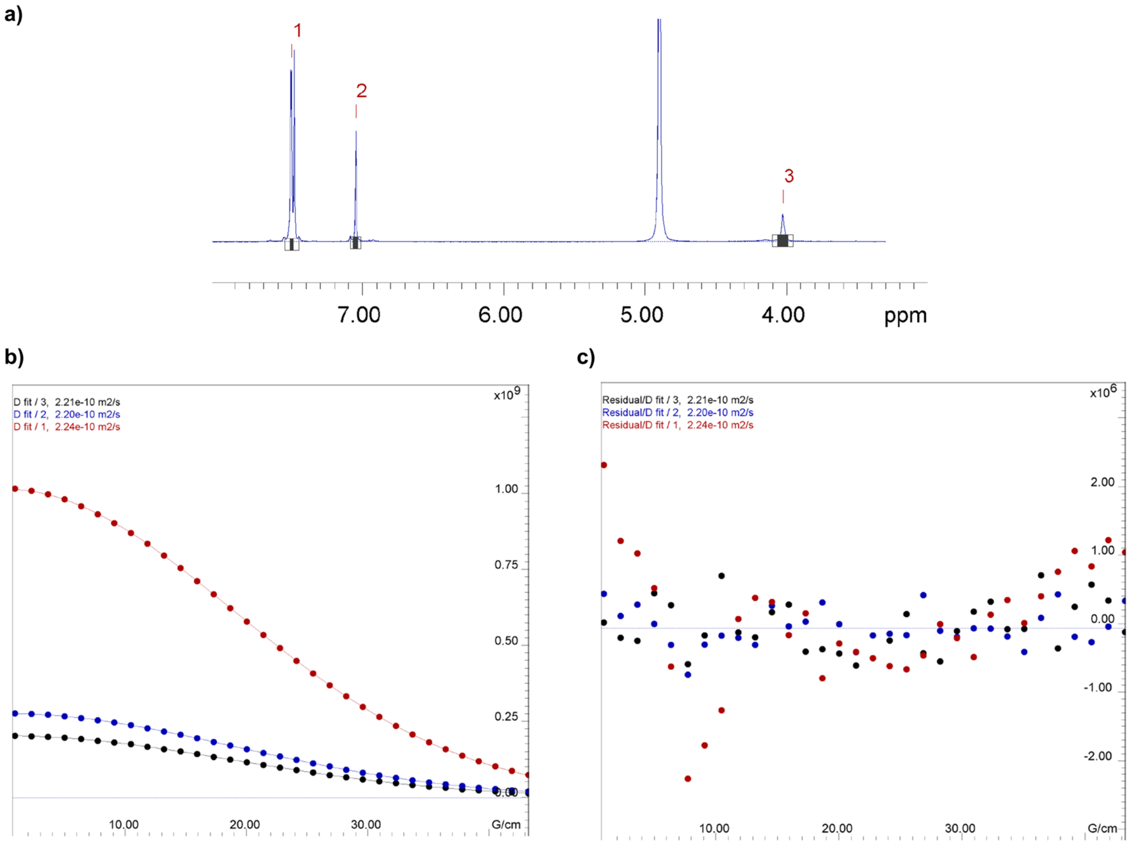

Figure 2.66. a) ^1H NMR of bivalent **Super-sCx4** (5 mM). Peak area integrals highlighted in grey were used to calculate diffusion coefficients. **b)** 1D DOSY plots for each selected integral, and **c)** the corresponding 1D residuals plot. Solution was in NaH_2PO_4/Na_2HPO_4 (50 mM, pD 7.4) in D_2O (500 MHz, 297 K).

Table 2.8. Parameters used in diffusion analysis of monovalent **sCx4-CH$_2$NHNH$_2$**.

Parameter	Used value
Used γ	26752 rad/(s*Gauss)
Used δ	0.0025000 s
Used Δ	0.099900 s

Table 2.9. Dynamics Center calculated diffusion coefficient outputs from defined integrals for monovalent **sCx4-CH$_2$NHNH$_2$**.

Peak name	F2 (ppm)	D (m^2/s)	error
1	7.73	2.82×10^{-10}	2×10^{-12}
2	7.55	2.76×10^{-10}	5×10^{-13}
3	6.64	2.73×10^{-10}	4×10^{-12}

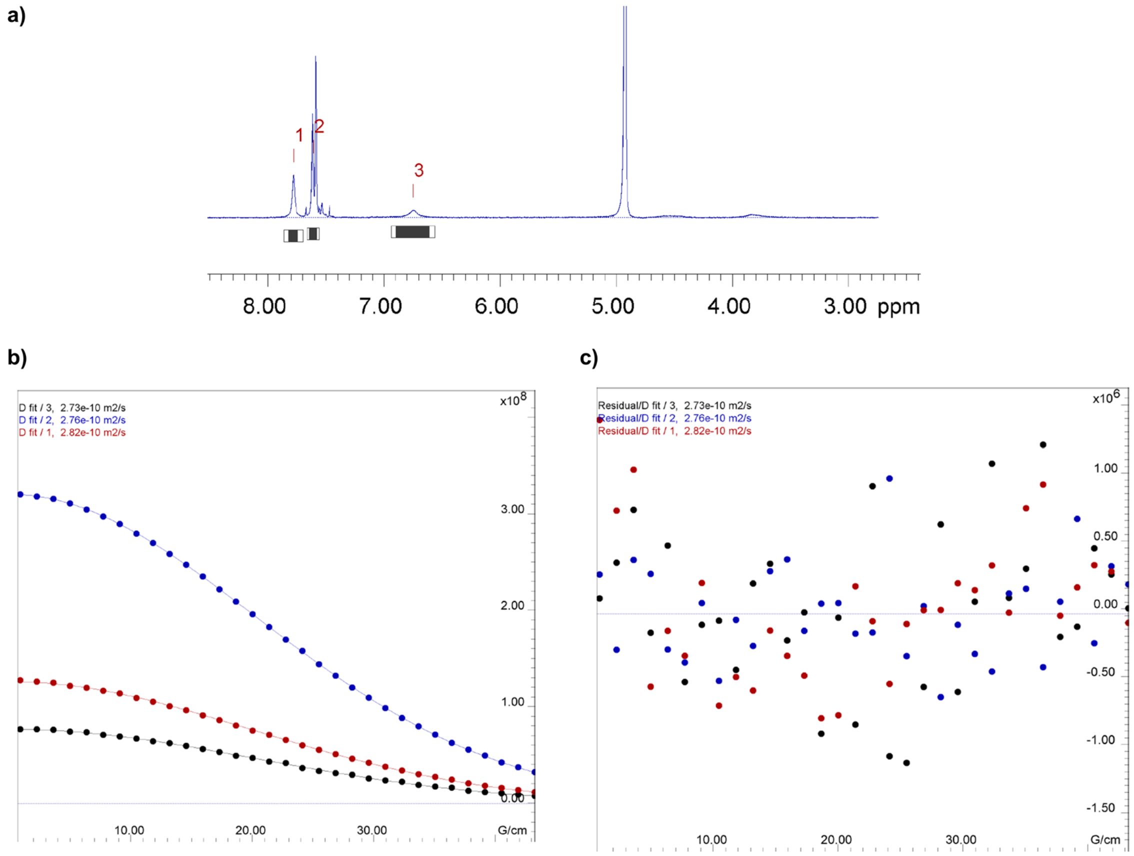

Figure 2.67. a) ^{1}H NMR of monovalent **sCx4-CH$_2$NHNH$_2$** (5 mM). Peak area integrals highlighted in grey were used to calculate diffusion coefficients. **b)** 1D DOSY plots for each integral, and **c)** the corresponding 1D residuals plot. Solution was in NaH$_2$PO$_4$/Na$_2$HPO$_4$ (50 mM, pD 7.4) in D$_2$O (500 MHz, 297 K).

Table 2.10. Parameters used in diffusion analysis of **Super-sCx4** and suxamethonium (1:1).

Parameter	Used value
γ	26752 rad/(s*Gauss)
δ	0.0025000 s
Δ	0.13990 s

Table 2.11. Dynamics Center calculated diffusion coefficients output from user defined integrals for **Super-sCx4** and suxamethonium (1:1).

Peak name	F2 (ppm)	D (m^2/s)	error
1	7.52	2.20×10^{-10}	2×10^{-13}
2	7.25	2.15×10^{-10}	5×10^{-13}
3	3.85	2.33×10^{-10}	2×10^{-12}
4	3.54	2.15×10^{-10}	2×10^{-12}
5	2.65	2.39×10^{-10}	5×10^{-13}
6	1.45	2.38×10^{-10}	2×10^{-13}

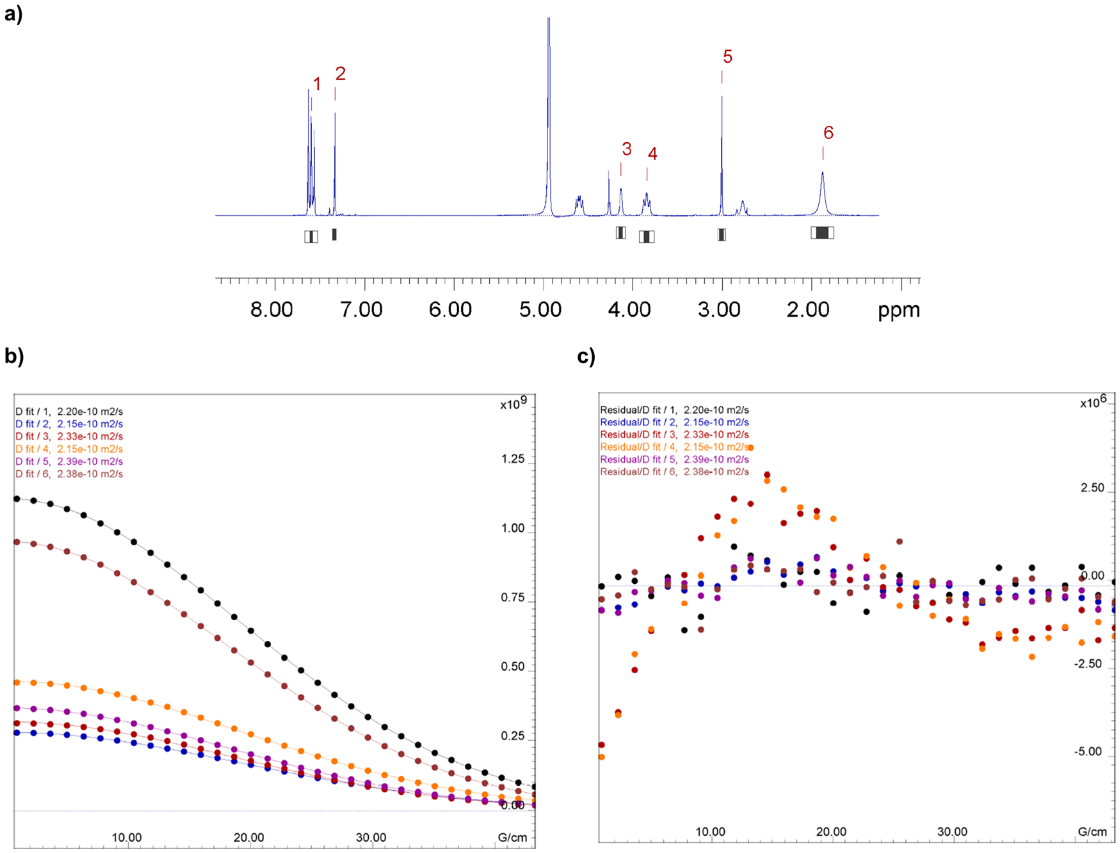

Figure 2.68. a) ^{1}H NMR of **Super-sCx4** (5 mM) and suxamethonium (5 mM). Peak area integrals highlighted in grey were used to calculate diffusion coefficients. **b)** 1D DOSY plots for each integral and **c)** the corresponding 1D residuals plot. Solution was in NaH_2PO_4/Na_2HPO_4 (50 mM, pD 7.4) in D_2O (500 MHz, 297 K).

Table 2.12. Parameters used in diffusion analysis of **sCx5-CHO**.

Parameter	Used value
γ	26752 rad/(s*Gauss)
δ	0.0025000 s
Δ	0.10990 s

Table 2.13. Dynamics Center calculated diffusion coefficient outputs from defined integrals for **sCx5-CHO**.

Peak name	F2 (ppm)	D (m^2/s)	error
1	9.43	2.80×10^{-10}	1×10^{-12}
2	7.45	2.75×10^{-10}	1×10^{-12}
3	7.49	2.77×10^{-10}	8×10^{-13}
4	7.56	2.80×10^{-10}	3×10^{-13}
5	7.61	2.84×10^{-10}	1×10^{-12}
6	3.81	2.78×10^{-10}	8×10^{-13}

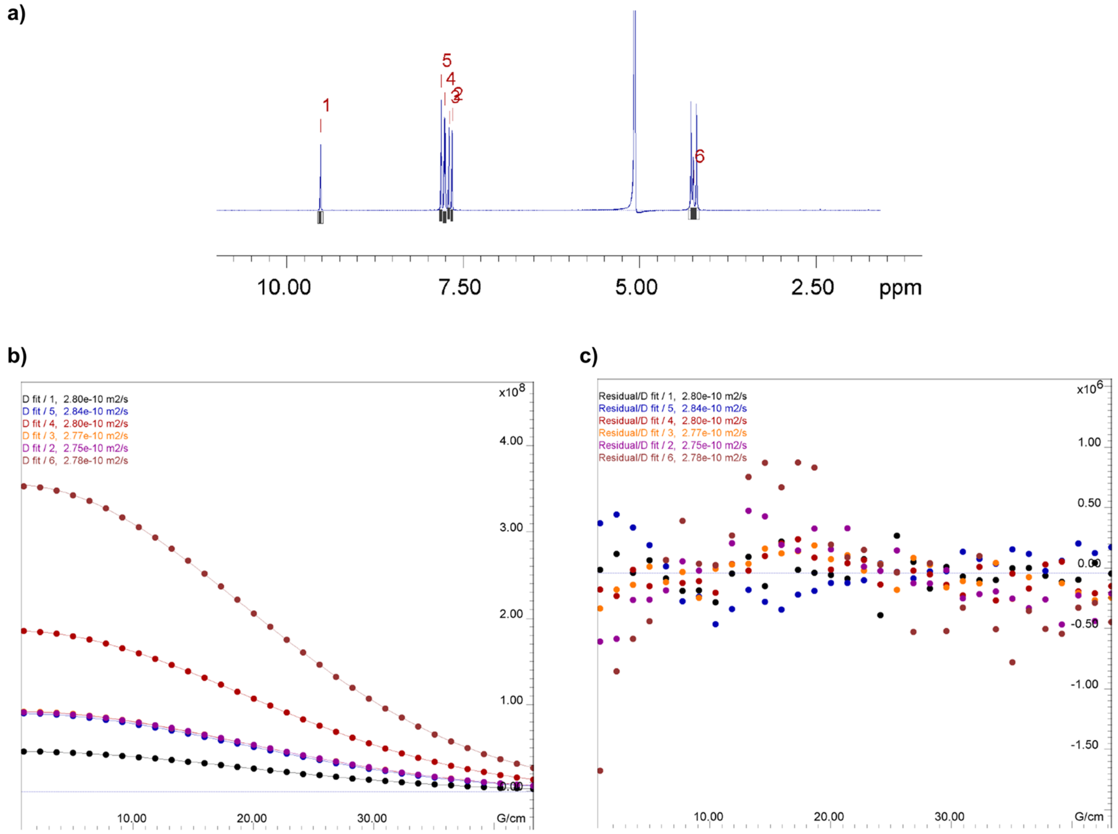

Figure 2.69. a) ^{1}H NMR of **sCx5-CHO** (5 mM). Peak area integrals highlighted in grey were used to calculate diffusion coefficients. **b)** 1D DOSY plots for each integral and **c)** the corresponding 1D residuals plot. Solution was in NaH_2PO_4/Na_2HPO_4 (50 mM, pD 7.4) in D_2O (500 MHz, 297 K).

Table 2.14. Parameters used in diffusion analysis of templated starting material **sCx5-CHO** and pancuronium (2:1).

Parameter	Used value
γ	26752 rad/(s*Gauss)
δ	0.0025000 s
Δ	0.12990 s

Table 2.15. Dynamics Center calculated diffusion coefficient outputs from user defined integrals for templated starting material **sCx5-CHO** and pancuronium (2:1).

Peak name	F2 (ppm)	D (m^2/s)	error
1	9.61	2.41×10^{-10}	1×10^{-12}
2	7.67	2.43×10^{-10}	2×10^{-13}
3	3.89	2.41×10^{-10}	1×10^{-12}
4	2.05	2.05×10^{-10}	4×10^{-13}
5	1.88	2.06×10^{-10}	7×10^{-13}
6	0.36	2.02×10^{-10}	8×10^{-13}

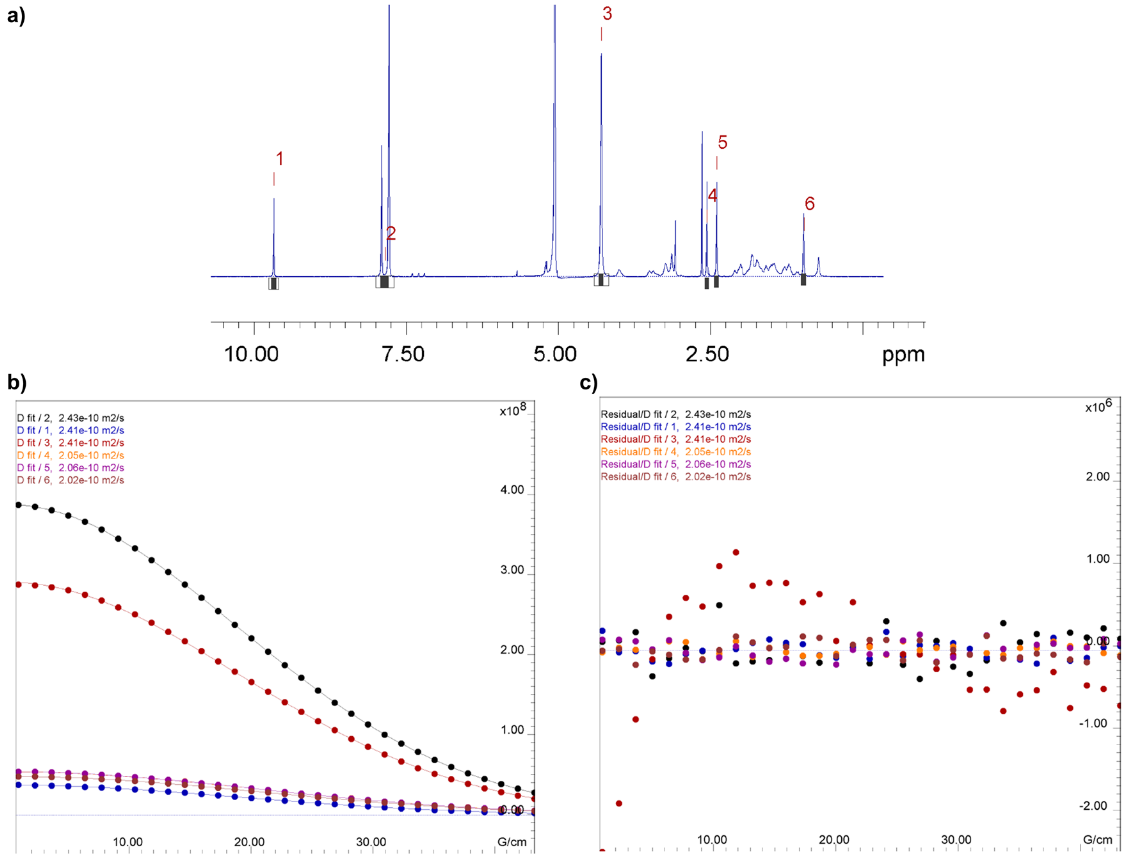

Figure 2.70. a) ^{1}H NMR of templated starting material **sCx5-CHO** (10 mM) and pancuronium (5 mM). Peak area integrals highlighted in grey were used to calculate diffusion coefficients. **b)** 1D DOSY plots for each integral, and **c)** the corresponding 1D residuals plot. Solution was in $(NH_4)_2CO_3$ (50 mM, pD 6.4) in D_2O (500 MHz, 297 K).

Table 2.16. Parameters used in diffusion analysis of monovalent **sCx5-CH$_2$NHNH$_2$**.

Parameter	Used value
γ	26752 rad/(s*Gauss)
δ	0.0025000 s
Δ	0.10990 s

Table 2.17. Dynamics Center calculated diffusion coefficient outputs from defined integrals for monovalent **sCx5-CH$_2$NHNH$_2$**.

Peak name	F2 (ppm)	D (m^2/s)	error
1	7.52	2.61×10^{-10}	4×10^{-13}
2	6.96	2.74×10^{-10}	8×10^{-13}
3	3.92	2.82×10^{-10}	5×10^{-13}
4	3.79	2.50×10^{-10}	9×10^{-13}

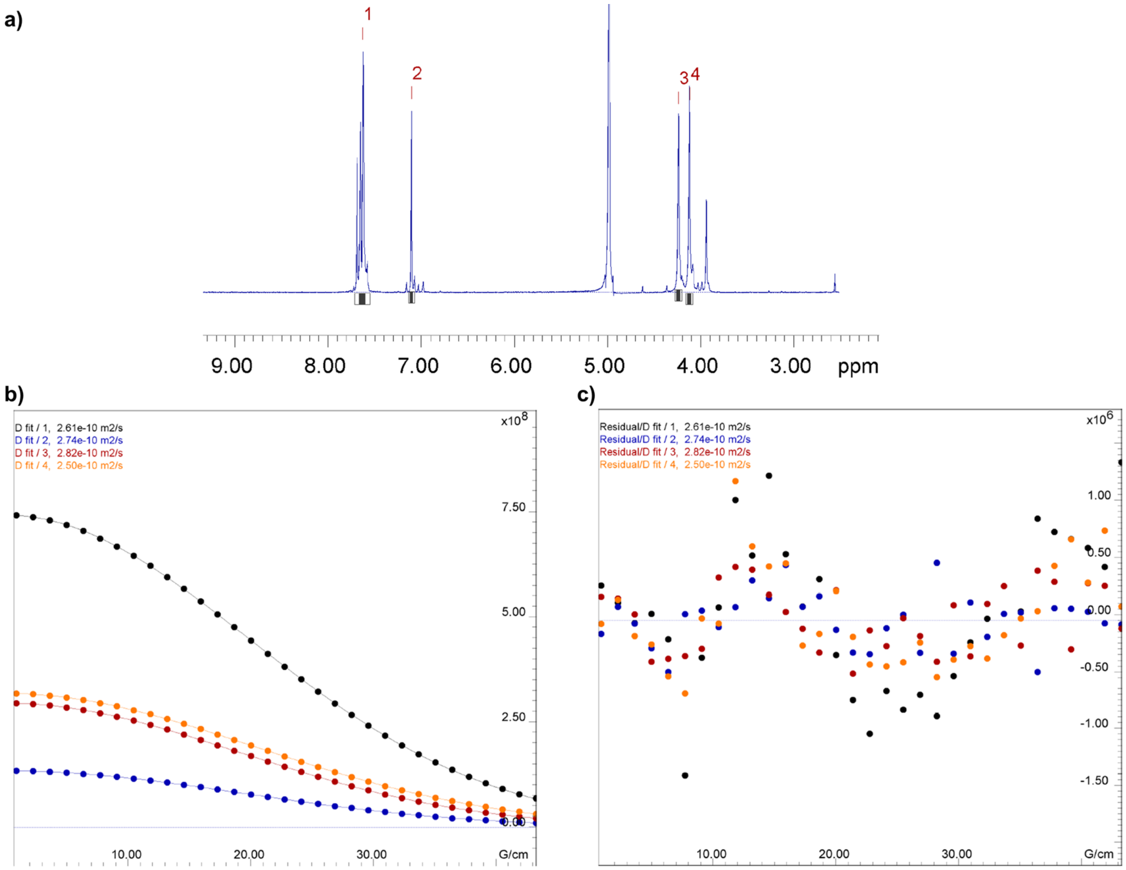

Figure 2.71. a) ^{1}H NMR of monovalent **sCx5-CH$_2$NHNH$_2$** (5 mM). Peak area integrals highlighted in grey were used to calculate diffusion coefficients. **b)** 1D DOSY plots for each integral, and **c)** the corresponding 1D residuals plot. Solution was in NaH$_2$PO$_4$/Na$_2$HPO$_4$ (50 mM, pD 7.4) in D$_2$O (500 MHz, 297 K).

Table 2.18. Parameters used in diffusion analysis of bivalent **Super-sCx5**.

Parameter	Used value
γ	26752 rad/(s*Gauss)
δ	0.0025000 s
Δ	0.14490 s

Table 2.19. Dynamics Center calculated diffusion coefficient outputs from defined integrals for bivalent **Super-sCx5**.

Peak name	F2 (ppm)	D (m^2/s)	error
1	7.45	2.03×10^{-10}	3×10^{-13}
2	6.92	1.98×10^{-10}	8×10^{-13}
3	3.77	1.99×10^{-10}	2×10^{-13}

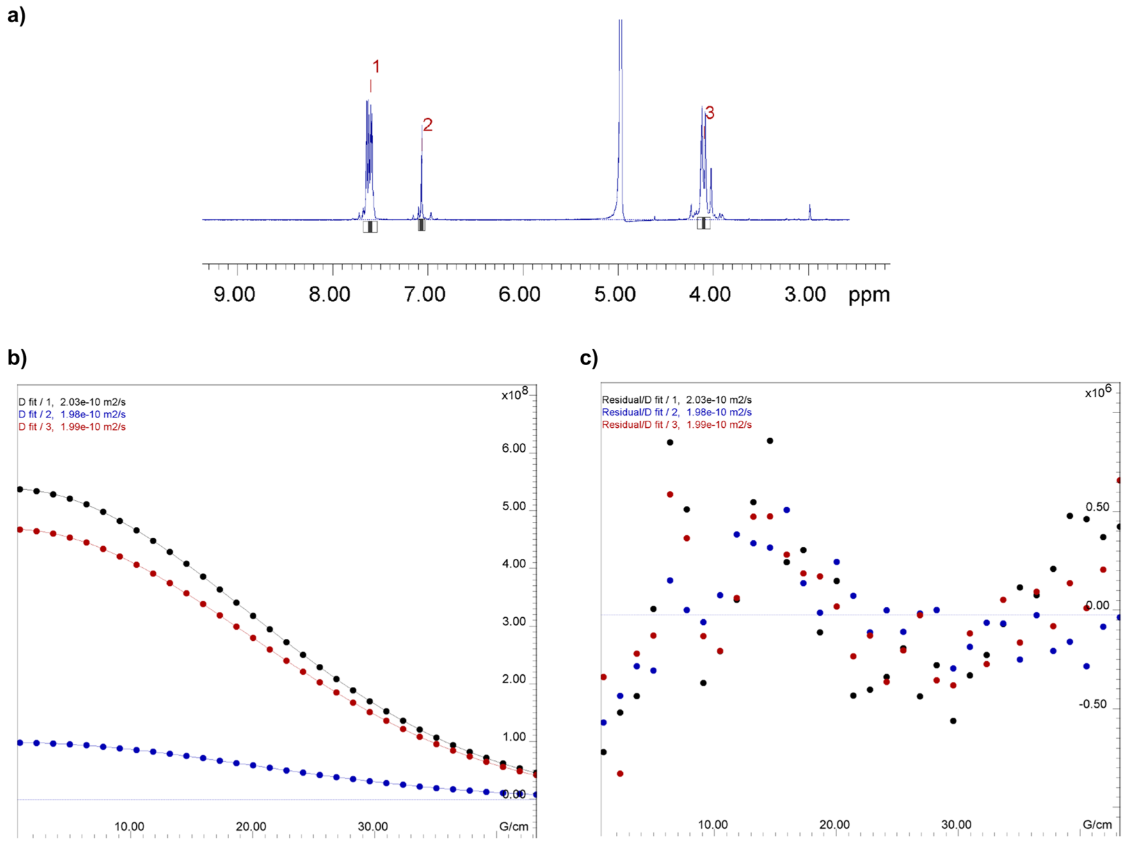

Figure 2.72. a) ^{1}H NMR of bivalent **Super-sCx5** (5 mM). Peak area integrals highlighted in grey were used to calculate diffusion coefficients. **b)** 1D DOSY plots for each integral, and **c)** the corresponding 1D residuals plot. Solution was in NaH_2PO_4/Na_2HPO_4 (50 mM, pD 7.4) in D_2O (500 MHz, 297 K).

Table 2.20. Parameters used in diffusion analysis of bivalent **Super-sCx5** and suxamethonium (1:1).

Parameter	Used value
Used γ	26752 rad/(s*Gauss)
Used δ	0.0025000 s
Used Δ	0.14990 s

Table 2.21. Dynamics Center calculated diffusion coefficient outputs from user defined integrals for bivalent **Super-sCx5** and suxamethonium (1:1).

Peak name	F2 (ppm)	D (m^2/s)	error
1	7.58	2.05×10^{-10}	3×10^{-13}
2	7.33	1.88×10^{-10}	2×10^{-12}
3	3.88	2.08×10^{-10}	1×10^{-12}
4	3.32	2.04×10^{-10}	3×10^{-12}
5	2.24	2.14×10^{-10}	1×10^{-12}
6	1.59	2.04×10^{-10}	1×10^{-12}

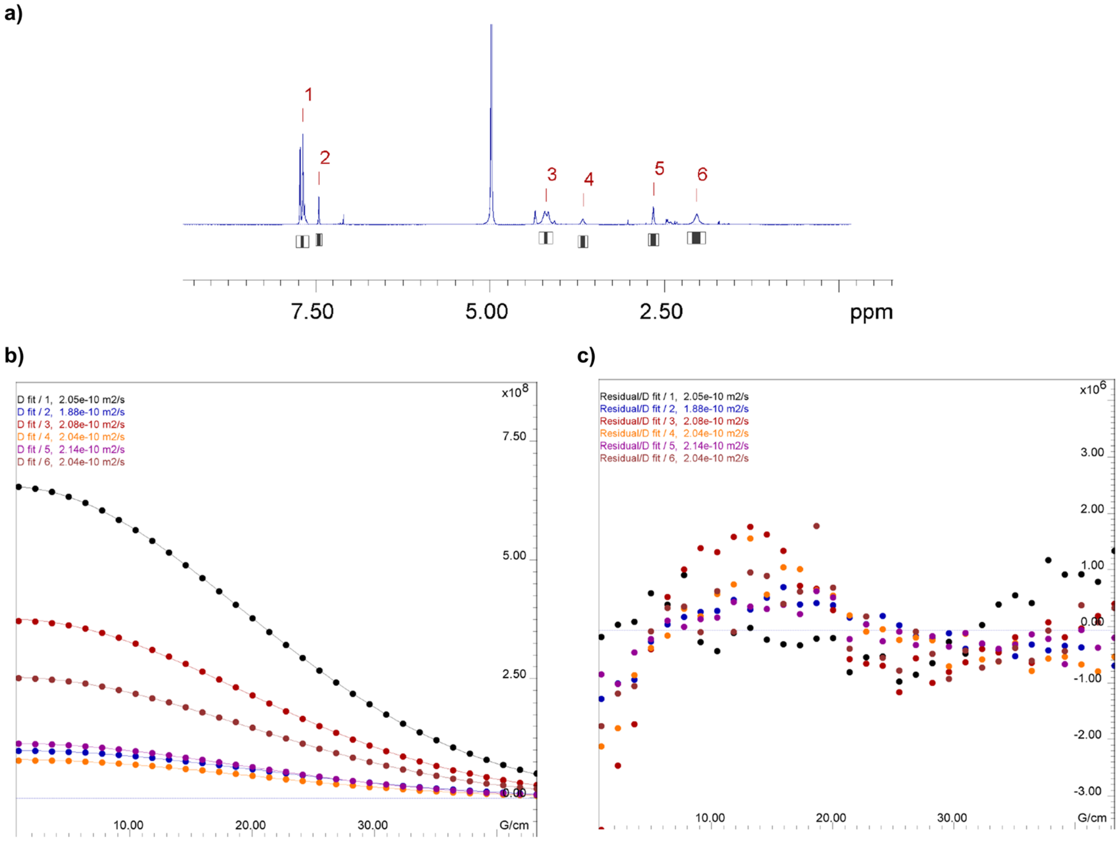

Figure 2.73. a) ^{1}H NMR of bivalent **Super-sCx5** (5 mM) and suxamethonium (5 mM). Peak area integrals highlighted in grey were used to calculate diffusion coefficients. **b)** 1D DOSY plots for each integral, and **c)** the corresponding 1D residuals plot. Solution was in NaH_2PO_4/Na_2HPO_4 (50 mM, pD 7.4) in D_2O (500 MHz, 297 K).

2.5.8 Molecular modelling

Host•guest complexes were modeled in Avogadro. Each individual host and guest compound was geometry optimized using the molecular mechanics forcefield MMFF94. A systematic rotor search was used to find the lowest energy conformers of each compound. Then geometry optimization of the lowest energy conformer was done using a 5000 step with a steepest descent algorithm and 10e-7 convergence. The pre-optimized structures were then combined to form a host•guest complex, where another systematic rotor search was used to find the lowest energy conformers for each host•guest pair. Optimization of the lowest energy host•guest conformers was completed using a 5000 step with a steepest descent algorithm and 10e-7 convergence.

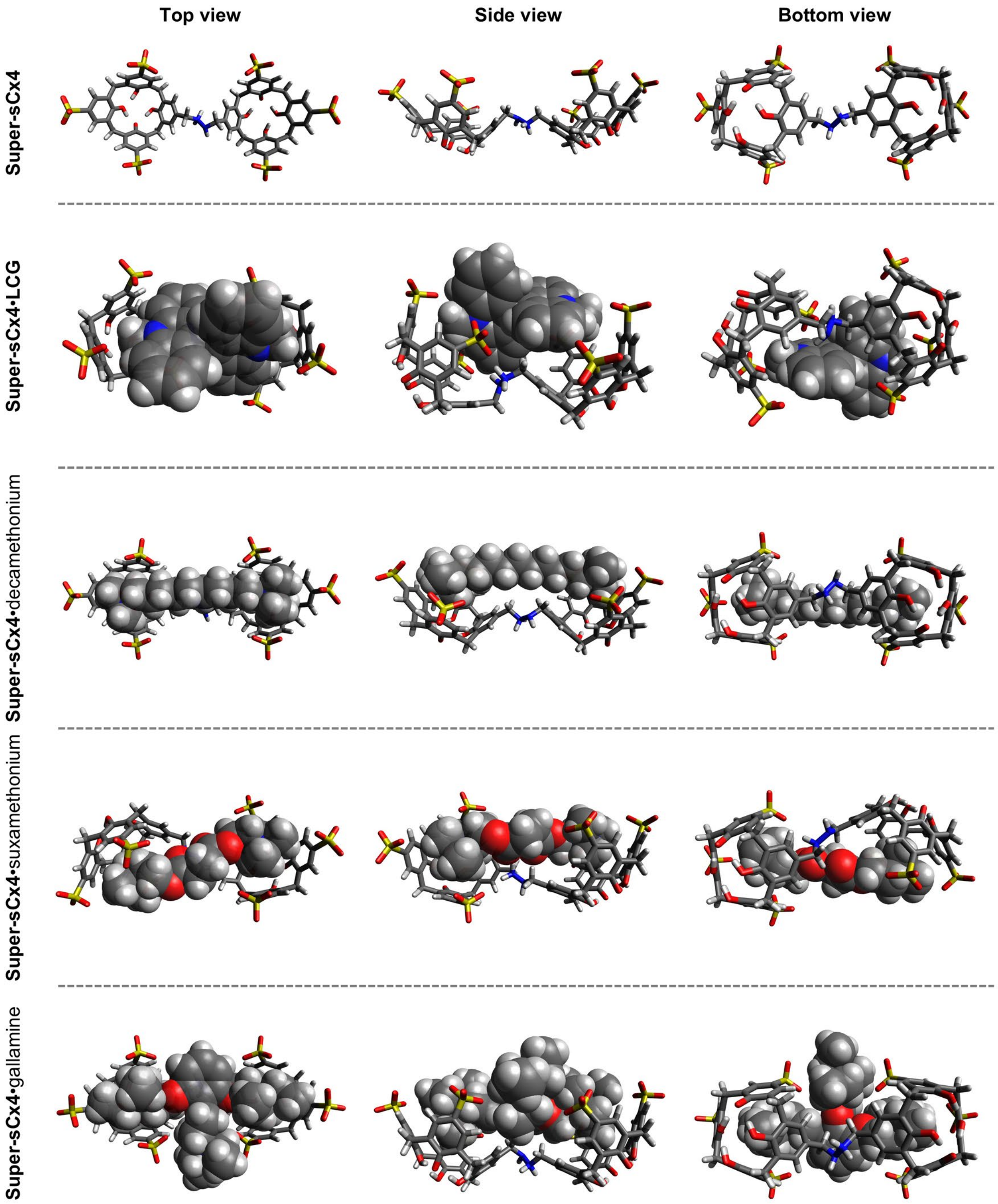

Figure 2.74. Molecular modelling of **Super-sCx4** shows 1:1 complexation with the dye **LCG** and the NMBA's decamethonium, suxamethonium and gallamine. In all cases the bisquaternary amines on the guest bind both cavity sites present on bivalent **Super-sCx4**.

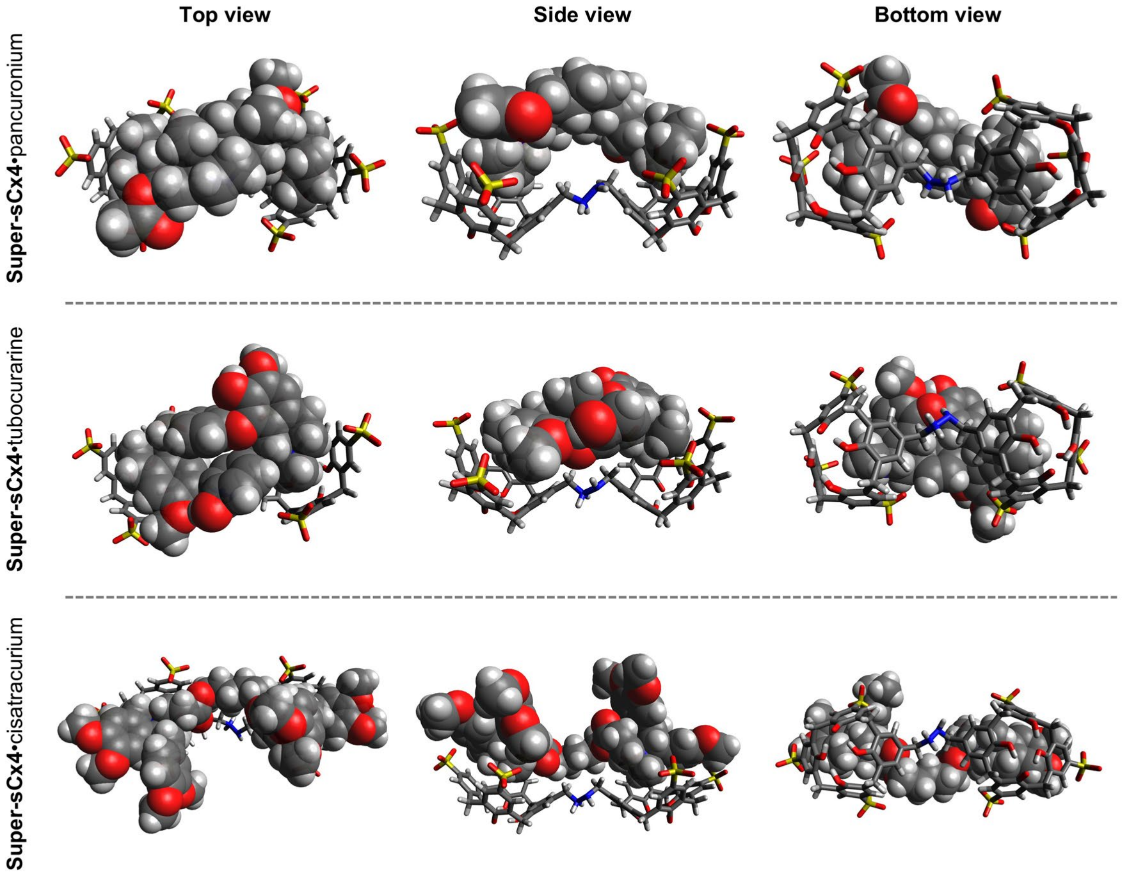

Figure 2.75. Molecular modelling of **Super-sCx4** shows 1:1 complexation with the NMBA's pancuronium, tubocurarine and cisatracurium. In all cases the bisquaternary amines on the guest bind both cavity sites present on bivalent **Super-sCx4**.

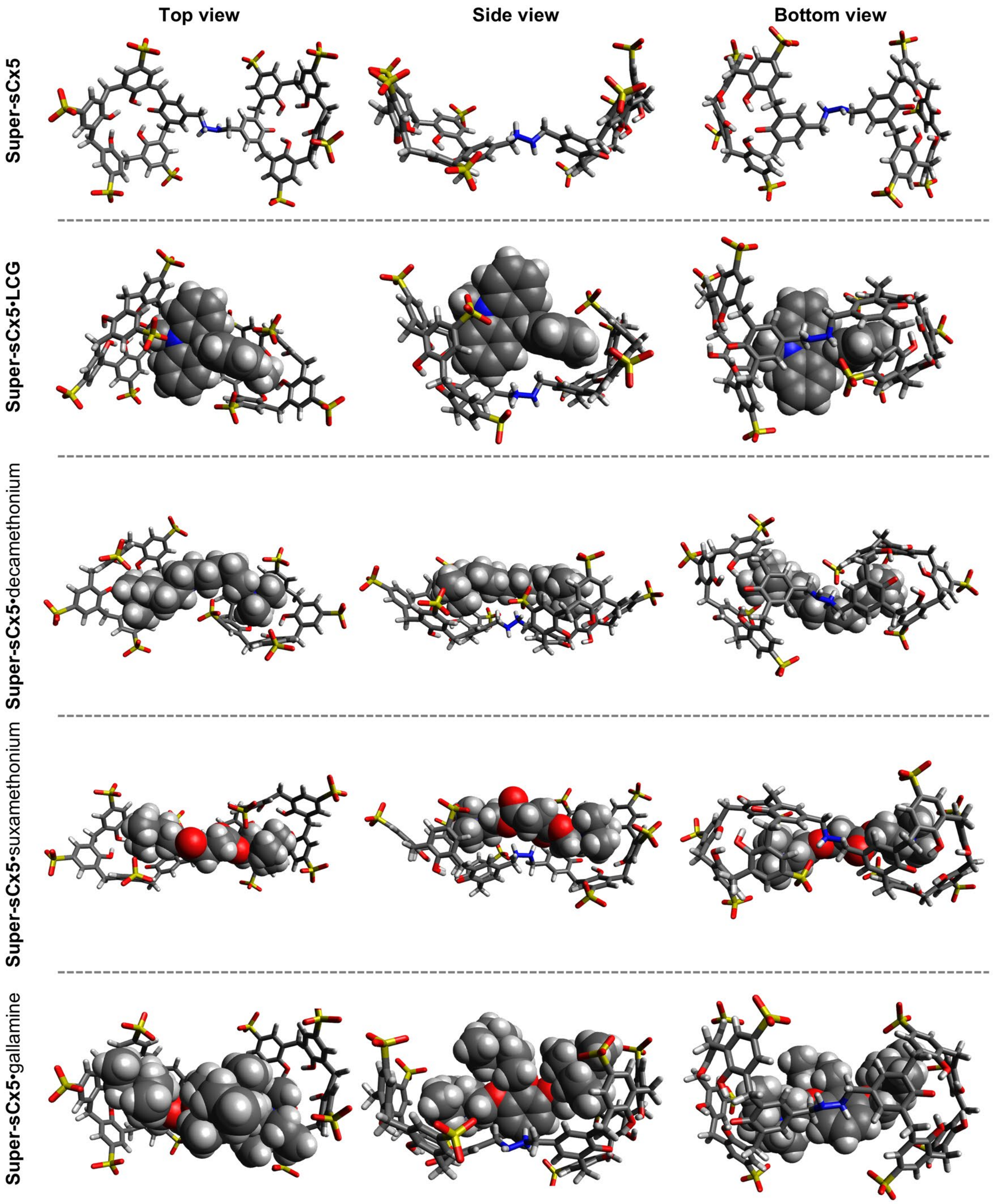

Figure 2.76. Molecular modelling of **Super-sCx5** shows 1:1 complexation with the dye **LCG** and the NMBA's decamethonium, suxamethonium and gallamine. In all cases the bisquaternary amines on the guest bind both cavity sites present on bivalent **Super-sCx5**.

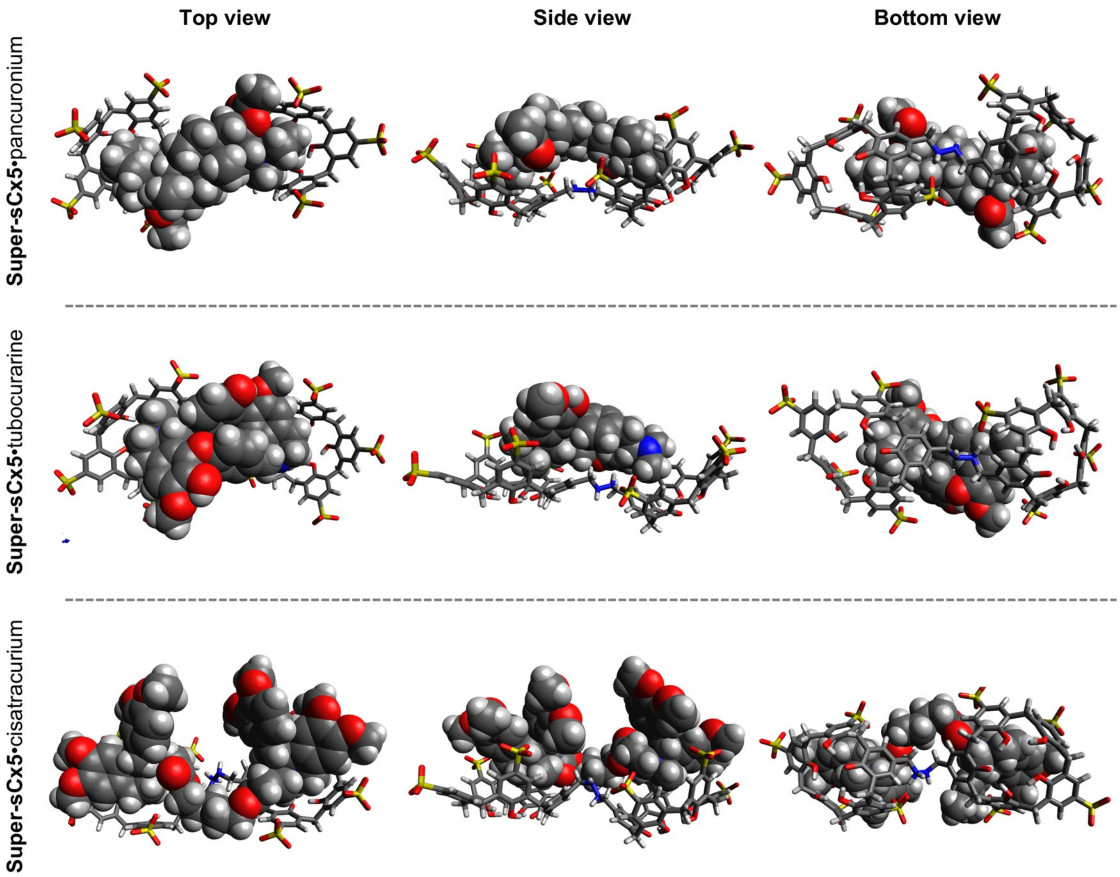

Figure 2.77. Molecular modelling of **Super-sCx5** shows 1:1 complexation with the NMBA's pancuronium, tubocurarine and cisatracurium. In all cases the bisquaternary amines of the guest bind both cavity sites present on the bivalent **Super-sCx5** host.

2.5.9 Isothermal titration calorimetry

Isothermal titration calorimetry (ITC) was performed using a VP-ITC calorimeter (MicroCal, Northampton, MA). Both host and suxamethonium samples were prepared in specified concentrations from solid in the same buffer, Na_2HPO_4/NaH_2PO_4 (50 mM, pH 7.4) in H_2O. Solutions were degassed immediately before use. Direct titrations were performed at 30°C by 29 injections (10 μL aliquots) of the suxamethonium solution into the ITC sample cell (volume = 1.4217 mL) containing the host compound solution.

Data was analyzed in Origin7.0 using the manufacturer's settings. A one set of sites model with the fitting parameters K_d, ΔH and N (number of sites) was used.[124] ΔS was calculated from K_d and ΔH. All ITC experiments were completed in duplicate. Final K_d, ΔH, −TΔS, N were reported as an average with propagated standard error.

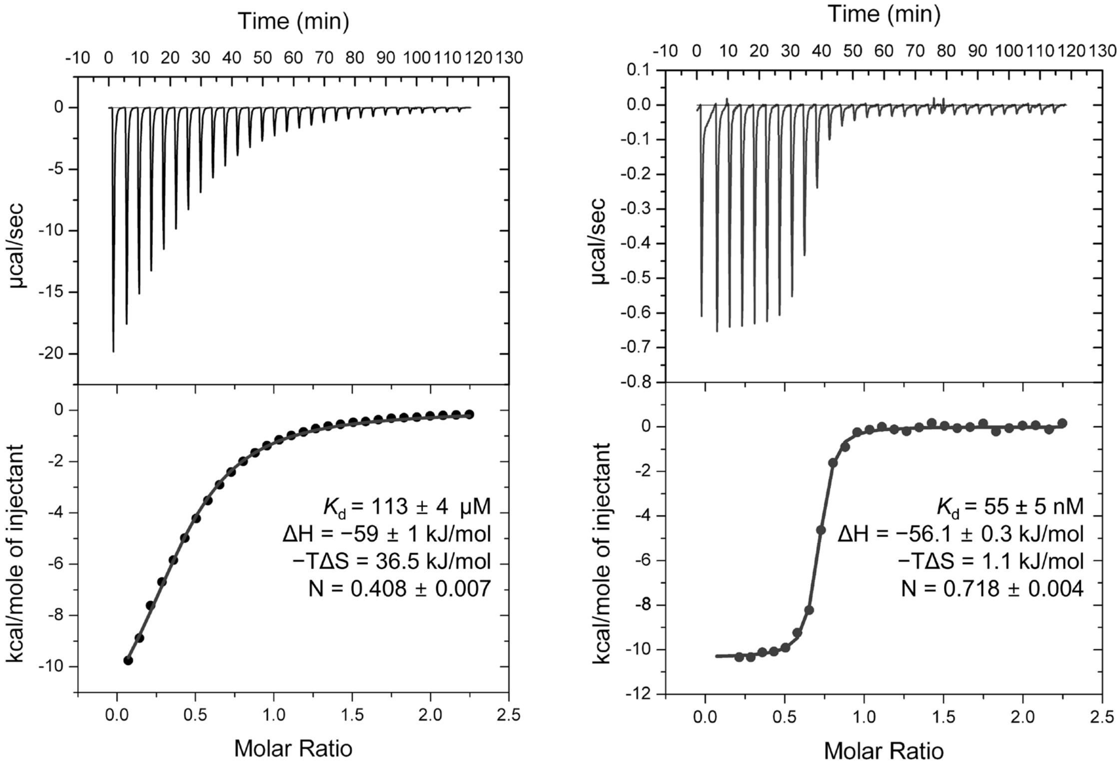

Figure 2.78. Exemplary ITC titrations of suxamethonium (7 mM) into **sCx4-CHO** (7 μM) (left) and suxamethonium (200 μM) into **Super-sCx4** (20 μM) (right) in NaH_2PO_4/Na_2HPO_4 (50 mM, pH 7.4) in H_2O at 30°C. Top panels shows the differential power between the reference and sample cell (μcal/sec) versus time, bottom panels show a plot of ΔH (kcal/mol) as a function of the molar ratio. Data was fit with a one set of sites binding model.

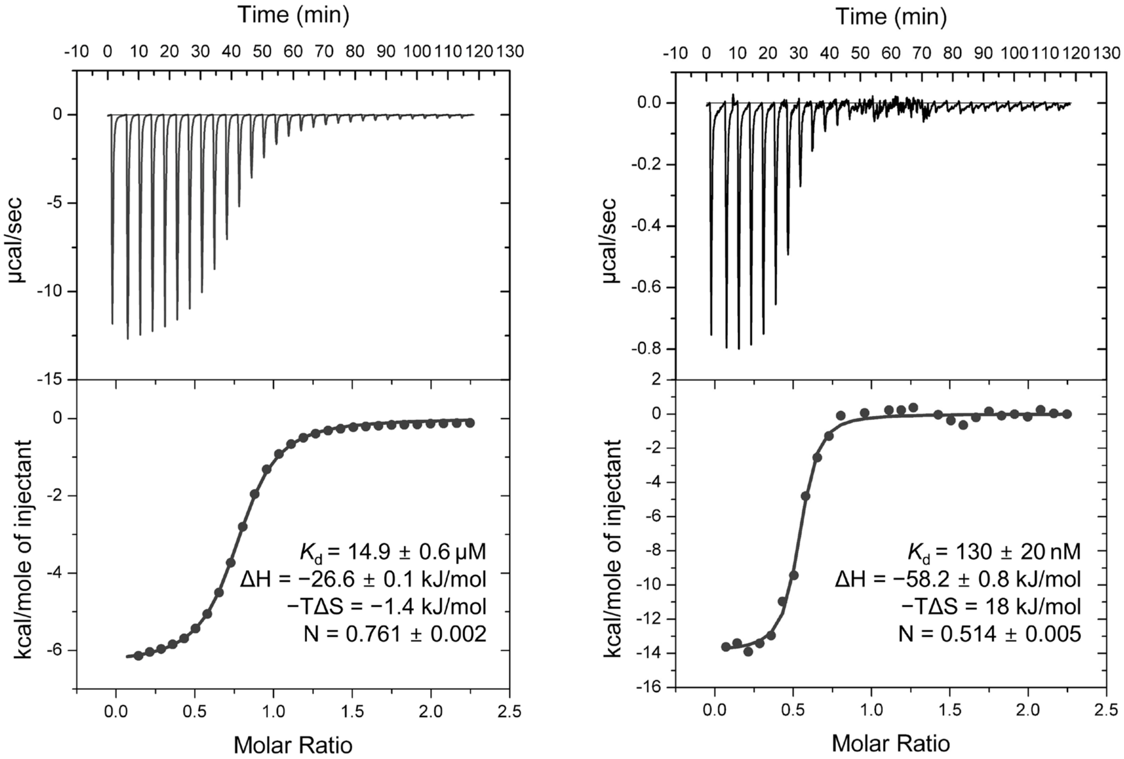

Figure 2.79. Exemplary ITC titrations of suxamethonium (7 mM) into **sCx5-CHO** (7 µM) (left) and suxamethonium (200 µM) into **Super-sCx5** (20 µM) (right) in NaH_2PO_4/Na_2HPO_4 (50 mM, pH 7.4) in H_2O at 30°C. Top panels shows the differential power between the reference and sample cell (µcal/sec) versus time, bottom panels show a plot of ΔH (kcal/mol) as a function of the molar ratio. Data was fit with a one set of sites binding model.

Table 2.22. ITC determined equilibrium dissociation constants and thermodynamic parameters of bivalent Super-sCx hosts and monovalent parent hosts with suxamethonium.

Host	Suxamethonium K_d (M)	ΔH (kJ/mol)	–TΔS (kJ/mol)	N
sCx4-CHO[a]	$(1.18 \pm 0.07) \times 10^{-4}$	−57 ± 2	35 ± 2	0.41 ± 0.01
Super-sCx4[b]	$(8 \pm 2) \times 10^{-8}$	−50 ± 9	1.7 ± 0.8	0.70 ± 0.02
sCx5-CHO[a]	$(1.8 \pm 0.4) \times 10^{-5}$	−26.1 ± 0.6	−1.42 ± 0.00	0.78 ± 0.03
Super-sCx5[b]	$(1.31 \pm 0.03) \times 10^{-7}$	−58.5 ± 0.4	18.5 ± 0.5	0.53 ± 0.02

[a] Direct titration of suxamethonium (7 mM) into monovalent parent host (700 µM). [b] Direct titration of suxamethonium (200 µM) into bivalent host (20 µM). All titrations done in NaH_2PO_4/Na_2HPO_4 (50 mM, pH 7.4) in H_2O at 30°C. A one set of sites binding model was used to fit the data. All values are reported as an average of two replicates with propagated standard error.

2.5.10 Cell viability assay

The AlamarBlue cell viability assay was used to assess the cytotoxicity of Super-sCx hosts in human embryonic kidney 293 (HEK293) and human hepatoblastoma (HepG2) cells. HEK293 and HepG2 cell lines and reagents for cell cultures were purchased from the American Type Culture Collection (ATCC; Manassas, VA). HEK293 and HepG2 cells were cultured in a 5% CO_2 incubator at 37°C, in Eagle's minimal essential medium (EMEM) supplemented with 10% fetal bovine serum (FBS) and 1% Penicillin-Streptomycin solution.

Super-sCx4 and **Super-sCx5** hosts were plated in direct comparison to **sCx4**, previously reported to have low toxicity in mice (100 mg/kg).[101] Melittin, a strongly lytic peptide towards bacteria and human cells, was used as a positive control (IC_{50} 0.941 ± 0.237 μM).[125] OT20, a non-membrane active receptor binding peptide, was used as a negative control (IC_{50} = >300 μM).[125] Triton X-100 detergent (TX-100) was used as a 100% cell death control. Host stock solutions were prepared in Na_2HPO_4/NaH_2PO_4 (10 mM, pH 7.4) in H_2O and sterilized by filtration through a 0.22 μm filter prior to use in the AlamarBlue cell viability assay.

AlamarBlue cell viability assay was conducted by distributing 1×10^4 cells to each well of a 96-well cell culture plate and allowing to adhere overnight. The compounds **sCx4**, **Super-sCx4**, **Super-sCx5**, Melittin, OT20 and TX-100 were added in respective wells. Dilutions of compounds were conducted in growth media with hosts ranging from 250 μM-128 pM (five-fold dilutions), Melittin and OT20 ranging from 128 μg/mL to 0.25 μg/mL (two-fold dilutions). TX-100 was used at a final concentration of 0.2%. Cells were then incubated for four hours. Following this incubation period, the media containing the compounds was replaced with fresh growth media and the cells were incubated for an additional twenty hours. The plates were imaged and qualitatively assessed as red being metabolically active and blue as inactive/dead.

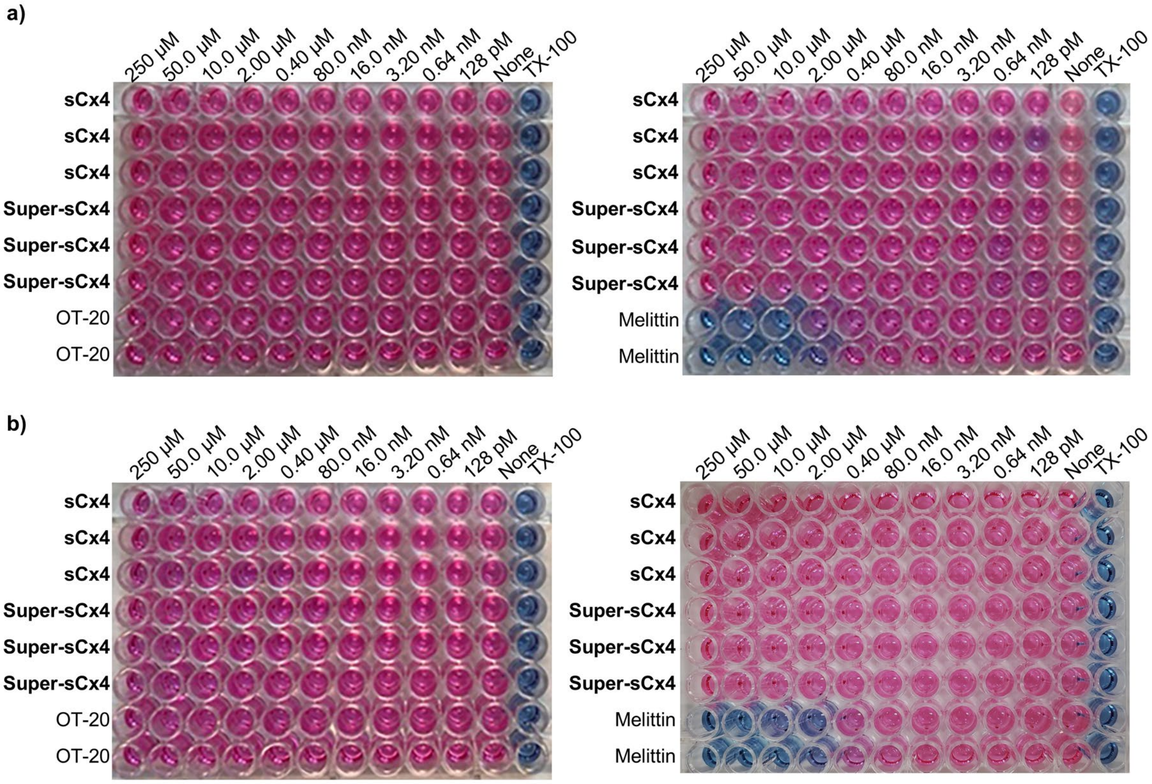

Figure 2.80. AlamarBlue cell viability assay microplates of **Super-sCx4** and **sCx4** in **a)** human HepG2 and **b)** HEK-293 cell lines. Calixarene concentrations are as indicated at the top of each image. OT-20 was used as a negative control (128 µg/mL to 0.25 µg/mL), Melittin as a positive control (128 µg/mL to 0.25 µg/mL), and TX-100 as a 100% cell death control (0.2% final concentration). Red indicates metabolically active cells, and blue indicates inactive/dead cells.

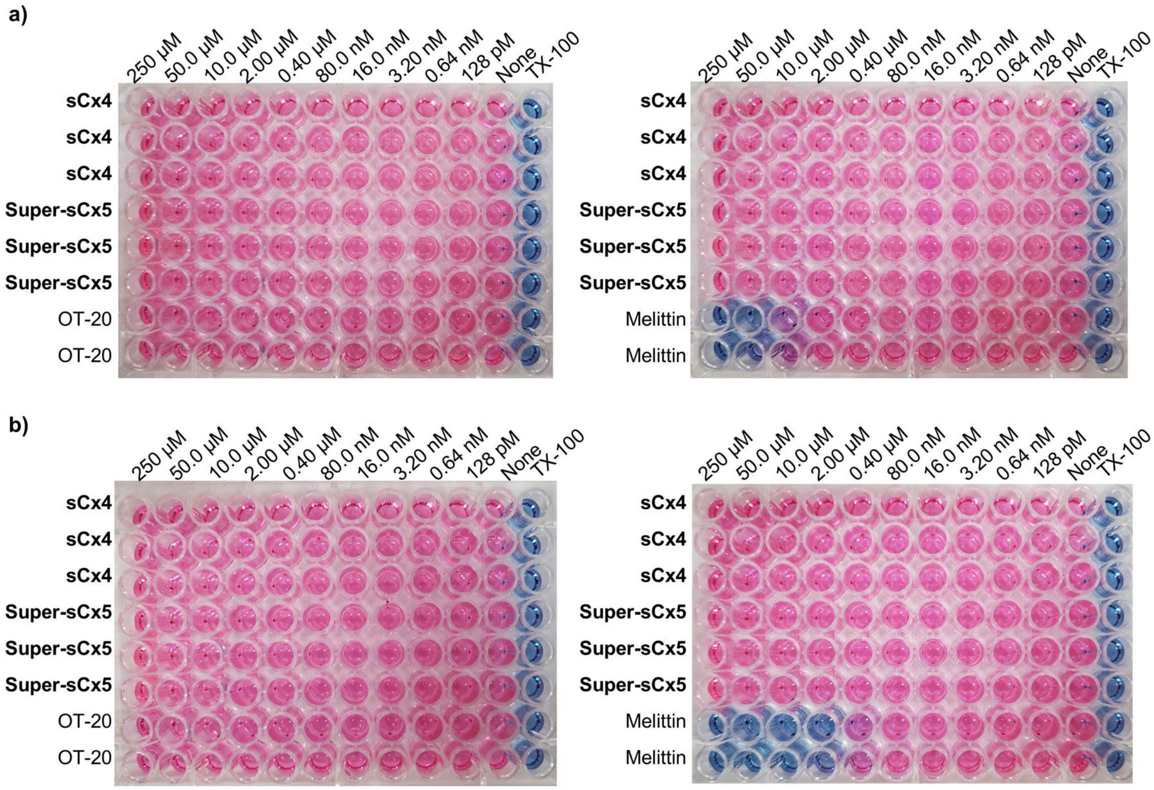

Figure 2.81. AlamarBlue cell viability assay microplates of **Super-sCx5** and **sCx4** in **a)** human HepG2 and **b)** HEK-293 cell lines. Calixarene concentrations are as indicated at the top of each image. OT-20 was used as a negative control (128 μg/mL to 0.25 μg/mL), Melittin as a positive control (128 μg/mL to 0.25 μg/mL), and TX-100 as a 100% cell death control (0.2% final concentration). Red indicates metabolically active cells, and blue indicates inactive/dead cells.

2.5.11 Comparative analysis of supramolecular NMBA reversal agents

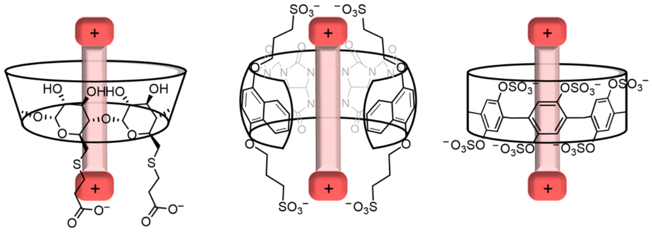

Figure 2.82. Reported supramolecular reversal agents Sugammadex (left), Calabadion 2 (middle) and Pillar[6]MaxQ (right) each contain a single binding motif, limiting NMBA binding to the size of the cavity and the fit of the NMBA.

Table 2.23. Supramolecular reversal agents reported dissociation constants of alkyl, steroidal and benzylisoquinoline NMBA's and their selectivity over **ACh**.

Host	Suxamethonium K_d (M)	Steroidal K_d (M)	Cisatracurium K_d (M)	**ACh** K_d (M)	Fold selectivity over **ACh** (suxamethonium, steroidal, cisatracuriam)
Super-sCx4	$(7.1 \pm 0.8) \times 10^{-5\,a}$	Pancuronium: $(1.0 \pm 0.2) \times 10^{-5\,a}$	$(2.0 \pm 0.4) \times 10^{-4\,a}$	$>1.0 \times 10^{-2\,a}$	>140, >960,>51
Super-sCx4	$(8 \pm 2) \times 10^{-8\,b}$	–	–	–	
Super-sCx5	$(1.4 \pm 0.3) \times 10^{-5\,a}$	Pancuronium: $(1.4 \pm 0.3) \times 10^{-5\,a}$	$(6 \pm 3) \times 10^{-6\,a}$	$>1.0 \times 10^{-2\,a}$	>550, >700, >2000
Super-sCx5	$(1.31 \pm 0.03) \times 10^{-7\,b}$	–	–	–	
Sugammadex	n.r.[94]	Rocuronium: $(9.5 \pm 0.1) \times 10^{-7\,b92}$	n.r.[94]	–	
Pillar[5]arene analog	–	Rocuronium: $2.2 \times 10^{-4\,d95}$	–	–	
WP[6]	$3.58 \times 10^{-6\,b96}$	–	–	$2.82 \times 10^{-5\,b96}$	8, –, –
WP[6]	–	Pancuronium: $(6.37 \pm 0.02) \times 10^{-7\,b97}$	$(9.52 \pm 0.09) \times 10^{-6\,b97}$	$(5.4 \pm 0.6) \times 10^{-6\,b97}$	–, 8, 0.56
		Rocuronium: $(7.0 \pm 0.2) \times 10^{-7\,b97}$			8
		Vecuronium: $(3.5 \pm 0.4) \times 10^{-7\,b97}$			15
Pillar[6]MaxQ	–	Pancuronium: $(1.4 \pm 0.2) \times 10^{-11\,c97}$	$(1.1 \pm 0.2) \times 10^{-6\,b97}$	$(1.9 \pm 0.1) \times 10^{-8\,c97}$	–, 1400, 0.02
		Rocuronium: $(1.58 \pm 0.02) \times 10^{-12\,c97}$			12000
		Vecuronium: $(1.0 \pm 0.4) \times 10^{-13\,c97}$			19000
Calabadion 2	–	Pancuronium: $(1.8 \pm 0.2) \times 10^{-9\,e98}$	$(2.1 \pm 0.4) \times 10^{-7\,e98}$	$(4.5 \pm 0.6) \times 10^{-6\,e98}$	–, 2900, 27
		Rocuronium: $(2.9 \pm 0.5) \times 10^{-10\,e98}$			19000
		Vecuronium: $(6.3 \pm 0.8) \times 10^{-10\,e98}$			9000

– not reported, n.r. reported as no reversal *in vitro* [a]measured by IDA, [b]measured by direct ITC, [c]measured by competitive ITC, [d]measured by UV-Vis direct titration [e]measured by UV-Vis displacement titration.

Chapter 3: Adaptive supramolecular networks – emergent sensing from complex systems

This work was adapted from a previously published paper.

Allison J. Selinger and Fraser Hof
Angew. Chem. Int. Ed., **2023**, 62, e202312407.

AJS and FH conceptualized the idea. AJS was the lead on investigation, formal analysis and methodology development. AJS contributed synthesis design and characterization of the novel sensors **hemiDD1Cx4** and **DD13Cx5** and synthesized previously reported **DD4Cx4** used in this work. All absorbance and fluorescence titrations, trypsin digestion experiments, protein extraction, PCA, and STD NMR experiments were designed, conducted, and analyzed by AJS. AJS wrote the original draft of the paper. AJS and FH contributed to reviewing and editing the paper.

3.1 Foreword

This Chapter introduces a fundamental study in developing complex adaptive sensing systems. Here I build on sensing system concepts outlined in Chapter 1. In Section 1.3, I introduced a panel of previously reported DimerDye sensors that operate in salty biological solutions. In our previous publications, DimerDyes had only been used in isolation, operating as discrete disassembly-driven turn-on sensors.[54, 72, 126] At the outset of this Chapter, I was driven by a general curiosity into how different DimerDyes would behave when mixed in solution (i.e. would they form self-sorting homodimers or would they cross-interact and form heterodimers)? Our idea was that constructing an interconnected network of sensor equilibria would maximize the diversity of photophysical responses that could be produced from a single solution. To test the value of increasing system complexity, I decided to make a direct comparison to an analogous commonly used approach, in which the same sensors are used in isolation within an array. As a proof of concept, I selected highly similar serum albumin (SA) proteins as challenging sensing targets for differentiation.

3.2 Introduction

In systems chemistry, networks of interacting and reacting molecules respond to changing conditions in complex ways. Complex systems can generate emergent properties that are hard or impossible to predict *a priori*. Some examples of system complexity explore kinetically trapped metastable self-assemblies,[127, 128] and out-of-equilibrium dissipative self-assemblies.[129, 130] Supramolecular complexity can also be introduced by building a system in which multiple building blocks simultaneously interact with each other and establish a complex web of interconnected equilibria.[131, 132]

Complex molecular systems have been used to create multi-responsive sensors. Different than analytical methods that rely on highly specific binding elements (e.g. antibodies) to detect a single bioactive analyte,[133] multi-responsive selective chemical sensors detect multiple target analytes and help characterize mixtures of analytes.[60] In this context, “multi-responsive” can mean both “responding to multiple analytes” and also “producing varying kinds of optical responses to any given analyte”. Supramolecular sensing that involves selectively binding individual analytes is routinely done through displacement assays, often utilizing an external reporter dye.[36, 40, 41, 43] Several host-type sensors are typically deployed in an array to generate characteristic analyte-patterned responses for discrimination (Figure 3.1a).[65, 134] This approach generally requires a large array of sensor elements used in isolation from each other (i.e. in different wells in a microwell plate). Alternative approaches of small molecule dynamic combinatorial libraries,[77, 79] and cross-reactive sensors have shown advantages in differential sensing.[135] The scope of biological targets and complexity of macrocyclic host-type sensors is being pushed with recent advances in arrays of covalently attached macrocycle-sensors to detect bioorganic analytes and misfolded proteins,[74, 78] noncovalent macrocyclic sensors to identify small modifications in DNA,[70, 82, 83] and new strategies of adjusting host•sensor combinations and solution environment to discriminate cell lines and complex protein mixtures.[84, 85]

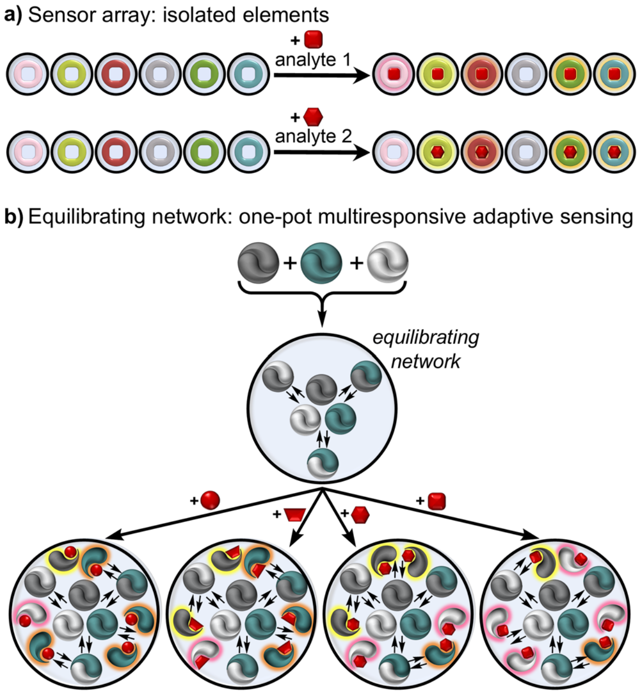

Figure 3.1. Complex systems offer information-rich outputs in a single solution. **a)** Array-based sensing requires a panel of individual sensor•analyte response patterns to achieve discrimination. **b)** We propose a one-pot adaptive sensing network, combining structurally and photochemically diverse sensors to produce fingerprint analyte responses within a single solution.

Here we report a one-pot systems chemistry sensing approach of interacting and reacting sensors that provide information-rich outputs in a single solution. The key to unlocking a functional adaptive network of sensors is using responsive sensor elements that contain homo- and hetero-assembly interactions, paired with a range of analyte binding properties. The reported output is influenced by a complex interconnected web of sensor•sensor and sensor•analyte equilibria (Figure 3.1b). Slight shifts in this network equilibrium position upon analyte binding are expressed through multi-responsive outputs from more than one mutually interacting sensor, even from sensor elements that might not directly bind the analyte. In this complex system, supramolecular emergent properties arise from the unpredictable adaptations of the network's overall equilibrium position. Photophysical emergent properties arise from the complex, unpredictable ground-state and excited-state interactions of heterodimeric sensors juxtaposing different chromophores. Unlike sensor arrays, the adaptive network of sensors operates within a single solution.

To explore this concept, we chose DimerDyes — a family of dimerizing calixarenes containing an integrated fluorophore.[54, 72, 126] DimerDyes operate by a disassembly-driven sensing mechanism. In the absence of analyte, individual DimerDyes self-assemble into homodimers, where two dyes stack in an antiparallel arrangement and the dyes' emission is quenched. The addition of a good analyte out-competes dimerization to form a DimerDye•analyte complex, resulting in a turn-on fluorescence response (Figure 3.2a). We postulated that a mixture of DimerDyes would self-assemble into homo- and hetero-dimers, thus creating a complex network of assembled sensors. Here, we report an adaptive network that arises from three sensors, combining different binding and optical properties in a single solution. Exploiting the combination of emergent supramolecular and photophysical properties, we show that sensing capabilities arise from an adaptive network of mutually assembling sensors, which prove to be more powerful than a sensor array built from the same components.

3.3 Results and discussion

Mixing three DimerDyes containing diverse photochemical properties and structures creates a complex, functional sensing network. We selected three merocyanine dyes — *N*-methyl pyridinium, *N*-phenyl pyridinium and indolinium — to span a range of absorbance and emission wavelengths and to encourage new photophysical properties to emerge from dye•dye interactions. To diversify analyte binding affinities, these fluorophores were integrated into *p*-sulfonatocalix[4]arene and *p*-sulfonatocalix[5]arene scaffolds, varying the upper-rim sulfonate anionic charge and hydrophobic cavity size (Figure 3.2b). Novel **hemiDD1Cx4** was synthesized through monosubstitution of a calix[4]arene dialdehyde (Scheme 3.1 and Scheme 3.2). Novel **DD13Cx5** was synthesized via aldehyde-functionalized calix[5]arene (Scheme 3.3 and Scheme 3.4). And previously reported **DD4Cx4** was synthesized through aldehyde-functionalized calix[4]arene (Scheme 3.5).[72] These isolated DimerDye sensors — **hemiDD1Cx4**, **DD4Cx4** and **DD13Cx5** — exhibit characteristic signs of homodimerization in aqueous solution, observed by ^{1}H NMR and fluorescence studies of each isolated sensor (see Section 3.5.3). Combining these three sensors in a one-pot mixture of homo- and hetero-assembled sensors creates a DimerDyeNetwork (DDNetwork), an adaptive network of self-assembling sensors with varied guest-binding and photophysical properties.

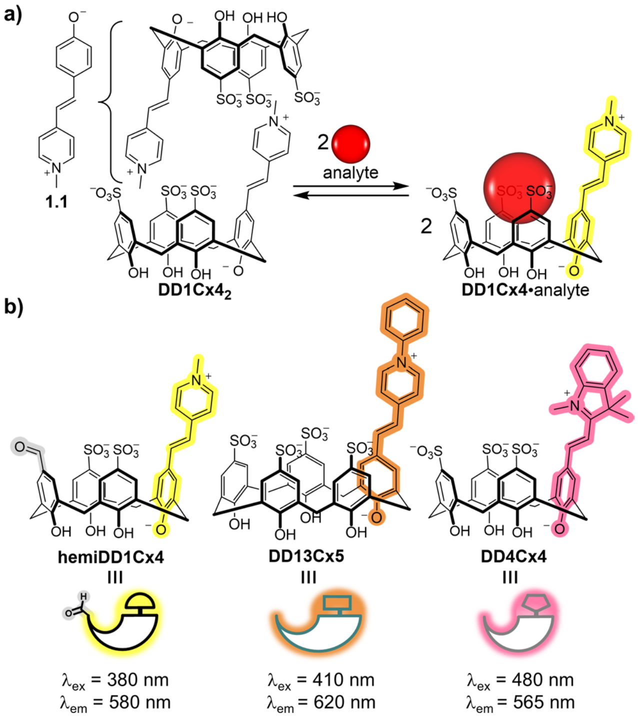

Figure 3.2. Structurally and photophysically diverse DimerDyes for cross-reactive one-pot sensing. **a)** Previously reported **DD1Cx4** integrates a merocyanine chromophore (**1.1**) into the *p*-sulfonatocalix[4]arene scaffold. **DD1Cx4₂** operates by a disassembly driven turn-on fluorescence sensing mechanism when an analyte binds the calixarene cavity.[54] **b)** Chemical structures of DimerDye sensors used in this work vary in optical properties, cavity size and anionic charge.

The DDNetwork contains both homodimers and heterodimers equilibrating in aqueous solution. If each calixarene in the mixture participated exclusively in homodimers (i.e. if the system underwent narcissistic self-sorting),[136] then the absorbance of the DDNetwork would equal the sum of its components studied individually. Instead, comparison of the DDNetwork's absorbance spectrum to the mathematically added spectra of the individual sensors shows strong differences in the absorbance profile. This supports that hetero-aggregates form in the DDNetwork (Figure 3.3b and Figure 3.19). In the absence of analyte, the DDNetwork maintains an overall quenched fluorescent state, similar to the individual sensors. The different absorbance properties and non-emissive state of the DDNetwork indicate that heterodimer formation occurs in solution. The presence of both homodimers and heterodimers in equilibrium is independently supported by ^{1}H NMR. When **hemiDD1Cx4** and **DD4Cx4** are combined, new resonances in slow exchange alongside those of each homodimer demonstrate the presence of hetero-aggregates (Figure 3.18). Information-rich outputs are obtained by observations at different wavelengths, when an analyte is added to a single solution of the adaptive network. DimerDye sensors **hemiDD1Cx4**, **DD4Cx4**, and **DD13Cx5** mixed in an equimolar ratio (1:1:1) have a certain distribution of homodimers and heterodimers. As the ratio of one DimerDye is increased in the network, the equilibrium shifts towards more homodimer, demonstrating that the network equilibrium responds as expected to changing concentrations (Figure 3.20). Upon the addition of choline (**Ch**), a promiscuous analyte that binds all DimerDyes to some extent, the DDNetwork is perturbed. This is evidenced by changes in absorbance and turn-on fluorescence responses within the network (Figure 3.3c). When the DDNetwork is saturated with excess **Ch** the equilibrium position is pushed entirely toward **Ch** bound monomers (Figure 3.21). Under this extreme saturating condition, the network should not contain any homo- or heterodimers and the spectra should resemble the data arising from monomeric host•analyte complexes. This is observed by the absorbance response of the DDNetwork to 200 eq **Ch** closely resembling the mathematically added spectra of the isolated DimerDyes under the same saturating conditions (Figure 3.21d). At sub-saturating amounts of analyte, the DDNetwork includes a mixture of self-assembled homodimers, heterodimers and analyte-bound monomers. In principle, the interconnected equilibria of the adaptive network should be highly sensitive to the identity of a given analyte, even without any specifically designed host•analyte recognition elements.

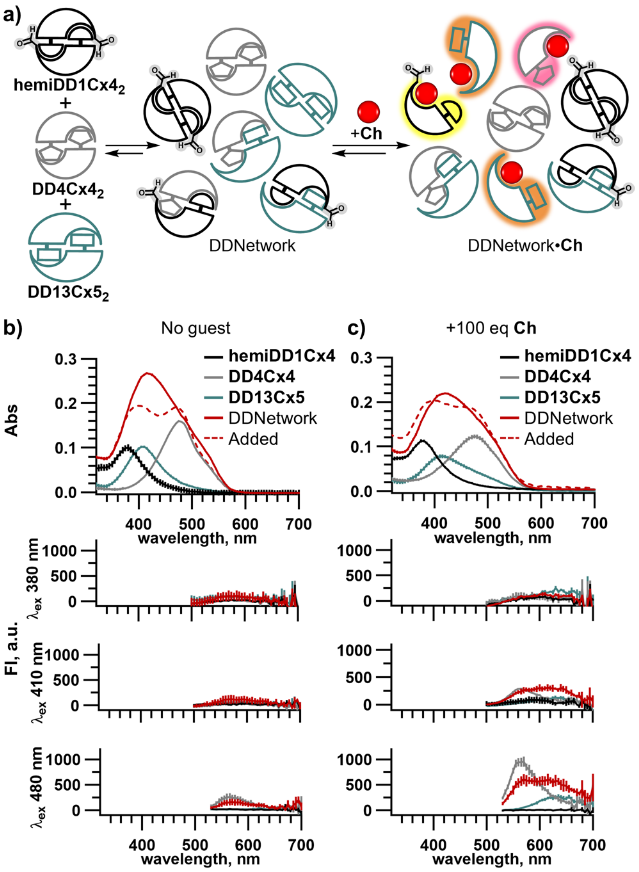

Figure 3.3. The adaptive DDNetwork behaves differently than the sum of its parts. **a)** Schematic of DDNetwork assembling into homodimers and heterodimers, followed by analyte binding perturbing the network and inducing a turn-on fluorescence response. **b)** Absorbance spectra of the DDNetwork (solid red line) and the mathematically added spectra (dashed red line) of the individual sensors (**hemiDD1Cx4** (black line), **DD4Cx4** (grey line) and **DD13Cx5** (teal line)) are not equal, indicating the presence of heterodimers in the DDNetwork. Fluorescence spectra show the DDNetwork maintains minimal or quenched fluorescence. **c)** Addition of the analyte **Ch** results in an absorbance profile change and a turn-on fluorescence response. Hosts in all samples are present at identical concentrations — [**hemiDD1Cx4**] = 12 μM, [**DD4Cx4**] = 12 μM and [**DD13Cx5**] = 12 μM — either mixed with each other or separate as indicated. All samples in NaH_2PO_4/Na_2HPO_4 (10 mM, pH 7.4) in H_2O.

We selected a panel of serum albumin (SA) proteins as challenging model analytes for discrimination by the adaptive network. Highly conserved amino acid content, surface charge distribution and crystal structure alignment are reported across several species.[137] We selected mammalian SA proteins ranging from 69% to 92% conserved amino acid identity (human (HSA), bovine (BSA), sheep (SSA), porcine (PSA), rat (RSA) and mouse (MSA)) (Figure 3.4b, Figure 3.23, Figure 3.22 and Table 3.1). Highly conserved sequence identity with homologous hydrophobic binding sites,[138] makes them extremely challenging for discrimination by supramolecular sensors.

A one-pot adaptive network successfully detects and discriminates highly similar proteins. The DDNetwork's complex photophysical responses to SA proteins was captured by absorbance spectral scans and fluorescence spectral scans, exciting at different wavelengths (λ_{ex} = 380, 410, 450, 480 and 510 nm). Each SA protein perturbed the DDNetwork in distinct ways (Figure 3.4c). Responses were analyzed by Principal Component Analysis (PCA), aiming to minimize the number of observations while achieving the best discrimination. Three absorbance wavelengths (440, 495, 515 nm) achieved complete discrimination of all SA proteins (Figure 3.4d and Figure 3.25a). Six selected emission responses from the DDNetwork (λ_{em} = 580 nm (λ_{ex} = 380 nm), λ_{em} 580 nm (λ_{ex} = 410 nm), λ_{em} 620 nm (λ_{ex} = 410 nm), λ_{em} 625 nm (λ_{ex} = 450 nm), λ_{em} 565 nm (λ_{ex} = 480 nm) and λ_{em} 580 nm (λ_{ex} = 510 nm)) achieved discrimination of four SA species, with BSA and PSA overlapping (Figure 3.28).

The adaptive network is more powerful than the equivalent array of individual sensors. The isolated DimerDye sensing responses to SA proteins were measured (Figure 3.25, Figure 3.29 to Figure 3.31). The limit of detection (LOD) for HSA and the individual DimerDyes were determined to range from 0.19 to 1.8 μM (Figure 3.24 and Table 3.2). Notably, isolated **DD13Cx5** exhibited the greatest variation in absorbance responses to SA binding. Shifts in λ_{max} up to ~100 nm (Figure 3.25d), along with observed ^{1}H NMR conformational flexibility (Figure 3.12 and Figure 3.37), indicates the *p*-sulfonatocalix[5]arene scaffold provides distinct conformational changes and sensing properties. **HemiDD1Cx4** exhibited the greatest variation in fluorescence intensity responses, possibly due to altered affinities from the upper-rim aldehyde handle (Figure 3.29). As a direct comparison, the same wavelengths used in PCA analysis of the DDNetwork were applied to the sensing responses of the three isolated DimerDyes in a sensor array. Therefore, sensor array analyses inherently had the advantage of including 3× the number of data observations relative to the one-pot adaptive network. PCA analysis comparison of the compiled isolated sensors in an array (9 absorbance observations, or 18 fluorescence observations) did not achieve complete discrimination with overlapping confidence ellipses of similar proteins (Figure 3.4f, Figure 3.26 and Figure 3.32).

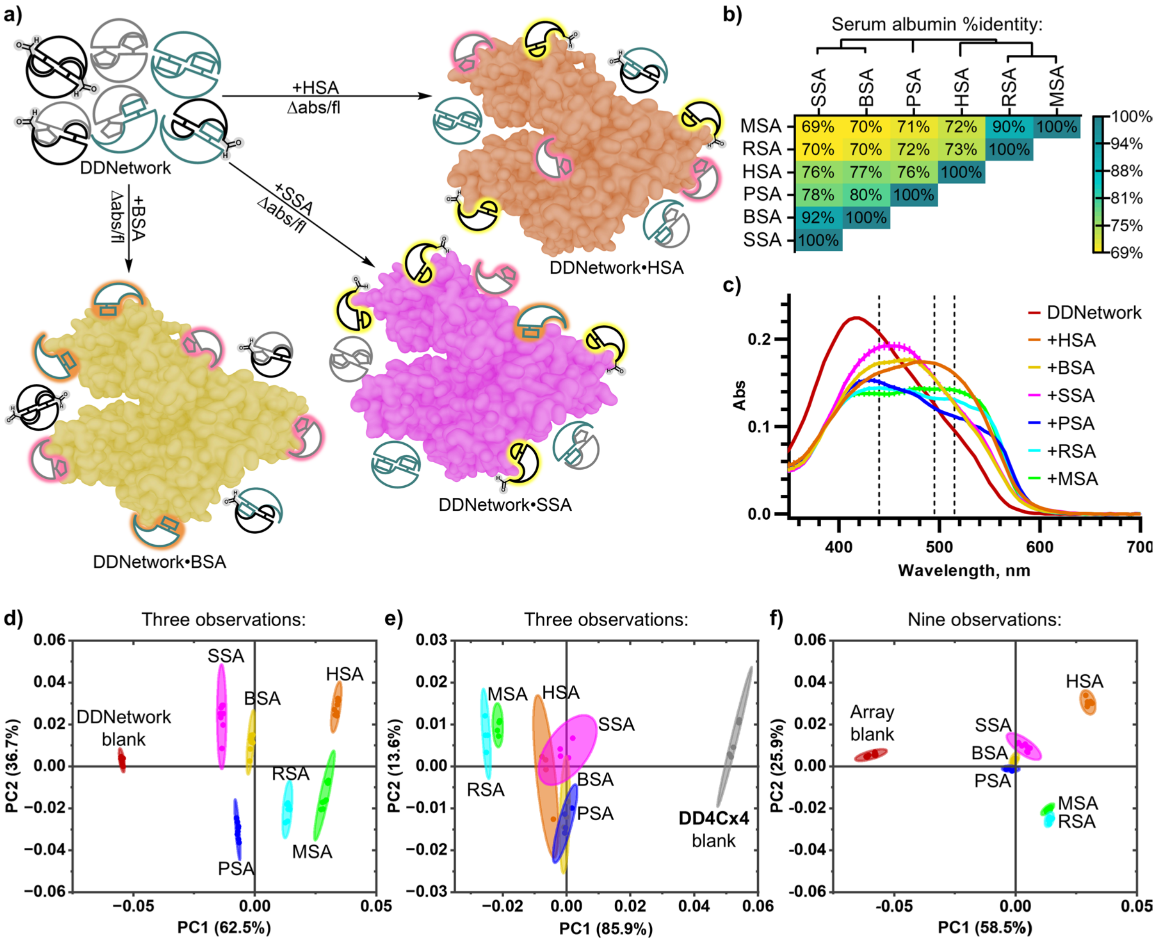

	SSA	BSA	PSA	HSA	RSA	MSA
MSA	69%	70%	71%	72%	90%	100%
RSA	70%	70%	72%	73%	100%	
HSA	76%	77%	76%	100%		
PSA	78%	80%	100%			
BSA	92%	100%				
SSA	100%					

Figure 3.4. A one-pot adaptive network discriminates highly similar model proteins. **a)** Schematic of the DDNetwork adaptive interactions with SA proteins resulting in fingerprint sensing patterns. **b)** SA protein sequence %identity is highly conserved across different species. Phylogenetic tree depicts evolutionary commonality between species. **c)** Unique absorbance profile changes occur upon DDNetwork binding to different SA proteins. Black dashed lines depict absorbance wavelengths used in PCA analysis. PCA scores plots of **d)** DDNetwork **e) DD4Cx4** and **f)** the compiled isolated sensor responses in an array; **hemiDD1Cx4**, **DD4Cx4** and **DD13Cx5**. PCA analysis was done using absorbance responses at 440, 495 and 515 nm. PCA (covariance) scores plots show each sample set (n = 8) enclosed by 95% confidence ellipses. DimerDyes in all samples are present at identical concentrations — [**hemiDD1Cx4**] = 12 µM, [**DD4Cx4**] = 12 µM and [**DD13Cx5**] = 12 µM — either mixed with each other or separate as indicated, [SA] = 32 µM. All samples are in NaH_2PO_4/Na_2HPO_4 (10 mM, pH 7.4) in H_2O.

The network can adapt quickly to provide real-time analysis of changing biological samples. Trypsin digest experiments of native HSA were conducted to test the DDNetwork's ability to adapt its equilibrium within a changing protein solution over time. Measurable changes in absorbance were observed on the time scale of minutes as HSA underwent proteolysis in both phosphate buffer (pH 7.4) and ammonium bicarbonate buffer (pH 8.0) (Figure 3.34).

The adaptive network components provide useful sensing readouts despite their undesigned engagement of protein surface elements. HSA was studied with individual DimerDyes using saturation transfer difference (STD) NMR, which shows how closely engaged ligand protons are to any part of a protein binding partner.[139] Positive STD NMR signals were observed for **hemiDD1Cx4**, **DD4Cx4** and **DD13Cx5** (Figure 3.35 to Figure 3.37), providing a general view of the collective complexes formed with HSA. STD intensities for **hemiDD1Cx4** (Figure 3.5b) indicate a predominant complexation geometry where the DimerDye pendant arm and cavity engage the protein and the calixarene lower rim points out towards solvent. To rule out binding in specific ligand-binding pockets, competitive STD NMR was done on **hemiDD1Cx4** using saturating amounts of known high affinity competitors that target the primary drug binding sites of HSA.[140-143] Warfarin was used to competitively probe Sudlow site I ($K_{\mathrm{d\ HSA}} \approx 3\ \mu\mathrm{M}$),[143, 144] and naproxen was used to competitively probe Sudlow site II ($K_{\mathrm{d\ HSA}} = 560\ \mathrm{nM}$).[145] The appearance of competitor STD signals was observed in both cases and little to no reduction in the STD signals of **hemiDD1Cx4** was observed (Figure 3.38-3.41). This data indicates DimerDyes engage SA proteins through surface binding interactions and do not target the primary ligand-binding sites Sudlow site I and II. These results align with crystallography reports of *p*-sulfonatocalix[4]arenes binding different proteins at positively charged surface lysine and arginine residues with multi-complexation interactions.[146-149]

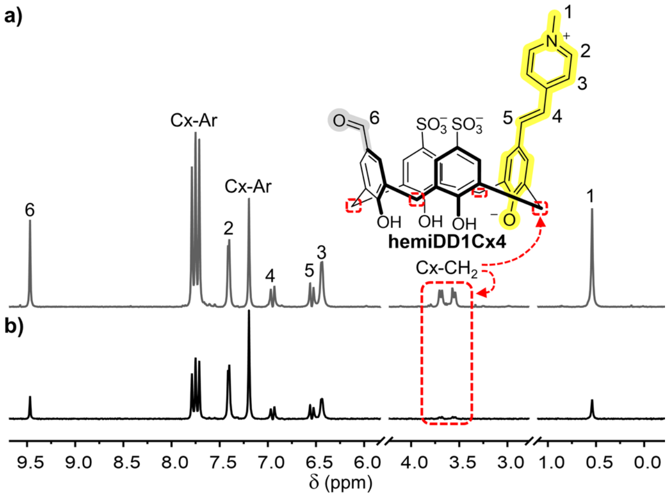

Figure 3.5. HemiDD1Cx4 binds HSA via pendant arm and upper rim interactions. **a)** Reference NMR and **b)** STD NMR of **hemiDD1Cx4** (1.2 mM) with HSA (20 µM). Red box indicates lower rim methylene protons have the least intense STD signal. Sample in NaH_2PO_4/Na_2HPO_4 (50 mM, pD 7.4) in 90% H_2O/10% D_2O.

Adaptive network sensing can be applied to the discrimination of real-world complex protein mixtures. To further investigate the networks sensing capabilities we extracted protein mixtures from a tissue sample of cod, halibut, rockfish and sole (Figure 3.6a). DDNetwork sensing produced variable absorbance and fluorescence responses. These results used in PCA analysis achieved discrimination of extracted protein mixtures from the different white fish varieties (Figure 3.6 and Figure 3.33). These results further demonstrate the ability of the adaptive network to operate in complex mixtures and illustrates its potential use in applications of tissue classification, food fraud and quality control.

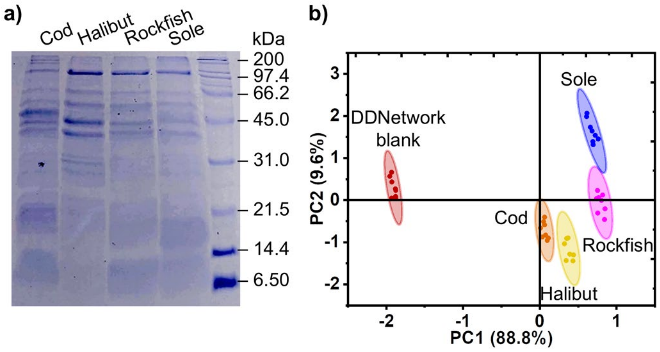

Figure 3.6. DDNetwork discriminates fish varieties from extracted protein mixtures. **a)** Sodium dodecyl sulfate polyacrylamide gel electrophoresis (SDS-PAGE) shows extracted protein mixtures obtained from a cod, halibut, rockfish and sole tissue sample. **b)** PCA (correlation) scores plot show each sample set (n = 8, technical replicates) enclosed by 95% confidence ellipses. Samples contain DDNetwork ([**hemiDD1Cx4**] = 12 µM, [**DD4Cx4**] = 12 µM and [**DD13Cx5**] = 12 µM) and [protein extract] = 1 mg/mL. All samples are in NaH_2PO_4/Na_2HPO_4 (10 mM, pH 7.4) in H_2O.

3.4 Conclusion

Combining sensors that interact directly with each other within a single complex system provide new kinds of information-rich outputs. The overall emergent profile changes in absorbance and fluorescence produced by the adaptive network provide more powerful tools for discrimination than increased/decreased signal intensities that arise from individual sensors. With the addition of a simple small molecule analyte, a total of 9 possible self-assemblies can occur (3 homodimers, 3 heterodimers and 3 analyte-bound monomers). When analytes become more complex in size and structure, there is an increased number of binding events, modes and equilibria. Varying host•host, host•analyte affinities, and induced host conformational changes are reflected in the range of optical outputs from the adaptive network, proving to be richer in information than the same sensors deployed as an array.

This work illustrates that a complex supramolecular system can be easily built by mixing components. Adaptive systems that embrace promiscuous sensing can be harnessed to achieve challenging sensing tasks. This approach can be applied in any system in which sensor•sensor and sensor•analyte interactions combine to create networked complexity.

3.5 Supplementary information

3.5.1 General materials and methods

3.5.1a Materials

The following proteins and compounds were used as purchased from Sigma Aldrich; human serum albumin (HSA, P02768), bovine serum albumin (BSA, P02769), sheep serum albumin (SSA, P14639), porcine serum albumin (PSA, P08835), rat serum albumin (RSA, P02770), mouse serum albumin (MSA, P07724), trypsin from bovine pancreas, warfarin analytical standard (98%) and (+)-naproxen pharmaceutical secondary standard (<= 100%). Choline chloride (**Ch**, >98%) was purchased from Alfa Aesar.

3.5.1b General NMR spectroscopy methods

Deuterated solvents were purchased from Sigma Aldrich. ^{1}H NMR performed in NaH_2PO_4/Na_2PO_4 (50 mM, pD 7.4) in D_2O was prepared using sodium phosphate monobasic and sodium phosphate dibasic in D_2O, the pD was adjusted with 1 M NaOD/DCl and determined using a pH meter.[118] All NMR spectra were recorded on a Bruker Avance Neo 500 at 298 K (^{1}H: 500 MHz, ^{13}C: 126 MHz). Spectra were processed using MestReNova by Mestrelab Research S.L. DimerDye pendant arm assignments were determined with the aid of ChemDraw Professional Predict ^{1}H NMR Shifts in d_6-DMSO.

3.5.1c General UPLC-MS, HPLC and HRMS methods

Crude DimerDye reaction mixtures were purified using an ACCQPrep HP125 HPLC equipped with a UV detector. All crude samples were filtered through a 13 mm syringe filter with a 0.45 mm PTFE membrane then injected onto a Phenomenex Luna C18, 250 mm × 22 mm, 5 µm preparative column. Compound purity was verified after purification using a Waters UPLC-MS equipped with an Acquity UPLC BEH C18 1.7 µm (21 mm × 50 mm) column, UV-Vis and QDa detector. A gradient of 90% H_2O (0.4% CH_2O_2)/10% CH_3CN (0.4% CH_2O_2) to 30% H_2O (0.4% CH_2O_2)/70% CH_3CN (0.4% CH_2O_2) over 5 min at 0.5 mL/min flow, was used for all purity traces. Accurate mass spectra of pure novel compounds were obtained by ESI using a Thermo Scientific™

Exactive™ Plus Orbitrap Ultimate 3000 LC-MS system, with 50:50 Milli-Q™ water and Optima™ Acetonitrile eluent.

3.5.1d General absorbance and fluorescence methods

Absorbance and fluorescence readings were collected on a BioTek Cytation-5. All samples for spectroscopic studies were prepared in Milli-Q™ ultrapure water. Stock solutions of individual DimerDyes were prepared by mass in NaH_2PO_4/Na_2HPO_4 (10 mM, pH 7.4) in H_2O. Experiments were plated in NUNC black-walled optical bottom 384-well plates, with 35 μL final well volumes.

3.5.2 Synthesis

Calixarene precursors were synthesized following adapted protocols reported for compounds **3.1**,[150] **3.2**,[151] **3.3**,[151] **sCx4-2CHO**,[151] **sCx5-CHO**,[152] and **sCx4-CHO**.[54] Heterocycle compounds **3.4**,[153] **3.5**,[154] and **3.6**,[155] were synthesized as previously reported. **DD4Cx4** was synthesized as previously reported.[72]

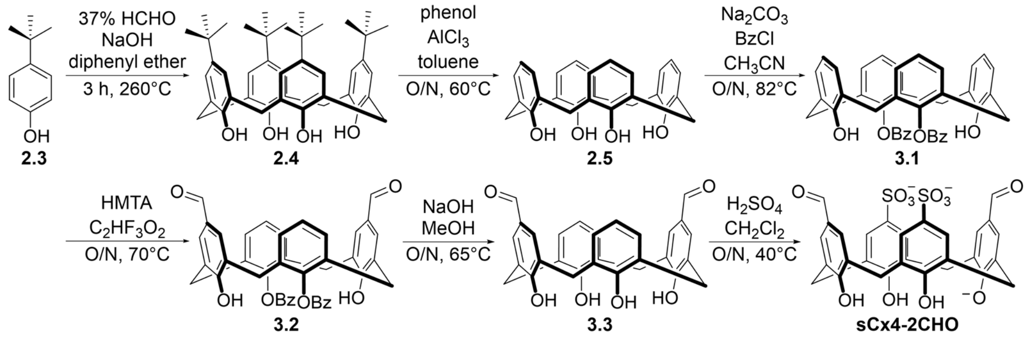

Scheme 3.1. Synthetic route of previously reported **sCx4-2CHO.**[151]

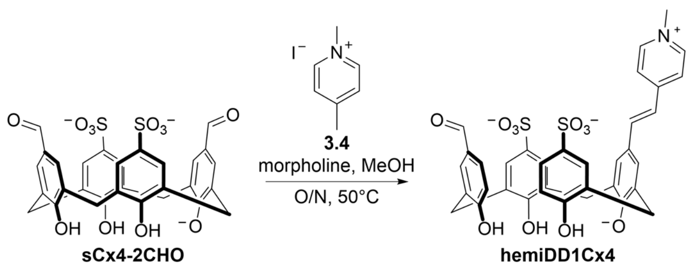

Scheme 3.2. Synthesis of novel **hemiDD1Cx4**.

hemiDD1Cx4. sCx4-2CHO (50 mg, 0.078 mmol) and morpholine (54 mL, 0.626 mmol) were dissolved in methanol (1.5 mL) and heated to 50°C. 4-methyl-1-methylpyridinium iodide (**3.4**) (18 mg, 0.078 mmol) was dissolved in methanol (0.5 mL) and added dropwise to the reaction mixture over 4 min. The reaction was heated at 50°C overnight forming a dark orange solution. The reaction mixture was cooled to room temperature and transferred to a 50 mL falcon tube. The reaction vessel was rinsed twice with ethyl acetate (~8 mL total) and transferred to the 50 mL falcon tube. Cold diethyl ether (0°C, ~30 mL) was added to the falcon tube, forming an orange suspension. The suspension was centrifuged (10 min, 5°C, 3750 rpm) into an orange pellet and the supernatant was decanted and discarded. The pellet was resuspended in cold diethyl ether (0°C, ~30 mL) with sonication; the centrifugation and decanting process was repeated. The pellet was left to air dry overnight. The pellet was dissolved in 50% DMSO/50% NaH_2PO_4/Na_2HPO_4 (50 mM, pH 7.4) in H_2O and purified by HPLC (gradient of 90% H_2O (0.1% $C_2HF_3O_2$)/10% CH_3CN (0.1% $C_2HF_3O_2$) to 45% H_2O (0.1% $C_2HF_3O_2$)/55% CH_3CN (0.1% $C_2HF_3O_2$) over 13 min). Fractions were collected then lyophilized, affording a yellow powder (16 mg, 28%). ^1H NMR (500 MHz, NaH_2PO_4/Na_2HPO_4 (50 mM, pD 7.4) in D_2O): δ (ppm) 9.49 (s, 1H), 7.82 (s, 2H), 7.79 (br s, 2H), 7.75 (br s, 2H), 7.43 (d, J = 6.5 Hz, 1H), 7.22 (s, 2H), 6.96 (d, J = 16.3 Hz, 1H), 6.55 (d, J = 16.3 Hz, 1 H), 6.47 (d, J = 6.4 Hz, 2H), 4.46 (d, J = 13.1 Hz, 2H), 4.41 (d, J = 13.2 Hz, 2H), 3.72 (d, J = 13.3 Hz, 2H), 3.58 (d, J = 13.2 Hz, 2H), 0.57 (s, 3H); ^{13}C NMR (126 MHz, 50% d_6-DMSO/50% NaH_2PO_4/Na_2HPO_4 (50 mM, pD 7.4) in D_2O): δ (ppm) 192.2, 154.8, 154.0, 153.5, 144.4, 140.9, 138.8, 131.8, 131.3, 130.9, 130.2, 129.7, 129.4, 127.9, 126.8, 123.8, 120.7, 44.5, 32.6, 31.6; HRMS (ESI): *m/z* calculated for $(C_{37}H_{29}NO_{11}S_2)_2^{4-}$ 363.55965 $[M_2\text{-}6H]^{4-}$; found 363.56038.

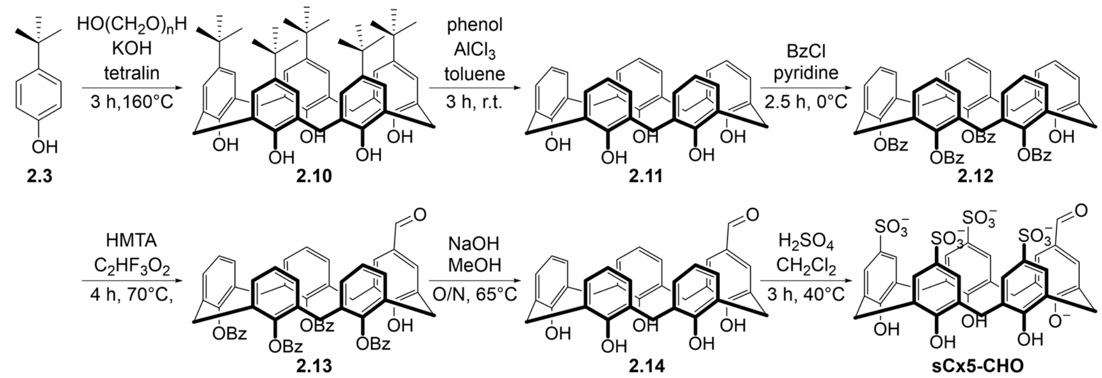

Scheme 3.3. Synthetic route of **sCx5-CHO**.[152]

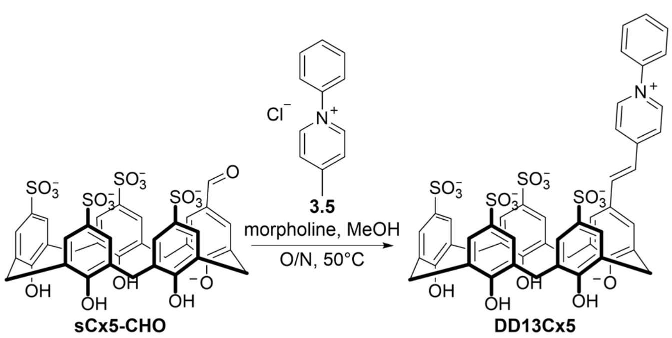

Scheme 3.4. Synthesis of novel **DD13Cx5**.

DD13Cx5. **sCx5-CHO** (50 mg, 0.057 mmol), 4-methyl-1-phenylpyridinium chloride (**3.5**) (13 mg, 0.063 mmol) and morpholine (197 mL, 2.29 mmol) were dissolved in methanol (2 mL) and heated at 50°C overnight, forming a dark orange solution. The reaction mixture was cooled to room temperature and transferred to a 50 mL falcon tube. The reaction vessel was rinsed twice with ethyl acetate (~8 mL total) and transferred to a 50 mL falcon tube. Cold diethyl ether (0°C, ~30 mL) was added to the falcon tube, forming an orange suspension. The suspension was centrifuged (10 min, 5°C, 3750 rpm) into an orange pellet and the supernatant was decanted and discarded. The pellet was resuspended in cold diethyl ether (0°C, ~30 mL) with sonication; the centrifugation and decanting process was repeated. The pellet was left to air dry overnight then dissolved in 90% H_2O (0.1% $C_2HF_3O_2$)/10% CH_3CN (0.1% $C_2HF_3O_2$) and purified by HPLC (gradient of 90% H_2O (0.1% $C_2HF_3O_2$)/10% CH_3CN (0.1% $C_2HF_3O_2$) to 60% H_2O (0.1% $C_2HF_3O_2$)/40% CH_3CN (0.1% $C_2HF_3O_2$) over 15 min). Fractions were collected then lyophilized, affording an orange powder (23 mg, 39%). ^1H NMR (500 MHz, *d*$_6$-DMSO): δ (ppm) 9.08 (d, *J* = 6.6

Hz, 2H), 8.29 (d, *J* = 6.6 Hz, 2H), 8.08 (d, *J* = 16.1 Hz, 1H), 7.85 (d, *J* = 7.5 Hz, 2H), 7.69-7.67 (m, 3H), 7.53 (s, 2H), 7.42-7.33 (m, 9H), 3.84-3.80 (m, 10H); ^{13}C NMR (126 MHz, d_6-DMSO): δ (ppm) 155.3, 154.5, 152.4, 152.0, 143.6, 143.0, 142.2, 139.3, 138.5, 130.7, 130.2, 130.0, 128.9, 127.9, 127.8, 127.6, 127.4, 127.0, 126.6, 126.5 (×3), 124.2, 123.3, 120.2, 31.7, 31.3, 31.2; HRMS (ESI): *m/z* calculated for $C_{48}H_{40}NO_{17}S_4^{1+}$ 1030.11736 $[M]^{1+}$; found 1030.11754.

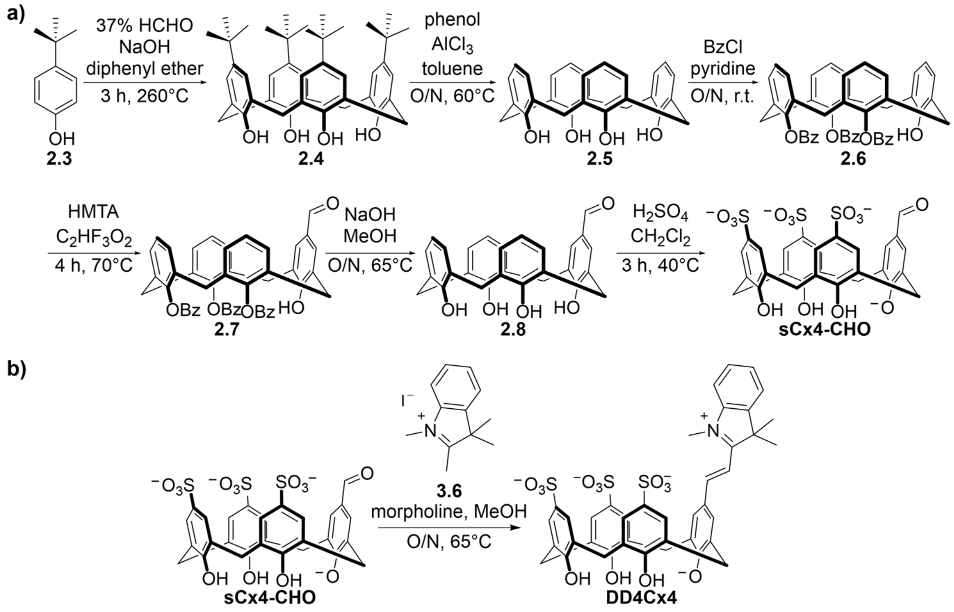

Scheme 3.5. Synthetic route of the previously reported **a) sCx4-CHO** precursor and **b) DD4Cx4**.

3.5.3 Characterization data – ^{1}H NMR, ^{13}C NMR and UPLC-MS

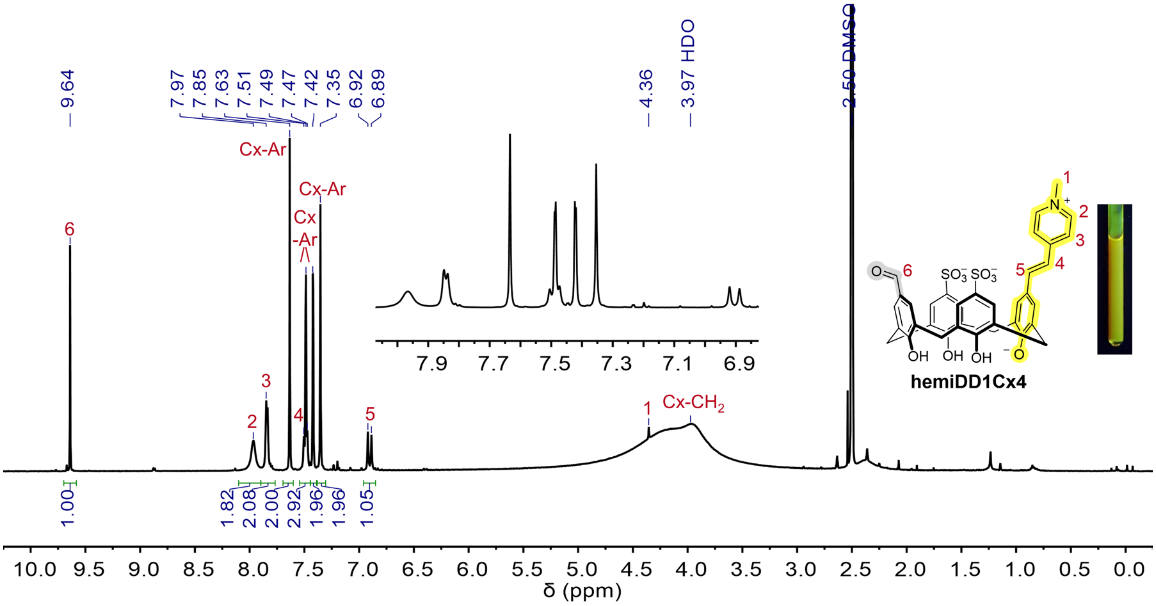

Figure 3.7. ^{1}H NMR spectrum of **hemiDD1Cx4** (5 mM) in d_6-DMSO (500 MHz, 298 K). The NMR chemical shifts and fluorescent appearance support the existence of the molecule as a monomer in DMSO. NMR tube irradiated with a hand-held UV lamp (λ_{ex} 356 ± 20 nm).

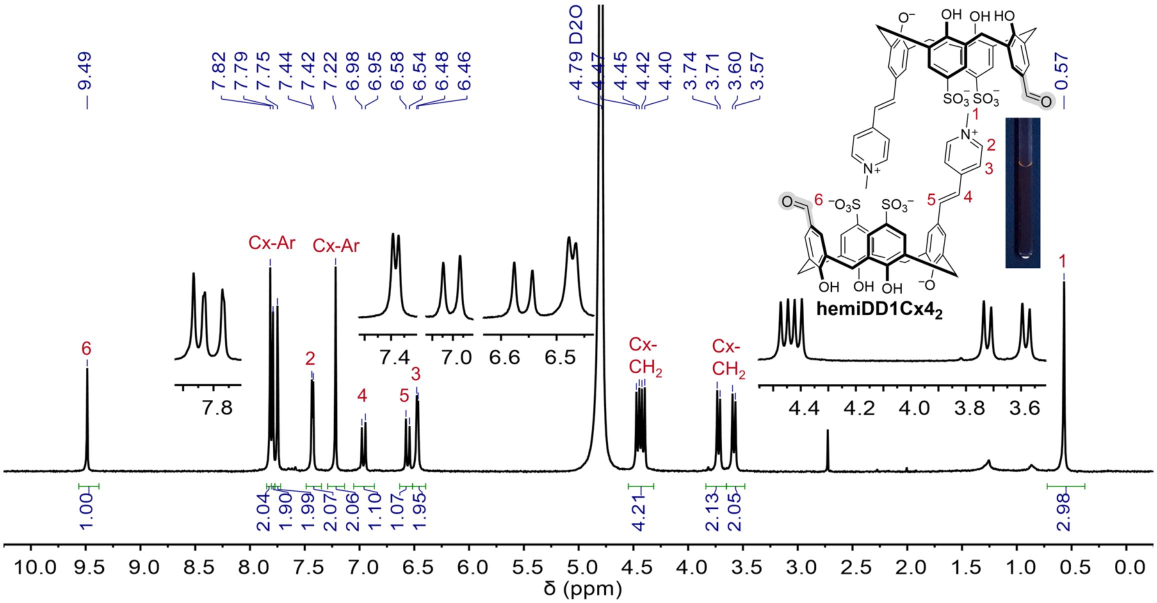

Figure 3.8. ^{1}H NMR spectrum of **hemiDD1Cx4** (5 mM) in NaH_2PO_4/Na_2HPO_4 (50 mM, pD 7.4) in D_2O (500 MHz, 298 K) shows upfield-shifted pendant arm methyl and aromatic protons. The NMR chemical shifts and non-fluorescent appearance support the existence of the molecule as a dimer (**hemiDD1Cx4$_2$**) in aqueous solution. NMR tube irradiated with a hand-held UV lamp (λ_{ex} 356 ± 20 nm).

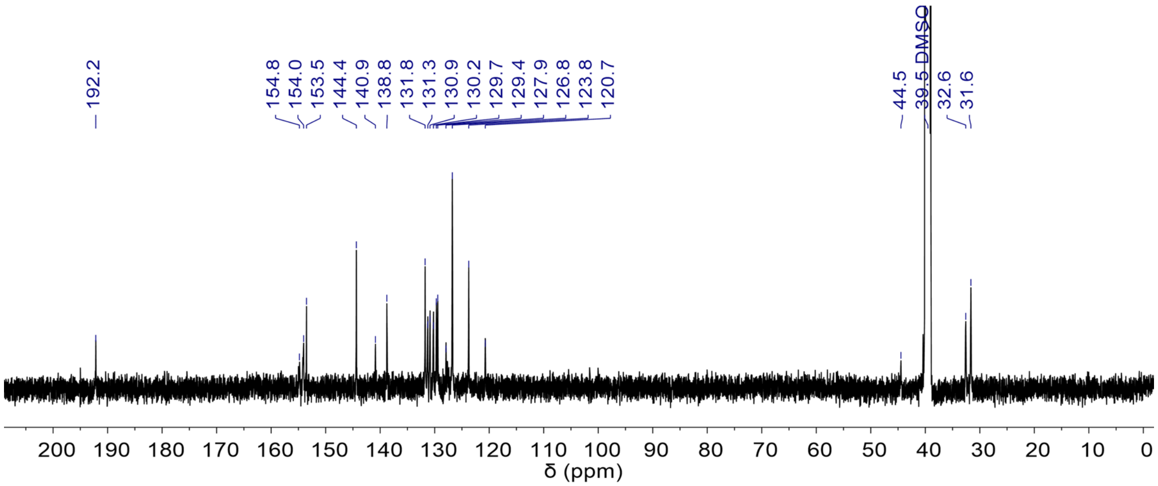

Figure 3.9. ^{13}C NMR spectrum of **hemiDD1Cx4** in 50% d_6-DMSO/50% NaH_2PO_4/Na_2HPO_4 (50 mM, pD 7.4) in D_2O (126 MHz, 298 K).

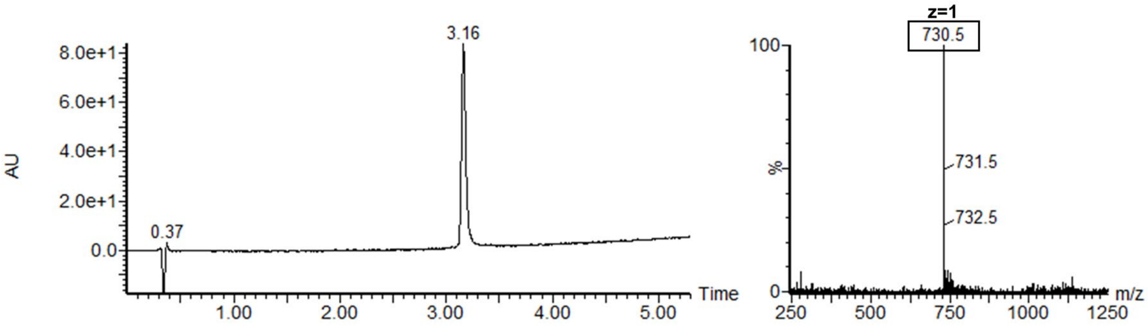

Figure 3.10. UPLC-MS (ES+) characterization of **hemiDD1Cx4**. Left = UV diode array detected chromatogram (190:400 nm). Right = positive ion mode ESI mass spectrum of the eluted peak.

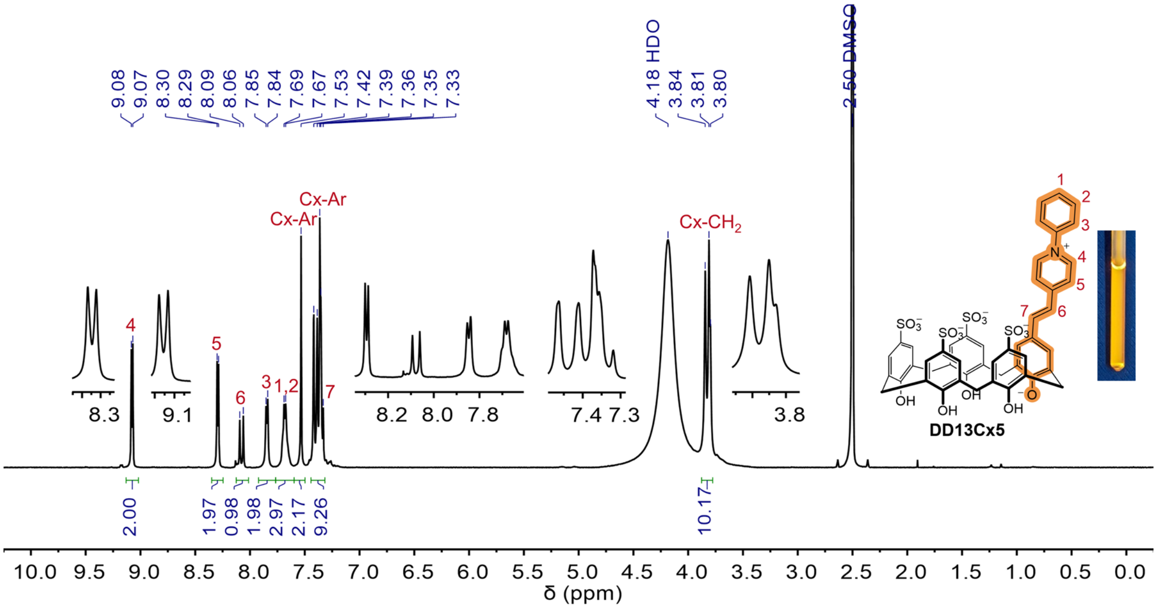

Figure 3.11. ^{1}H NMR spectrum of **DD13Cx5** (5 mM) in d_6-DMSO (500 MHz, 298 K). The NMR chemical shifts and fluorescent appearance support the existence of the molecule as a monomer in DMSO. NMR tube irradiated with a hand-held UV lamp (λ_{ex} 356 ± 20 nm).

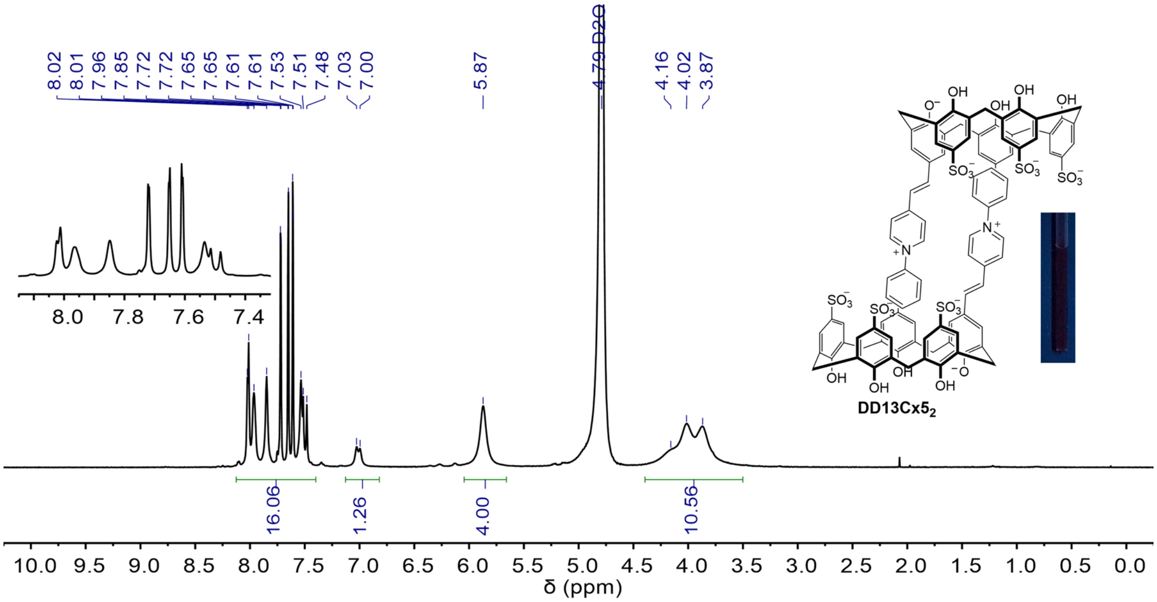

Figure 3.12. ^{1}H NMR spectrum of **DD13Cx5** (5 mM) in NaH_2PO_4/Na_2HPO_4 (50 mM, pD 7.4) in D_2O (500 MHz, 298 K) shows upfield-shifted aromatic protons. Increased conformational flexibility is observed by broadening of the methylene bridges.[156] The NMR chemical shifts and non-fluorescent appearance support the existence of the molecule as a dimer (**DD13Cx5$_2$**) in aqueous solution. Specific assignments unclear due to the large number of overlapping aromatic protons. NMR tube irradiated with a hand-held UV lamp (λ_{ex} 356 ± 20 nm).

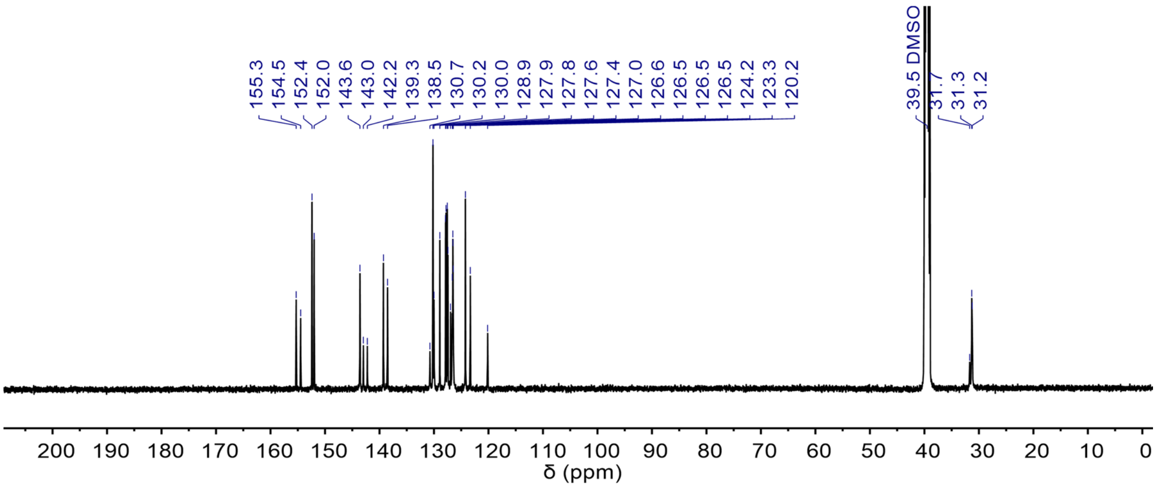

Figure 3.13. ^{13}C NMR spectrum of **DD13Cx5** in d_6-DMSO (126 MHz, 298 K).

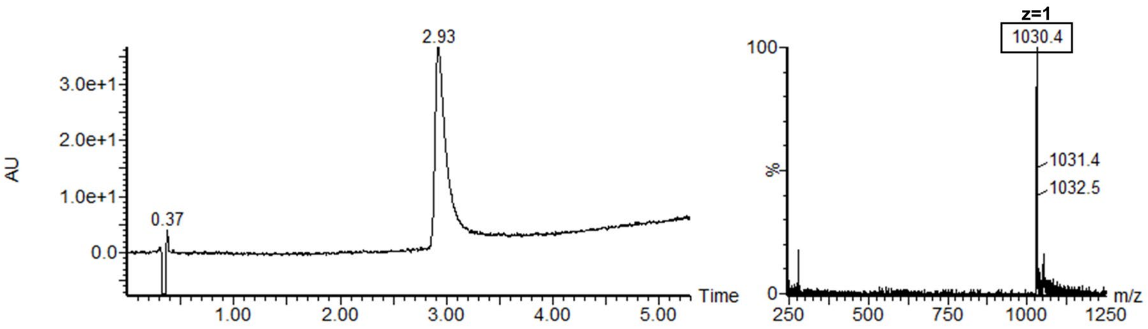

Figure 3.14. UPLC-MS (ES+) characterization of **DD13Cx5**. Left = UV diode array detected chromatogram (190:400 nm). Right = positive ion mode ESI mass spectrum of the eluted peak.

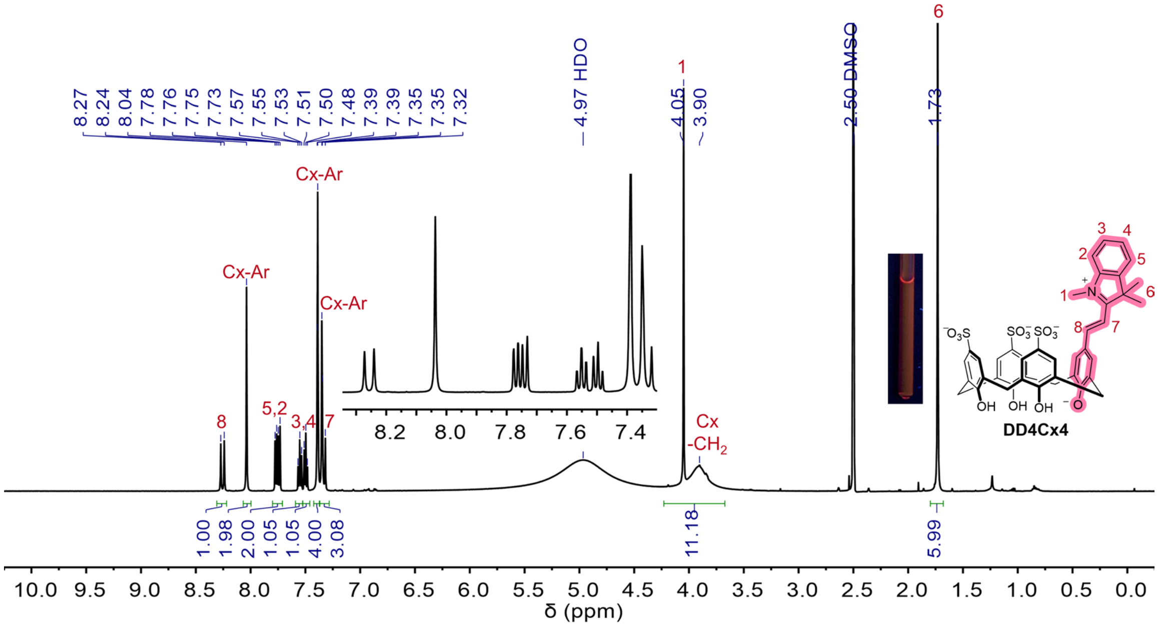

Figure 3.15. ^{1}H NMR spectrum of **DD4Cx4** (5 mM) in *d*$_6$-DMSO (500 MHz, 298 K). The NMR chemical shifts and fluorescent appearance support the existence of the molecule as a monomer in DMSO. NMR tube irradiated with a hand-held UV lamp (λ_{ex} 356 ± 20 nm).

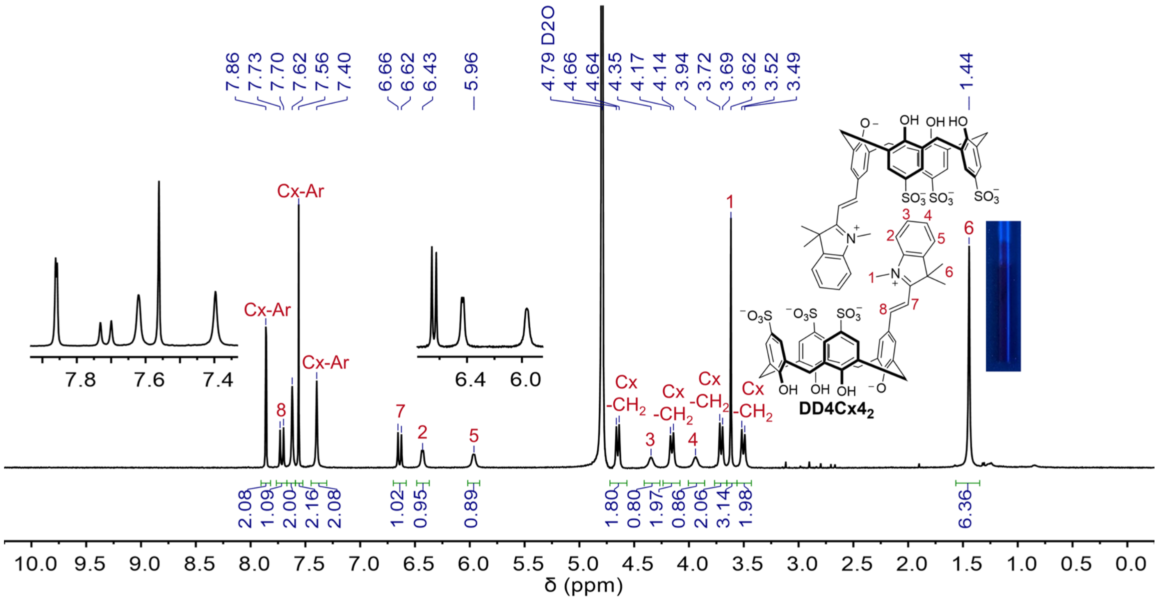

Figure 3.16. ^{1}H NMR spectrum of **DD4Cx4** (5 mM) in NaH_2PO_4/Na_2HPO_4 (50 mM, pD 7.4) in D_2O (500 MHz, 298 K) shows upfield-shifted pendant arm methyl and aromatic protons. The NMR chemical shifts and non-fluorescent appearance support the existence of the molecule as a dimer (**DD4Cx4$_2$**) in aqueous solution. NMR tube irradiated with a hand-held UV lamp (λ_{ex} 356 ± 20 nm).

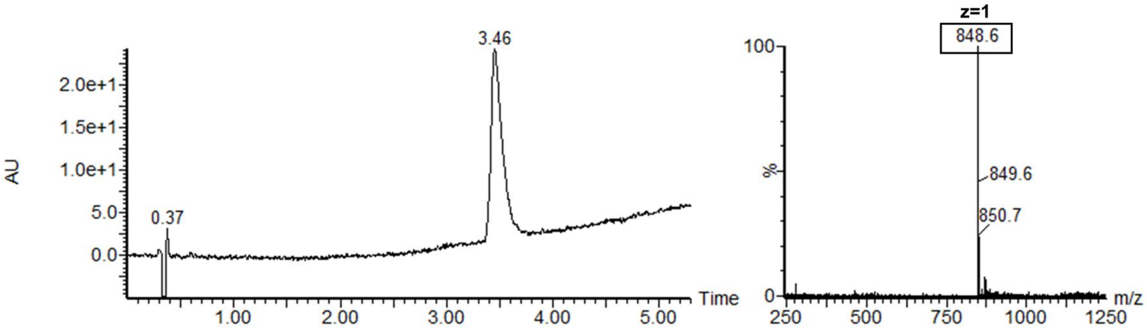

Figure 3.17. UPLC-MS (ES+) characterization of **DD4Cx4**. Left = UV diode array detected chromatogram (190:400 nm). Right = positive ion mode ESI mass spectrum of the eluted peak.

3.5.4 DDNetwork characterization – ^{1}H NMR, absorbance and fluorescence

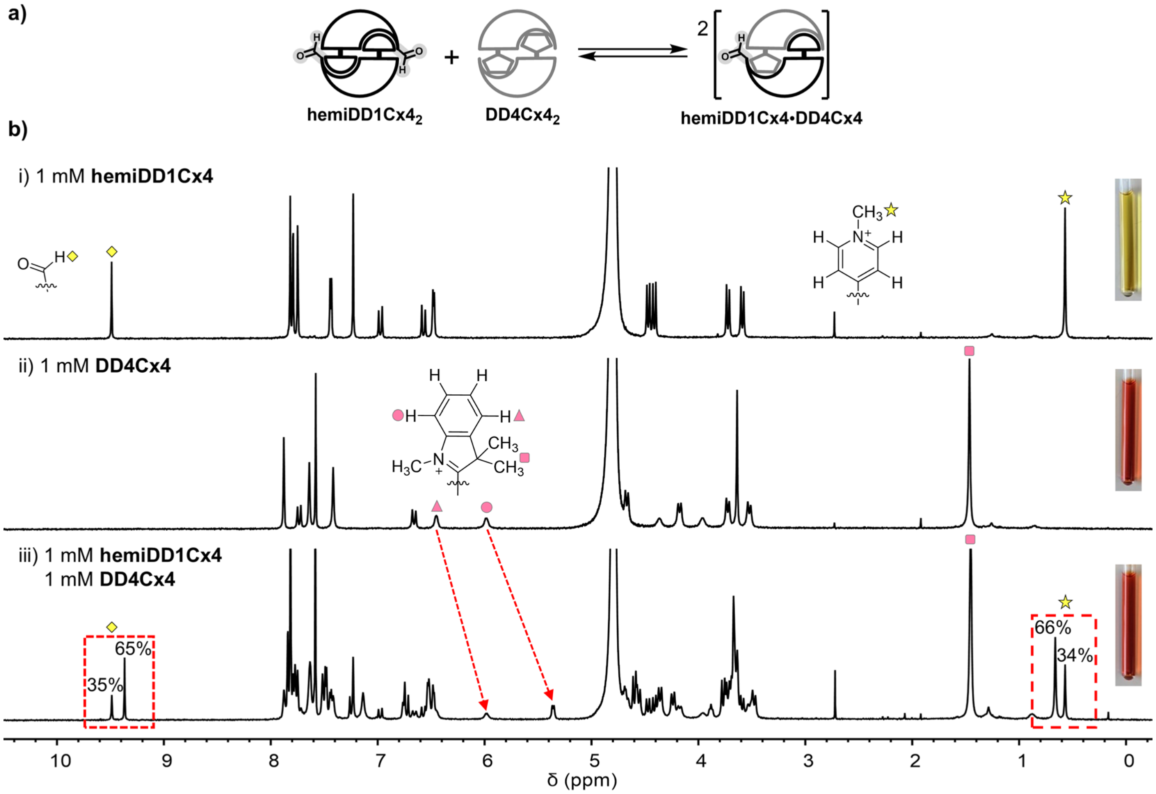

Figure 3.18. Evidence that heterodimers form when **hemiDD1Cx4** and **DD4Cx4** are combined. **a)** Schematic of heterodimer formation in equilibrium. **b)** ^{1}H NMR of i) **hemiDD1Cx4** (1 mM) in fast exchange, upfield-shifted methyl peak shows diagnostic features of dimerization, ii) **DD4Cx4** (1 mM) in fast exchange, upfield-shifted aromatic and methyl peaks show diagnostic features of dimerization, and iii) **hemiDD1Cx4** (1 mM) and **DD4Cx4** (1 mM) combined in solution show homodimers and heterodimers present in slow exchange by the aldehyde peaks and upfield-shifted methyl peaks present on **hemiDD1Cx4** (red boxes). The further upfield-shifted aromatic peaks of **DD4Cx4** in fast exchange also support the presence of heterodimers (red arrows). All samples are in NaH_2PO_4/Na_2HPO_4 (50 mM, pD 7.4) in D_2O (500 MHz, 298 K).

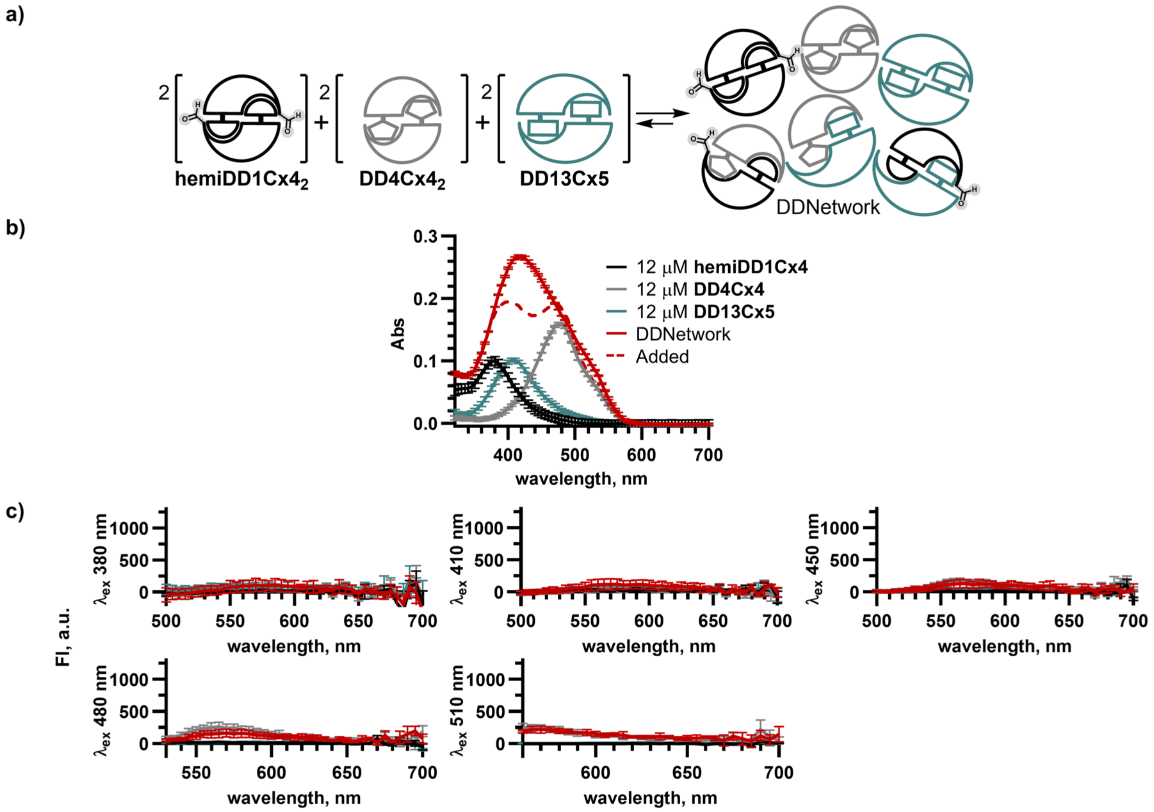

Figure 3.19. The mixing of all three hosts in solution leads to the formation of a network of non-emissive homo- and heterodimers. **a)** Schematic of DDNetwork assembling into homo- and heterodimers. **b)** The comparison of absorbance spectra for the DDNetwork (solid red line) and the mathematically added spectra (dashed red line) of the individual DimerDyes; **hemiDD1Cx4** (black line), **DD4Cx4** (grey line) and **DD13Cx5** (teal line), show that the optical properties of the DDNetwork are not equal to the sum of the individual parts. This supports the presence of a complex network containing heterodimers with absorbance properties that are different than the isolated hosts. **c)** Fluorescence spectra show the DDNetwork maintains minimal or quenched fluorescence, similar to the individual DimerDyes. Hosts in all samples are present at identical concentrations — [**hemiDD1Cx4**] = 12 µM, [**DD4Cx4**] = 12 µM and [**DD13Cx5**] = 12 µM — either mixed with each other or as separate samples as indicated. All samples are in NaH_2PO_4/Na_2HPO_4 (10 mM, pH 7.4) in H_2O. Absorbance and fluorescence spectra are plotted as the mean of experiments done in triplicate with error bars corresponding to the standard deviation.

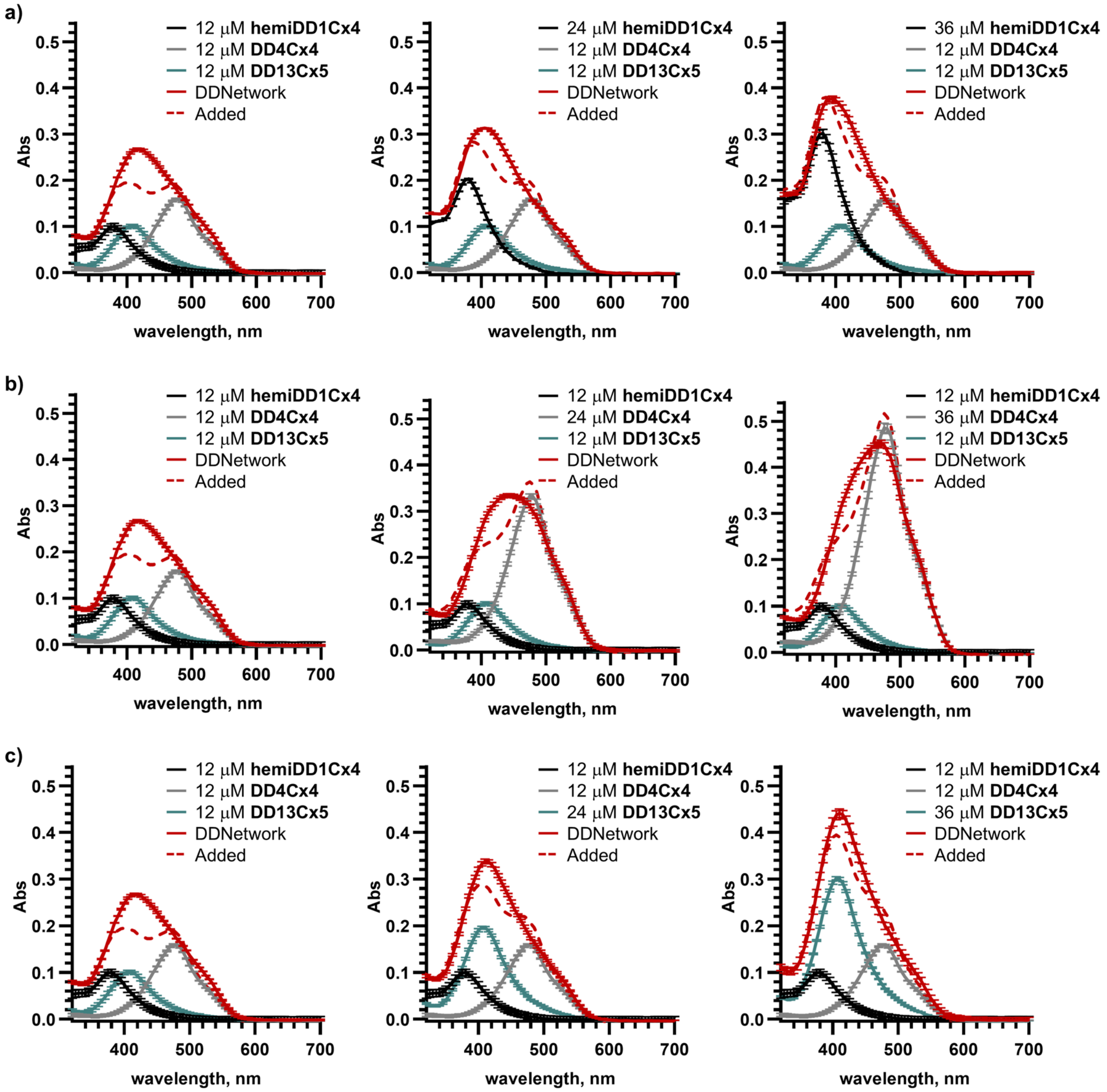

Figure 3.20. Increasing the ratio of one DimerDye shifts the network equilibrium towards more homodimers. Absorbance spectra of the DDNetwork (solid red line) compared to the mathematically added spectra (dashed red line) of the individual DimerDyes, adjusting the ratio of DimerDyes (**hemiDD1Cx4** (black line): **DD4Cx4** (grey line): **DD13Cx5** (teal line)) one at a time; **a)** 1:1:1, 2:1:1 and 3:1:1, **b)** 1:1:1, 1:2:1 and 1:3:1, **c)** 1:1:1, 1:1:2, and 1:1:3. Increasing the ratio of one DimerDye in the network shifts the absorbance profile towards that of the added spectra, demonstrating that the network equilibrium responds as expected to changing concentrations. Operating at an equal molar ratio of DimerDye sensors (1:1:1) exploits the distinctive absorbance features that arise from the interacting complex mixture. All samples are in NaH_2PO_4/Na_2HPO_4 (10 mM, pH 7.4) in H_2O. Absorbance and fluorescence spectra are plotted as the mean of experiments done in triplicate with error bars corresponding to the standard deviation.

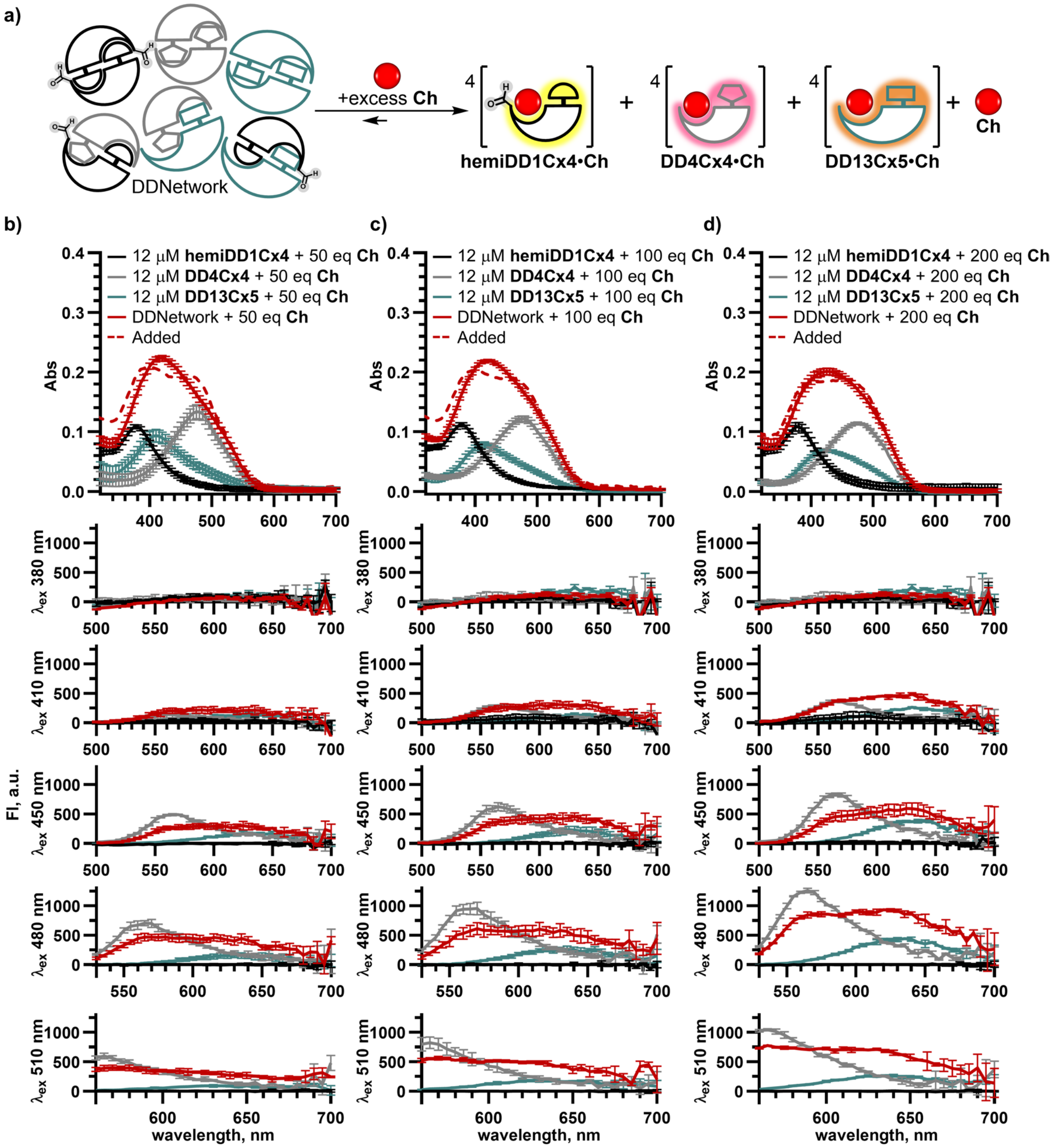

Figure 3.21. Saturating the DDNetwork with a promiscuous analyte pushes the network's equilibrium position towards host monomers with turn-on fluorescence responses. **a)** Schematic of excess **Ch** binding all DimerDye hosts and shifting the equilibrium towards all fluorescent monomers. Absorbance and fluorescence responses of the DDNetwork with the addition of **b)** 50 eq **c)** 100 eq and **d)** 200 eq **Ch**. In the presence of saturating amounts of promiscuous analyte, the absorbance spectra for DDNetwork (solid red line) and the mathematical added spectra (dashed red line) of individual DimerDyes; **hemiDD1Cx4** (black line), **DD4Cx4** (grey line) and **DD13Cx5** (teal line), closely resemble each other. This demonstrates that the network has shifted to analyte-bound monomers and away from homo- and heterodimers. The bottom panels show turn-on fluorescence responses observed in both the DDNetwork and individual host solutions, as expected for systems that are moving completely toward emissive monomers. Hosts in all samples are present at identical concentrations — [**hemiDD1Cx4**] = 12 μM, [**DD4Cx4**] = 12 μM and [**DD13Cx5**] = 12 μM — either mixed with each other or separate samples as indicated. All samples in NaH_2PO_4/Na_2HPO_4 (10 mM, pH 7.4) in H_2O. Absorbance and fluorescence spectra are plotted as the mean of experiments done in triplicate with error bars corresponding to the standard deviation.

3.5.5 Serum albumin parameters, sequence alignment and %identity

The Sigma provided UniProt accession numbers of the SA proteins were used to retrieve the FASTA sequences of each pre-proalbumin. Parameter determination was based on pre-proalbumin sequences which contain an N-terminus tail. In blood the tail is cleaved to form mature proalbumin (e.g. 24 amino acids are cleaved from the N-terminus of HSA pre-proalbumin to form the 585 amino acid proalbumin found in the blood).[157, 158]

Computational physical and chemical parameters were calculated using FASTA sequences in Expasy ProtParam: https://web.expasy.org/protparam/ (Table 3.1).[159] SA sequences were aligned using Clustal Omega Multiple Sequence Alignment: https://www.ebi.ac.uk/Tools/msa/clustalo/.[160] The % identity matrix of all pairs of SA proteins was plotted as a heat map in OriginPro 2022b along with a phylogenetic tree, using the Phylogenetic Tree App (Version: 2.10, File Name:PhylogeneticTree.opx).

Table 3.1. Expasy Prot Param computational physical and chemical parameters of SA proteins.

Protein	UniProt accession no.	#amino acids	MW (g/mol)	pI	Asp, Glu	Arg, Lys	$\varepsilon_{280\ \mathrm{nm}}$ ($M^{-1}cm^{-1}$)	Aliphatic index[a]	Grand average of hydropathy (GRAVY)[b]
HSA	P02768	609	69366.68	5.92	98	87	41435	77.57	-0.354
BSA	P02769	607	69293.41	5.82	99	86	49915	77.46	-0.429
SSA	P14639	607	69188.28	5.80	100	86	49915	77.31	-0.422
PSA	P08835	607	69692.17	6.08	97	87	52895	82.31	-0.370
RSA	P02770	608	68730.80	6.09	89	81	44415	75.95	-0.380
MSA	P07724	608	68692.51	5.75	90	76	46030	74.51	-0.381

Calculations based on UNIPROT pre-proalbumin sequences. [a]Aliphatic index is defined as the relative volume occupied by aliphatic side chains (alanine, valine, isoleucine, and leucine), a positive factor for increased protein thermostability. [b]GRAVY is defined as the sum of the hydropathy amino acid values divided by the number of residues in the sequence, where a negative value indicates non-polar and a positive value indicates polar.[159]

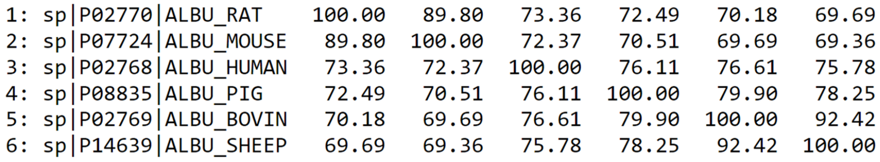

```
1: sp|P02770|ALBU_RAT    100.00   89.80   73.36   72.49   70.18   69.69
2: sp|P07724|ALBU_MOUSE   89.80  100.00   72.37   70.51   69.69   69.36
3: sp|P02768|ALBU_HUMAN   73.36   72.37  100.00   76.11   76.61   75.78
4: sp|P08835|ALBU_PIG     72.49   70.51   76.11  100.00   79.90   78.25
5: sp|P02769|ALBU_BOVIN   70.18   69.69   76.61   79.90  100.00   92.42
6: sp|P14639|ALBU_SHEEP   69.69   69.36   75.78   78.25   92.42  100.00
```

Figure 3.22. Clustal Omega percent identity matrix of SA proteins.

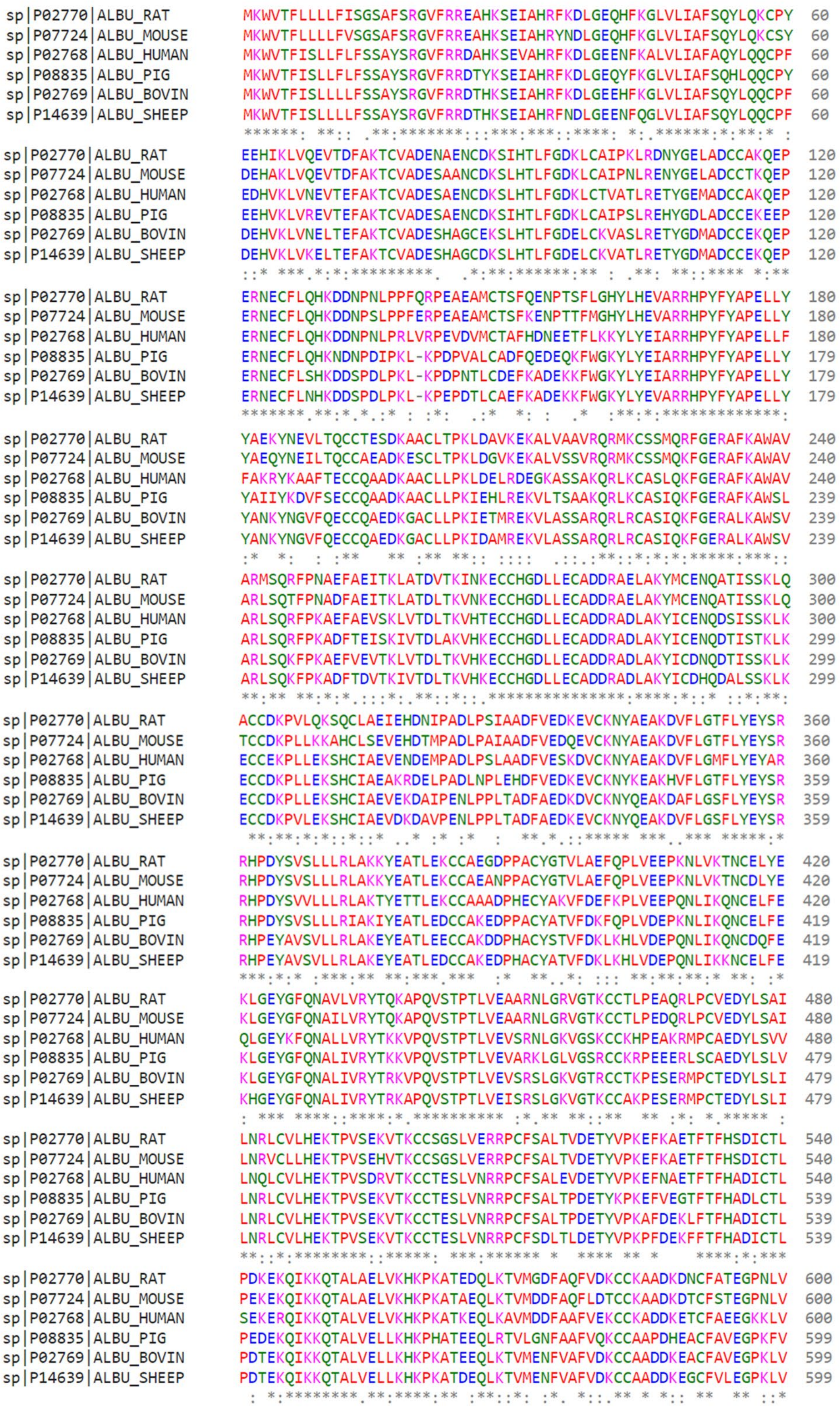

```
sp|P02770|ALBU_RAT      MKWVTFLLLLFISGSAFSRGVFRREAHKSEIAHRFKDLGEQHFKGLVLIAFSQYLQKCPY  60
sp|P07724|ALBU_MOUSE    MKWVTFLLLLFVSGSAFSRGVFRREAHKSEIAHRYNDLGEQHFKGLVLIAFSQYLQKCSY  60
sp|P02768|ALBU_HUMAN    MKWVTFISLLFLFSSAYSRGVFRRDAHKSEVAHRFKDLGEENFKALVLIAFAQYLQQCPF  60
sp|P08835|ALBU_PIG      MKWVTFISLLFLFSSAYSRGVFRRDTYKSEIAHRFKDLGEQYFKGLVLIAFSQHLQQCPY  60
sp|P02769|ALBU_BOVIN    MKWVTFISLLLLFSSAYSRGVFRRDTHKSEIAHRFKDLGEEHFKGLVLIAFSQYLQQCPF  60
sp|P14639|ALBU_SHEEP    MKWVTFISLLLLFSSAYSRGVFRRDTHKSEIAHRFNDLGEENFQGLVLIAFSQYLQQCPF  60
                        ******: **:: .**:*******:::***:***::****: *:.******:*:**:* :

sp|P02770|ALBU_RAT      EEHIKLVQEVTDFAKTCVADENAENCDKSIHTLFGDKLCAIPKLRDNYGELADCCAKQEP  120
sp|P07724|ALBU_MOUSE    DEHAKLVQEVTDFAKTCVADESAANCDKSLHTLFGDKLCAIPNLRENYGELADCCTKQEP  120
sp|P02768|ALBU_HUMAN    EDHVKLVNEVTEFAKTCVADESAENCDKSLHTLFGDKLCTVATLRETYGEMADCCAKQEP  120
sp|P08835|ALBU_PIG      EEHVKLVREVTEFAKTCVADESAENCDKSIHTLFGDKLCAIPSLREHYGDLADCCEKEEP  120
sp|P02769|ALBU_BOVIN    DEHVKLVNELTEFAKTCVADESHAGCEKSLHTLFGDELCKVASLRETYGDMADCCEKQEP  120
sp|P14639|ALBU_SHEEP    DEHVKLVKELTEFAKTCVADESHAGCDKSLHTLFGDELCKVATLRETYGDMADCCEKQEP  120
                        ::* ***.*:*:*********.  .*:**:******:** : .**: **::**** *:**

sp|P02770|ALBU_RAT      ERNECFLQHKDDNPNLPPFQRPEAEAMCTSFQENPTSFLGHYLHEVARRHPYFYAPELLY  180
sp|P07724|ALBU_MOUSE    ERNECFLQHKDDNPSLPPFERPEAEAMCTSFKENPTTFMGHYLHEVARRHPYFYAPELLY  180
sp|P02768|ALBU_HUMAN    ERNECFLQHKDDNPNLPRLVRPEVDVMCTAFHDNEETFLKKYLYEIARRHPYFYAPELLF  180
sp|P08835|ALBU_PIG      ERNECFLQHKNDNPDIPKL-KPDPVALCADFQEDEQKFWGKYLYEIARRHPYFYAPELLY  179
sp|P02769|ALBU_BOVIN    ERNECFLSHKDDSPDLPKL-KPDPNTLCDEFKADEKKFWGKYLYEIARRHPYFYAPELLY  179
sp|P14639|ALBU_SHEEP    ERNECFLNHKDDSPDLPKL-KPEPDTLCAEFKADEKKFWGKYLYEVARRHPYFYAPELLY  179
                        *******.**:*.*.:* : :*:  .:*  *: :  .*  :**:*:*************:

sp|P02770|ALBU_RAT      YAEKYNEVLTQCCTESDKAACLTPKLDAVKEKALVAAVRQRMKCSSMQRFGERAFKAWAV  240
sp|P07724|ALBU_MOUSE    YAEQYNEILTQCCAEADKESCLTPKLDGVKEKALVSSVRQRMKCSSMQKFGERAFKAWAV  240
sp|P02768|ALBU_HUMAN    FAKRYKAAFTECCQAADKAACLLPKLDELRDEGKASSAKQRLKCASLQKFGERAFKAWAV  240
sp|P08835|ALBU_PIG      YAIIYKDVFSECCQAADKAACLLPKIEHLREKVLTSAAKQRLKCASIQKFGERAFKAWSL  239
sp|P02769|ALBU_BOVIN    YANKYNGVFQECCQAEDKGACLLPKIETMREKVLASSARQRLRCASIQKFGERALKAWSV  239
sp|P14639|ALBU_SHEEP    YANKYNGVFQECCQAEDKGACLLPKIDAMREKVLASSARQRLRCASIQKFGERALKAWSV  239
                        :*  *:  : :**   ** :** **:: ::::  .::.:**::*:*:*:*****:***::

sp|P02770|ALBU_RAT      ARMSQRFPNAEFAEITKLATDVTKINKECCHGDLLECADDRAELAKYMCENQATISSKLQ  300
sp|P07724|ALBU_MOUSE    ARLSQTFPNADFAEITKLATDLTKVNKECCHGDLLECADDRAELAKYMCENQATISSKLQ  300
sp|P02768|ALBU_HUMAN    ARLSQRFPKAEFAEVSKLVTDLTKVHTECCHGDLLECADDRADLAKYICENQDSISSKLK  300
sp|P08835|ALBU_PIG      ARLSQRFPKADFTEISKIVTDLAKVHKECCHGDLLECADDRADLAKYICENQDTISTKLK  299
sp|P02769|ALBU_BOVIN    ARLSQKFPKAEFVEVTKLVTDLTKVHKECCHGDLLECADDRADLAKYICDNQDTISSKLK  299
sp|P14639|ALBU_SHEEP    ARLSQKFPKADFTDVTKIVTDLTKVHKECCHGDLLECADDRADLAKYICDHQDALSSKLK  299
                        **:** **:*:*.:::*:.**::*::.***************:****:*::* ::*:**:

sp|P02770|ALBU_RAT      ACCDKPVLQKSQCLAEIEHDNIPADLPSIAADFVEDKEVCKNYAEAKDVFLGTFLYEYSR  360
sp|P07724|ALBU_MOUSE    TCCDKPLLKKAHCLSEVEHDTMPADLPAIAADFVEDQEVCKNYAEAKDVFLGTFLYEYSR  360
sp|P02768|ALBU_HUMAN    ECCEKPLLEKSHCIAEVENDEMPADLPSLAADFVESKDVCKNYAEAKDVFLGMFLYEYAR  360
sp|P08835|ALBU_PIG      ECCDKPLLEKSHCIAEAKRDELPADLNPLEHDFVEDKEVCKNYKEAKHVFLGTFLYEYSR  359
sp|P02769|ALBU_BOVIN    ECCDKPLLEKSHCIAEVEKDAIPENLPPLTADFAEDKDVCKNYQEAKDAFLGSFLYEYSR  359
sp|P14639|ALBU_SHEEP    ECCDKPVLEKSHCIAEVDKDAVPENLPPLTADFAEDKEVCKNYQEAKDVFLGSFLYEYSR  359
                         **:**:*:*::*::* ..* :* :*  :  **.*.::***** ***..*** *****:*

sp|P02770|ALBU_RAT      RHPDYSVSLLLRLAKKYEATLEKCCAEGDPPACYGTVLAEFQPLVEEPKNLVKTNCELYE  420
sp|P07724|ALBU_MOUSE    RHPDYSVSLLLRLAKKYEATLEKCCAEANPPACYGTVLAEFQPLVEEPKNLVKTNCDLYE  420
sp|P02768|ALBU_HUMAN    RHPDYSVVLLLRLAKTYETTLEKCCAAADPHECYAKVFDEFKPLVEEPQNLIKQNCELFE  420
sp|P08835|ALBU_PIG      RHPDYSVSLLLRIAKIYEATLEDCCAKEDPPACYATVFDKFQPLVDEPKNLIKQNCELFE  419
sp|P02769|ALBU_BOVIN    RHPEYAVSVLLRLAKEYEATLEECCAKDDPHACYSTVFDKLKHLVDEPQNLIKQNCDQFE  419
sp|P14639|ALBU_SHEEP    RHPEYAVSVLLRLAKEYEATLEDCCAKEDPHACYATVFDKLKHLVDEPQNLIKKNCELFE  419
                        ***:*:* :***:** **:***.***  :*  **..*: ::: **:**:**:* **: :*

sp|P02770|ALBU_RAT      KLGEYGFQNAVLVRYTQKAPQVSTPTLVEAARNLGRVGTKCCTLPEAQRLPCVEDYLSAI  480
sp|P07724|ALBU_MOUSE    KLGEYGFQNAILVRYTQKAPQVSTPTLVEAARNLGRVGTKCCTLPEDQRLPCVEDYLSAI  480
sp|P02768|ALBU_HUMAN    QLGEYKFQNALLVRYTKKVPQVSTPTLVEVSRNLGKVGSKCCKHPEAKRMPCAEDYLSVV  480
sp|P08835|ALBU_PIG      KLGEYGFQNALIVRYTKKVPQVSTPTLVEVARKLGLVGSRCCKRPEEERLSCAEDYLSLV  479
sp|P02769|ALBU_BOVIN    KLGEYGFQNALIVRYTRKVPQVSTPTLVEVSRSLGKVGTRCCTKPESERMPCTEDYLSLI  479
sp|P14639|ALBU_SHEEP    KHGEYGFQNALIVRYTRKAPQVSTPTLVEISRSLGKVGTKCCAKPESERMPCTEDYLSLI  479
                        : *** ****::****:*.********** :*.** **::**  ** :*: *.***** :

sp|P02770|ALBU_RAT      LNRLCVLHEKTPVSEKVTKCCSGSLVERRPCFSALTVDETYVPKEFKAETFTFHSDICTL  540
sp|P07724|ALBU_MOUSE    LNRVCLLHEKTPVSEHVTKCCSGSLVERRPCFSALTVDETYVPKEFKAETFTFHSDICTL  540
sp|P02768|ALBU_HUMAN    LNQLCVLHEKTPVSDRVTKCCTESLVNRRPCFSALEVDETYVPKEFNAETFTFHADICTL  540
sp|P08835|ALBU_PIG      LNRLCVLHEKTPVSEKVTKCCTESLVNRRPCFSALTPDETYKPKEFVEGTFTFHADLCTL  539
sp|P02769|ALBU_BOVIN    LNRLCVLHEKTPVSEKVTKCCTESLVNRRPCFSALTPDETYVPKAFDEKLFTFHADICTL  539
sp|P14639|ALBU_SHEEP    LNRLCVLHEKTPVSEKVTKCCTESLVNRRPCFSDLTLDETYVPKPFDEKFFTFHADICTL  539
                        **::*:********::*****: ***:****** *  **** ** *    ****:*:***

sp|P02770|ALBU_RAT      PDKEKQIKKQTALAELVKHKPKATEDQLKTVMGDFAQFVDKCCKAADKDNCFATEGPNLV  600
sp|P07724|ALBU_MOUSE    PEKEKQIKKQTALAELVKHKPKATAEQLKTVMDDFAQFLDTCCKAADKDTCFSTEGPNLV  600
sp|P02768|ALBU_HUMAN    SEKERQIKKQTALVELVKHKPKATKEQLKAVMDDFAAFVEKCCKADDKETCFAEEGKKLV  600
sp|P08835|ALBU_PIG      PEDEKQIKKQTALVELLKHKPHATEEQLRTVLGNFAAFVQKCCAAPDHEACFAVEGPKFV  599
sp|P02769|ALBU_BOVIN    PDTEKQIKKQTALVELLKHKPKATEEQLKTVMENFVAFVDKCCAADDKEACFAVEGPKLV  599
sp|P14639|ALBU_SHEEP    PDTEKQIKKQTALVELLKHKPKATDEQLKTVMENFVAFVDKCCAADDKEGCFVLEGPKLV  599
                         : *:********.**:****:** :**::*: :*. *::.** * *:: **  ** ::*
```

Figure 3.23. Clustal Omega multiple sequence alignment of SA proteins. Red represents small and hydrophobic residues, blue represents acidic residues, magenta represent basic residues, green represents hydroxyl, sulfhydryl, amine and G residues. "*" indicates a position of a single fully conserved residue, ":" indicates conservation between groups of strongly similar properties and "." Indicates conservation between groups of weakly similar properties.

3.5.6 Titrations of hemiDD1Cx4, DD4Cx4, and DD13Cx5 with HSA

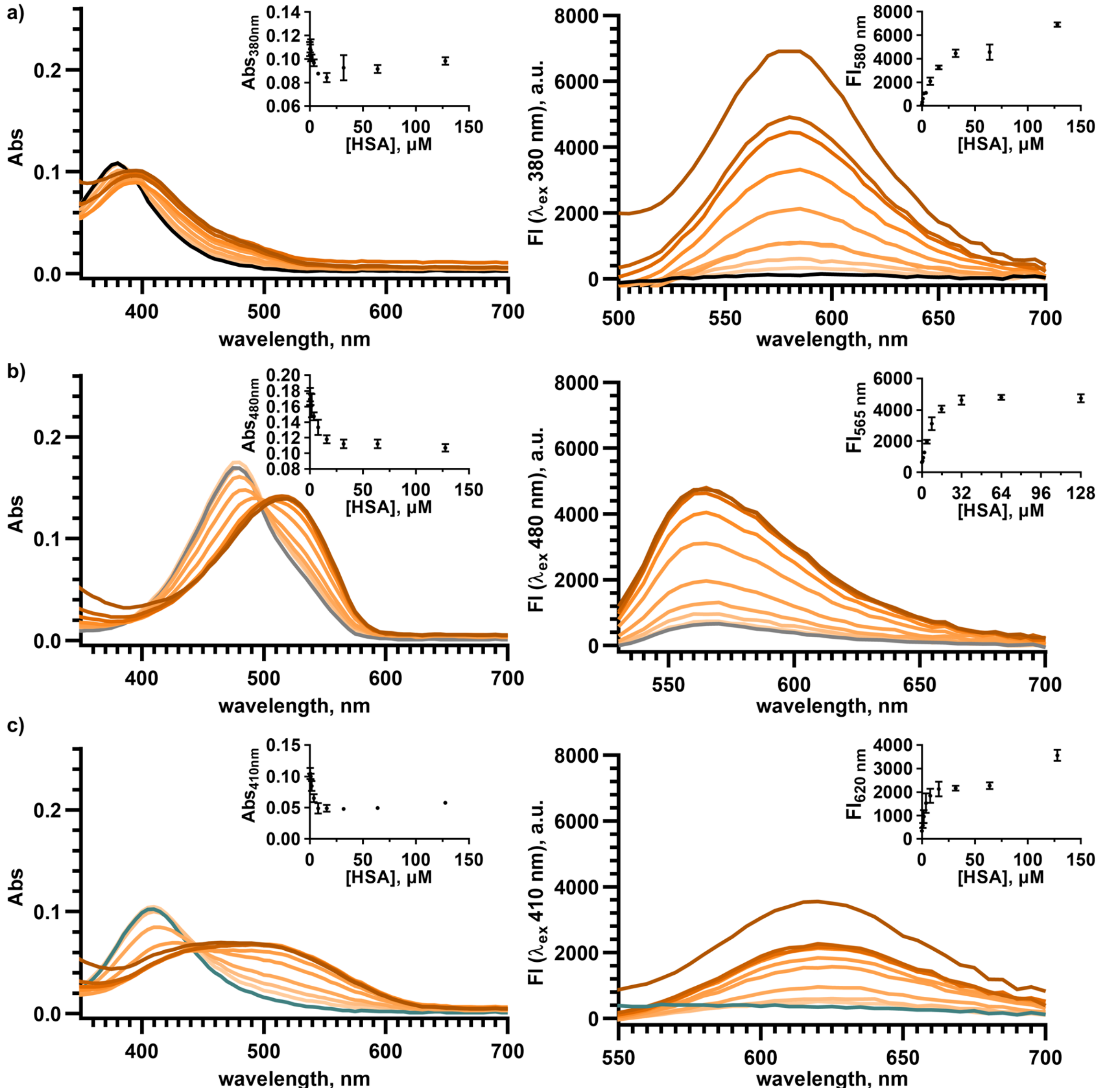

Figure 3.24. HSA titrations into individual DimerDyes shows red shifts in absorbance and turn on fluorescence responses. HSA titrations into **a) hemiDD1Cx4** (12 μM) **b) DD4Cx4** (12 μM) and **c) DD13Cx5** (12 μM) are monitored by absorbance (left spectra) and fluorescence (right spectra). The darkest orange line represents the highest concentration of HSA (128 μM) and the lightest orange line represents the lowest concentration of HSA (0.5 μM). Blank traces of the individual DimerDyes, **hemiDD1Cx4** (black line), **DD4Cx4** (grey line) and **DD13Cx5** (teal line), are shown on the respective graphs. Insets show the binding isotherms monitored at the absorbance λ_{max} and the emission λ_{max} response for each DimerDye. All solutions in NaH_2PO_4/Na_2HPO_4 (10 mM, pH 7.4) in H_2O. Absorbance and fluorescence spectra are plotted as the mean of experiments done in triplicate. Inset binding isotherms are shown with error bars corresponding to the standard deviation and are not visible in cases where the error is smaller than the depicted data point.

Limits of detection (LOD) were determined by fitting a linear regression to the initial linear region of each HSA titration curve and calculated using, $LOD = \frac{3.3\sigma}{m}$, where σ is the standard deviation of the y-intercept and m is the slope of the linear regression.[161]

Table 3.2. LOD of HSA with DimerDyes in NaH_2PO_4/Na_2HPO_4 (10 mM, pH 7.4) in H_2O.

	HSA_{abs}			HSA_{fl}		
	σ	m	LOD (μM)	σ	m	LOD (μM)
hemiDD1Cx4	0.0015	-0.0028	1.8	26.8	478	0.19
DD4Cx4	0.0029	-0.0052	1.8	54.6	313	0.58
DD13Cx5	0.0025	-0.010	0.83	77.6	300	0.85

3.5.7 Principal component analysis – absorbance and fluorescence

Full absorbance spectral scans, and fluorescence emission spectral scans were taken to cover binding-induced changes in shape, λ_{max}, and intensity arising from complex supramolecular and photophysical processes. Excitation wavelengths at the maxima of each isolated DimerDye (**hemiDD1Cx4** λ_{ex} = 380 nm, **DD4Cx4** λ_{ex} = 480 nm, **DD13Cx5** λ_{ex} = 410 nm) were selected. To cover the shifting absorbance properties of the network mixture, excitation wavelengths between (λ_{ex} = 450 nm) and above (λ_{ex} = 510 nm) the DimerDye regions were selected. Collected raw data was preprocessed by subtracting a buffer blank from absorbance and fluorescence readings. Absorbance and fluorescence wavelengths that provided discrimination of protein samples were selected for PCA, while aiming to use a minimal number of observations. PCA analysis was done using a covariance matrix in cases where only absorbance or only fluorescence measurements were used. In cases where absorbance and fluorescence measurements were combined, a correlation matrix was used. PCA scores plots with confidence ellipses (95%) and loading vectors were plotted on sample sets of 8 replicates using OriginPro 2022b Principal Component Analysis App (Version: 1.50, File Name: PCAC.opx).

3.5.7a Identifying serum albumin proteins

All SA stock solutions were prepared from solid in NaH_2PO_4/Na_2HPO_4 (10 mM, pH 7.4) in H_2O. Protein stock concentrations were determined by a Take3 Microarray Nanodrop (Biotek) using the molar extinction coefficient at 280 nm and the molecular weight (Table 3.1). Stock solutions of individual DimerDyes were prepared by mass in NaH_2PO_4/Na_2HPO_4 (10 mM, pH 7.4) in H_2O. Discriminant analysis experiments were plated in NUNC black-walled optical bottom 384-well plates, with 35 μL final well volumes. Final solutions contained DDNetwork ([**hemiDD1Cx4**] = 12 μM, [**DD4Cx4**] = 12 μM and [**DD13Cx5**] = 12 μM), and SA (32 μM) in NaH_2PO_4/Na_2HPO_4 (10 mM, pH 7.4) in H_2O. Each individual DimerDye was tested at identical concentrations and conditions. A blank of each SA alone (HSA, BSA, MSA, RSA, PSA, SSA) was measured to ensure no signal overlap in the DimerDye regions. A second set of absorbance spectral scans were taken after the experiment was completed and compared to the absorbance spectral scans from the start of the experiment. This was done to ensure that the system maintained a steady equilibrium throughout the course of the experimental measurements. The absorbance integral of each SA sensing sample relative to the respective isolated DimerDye varied with no particular trend (2% to 30% variation), indicating possible changes in the ground state upon DimerDye complexation with SA proteins.

Table 3.3. Absorbance wavelengths used in PCA analysis of SA proteins.

λ_{abs} (nm)
440
495
515

Table 3.4. Fluorescence excitation and emission wavelengths used in PCA analysis of SA proteins.

λ_{ex} (nm)	λ_{em} (nm)
380	580
410	580
410	620
450	625
480	565
510	580

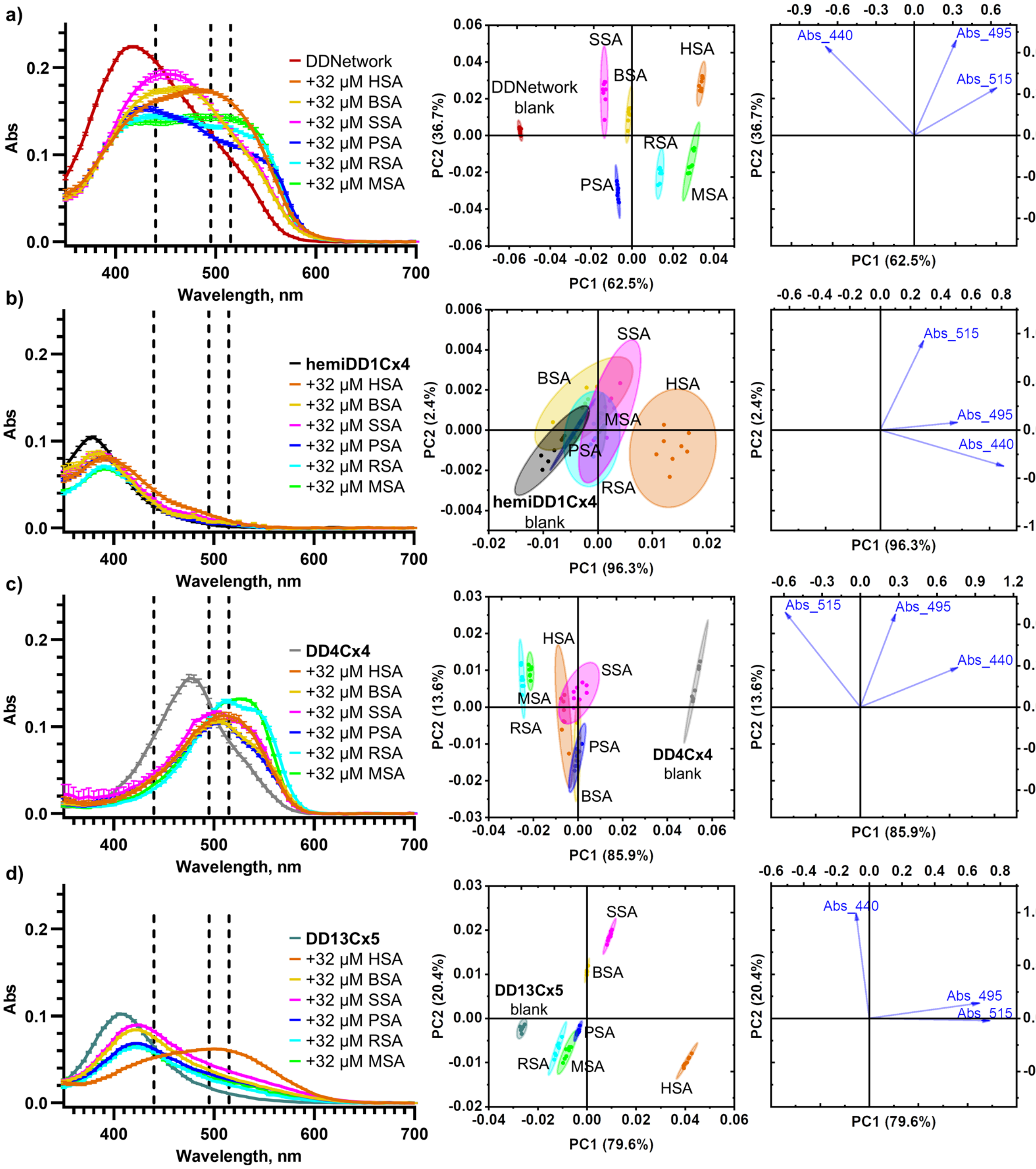

Figure 3.25. Absorbance responses of the DDNetwork completely discriminate highly similar SA proteins, whereas absorbance responses from the individual DimerDyes do not. **a)** PCA analysis of DDNetwork shows complete discrimination of SA proteins and the network, with no overlapping confidence ellipses. PCA analysis of isolated **b) hemiDD1Cx4**, **c) DD4Cx4** and **d) DD13Cx5** do not achieve complete discrimination, displaying overlapping confidence ellipses. Absorbance wavelengths used in all PCA analyses are shown as black dashed lines in absorbance spectra (440, 495 and 515 nm). PCA (covariance) scores plots show each sample set (n = 8) enclosed by 95% confidence ellipses with the respective loading plots shown as blue arrows. DimerDyes in all samples are present at identical concentrations — [**hemiDD1Cx4**] = 12 µM, [**DD4Cx4**] = 12 µM and [**DD13Cx5**] = 12 µM — either mixed with each other or separate as indicated, [SA] = 32 µM. All samples are in NaH_2PO_4/Na_2HPO_4 (10 mM, pH 7.4) in H_2O.

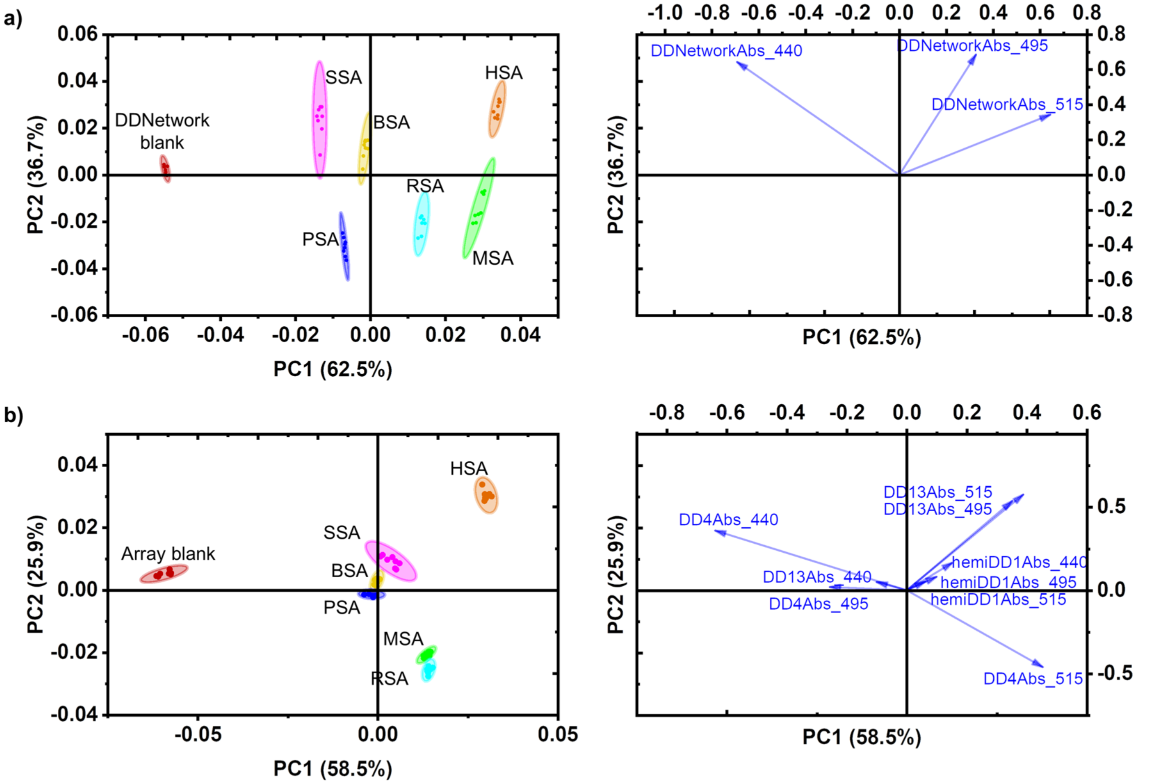

Figure 3.26. Absorbance PCA analysis shows the DDNetwork provides better discrimination than the sensor array. **a)** Three absorbance responses from the DDNetwork completely discriminate all SA proteins and the network, with no overlapping confidence ellipses. **b)** Nine compiled absorbance responses from **hemiDD1Cx4**, **DD4Cx4** and **DD13Cx5** in a sensor array do not achieve complete discrimination, with overlapping confidence ellipses of highly similar SA proteins. PCA analysis was done using absorbance responses at 440, 495 and 515 nm. PCA (covariance) scores plots show each sample set (n = 8) enclosed by 95% confidence ellipses with the respective loading plots shown as blue arrows. DimerDyes in all samples are present at identical concentrations — [**hemiDD1Cx4**] = 12 µM, [**DD4Cx4**] = 12 µM and [**DD13Cx5**] = 12 µM — either mixed with each other or separate as indicated, [SA] = 32 µM. All samples are in NaH_2PO_4/Na_2HPO_4 (10 mM, pH 7.4) in H_2O.

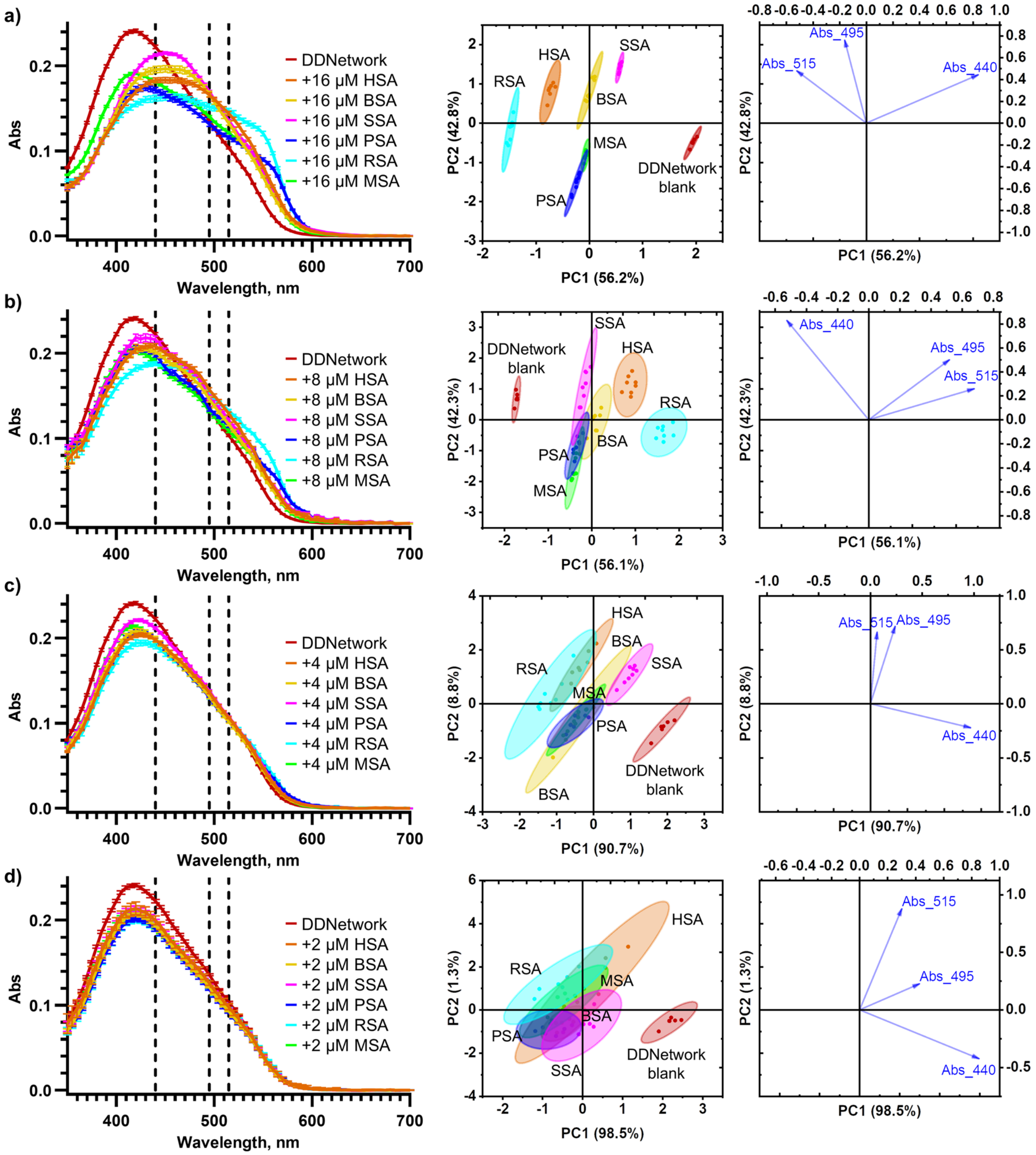

Figure 3.27. Absorbance responses of the DDNetwork to SA protein concentrations of **a)** 16 µM **b)** 8 µM **c)** 4 µM and **d)** 2 µM. Absorbance wavelengths used in PCA analysis are shown as black dashed lines in absorbance spectra (440, 495 and 515 nm). PCA (covariance) scores plots show each sample set (n = 8) enclosed by 95% confidence ellipses with the respective loading plots shown as blue arrows. Samples contain DDNetwork ([**hemiDD1Cx4**] = 12 µM, [**DD4Cx4**] = 12 µM and [**DD13Cx5**] = 12 µM) with [SA] = 16, 8, 4 and 2 µM. All samples are in NaH_2PO_4/Na_2HPO_4 (10 mM, pH 7.4) in H_2O.

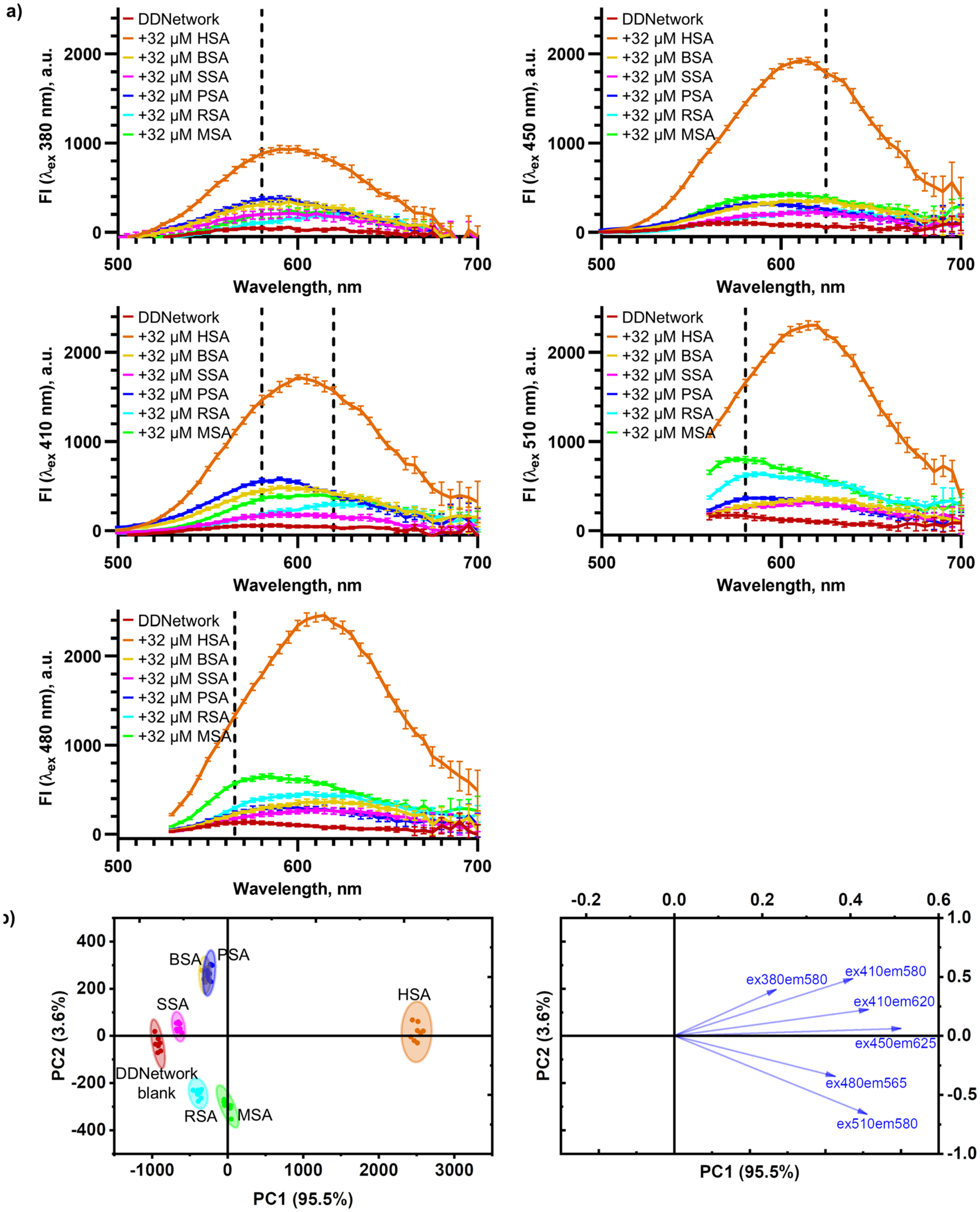

Figure 3.28. Fluorescence responses and PCA analysis of the DDNetwork. **a)** Fluorescence spectral scans of the DDNetwork. Fluorescence observations used in PCA analysis are shown as black dashed lines (λ_{em} = 580 nm (λ_{ex} = 380 nm), λ_{em} = 580 nm (λ_{ex} = 410 nm), λ_{em} = 620 nm (λ_{ex} = 410 nm), λ_{em} = 625 nm (λ_{ex} = 450 nm), λ_{em} = 565 nm (λ_{ex} = 480 nm) and λ_{em} = 580 nm (λ_{ex} = 510 nm)). **b)** PCA analysis does not achieve complete discrimination. PCA (covariance) scores plot shows each sample set (n = 8) enclosed by 95% confidence ellipses with the respective loading plot shown as blue arrows. Samples contain DDNetwork ([**hemiDD1Cx4**] = 12 μM, [**DD4Cx4**] = 12 μM and [**DD13Cx5**] = 12 μM) with [SA] = 32 μM. All samples are in NaH_2PO_4/Na_2HPO_4 (10 mM, pH 7.4) in H_2O.

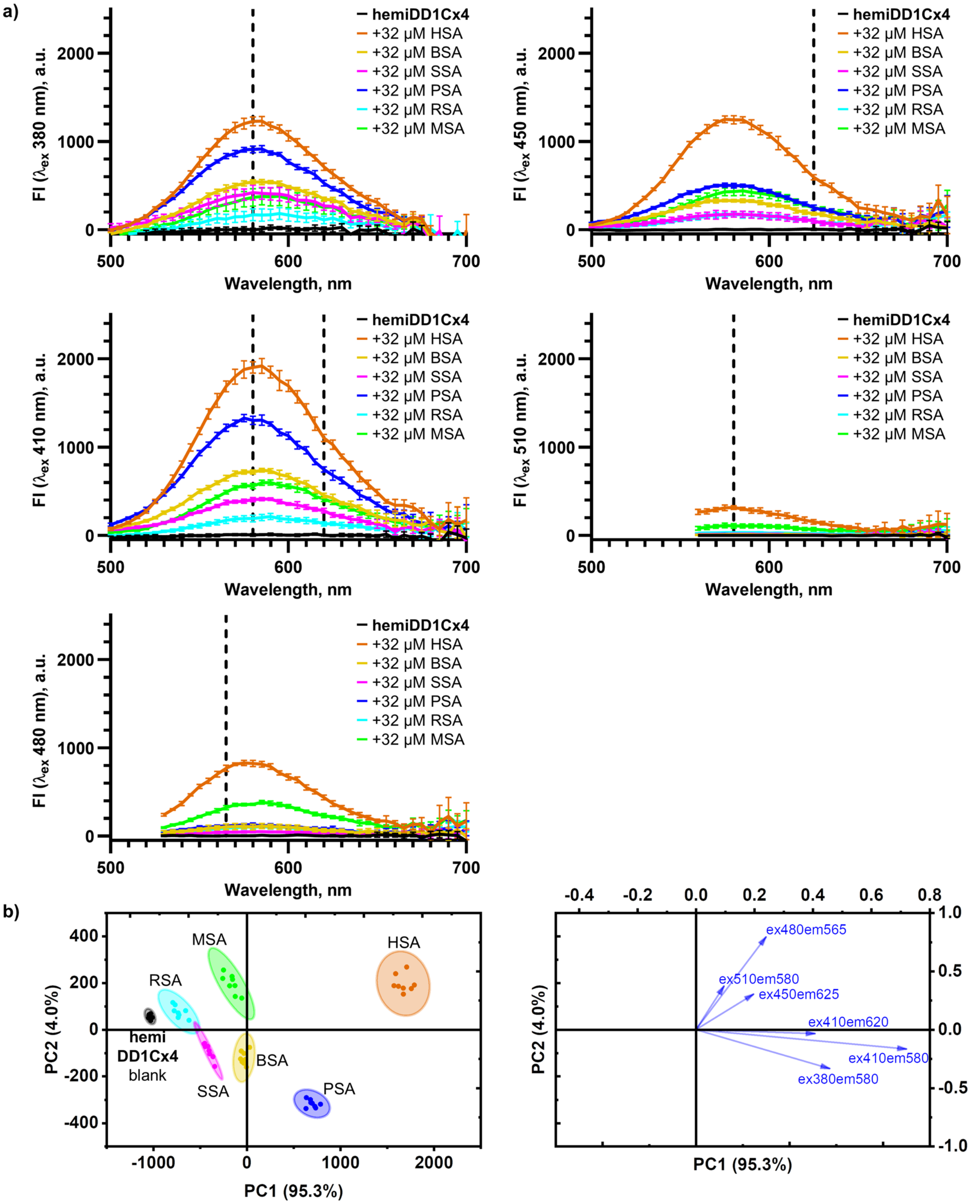

Figure 3.29. Fluorescence responses and PCA analysis of **hemiDD1Cx4**. **a)** Fluorescence spectral scans of **hemiDD1Cx4**. Fluorescence observations used in PCA analysis are shown as black dashed lines (λ_{em} = 580 nm (λ_{ex} = 380 nm), λ_{em} = 580 nm (λ_{ex} = 410 nm), λ_{em} = 620 nm (λ_{ex} = 410 nm), λ_{em} = 625 nm (λ_{ex} = 450 nm), λ_{em} = 565 nm (λ_{ex} = 480 nm) and λ_{em} = 580 nm (λ_{ex} = 510 nm)). **b)** PCA analysis does not achieve complete discrimination. PCA (covariance) scores plot shows each sample set (n = 8) enclosed by 95% confidence ellipses with the respective loading plot shown as blue arrows. Samples contain [**hemiDD1Cx4**] = 12 μM with [SA] = 32 μM. All samples are in NaH_2PO_4/Na_2HPO_4 (10 mM, pH 7.4) in H_2O.

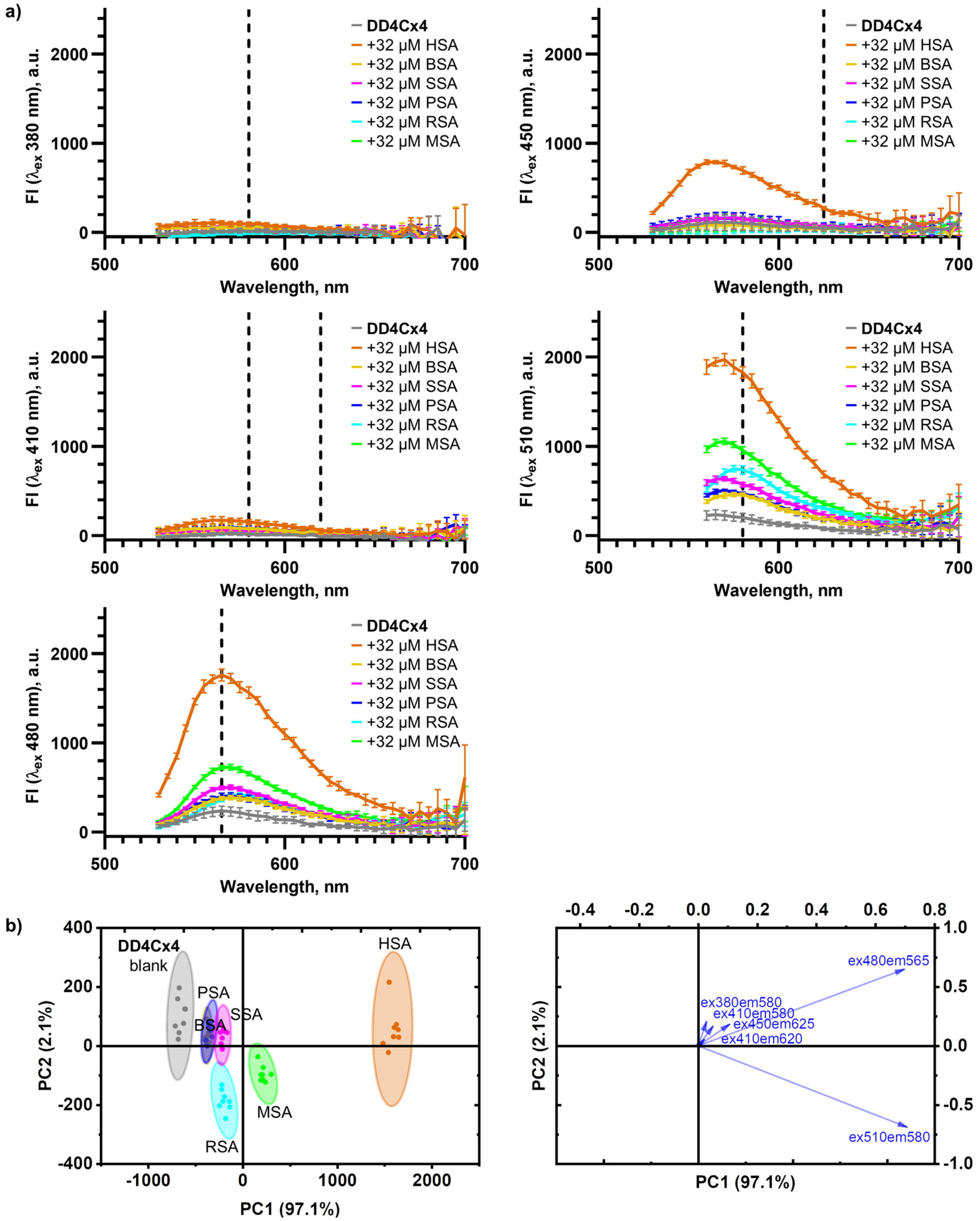

Figure 3.30. Fluorescence responses and PCA analysis of **DD4Cx4**. **a)** Fluorescence spectral scans of **DD4Cx4**. Fluorescence observations used in PCA are shown as black dashed lines (λ_{em} = 580 nm (λ_{ex} = 380 nm), λ_{em} = 580 nm (λ_{ex} = 410 nm), λ_{em} = 620 nm (λ_{ex} = 410 nm), λ_{em} = 625 nm (λ_{ex} = 450 nm), λ_{em} = 565 nm (λ_{ex} = 480 nm) and λ_{em} = 580 nm (λ_{ex} = 510 nm)). **b)** PCA analysis does not achieve complete discrimination. PCA (covariance) scores plot shows each sample set (n = 8) enclosed by 95% confidence ellipses with the respective loading plot shown as blue arrows. Samples contain [**DD4Cx4**] = 12 µM with [SA] = 32 µM. All samples are in NaH_2PO_4/Na_2HPO_4 (10 mM, pH 7.4) in H_2O.

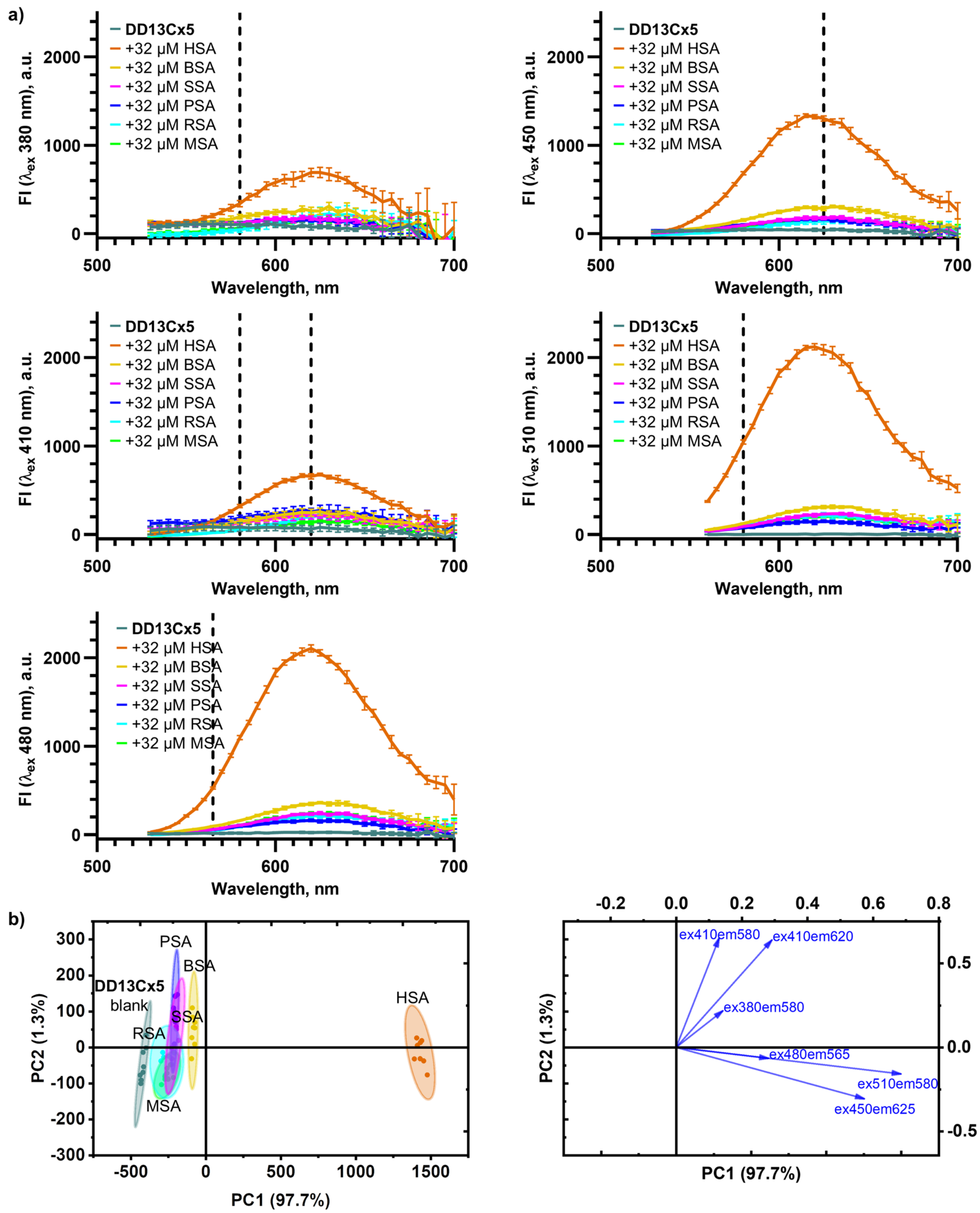

Figure 3.31. Fluorescence responses and PCA analysis of **DD13Cx5**. **a)** Fluorescence spectral scans of **DD13Cx5**. Fluorescence observations used in PCA analysis are shown as black dashed lines (λ_{em} = 580 nm (λ_{ex} = 380 nm), λ_{em} = 580 nm (λ_{ex} = 410 nm), λ_{em} = 620 nm (λ_{ex} = 410 nm), λ_{em} = 625 nm (λ_{ex} = 450 nm), λ_{em} = 565 nm (λ_{ex} = 480 nm) and λ_{em} = 580 nm (λ_{ex} = 510 nm)). **b)** PCA analysis does not achieve complete discrimination. PCA (covariance) scores plot shows each sample set (n = 8) enclosed by 95% confidence ellipses with the respective loading plot shown as blue arrows. Samples contain [**DD13Cx5**] = 12 µM with [SA] = 32 µM. All samples are in NaH_2PO_4/Na_2HPO_4 (10 mM, pH 7.4) in H_2O.

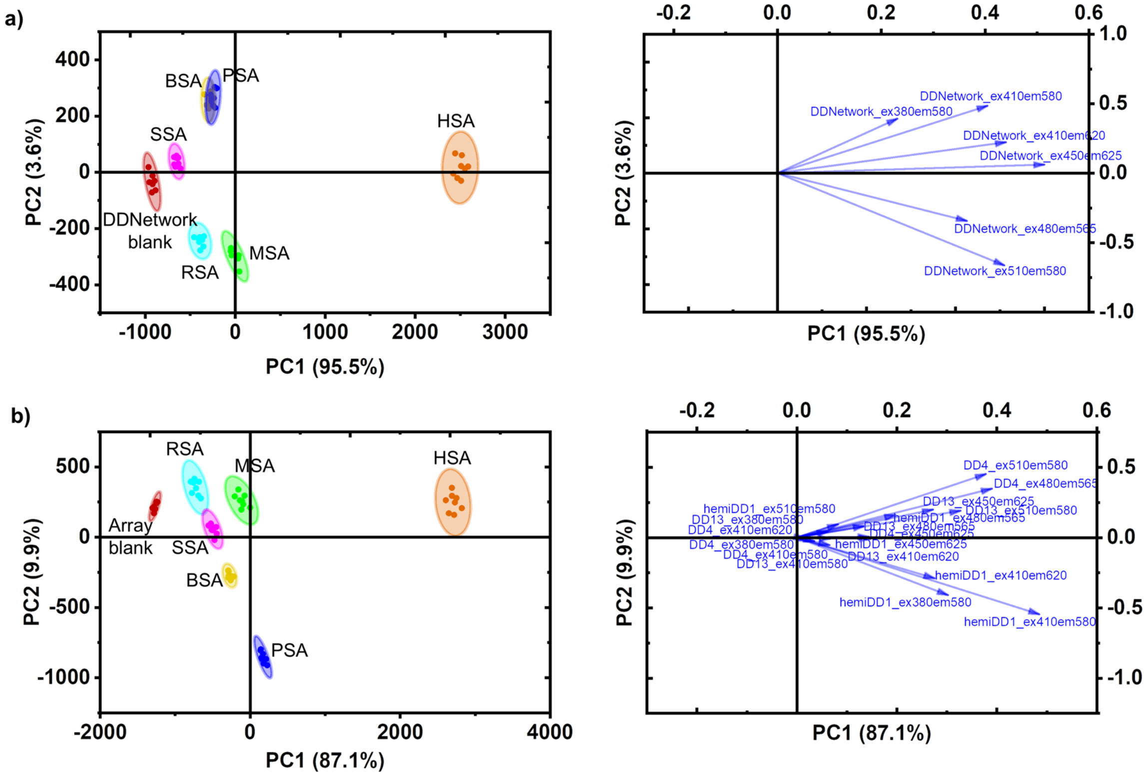

Figure 3.32. Fluorescence PCA analysis of the DDNetwork compared to the sensor array. **a)** Six fluorescence responses from the DDNetwork do not achieve complete discrimination, with two overlapping SA protein confidence ellipses. **b)** Eighteen compiled fluorescence responses from **hemiDD1Cx4**, **DD4Cx** and **DD13Cx5** in a sensor array do not achieve complete discrimination, with two SA confidence ellipses overlapping. PCA analysis was done using fluorescence responses at λ_{em} = 580 nm (λ_{ex} = 380 nm), λ_{em} = 580 nm (λ_{ex} = 410 nm), λ_{em} = 620 nm (λ_{ex} = 410 nm), λ_{em} = 625 nm (λ_{ex} = 450 nm), λ_{em} = 565 nm (λ_{ex} = 480 nm) and λ_{em} = 580 nm (λ_{ex} = 510 nm). PCA (covariance) scores plots show each sample set (n = 8) enclosed by 95% confidence ellipses with the respective loading plots shown as blue arrows. DimerDyes in all samples are present at identical concentrations — [**hemiDD1Cx4**] = 12 μM, [**DD4Cx4**] = 12 μM and [**DD13Cx5**] = 12 μM — either mixed with each other or separate as indicated, [SA] = 32 μM. All samples are in NaH_2PO_4/Na_2HPO_4 (10 mM, pH 7.4) in H_2O.

3.5.7b Identifying fish varieties from tissue protein extracts

Fresh fish tissue samples of Ocean Wise Icelandic Cod, Ocean Wise Halibut, Pacific Rockfish and Pacific Sole were purchased from a local grocery store and processed the same day. Fish tissue sample (150 mg) and Thermo Scientific T-PER^{TM} Tissue-Protein Extraction Reagent (1.5 mL) were added to Qiagen PowerBead lysis tubes containing 1.4 mm ceramic beads. Fish tissue samples were homogenized using a PowerLyzer 24$^{®}$ Homogenizer at 3,500 speed, 2 cycles of 45 s each, with a 30 s pause. Homogenized fish tissue samples were transferred to epis (1.5 mL) and centrifuged (10 min, 5°C, 14,000 × g) to pellet out cell debris. The soluble protein supernatant was collected and pooled into Amicon® Ultra centrifugal filters (10 kDa molecular weight cut-off). Protein samples were concentrated by centrifugation (10 min, 5°C, 14,000 × g), then reconstituted in NaH_2PO_4/Na_2HPO_4 (10 mM, pH 7.4) in H_2O. The centrifugation and reconstitution process was repeated three times to exchange protein buffer conditions to NaH_2PO_4/Na_2HPO_4 (10 mM, pH 7.4) in H_2O. The supernatants were transferred to epis and centrifuged (10 min, 5°C, 14,000 × g) to ensure only soluble proteins remained. Fish tissue protein extract concentration (mg/mL) was determined using a Take3 Microarray Nanodrop (Biotek).

Sodium dodecyl sulfate polyacrylamide gel electrophoresis (SDS-PAGE) was run to verify the presence of a mixture of proteins from the extracted fish tissue samples. Protein extract samples (0.5 µg/µL) were prepared in 2× loading buffer (4% SDS, 20% glycerol, 200 mM dithiothreitol, 0.01% bromophenol blue, 0.1 M Tris pH 6.8). Samples were boiled (100°C, 5 min) and loaded (20 µL) into a SDS-PAGE gel (1 mm thick) containing 15% acrylamide, along with a molecular weight standard broad range ladder. The gel was run at 196 V, then stained using R-250 Coomassie Blue stain.

Discriminant analysis experiments were plated in NUNC black-walled optical bottom 384-well plates, with 35 µL final well volumes. Final solutions contained DDNetwork ([**hemiDD1Cx4**] = 12 µM, [**DD4Cx4**] = 12 µM and [**DD13Cx5**] = 12 µM), and fish protein extract (1 mg/mL) in NaH_2PO_4/Na_2HPO_4 (10 mM, pH 7.4) in H_2O. A blank of the fish protein extracts alone were measured to ensure no signal overlap in the DimerDye regions.

Table 3.5. Absorbance wavelength used in PCA analysis of fish tissue protein extracts.

λ_{abs} (nm)
415

Table 3.6. Fluorescence excitation and emission wavelengths used in PCA analysis of fish tissue protein extract.

λ_{ex} (nm)	λ_{em} (nm)
380	570
410	620
450	620
480	580
510	620

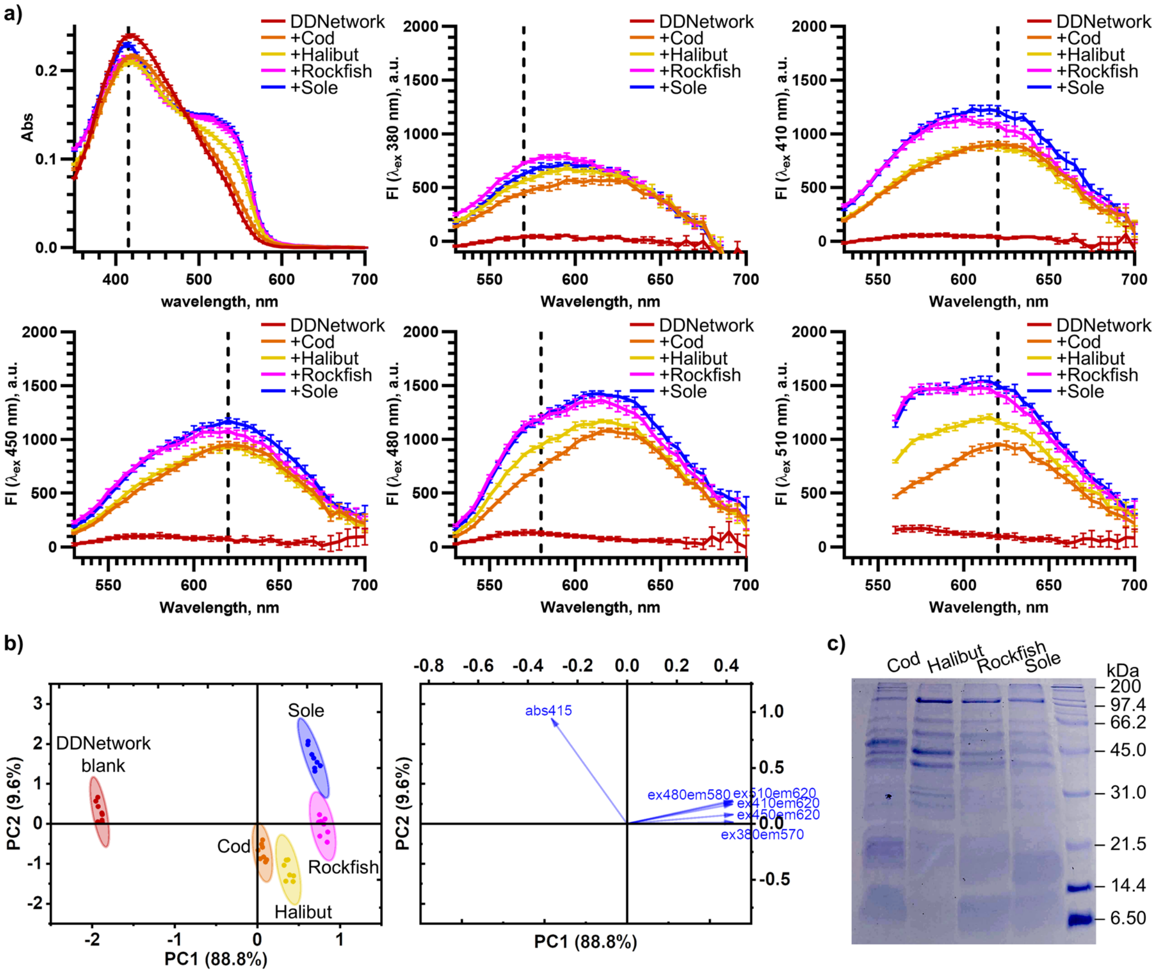

Figure 3.33. DDNetwork absorbance and fluorescence responses can discriminate protein mixtures extracted from different fish species. **a)** Absorbance and fluorescence responses of the DDNetwork to protein mixtures extracted from a cod, halibut, rockfish and sole tissue sample. Wavelengths used in PCA analysis are shown as black dashed lines (λ_{abs} = 415 nm, λ_{em} = 570 nm (λ_{ex} = 380 nm), λ_{em} = 620 nm (λ_{ex} = 410 nm), λ_{em} = 620 nm (λ_{ex} = 450 nm), λ_{em} = 580 nm (λ_{ex} = 480 nm) and λ_{em} = 620 nm (λ_{ex} = 510 nm)) **b)** PCA (correlation) scores plot shows each sample set (n = 8, technical replicates) enclosed by 95% confidence ellipses (left) with the respective loading plots shown as blue arrows (right). Samples contain DDNetwork ([**hemiDD1Cx4**] = 12 μM, [**DD4Cx4**] = 12 μM and [**DD13Cx5**] = 12 μM) and [fish protein extract] = 1 mg/mL. All samples are in NaH_2PO_4/Na_2HPO_4 (10 mM, pH 7.4) in H_2O. **c)** SDS-PAGE analysis verifies a mixture of proteins present in extracted fish tissue samples.

3.5.8 Native HSA trypsin digests

Trypsin digest experiments were carried out using a SpectraMax M5 Multi-Mode Microplate Reader. The cuvette chamber incubator was preheated to 37°C. Samples were measured in a HellmaAnalytics quartz glass high precision micro cell, 10 × 2 mm light path with a PTFE stopper to prevent sample evaporation. Digests were performed using a 1:100 protease:protein ratio with trypsin from bovine pancrease and native HSA. Digest solutions contained DDNetwork ([**hemiDD1Cx4**] = 12 μM, [**DD4Cx4**] = 12 μM and [**DD13Cx5**] = 12 μM), HSA (32 μM) and trypsin (0.32 μM). Digest experiments were done in Na_2HPO_4/NaH_2PO_4 (10 mM, pH 7.4) in H_2O and in NH_4HCO_3 (10 mM, pH 8.0) in H_2O. Absorbance spectral scan speed-reads were taken at 10 min time intervals over the course of 6 h. Control experiments of HSA (32 μM) and trypsin (0.32 μM) were measured to ensure the proteins alone did not contribute to the measured signals. A control experiment of DDNetwork ([**hemiDD1Cx4**] = 12 μM, [**DD4Cx4**] = 12 μM and [**DD13Cx5**] = 12 μM) with trypsin (0.32 μM) was measured, to ensure that trypsin was not interacting with the DDNetwork and did not contribute a change in absorbance. The raw data was calibrated to account for speed-read absorbance adjustments. A buffer blank was subtracted from all reads.

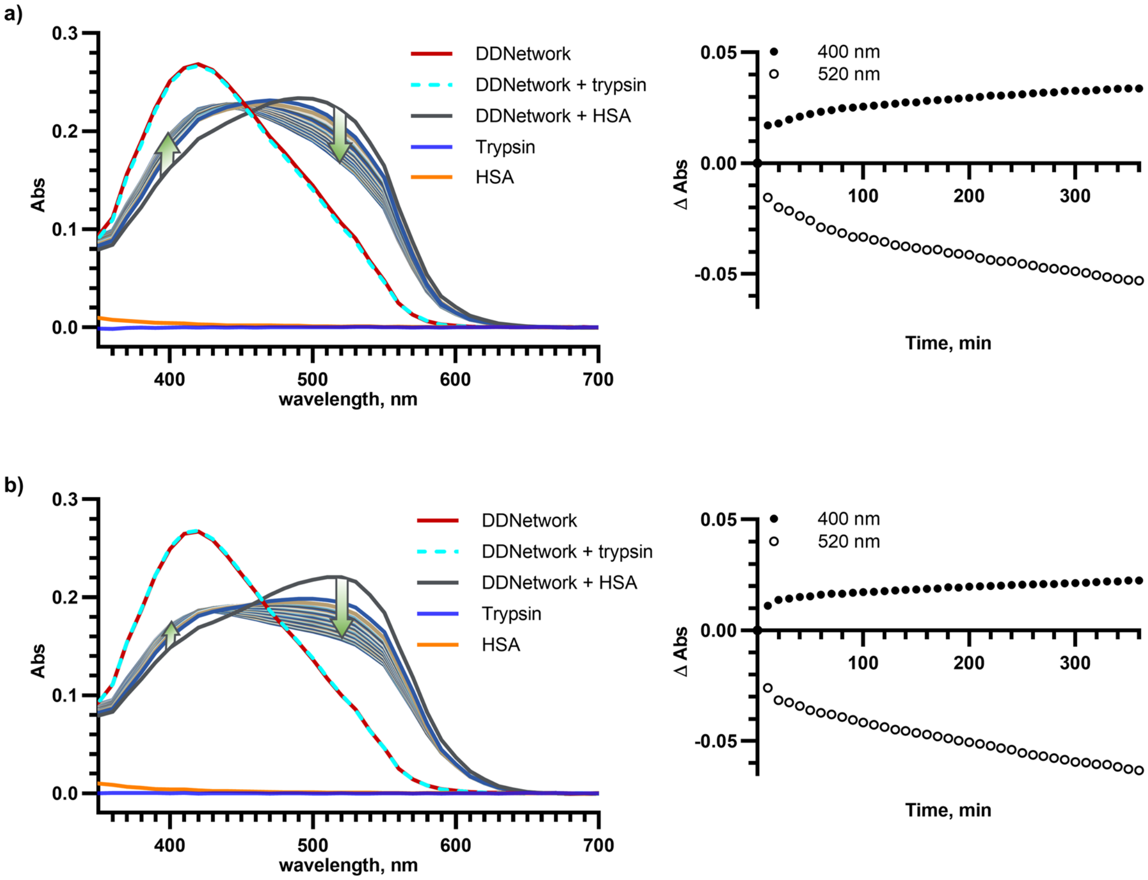

Figure 3.34. DDNetwork adapts within minutes to changes in biological samples providing real-time analysis. Native HSA trypsin digestion shows monitorable changes in the DDNetwork over 6 h by monitoring full spectral scans and individual wavelengths in **a)** H_2PO_4/Na_2HPO_4 (10 mM, pH 7.4) in H_2O and **b)** NH_4HCO_3 (10 mM, pH 8.0) in H_2O. Dark grey line illustrates the DDNetwork response to HSA. Green arrows depict the change in DDNetwork response over time as HSA undergoes trypsin digestion. Samples contain [**hemiDD1Cx4**] = 12 μM, [**DD4Cx4**] = 12 μM and [**DD13Cx5**] = 12 μM), [HSA] = 32 μM and [trypsin] = 0.32 μM.

3.5.9 Saturation transfer difference NMR

All STD NMR samples were prepared from solid, with final solutions containing DimerDye (1.2 mM) and HSA (20 μM) in NaH_2PO_4/Na_2HPO_4 (50 mM, pD 7.4) in 90% H_2O/10% D_2O. Competitive STD NMR experiments were done using saturating amounts of known high affinity competitors to probe the primary drug binding sites. Warfarin was used as a competitive probe for Sudlow site I ($K_{\mathrm{d\,HSA}} \approx 3$ μM),[143, 144] with a final sample solution of **hemiDD1Cx4** (1.2 mM), HSA (20 μM) and warfarin (1.2 mM) in NaH_2PO_4/Na_2HPO_4 (50 mM, pD 7.4) in 87.3% H_2O/9.7% D_2O/3% d_6-DMSO. Naproxen was used as a competitive probe for Sudlow site II ($K_{\mathrm{d\,HSA}} = 560$ nM),[145] with a final sample solution of **hemiDD1Cx4** (1.2 mM), HSA (20 μM) and naproxen (1.2 mM) in

NaH_2PO_4/Na_2HPO_4 (50 mM, pD 7.4) in 90% H_2O/10% D_2O. Control ^1H NMRs of each competitor with **hemiDD1Cx4** were taken in the respective deuterated solution conditions to ensure minimal to no binding to the calixarene cavity at concentrations used in STD NMR.

For STD NMR experiments the 90° pulse was first determined for the sample buffering conditions by measuring the pulse length at 360° with a zg pulse sequence and dividing by four. The determined 90° pulse was used as the P1 in STD NMR experiments, and also the basis for determining correct power settings for the spinlock and shaped pulses. For each STD NMR sample the shift of the water peak (O1) was determined for water peak suppression, using a zg30 pulse sequence with the receiver gain (RG) set to 1. STD NMR experiments were performed using the Bruker pulse sequence stddiffesgp.3,[162] which uses excitation sculpting for water suppression and a spinlock to suppress resonances from the protein.[163] The selective saturation pulse on F2 (SPW9) was set to 40 dB, the spin lock time for protein background suppression (D29) was set to 50 ms, the saturation time (D20) was set to 2 s and the relaxation delay (D1) was set to 2 s. An off-resonance irradiation position of 20000 Hz was used for all experiments. On-resonance positions were chosen to selectively saturate the protein. An on-resonance position of 1250 Hz (2.5 ppm) was used for **hemiDD1Cx4**•HSA, **DD4Cx4**•HSA, **DD13Cx5**•HSA and competitive **hemiDD1Cx4**•HSA•naproxen experiments. An on-resonance position of 500 Hz (1 ppm) was used for the competitive **hemiDD1Cx4**•HSA•warfarin experiment. Spectra were processed using the Bruker Topspin macro stdsplit, providing the off-resonance-irradiated reference spectrum and performing the spectral subtraction for the STD difference spectrum. The highest intensity STD signal was matched to the reference spectrum in all figures for qualitative observation of the closest interacting protons.

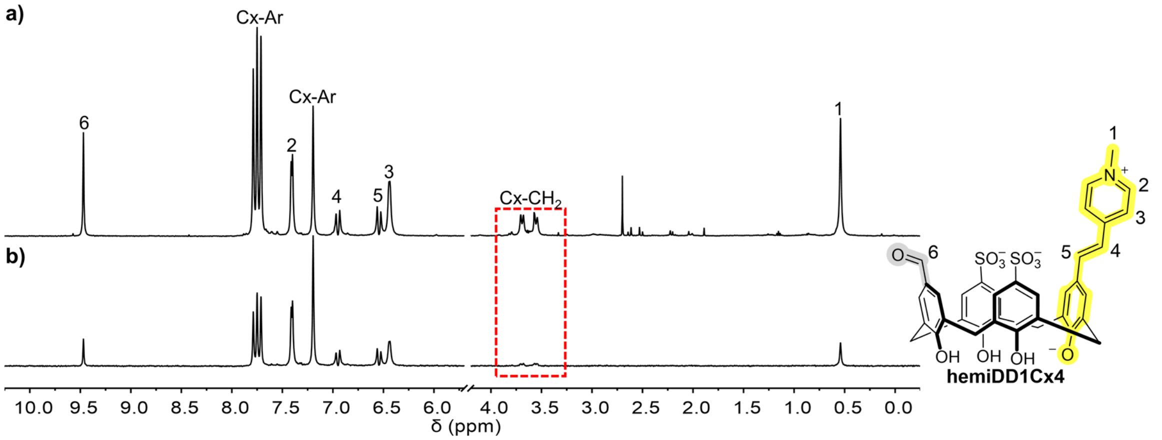

Figure 3.35. HemiDD1Cx4 binds HSA via pendant arm and upper rim interactions. **a)** Reference NMR and corresponding **b)** STD NMR of **hemiDD1Cx4** (1.2 mM) and HSA (20 µM). Red box indicates lower rim methylene protons have the least intense STD signal. Solution in NaH_2PO_4/Na_2HPO_4 (50 mM, pD 7.4) in 90% H_2O/10% D_2O (500 MHz, 298 K). Note: not all methylene protons are visible due to water peak suppression.

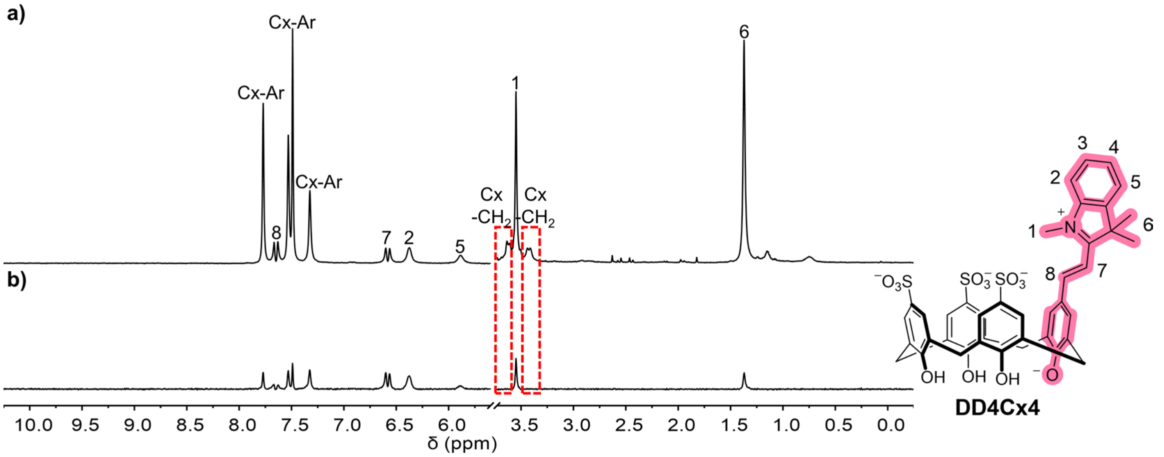

Figure 3.36. DD4Cx4 binds HSA via pendant arm and upper rim interactions. **a)** Reference NMR and corresponding **b)** STD NMR of **DD4Cx4** (1.2 mM) with HSA (20 µM). Red boxes indicate the lower rim methylene protons have the least intense STD signal. Solution in NaH_2PO_4/Na_2HPO_4 (50 mM, pD 7.4) in 90% H_2O/10% D_2O (500 MHz, 298 K). Note: protons 3, 4 and not all methylene protons are visible due to water peak suppression.

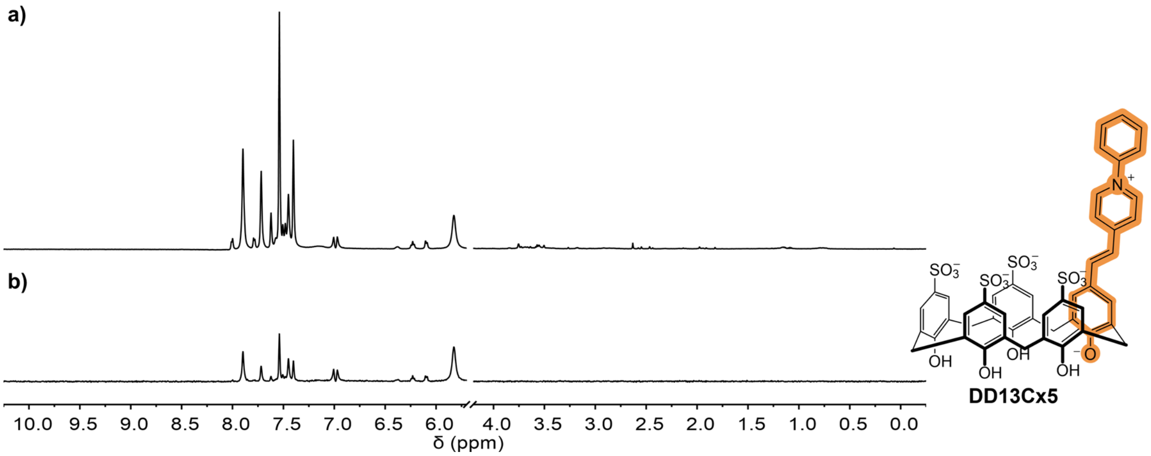

Figure 3.37. DD13Cx5 binds HSA. **a)** Reference NMR and corresponding **b)** STD NMR of **DD13Cx5** (1.2 mM) and HSA (20 µM). STD signals observed in aromatic region indicates binding interactions to HSA, intractable proton signals due to multiple conformations. Methylene protons are at coalescence on the NMR timescale and not visible in reference or STD NMR. Solution in NaH_2PO_4/Na_2HPO_4 (50 mM, pD 7.4) in 90% H_2O/10% D_2O (500 MHz, 298 K).

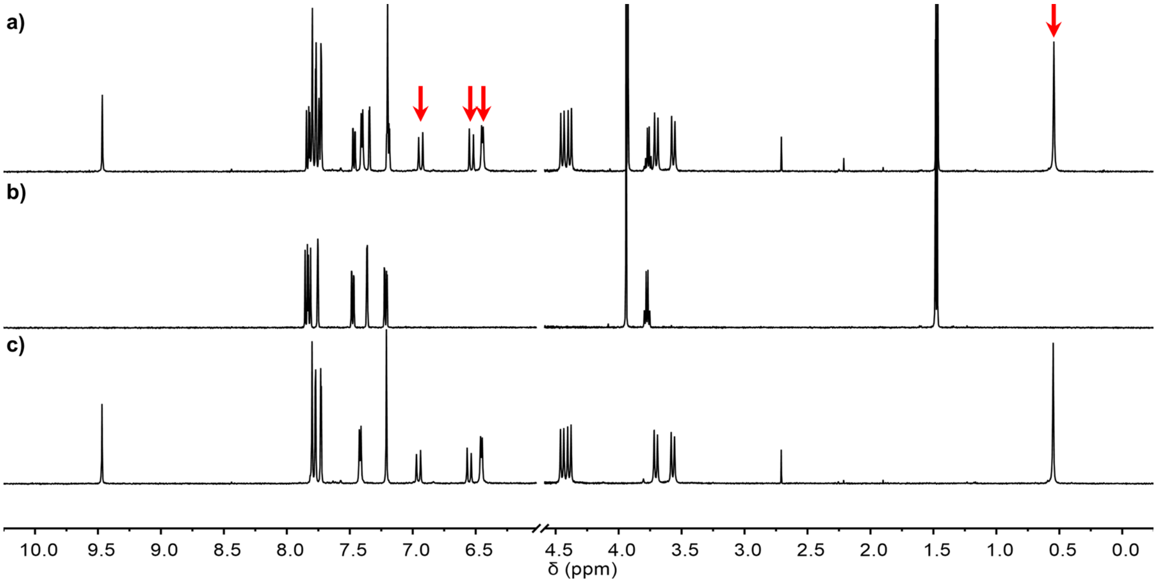

Figure 3.38. ^1H NMR of **hemiDD1Cx4** and naproxen (1:1) show minimal changes to **hemiDD1Cx4** resonances indicating naproxen does not disrupt the dimer (red arrows). **a) HemiDD1Cx4** (1.2 mM) combined with naproxen (1.2 mM), **b)** naproxen (1.2 mM) and **c) hemiDD1Cx4** (1.2 mM). Solutions in NaH_2PO_4/Na_2HPO_4 (50 mM, pD 7.4) in D_2O (500 MHz, 298 K).

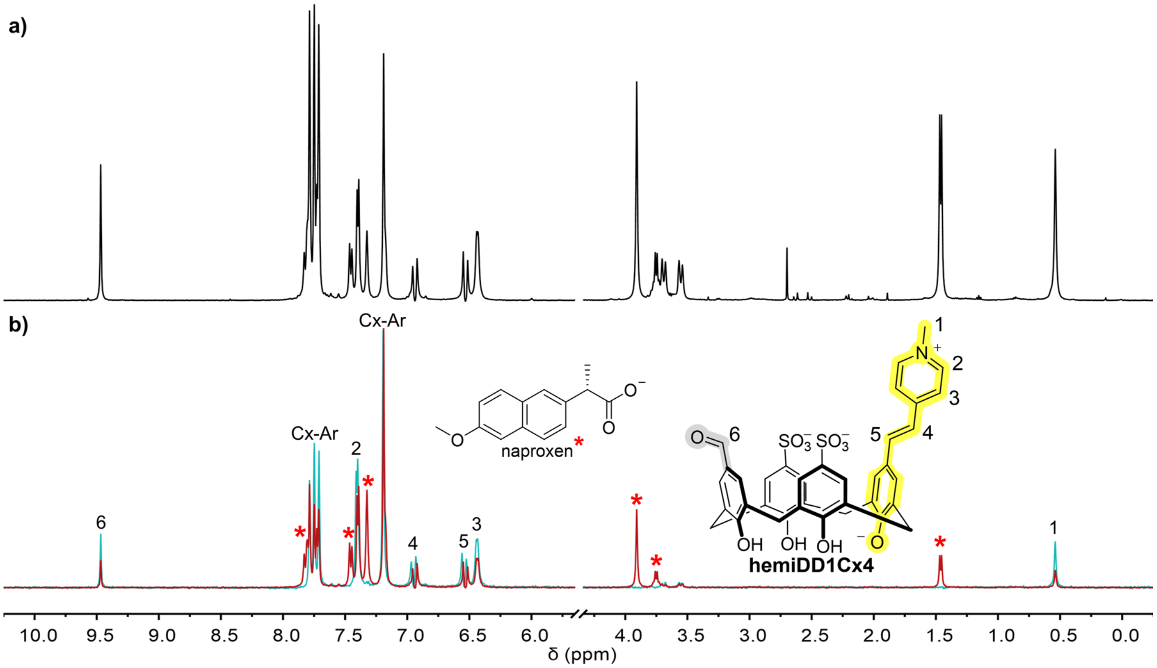

Figure 3.39. Naproxen competitive STD NMR shows **hemiDD1Cx4** does not target Sudlow site II in HSA. **a)** Reference competitive STD NMR of **hemiDD1Cx4** (1.2 mM), HSA (20 µM) and naproxen (1.2 mM). **b)** The corresponding competitive STD NMR (red trace) compared to the STD NMR prior to the addition of naproxen (blue trace). The appearance of naproxen STD signals indicates binding of the competitor to the protein (red asterisks). Minimal reduction of **hemiDD1Cx4** STD signals in the presence of saturating amounts of competitor conclude **hemiDD1Cx4** does not target Sudlow site II. Solution in NaH_2PO_4/Na_2HPO_4 (50 mM, pD 7.4) in 90% H_2O/10% D_2O (500 MHz, 298 K).

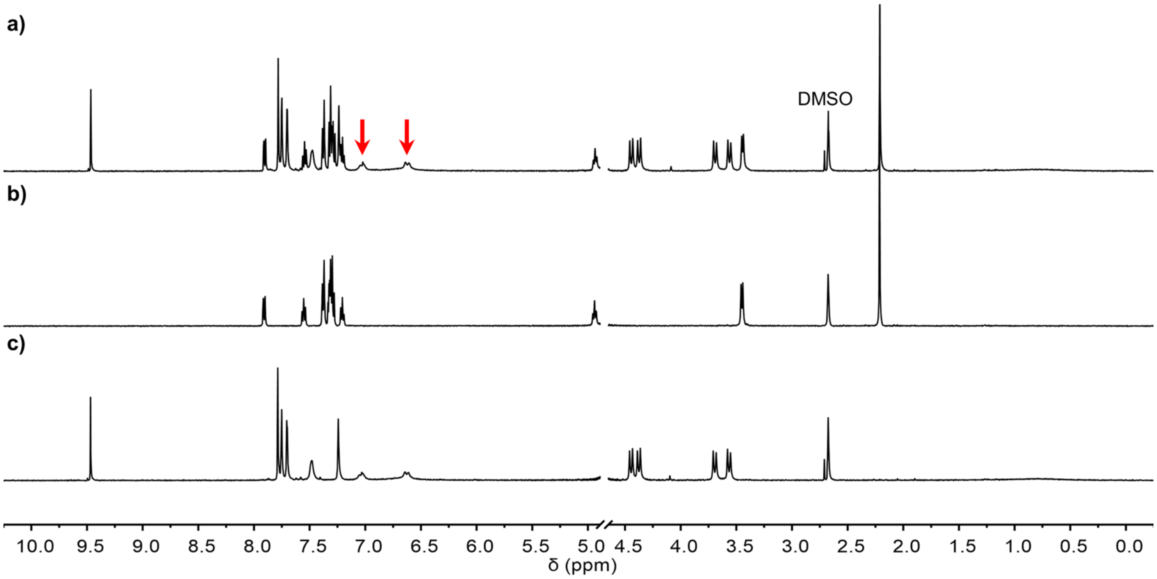

Figure 3.40. ^{1}H NMR of **hemiDD1Cx4** and warfarin (1:1) show minimal changes in **hemiDD1Cx4** resonances indicating warfarin does not disrupt the dimer (red arrows). **a) hemiDD1Cx4** (1.2 mM) combined with warfarin (1.2 mM), **b)** warfarin (1.2 mM) and **c) hemiDD1Cx4** (1.2 mM). Dimerization of **hemiDD1Cx4** is observed by the upfield-shifted alkene protons (red arrows). The methyl peak of **hemiDD1Cx4** broadens into the baseline in solution conditions of NaH_2PO_4/Na_2HPO_4 (50 mM, pD 7.4) in 97% D_2O/3% *d*$_6$-DMSO (500 MHz, 298 K).

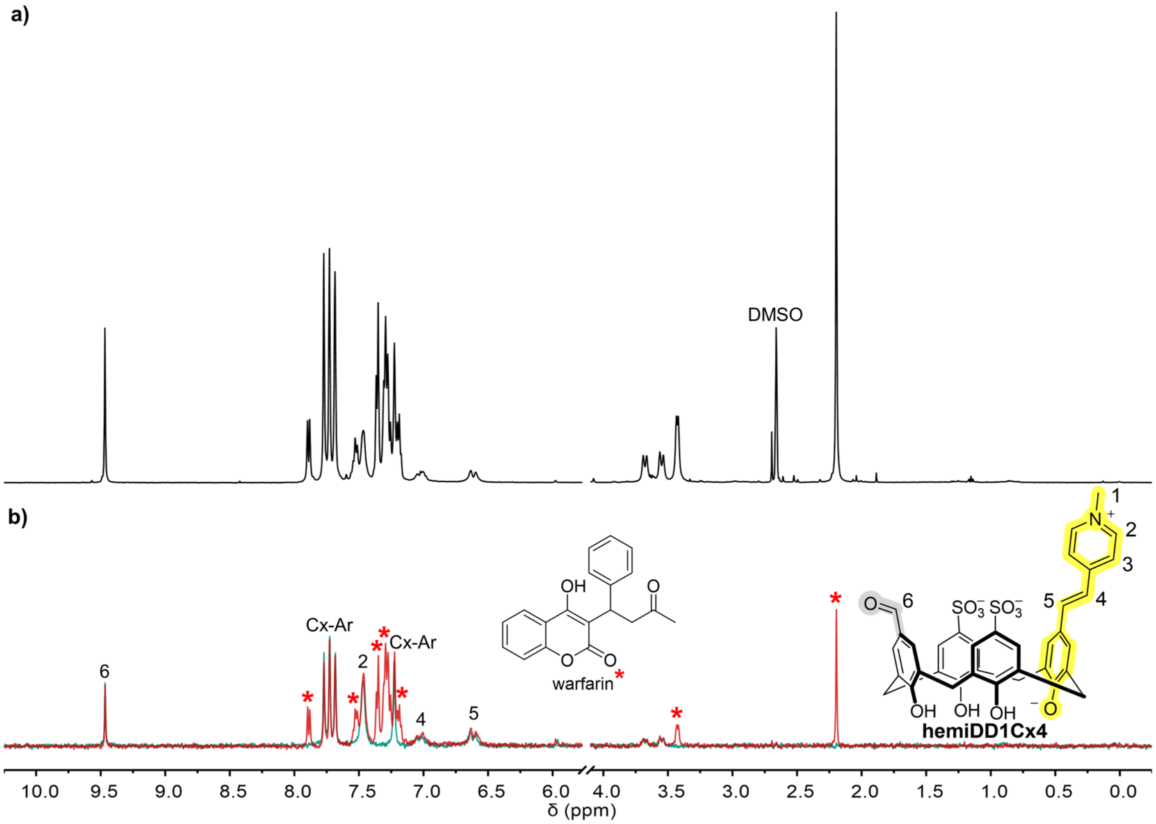

Figure 3.41. Warfarin competitive STD NMR shows **hemiDD1Cx4** does not target Sudlow site I in HSA. **a)** Reference competitive STD NMR of **hemiDD1Cx4** (1.2 mM), HSA (20 μM) and warfarin (1.2 mM). **b)** The corresponding competitive STD NMR (red trace) compared to STD NMR prior to the addition of naproxen (blue trace). The appearance of warfarin STD signals indicates binding of the competitor to the protein (red asterisks). Minimal reduction of **hemiDD1Cx4** STD signals in the presence of saturating amounts of competitor conclude **hemiDD1Cx4** does not target Sudlow site I. Solution in NaH$_2$PO$_4$/Na$_2$HPO$_4$ (50 mM, pD 7.4) in 90% H$_2$O/10% D$_2$O (500 MHz, 298 K).

Chapter 4: Mixed host co-assembled systems for broad-scope analyte sensing

This work was adapted from a previously published paper.

Allison J. Selinger,[‡] Joana Krämer,[‡] Eric Poarch, Dennis Hore, Frank Biedermann, and Fraser Hof
Chem. Sci., **2024**, 15, 12388-12397.
[‡]AJS and JK contributed equally.

This work was conducted in collaboration with JK, FB (Institute of Nanotechnology, Karlsruhe Institute of Technology, Karlsruhe, Germany), EP and DH (Canadian Institute for Substance Use Research, University of Victoria, Victoria, BC, Canada). AJS, JK, FB and FH conceptualized the idea. AJS and JK contributed to investigation, formal analysis and methodology, with some of the work done during a visit by JK to work directly with AJS at University of Victoria. AJS synthesized previously reported **DD4Cx4**, **DD8Cx4**, and **DD13Cx4**. JK provided **CB8**. JK conducted preliminary mixed host screening experiments. The final reported mixed host screening results were completed by AJS. AJS conducted the absorbance/fluorescence mixed host titrations presented in this work. AJS designed, conducted, and analyzed the ^{1}H NMR, absorbance/fluorescence and MALDI-TOF MS experiments that investigated the co-assembly mechanism. FB provided the DFT model. AJS completed LOD experiments with cocaine. JK completed PCA experiments of the mixed host sensors with isolated illicit drugs and adulterants. AJS completed the correspond control sensor array PCA experiments. EP under supervision of DH selected and provided multi-component street drug samples from Substance, the Vancouver Island Drug Checking Project. AJS completed PCA experiments with the multi-component street drug samples for both mixed host co-assembled sensors and the control sensor array. AJS independently wrote the complete initial draft of the paper. All authors contributed to reviewing and editing the paper.

4.1 Foreword

This Chapter explores a new system design of mixed host co-assembly for enhancing sensing scope. In Chapter 3 we learned that a system comprised of different interacting reporter fluorophores can produce information-rich photophysical outputs. In this Chapter we were interested in exploring self-assembling systems that incorporate different receptor host elements, with the aim of further diversifying analyte interactions. The motivation behind this work was to overcome one of the main limitations of DimerDye *p*-sulfonatocalix[*n*]arenes, only binding and responding to cationic molecules. We incorporated a cucurbit[*n*]uril host scaffold that binds hydrophobic, neutral and cationic molecules, in collaboration with Dr. Frank Biedermann and a visiting exchange PhD student, Joana Krämer (Institute of Nanotechnology, Karlsruhe Institute of Technology, Karlsruhe, Germany). Together we established that co-assemblies made up of multiple kinds of hosts can achieve sensing of analytes with diverse chemical properties. To further explore analyte complexity, we applied co-assembled mixed host sensing systems to the profiling of illicit street drug samples, which are each made up of multiple hydrophobic, neutral and/or cationic molecules.

4.2 Introduction

Synthetic receptors are a powerful tool for molecular recognition-based sensing. Chemosensors have a broad range of applications, such as the detection of biorelevant compounds for diagnostics, and monitoring biophysical and enzymatic processes.[4, 164] An ultimate goal for synthetic sensors is to mimic the human olfactory system, containing the ability to identify many different entities from a single sensory tool.[60, 165] More recently, the conceptual development of sensors has advanced towards information-rich chemical nose or cross-reactive sensors to achieve more prolific unique sensing profiles. This is done through either synthetic design or supramolecular assembly, combining multiple receptor and/or reporter elements into one sensing unit.[60, 166] These design strategies are highlighted by examples of unimolecular probes that covalently integrate multiple complexing receptor and/or reporter components,[167, 168] and biological noncovalent self-assembly-based probes that function through multi-complexing systems.[135, 169-171]

Macrocyclic hosts are well-defined synthetic receptors for the detection of small molecules and biomacromolecules.[23, 172, 173] Host-based sensing is traditionally done using an indicator displacement assay (IDA) that operates through competitive binding of an analyte to a preformed host•indicator complex. This generally results in a fluorescence response, where sensitivity is dictated by binding affinity.[36, 39, 40] Singular host sensing systems provide limited information, typically in the form of a single output (turn-on or turn-off fluorescence) for one particular class of analyte and often fail to achieve specificity when faced with structurally similar analytes. To attain analyte differentiation a suite of individual host•indicator sensors are often applied, where varied response patterns arise from affinity differences, producing an optical fingerprint for discrimination.[134] This strategy has been employed in macrocyclic host-based sensor arrays with some recent examples in differentiating neurotransmitters,[73] small molecule bioorganic analytes,[78] folded DNA G-quadruplexes,[70, 82, 83] insect pheromones,[174] natural amino acids,[175] and amyloid structures.[74]

The power of cross-reactive self-assemblies is demonstrated by macrocyclic host-based sensors that co-assemble multiple receptor or reporter elements within the same solution. The majority of reported multi-macrocyclic host systems rely on non-specific amphiphilic aggregation to co-assemble different host classes, allowing for detection of larger peptide biotargets,[57] and the ability to differentiate model proteins[84] and cells.[85] A recent report shows that macrocycles containing different integrated fluorophores have improved discrimination power when they are combined in solution, forming an adaptive network of sensors.[176] Despite these advances, one consistent limitation of supramolecular sensors is they tend to sense only a single class of analyte. The current conceptual framework would have us overcome these limitations through synthesis of new sensors, an approach that is often inefficient and incapable of achieving sensing within multi-component mixtures and real-world samples.

Here we present a new concept in which a mixed host sensor positions a single dye within a complex system, conferring the ability to generate different kinds of optical responses to hydrophobic, neutral, and cationic analytes. Supramolecular hosts tend to bind one type of guest analyte, therefore limiting the scope and applicability of any host-based sensing approach that relies on one host class.[177] In this work, we overcome this limitation by co-assembling two different classes of macrocyclic hosts, DimerDye *p*-sulfonatocalix[4]arenes and cucurbit[*n*]urils, into a single composite mixed host sensor (Figure 4.1). Key to this approach is the integration of a dye into the *p*-sulfonatocalix[4]arene scaffold, which both facilitates co-assembly and acts as a reporter for all host•host and host•analyte interactions. The equilibrium of any one pre-assembled mixed host sensor is poised to go in different directions depending on the nature of the analyte added, producing multi-responsive outputs, where we define multi-responsive as both "responding to multiple analytes" and also "producing varying kinds of optical responses to a given analyte" (Figure 4.1b). We prove the benefits of this simple co-assembly approach in an array-based platform through the differentiation of hydrophobic, cationic, neutral and anionic drugs. We then apply these mixed host sensing systems to the highly challenging task of typing illicit drug samples that were collected from people who use drugs. Since these samples come from unregulated supplies they represent a leap forward in sample complexity compared to all prior efforts in our group.[72]

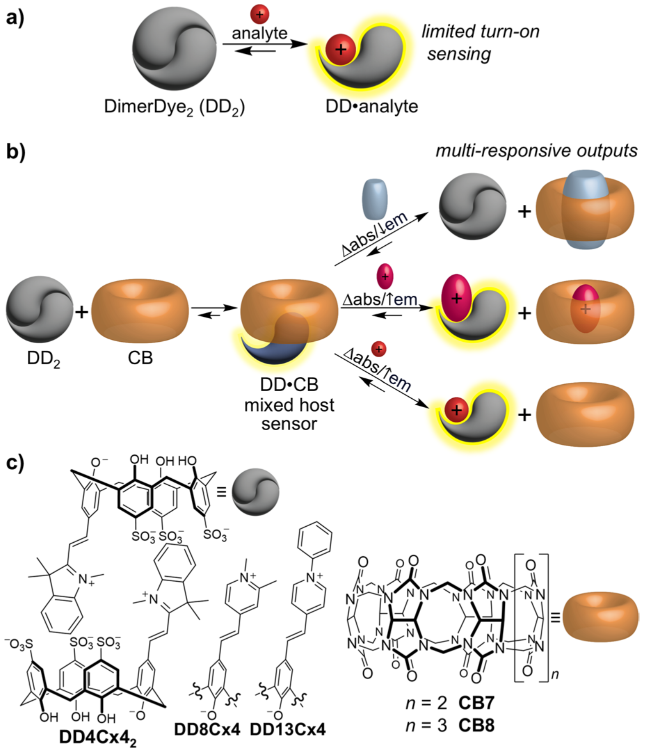

Figure 4.1. A mixed host sensor produces multi-responsive outputs, increasing the scope of analyte detection. **a)** Schematic illustration of DimerDye disassembly-driven turn-on fluorescence sensing of cationic analytes. **b)** This work establishes mixed host co-assembled sensors that produce multi-responsive outputs for a wide range of hydrophobic, neutral, and cationic analytes. DimerDye complexation with cucurbit[*n*]uril forms a mixed host sensor with moderate changes in absorbance/fluorescence. The subsequent addition of an analyte that favours cucurbit[*n*]uril binding produces a change in absorbance and/or decreased fluorescence, whereas an analyte that prefers DimerDye binding results in a change in absorbance and/or increased fluorescence. The schematic shown represents the expected behaviours for **CB7**, while additional higher-order complexes are possible for **CB8**. Structures of **c)** DimerDye host sensors **DD4Cx4**, **DD8Cx4**, and **DD13Cx4**, and cucurbit[*n*]uril hosts **CB7** and **CB8** used in this work.

4.2 Results and discussion

Two distinct host classes were selected to encourage host•host co-assembly. Previously reported DimerDye *p*-sulfonatocalix[4]arenes **DD4Cx4**, **DD8Cx4**, and **DD13Cx4**,[72] and cucurbit[*n*]uril hosts, **CB7** and **CB8** were selected to promote hetero co-assembly while contributing different analyte binding properties (Figure 4.1c). *p*-

Sulfonatocalix[4]arenes contain a flexible chalice-shaped cavity and negatively charged upper rim.[99] In aqueous solution the DimerDye analogs form a homodimer, stacking two fluorophores in an antiparallel quenched arrangement. Upon analyte binding, DimerDyes provide turn-on fluorescence detection through a disassembly-driven sensing mechanism (Figure 4.1a).[54, 72, 126] The selected DimerDyes (**DD4Cx4**, **DD8Cx4**, and **DD13Cx4**) cover a range of structural, absorbance, and emission properties, however, they are limited to binding cationic analytes. Conversely, cucurbit[*n*]utils have a larger range of reported analyte interactions.[178, 179] They contain a barrel-shaped rigid nonpolar cavity lined with neutral polar carbonyl portals, reporting strong binding with neutral hydrophobic guests complementary in size and shape,[180, 181] and amphiphilic cationic ammonium or diammonium guests that favour hydrophobic and ion-dipole interactions.[178] We selected **CB7** and **CB8** to accommodate different sized guests, where the larger **CB8** cavity offers binding to bulkier hydrophobic drugs.[182, 183] We predicted the combination of these two host classes would co-assemble through hydrophobic and ion-dipole interactions from the DimerDye pendant arm binding the cucurbit[*n*]uril cavity and interacting with the polar carbonyl portals.

Different pairs of one DimerDye and one cucurbit[*n*]uril can co-assemble to form a mixed host sensor with distinct photophysical properties. Combinations of **DD4Cx4**, **DD8Cx4** and **DD13Cx4** with **CB7** and **CB8** were screened for induced changes in DimerDye absorbance and/or fluorescence (Figure 4.16). The mixed host pairs that displayed significant changes in absorbance and/or fluorescence (**DD4Cx4•CB8**, **DD8Cx4•CB8**, **DD13Cx4•CB8**, and **DD13Cx4•CB7**) were selected for further study. To establish the formation of these hetero host•host complexes, changes in DimerDye absorbance and emission were monitored during titrations with increasing concentrations of cucurbit[*n*]uril. Titrations of **CB8** into **DD4Cx4** and **CB7** into **DD13Cx4** resulted in both changes in absorbance and turn-on fluorescence (Figure 4.2a,b and Figure 4.17). These results indicate the parent DimerDye disassembles from its native homodimer state, with the turn-on fluorescence response strongly supporting the formation of a hetero-complex between the two hosts. Independently, ^{1}H NMR experiments further support the formation of hetero-complexes **DD4Cx4•CB8** and **DD13Cx4•CB7** by the appearance of new upfield-shifted and broadened resonances, attributed to the DimerDye pendant arm protons being in a shielded environment (Figure 4.2d, Figure 4.19 and Figure 4.20). The broadened **CB7** and **CB8** peaks indicate possible aggregate formation at concentrations used in NMR, coinciding with the low solubilities of these mixed host assemblies (Figure 4.2d, Figure 4.19 and Figure 4.20). Upon addition of **CB8**, the DimerDyes **DD8Cx4** and **DD13Cx4**, exhibited shifts in absorbance, indicating that **CB8** forms a hetero-complex with **DD8Cx4** and **DD13Cx4** (Figure 4.17). However, these complexation events caused minimal changes in emission (Figure 4.17). In cases where both a colour change and turn-on emission are observed (**DD4Cx4•CB8** and **DD13Cx4•CB7**), we suspect the homodimer disassembly is driven by the pendant arm binding to cucurbit[*n*]uril, producing a turn-on fluorescence response. A molecular model of a possible 1:1 co-assembly of **DD13Cx4** with **CB7** is presented in Figure 4.22. Matrix-assisted laser desorption ionization-time of flight mass spectrometry (MALDI-TOF MS) further confirmed 1:1 complexation, reporting a **DD13Cx4•CB7** co-assembly peak of m/z 2006.4606 (Figure 4.2c). In cases where only a colour change is observed (**DD8Cx4•CB8** and **DD13Cx4•CB8**) it is evident that hetero-host interactions are occurring. We suspect the non-fluorescent state is a result of assemblies where the DimerDye pendant arms are in a stacked quenched arrangement. These possible complexes include cucurbit[*n*]uril outer-surface binding interactions,[184] where multi-hetero assemblies with *p*-sulfonatocalix[4]arenes in aqueous solution have been reported,[185, 186] as well as potential ternary complexes inside the larger **CB8** cavity,[187-189] where two DimerDye pendant arms could potentially bind stacked inside the **CB8** cavity. Irrespective of the exact complexes occurring in solution, these co-assemblies constitute different mixed host sensors from which distinct absorbance and fluorescence sensing outputs can arise (Figure 4.1b).

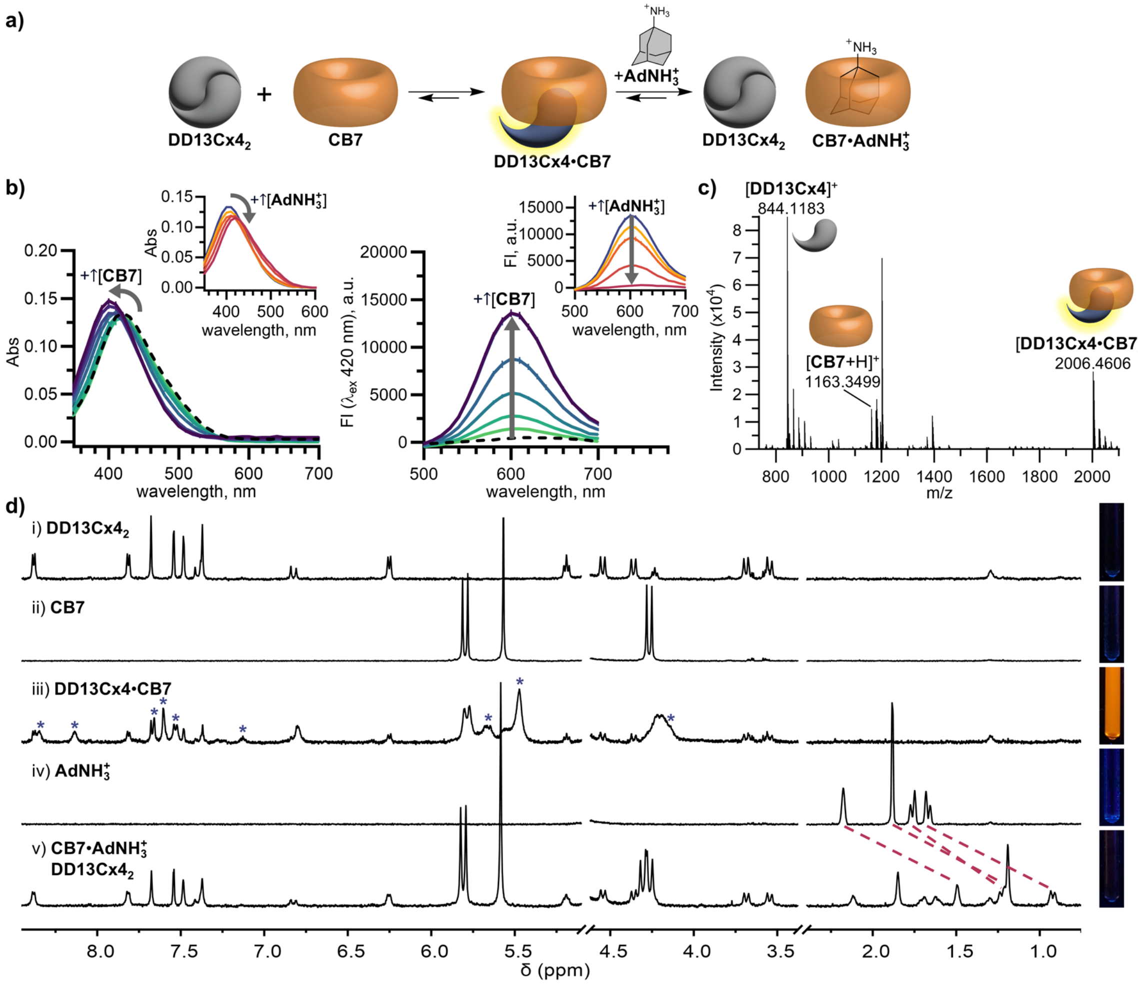

Figure 4.2. Mixed host **DD13Cx4•CB7** co-assembly functions as a turn-off sensor for strong binding guests of **CB7**. **a)** Schematic of **DD13Cx4•CB7** formation and sensing mechanism of **AdNH$_3^+$**. **b)** The addition of increasing concentrations of **CB7** (1.3 to 84 μM) into **DD13Cx4** (10.5 μM) results in a blue shift in absorbance (left) and increased fluorescence (right). Black dashed line represents **DD13Cx4** (10.5 μM). Insets show the addition of increasing concentrations of **AdNH$_3^+$** (2.6 to 21 μM) to the co-assembled **DD13Cx4•CB7** sensor, induces a red shift in absorbance (left) and turn-off fluorescence (right). Inset blue line represents **DD13Cx4** (10.5 μM) with **CB7** (21 μM). All samples in NaH_2PO_4/Na_2HPO_4 (10 mM, pH 7.4) in H_2O. **c)** MALDI-TOF MS of **DD13Cx4** (50 μM) with **CB7** (50 μM) confirms **DD13Cx4•CB7** co-assembly. **d)** ^{1}H NMR of iii) **DD13Cx4** (100 μM) with **CB7** (100 μM) shows evidence of hetero host co-assembly by the appearance of new upfield-shifted **DD13Cx4** peaks and new **CB7** peaks (blue stars). Disassembly of the homodimer **DD13Cx4$_2$** is supported by the fluorescent appearance of the NMR tube. v) The addition of **AdNH$_3^+$** (100 μM) displaces the **DD13Cx4•CB7** complex, indicated by the upfield-shifted **AdNH$_3^+$** peaks (red dashed lines) and return of native homodimer **DD13Cx4$_2$** peaks. The non-fluorescent appearance further supports the reformation of the homodimer **DD13Cx4$_2$**. All samples in NaH_2PO_4/Na_2HPO_4 (10 mM, pD 7.4) in D_2O (500 MHz, 298 K). NMR tubes irradiated with a hand-held UV lamp (λ_{ex} 356 ± 20 nm).

Mixed host mechanistic studies with a CB-selective guest demonstrate multi-responsive emergent sensing properties that are not present in the parent sensor. To validate the contribution of cucurbit[*n*]uril sensing responses, we selected amantadine (**AdNH$_3^+$**) as a high affinity guest for **CB7** (K_d = 240 fM),[190] while the adamantane moiety has been shown to scarcely interact with sulfonated calixarenes.[191] Our ^{1}H NMR experiments corroborate this, showing minimal binding of $\mathbf{AdNH_3^+}$ to **DD13Cx4** (Figure 4.21d). In contrast, the addition of $\mathbf{AdNH_3^+}$ to the pre-assembled moderately fluorescent co-assembled mixed host sensor **DD13Cx4•CB7** resulted in a turn-off fluorescence response and red shifted absorbance (Figure 4.2b). ^{1}H NMR studies independently confirmed the turn-off fluorescence response is due to the reformation of the quenched homodimer complex $\mathbf{DD13Cx4_2}$ and assembly of the host•guest complex $\mathbf{CB7{\bullet}AdNH_3^+}$ (Figure 4.2d and Figure 4.21). These results show that mixed host co-assemblies can produce photophysical responses through analyte binding to the non-fluorophore-containing host, effectively increasing the scope of analyte detection from a single sensing assembly.

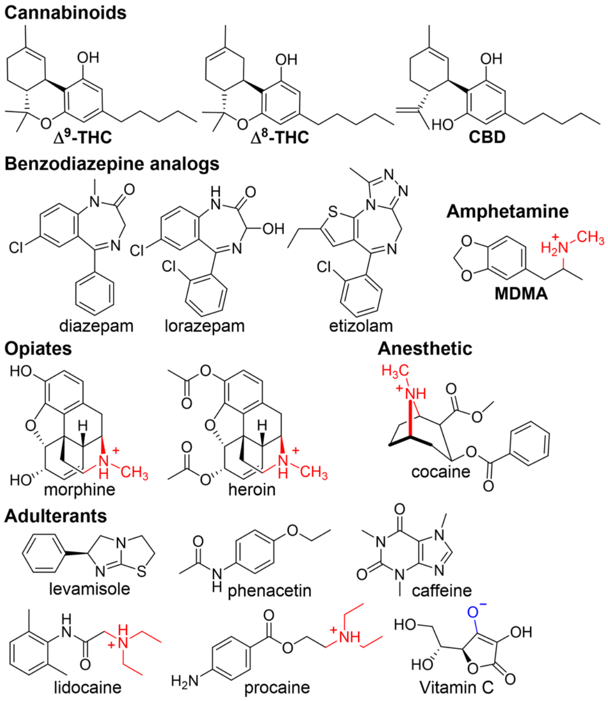

Figure 4.3. Chemical structures of illicit drugs and adulterants ranging in hydrophobic, neutral, cationic and anionic properties.

Mixed host sensors further expand detection capabilities to new classes of analytes. On their own, DimerDyes have been reported to detect cationic illicit drugs.[72] To determine if mixed host sensors expand sensing abilities we selected cocaine, cannabidiol (**CBD**) and Vitamin C as analytes, representing cationic, neutral and anionic classes of drugs (Figure 4.3). As a direct comparison, we measured the fluorescence responses of the mixed host sensor **DD13Cx4•CB7** and isolated **DD13Cx4**$_2$ (Figure 4.4). Assays with only DimerDye provided limited information for these drugs, only producing a turn-on fluorescence response to the cationic analyte, cocaine and insignificant responses to the neutral and anionic analytes (Figure 4.4b). However, the mixed host sensor **DD13Cx4•CB7** produced varied emergent responses to the different analyte classes; with increased and blue-shifted emission for cationic cocaine, decreased and blue-shifted emission for neutral **CBD**, and a slight, non-shifted decrease in emission to anionic Vitamin C (Figure 4.4a). We probed whether the co-assembly of sensors would affect the emission intensities and limits of detection (LODs), using cationic cocaine as a test analyte. The LODs of cocaine with mixed host sensors (**DD4Cx4•CB8**, **DD8Cx4•CB8**, **DD13Cx4•CB8** and **DD13Cx4•CB7**) were of similar magnitude to the parent DimerDyes (**DD4Cx4**, **DD8Cx4** and **DD13Cx4**), ranging from 0.5 to 3.6 μM (Table 4.2). Interestingly, mixed host sensors **DD4Cx4•CB8**, **DD13Cx4•CB8** and **DD13Cx4•CB7** showed an overall enhancement of fluorescence in comparison to the isolated parent DimerDyes (**DD4Cx4** and **DD13Cx4**), displaying larger changes in amplitude (Figure 4.23 to Figure 4.25). Although mixed-host systems have competing host•analyte and host•host interactions, these results emphasize favourable emergent photophysical properties, providing varied responses to different analytes, including those that otherwise wouldn't bind.

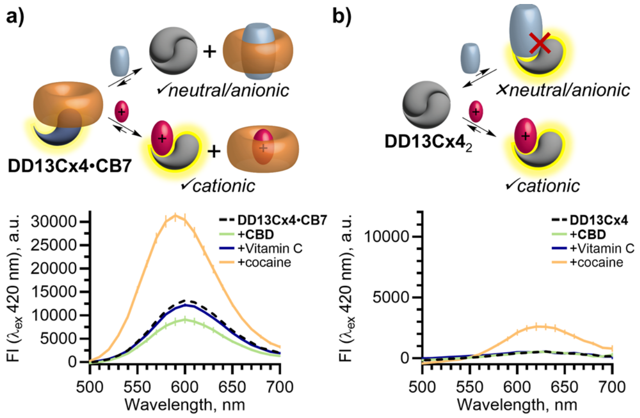

Figure 4.4. A mixed host sensor has multi-capable responses to neutral, cationic and anionic structures. **a)** Fluorescence response of mixed host co-assembled sensor **DD13Cx4•CB7** to anionic Vitamin C, neutral **CBD** and cationic cocaine. Samples contain [**DD13Cx4**] = 10.5 μM, [**CB7**] = 21 μM and [drug] = 105 μM. **b)** Fluorescence response of isolated **DD13Cx4** to anionic Vitamin C, neutral **CBD** and cationic cocaine. Samples contain [**DD13Cx4**] = 10.5 μM and [drug] = 105 μM. All samples are in NaH_2PO_4/Na_2HPO_4 (8.4 mM, pH 7.4) in H_2O with 2% MeOH.

To further probe the power of using mixed host sensors, a large set of bulky, hydrophobic, cationic, neutral and anionic drugs and adulterants were selected for differentiation (Figure 4.3). The analytes were chosen to test the sensing range capabilities of our mixed host co-assembled sensors while targeting compounds commonly found in harm-reduction-based drug checking of Canadian illicit street drugs.[192] An array of mixed host sensors (**DD4Cx4•CB8**, **DD8Cx4•CB8**, **DD13Cx4•CB8**, and **DD13Cx4•CB7**) were screened for sensing responses, measuring select absorbance and fluorescence wavelengths (Table 4.3). Principal component analysis (PCA) was then used to analyze the fingerprint response patterns, aiming to discriminate samples while minimizing the number of required observations, see Section 4.5.5 for systematic PCA process.[65]

Mixed host sensors can generate surprising emergent properties, including the differentiation of drugs for which neither host is considered to be a canonical binder. Cannabinoids pose a challenge for detection by supramolecular hosts as their neutral structure makes them poor guests. Hooley and co-workers showed that water-soluble deep cavitand sensors bind tetrahydrocannabinol (THC), and can detect and discriminate THC from its metabolites.[193] DimerDyes alone prefer cationic guests and do not give any detectable change in fluorescence response to cannabinoids and are therefore unable to achieve cannabinoid discrimination (Figure 4.4b, Figure 4.5b and Figure 4.27). Although THC has been reported not to bind **CB7**,[194] we found our mixed host sensors **DD13Cx4•CB7** and **DD13Cx4•CB8** each produced variable, information-rich responses. We postulate that the decreased emission observed from **DD13Cx4•CB7** upon addition of **CBD** (Figure 4.4a), is a result of higher-order complexation events that either disrupt mixed host co-assembly or otherwise perturb the emission of the DimerDye fluorophore. Not only was cannabinoid sensing possible from the mixed host sensors, but the combination of absorbance and fluorescence outputs from only two mixed host sensors in an array (**DD13Cx4•CB7** and **DD13Cx4•CB8**) allowed for the complete discrimination of highly similar **Δ^8-THC** and **Δ^9-THC** isomers, which differ only in the position of a double bond (Figure 4.5a and Figure 4.26). These results show that emergent properties are produced from the co-assembly with cucurbit[*n*]uril hosts, providing superior information-rich responses (Figure 4.5).

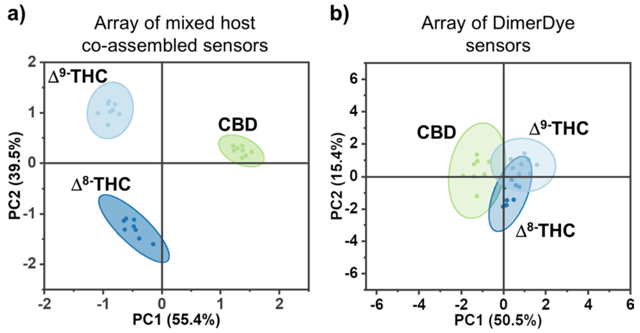

Figure 4.5. An array of mixed host sensors discriminates highly similar neutral cannabinoids. **a)** PCA scores plot of a mixed host co-assembled DD•CB sensor array completely discriminates **CBD**, **Δ^8-THC** and **Δ^9-THC** isomers. Sensor array includes absorbance and fluorescence responses of mixed host sensing pairs **DD13Cx4•CB8** and **DD13Cx4•CB7**. Samples contain [DD] = 10.5 µM, [CB] = 21 µM and [drug] = 105 µM. **b)** On their own, DimerDye sensors do not discriminate cannabinoids. Sensor array contains absorbance and fluorescence responses of **DD4Cx4**, **DD8Cx4** and **DD13Cx4**. Samples contain [DD] = 10.5 µM and [drug] = 105 µM. PCA (correlation) scores plots show each sample set (n = 8) enclosed by 95% confidence ellipses. All samples are in NaH_2PO_4/Na_2HPO_4 (8.4 mM, pH 7.4) in H_2O with 2% MeOH.

A small array of mixed host sensors achieves discrimination of a large set of illicit drugs and adulterants from many distinct chemical classes. We first focused on a test set containing illicit central nervous system depressants, which included both neutral benzodiazepines and cationic opiates. In this analysis, the benzodiazepines etizolam and diazepam displayed overlapping confidence ellipses while the other depressants were discriminated (Figure 4.6a and Figure 4.28). Next, we studied a test set including cocaine and **MDMA**, along with a set of pharmacologically active adulterants commonly added for their synergistic effects (Figure 4.6b and Figure 4.29).[195, 196] The prescription adulterants procaine, lidocaine, levamisole, and phenacetin, were discriminated from the illicit drugs cocaine and **MDMA**, whereas the adulterants with fewer health repercussions, Vitamin C and caffeine, overlapped with each other. Lastly, a plot combining all tested drugs maintained similar discrimination patterns among the combined test set, with similar deficiencies in the overlap of two benzodiazepines and the adulterants Vitamin C and caffeine (Figure 4.6c and Figure 4.30).

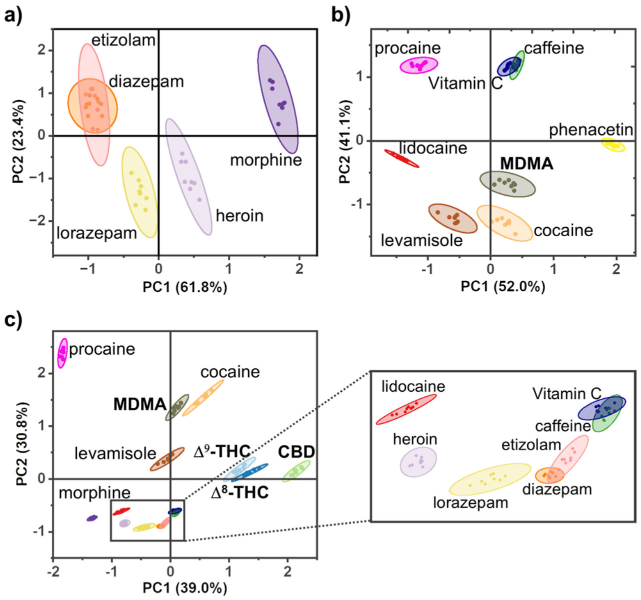

Figure 4.6. An array of mixed host co-assembled sensors distinguishes between different classes of cationic and neutral illicit drugs and adulterants. **a)** PCA analysis of central nervous system depressants (neutral benzodiazepines and cationic opiates). The array of mixed host sensors includes absorbance and fluorescence responses from **DD8Cx4•CB8**, **DD13Cx4•CB8** and **DD13Cx4•CB7**. **b)** PCA plot discriminates anesthetics and amphetamine from common adulterants. The array of mixed host sensors includes responses from **DD4Cx4•CB8**, **DD13Cx4•CB8**, and **DD13Cx4•CB7**. **c)** PCA analysis of all tested drugs and adulterants. The array of mixed host sensors includes responses from **DD4Cx4•CB8**, **DD8Cx4•CB8**, **DD13Cx4•CB8** and **DD13Cx4•CB7**. PCA (correlation) scores plot shows each sample set (n = 8) enclosed by 95% confidence ellipses. Samples contain [DD] = 10.5 µM, [CB] = 21 µM and [drug] = 105 µM. All samples are in NaH_2PO_4/Na_2HPO_4 (8.4 mM, pH 7.4) in H_2O with 2% MeOH.

Real-world illicit street drug samples represent a challenging set of multi-component targets for identification. Tests that merely reveal the presence or absence of potent substances like fentanyl are less informative tools for harm reduction in the context of the drug overdose crisis.[197] People who use drugs access drug checking services to reduce risks by obtaining an understanding of the complete composition (all active illicit drugs, adulterants, and inert compounds), with specific quantities to assess potency and dangers.[198] Currently, multiple instrument-based techniques are employed, such as combinations of immunoassay test strips, chromatography, mass spectrometry, Raman, and infrared (IR) spectroscopic methods.[199] Typing drug samples using a sensor array would provide a complementary technique to current instrument-based analysis. Here we aimed to see if our mixed host sensors could be applied to illicit multi-component street drug samples to distinguish different composition profiles previously encountered within the drug-checking ecosystem. Street drug samples were provided by people who use drugs through Substance, the Vancouver Island Drug Checking Project,[200, 201] where drug composition and quantification were determined using Fourier transform infrared (FTIR) spectroscopy and paper spray mass spectrometry (PS-MS) (Table 4.1 and Figure 4.31). To capture the landscape of street drugs commonly in use in British Columbia, Canada, we studied representative samples from different drug classes (A-E), as well as several fentanyl-containing samples that varied slightly in composition (E-H). We also included two fentanyl samples of the same composition that arrived at the drug-checking site from two distinct users but originating from the same batch and supplier (H and I). Similar to the current protocols used for drug checking, we prepared the street drug samples for sensing experiments dissolving 1.5 mg in 1 mL methanol.[202] These stock solutions were then further diluted down to 0.03 mg/mL in all sensing experiments.

Table 4.1. Multi-component illicit street drug sample compositions.

Street drug sample	Composition[a]
A	Cocaine (90%), sorbitol
B	Bromazolam (>80% single component)
C	Methylenedioxymethamphetamine (**MDMA**, >80% single component)
D	Methylenedioxyamphetamine (**MDA**, 50%), dimethyl sulfone
E	Fentanyl (20%), caffeine, erythritol
F	Fentanyl (13%), fluorofentanyl (1%), caffeine
G	Fentanyl (6%), bromazolam (5%), chloroisobutyryl fentanyl (0.1%), caffeine
H*	Fentanyl (16%), fluorofentanyl (14%), 4-anilino-N-phenethyl-piperidine (**ANPP**, 3.7%), erythritol, caffeine
I*	Fentanyl (18%), fluorofentanyl (16%), **ANPP** (3.5%), erythritol, caffeine

[a] Street drug samples were acquired through Substance, the Vancouver Island Drug Checking Project, located in Victoria, Canada where sample composition was evaluated by FTIR and sample quantification was determined by PS-MS. *Samples H and I were provided by two different people who use drugs reporting the same drug from the same batch and supplier.

Mixed host sensors identify multi-component street drug samples where a comparable traditional sensor array cannot. Full spectral absorbance and fluorescence responses of each mixed host sensor (**DD4Cx4•CB8**, **DD8Cx4•CB8**, **DD13Cx4•CB8** and **DD13Cx4•CB7**) were acquired for all multi-component street drug samples, to determine if mixed host sensing operated in more complex sample matrices (Figure 4.32). To provide a direct comparison to a traditional sensor array, responses of each isolated DimerDye (**DD4Cx4**, **DD8Cx4**, and **DD13Cx4**) were also collected (Figure 4.33). Mixed host sensors provided responses of increased emission to cationic cocaine (A), **MDMA** (C) and **MDA** (D) multi-component samples, and varying decreased emission responses to neutral bromazolam (B) and fentanyl samples (E-I) (Figure 4.7a and Figure 4.32). In comparison, DimerDye sensors alone produced sensing responses smaller in amplitude, only providing increased emission responses for cationic samples A, C and D (Figure 4.7c and Figure 4.33). Select absorbance and fluorescence wavelengths from the array of mixed host sensors (Table 4.5) were applied to PCA analysis, providing discrimination of all multi-component samples (Figure 4.7b and Figure 4.34). The samples H and I were essentially identical by instrument-based drug checking analysis, having been reported as the same drug from the same supplier. The results of the mixed host sensor array overlap, and therefore correctly identify H and I as the same street drug sample. The same observations (Table 4.6) were applied to PCA analysis of the isolated DimerDye as a direct comparison of the classical single-host-class sensor array. Only discrimination of cationic samples A, C, and D were achieved, with the remaining samples (B, E-I) overlapping (Figure 4.7d and Figure 4.35). These results show the combination of multiple host classes introduces useful variability in binding interactions. The information-rich sensing responses provide a dramatic enhancement of the overall performance.

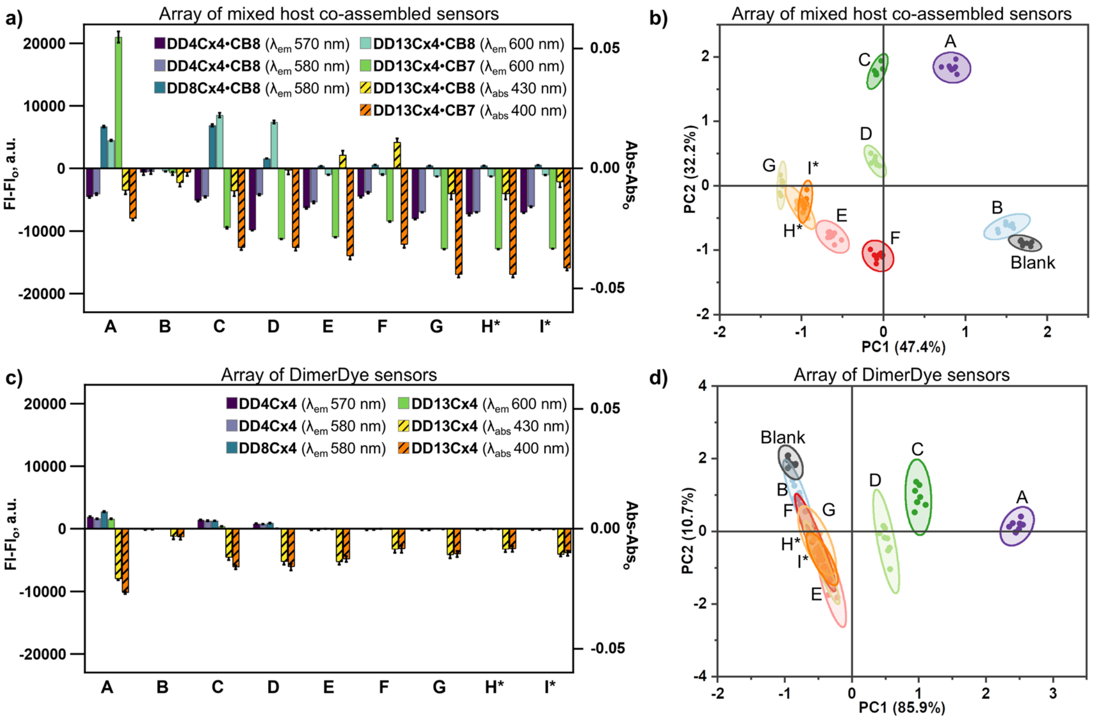

Figure 4.7. An array of mixed host co-assembled sensors provides information-rich responses that discriminate multi-component street drug samples. **a)** An array of mixed host co-assembled sensors shows diverse response patterns of absorbance and fluorescence to multi-component street drug samples A-I. **b)** PCA analysis using responses from **DD4Cx4•CB8**, **DD8Cx4•CB8**, **DD13Cx4•CB8**, and **DD13Cx4•CB7**. Samples contain [DD] = 10.5 µM, [CB] = 21 µM and [street drug sample] = 0.03 mg/mL. **c)** An array of DimerDye sensors shows similar response patterns of absorbance and fluorescence to multi-component street drug samples A-I. **d)** DimerDye sensors on their own do not discriminate multi-component street drug samples. Sensor array contains absorbance and fluorescence responses of **DD4Cx4**, **DD8Cx4** and **DD13Cx4**. Samples contain [DD] = 10.5 µM and [drug] = 0.03 mg/mL. PCA (correlation) scores plots show each sample set (n = 8) enclosed by 95% confidence ellipses. All samples are in NaH_2PO_4/Na_2HPO_4 (8.4 mM, pH 7.4) in H_2O with 2% MeOH.

4.4 Conclusion

This work shows the value of increased systems chemistry complexity through easily co-assembled mixed host sensors. Interconnected equilibria are created by combining multiple binding sites of different inherent affinities within the same sensing solution. In doing so, this approach harnesses simple combinations of macrocycles to generate more information-rich sensing fingerprints than aren't possible using the macrocycles in isolation from each other. This self-assembly-based design provides a facile route to broadening the scope of analytes, where the ability to detect untargeted analytes emerges through unexpected higher-order complexation interactions. This tactic can be easily applied to a wide range of established reporter chromophores, fluorophores, and recognition binding elements, offering almost unlimited possibilities for enhancing current sensing systems.

4.5 Supporting information

4.5.1 General materials and methods

4.5.1a Materials

The following chemicals were used as received without further purification. Cucurbit[7]uril hydrate (**CB7**), berberine chloride (**BC**), phenacetin (≥98.0%), procaine hydrochloride (≥97%), lidocaine hydrochloride monohydrate and levamisole hydrochloride were purchased from Sigma Aldrich. L-ascorbic acid (≥99.0%) was purchased from Fisher Scientific. 1-Adamantanamine (**$\mathbf{AdNH_3^+}$**) hydrochloride (≥99.0%) was purchased from TCI. Analytical drug samples from Cerilliant® were purchased through Sigma Aldrich as 1 mg/mL ampules in methanol or acetonitrile: morphine solution, diazepam solution, etizolam solution, cannabidiol (**CBD**) solution, Δ^9-tetrahydrocannabinol (**Δ^9-THC**) solution, (−)-Δ^8- tetrahydrocannabinol (**Δ^8-THC**) solution, (±)-3,4-methylenedioxymethamphetamine (**MDMA**) solution, cocaine hydrochloride solution, heroin solution and lorazepam solution.

The DimerDyes **DD4Cx4**, **DD8Cx4**, and **DD13Cx4** were synthesized and purified following reported protocols.[72] Cucurbit[8]uril (**CB8**) was synthesized and purified following literature procedures.[203, 204] *N,N'*-dimethyl-2,7-diazapyrenium diiodide (**MDAP**) was synthesized and purified following the reported protocol.[205]

Street drug samples were collected from Substance, the Vancouver Island Drug Checking Project, located in Victoria, BC, Canada.[200, 206] Solid samples (<10 mg) were submitted by people who use drugs as part of the drug checking service and were analyzed at Substance using established protocols. Fourier transform infrared (FTIR) spectra were collected using a 45° single-bounce attenuated total reflection (ATR) element. The resulting IR spectra were analyzed using classification models for the presence or absence of trace actives.[207] Paper spray-mass spectrometry (PS-MS) analysis was performed to confirm the presence of select target compounds and to provide quantitative concentration information.[202, 208-210] Cases where measurements were above the limit of quantification are reported as >80%, where the lower limit of quantification is approximately 0.1% (weight/weight).[206]

4.5.1b General UPLC-MS, NMR and MALDI-TOF methods

DimerDye purity was verified using a Waters UPLC-MS equipped with an Acquity UPLC BEH C18 1.7 µm (21 mm × 50 mm) column, UV-Vis and QDa detector. A gradient of 90% H_2O (0.4% CH_2O_2)/10% CH_3CN (0.4% CH_2O_2) to 30% H_2O (0.4% CH_2O_2)/70% CH_3CN (0.4% CH_2O_2) over 5 min at 0.5 mL/min flow was used for all purity traces. All NMR spectra were recorded on a Bruker Avance Neo 500 at 298 K (^{1}H: 500 MHz). ^{1}H NMR performed in NaH_2PO_4/Na_2PO_4 (50 mM, pD 7.4) was prepared using sodium phosphate monobasic and sodium phosphate dibasic in D_2O, the pD was adjusted with 1 M NaOD/DCl and determined using a pH meter.[118]

Mixed host co-assembly of **DD13Cx4•CB7** was verified by MALDI-TOF MS performed on a Bruker timsTOF *flex* MALDI-2 instrument (Bruker, Breman, Germany) in the positive ion mode. The instrument was calibrated before the experiment in an electrospray mode by a direct infusion of Agilent Calibration mix (Agilent Technologies, Santa Clara, CA, USA). A sample of **DD13Cx4** (50 µM) and **CB7** (50 µM) in NaH_2PO_4/Na_2HPO_4 (2 mM, pH 7.4) in H_2O was deposited (2 uL) onto a steel target plate and then dried under vacuum. A matrix solution was separately prepared by dissolving α-cyano-4-hydroxycinnamic acid (CHCA, 12 mg) and ammonium citrate dibasic (3.6 mg) in 30% H_2O/70% CH_3CN with 0.1% $C_2HF_3O_2$ (4 mL). The CHCA matrix solution was then deposited (2 µL) on top of the dried sample spot, the plate was dried again under vacuum prior to running.

4.5.1c General sample preparation – absorbance and fluorescence

Absorbance and fluorescence readings were collected on a BioTek Cytation-5 in NUNC black-walled optical bottom 384-well plates. All samples for spectroscopic studies were prepared in Milli-Q™ ultrapure water. Stock solutions of cucurbit[*n*]uril hosts **CB7** and **CB8** and dyes **MDAP** and **BC** were prepared in Milli-Q™ ultrapure water. The concentrations of stock dye solutions **MDAP** and **BC** were determined by UV-Vis titration measurements using the reported extinction coefficients (**BC**, $\varepsilon_{344\ \mathrm{nm}} = 22300\ \mathrm{M^{-1}cm^{-1}}$ and **MDAP**, $\varepsilon_{393\ \mathrm{nm}} = 7800\ \mathrm{M^{-1}cm^{-1}}$) and Beer-Lambert Law.[211-213] The concentration of cucurbit[*n*]uril stock solutions (**CB7** and **CB8**) were determined in H_2O following reported titration protocols with known strong binding dyes (**MDAP** and **BC**, respectively).[211, 212] **CB7** was titrated into **MDAP**, recording the emission at $\lambda_{em} = 454$ nm ($\lambda_{ex} = 393$ nm). **CB8** was titrated into **BC**, recording the emission at $\lambda_{em} = 542$ nm ($\lambda_{ex} = 421$ nm). Stock solutions of DimerDyes (1 mM) were prepared by mass in NaH_2PO_4/Na_2HPO_4 (10 mM, pH 7.4) in H_2O. Analytical drug ampules were evaporated overnight under a gentle air stream and redissolved in analytical-grade methanol to form 5.2 mM stock solutions used in the preparation of sensing samples. Solid multi-component street drug samples were dissolved in analytical-grade methanol to form 1.5 mg/mL stock solutions used in the preparation of sensing samples.

4.5.2. Macrocyclic host synthesis and purity – ^{1}H NMR and UPLC-MS

The calix[4]arene intermediate **sCx4-CHO** was synthesized following reported protocols.[54] DimerDyes **DD4Cx4**, **DD8Cx4** and **DD13Cx4** were synthesized and purified following reported protocols (Scheme 4.1).[72]

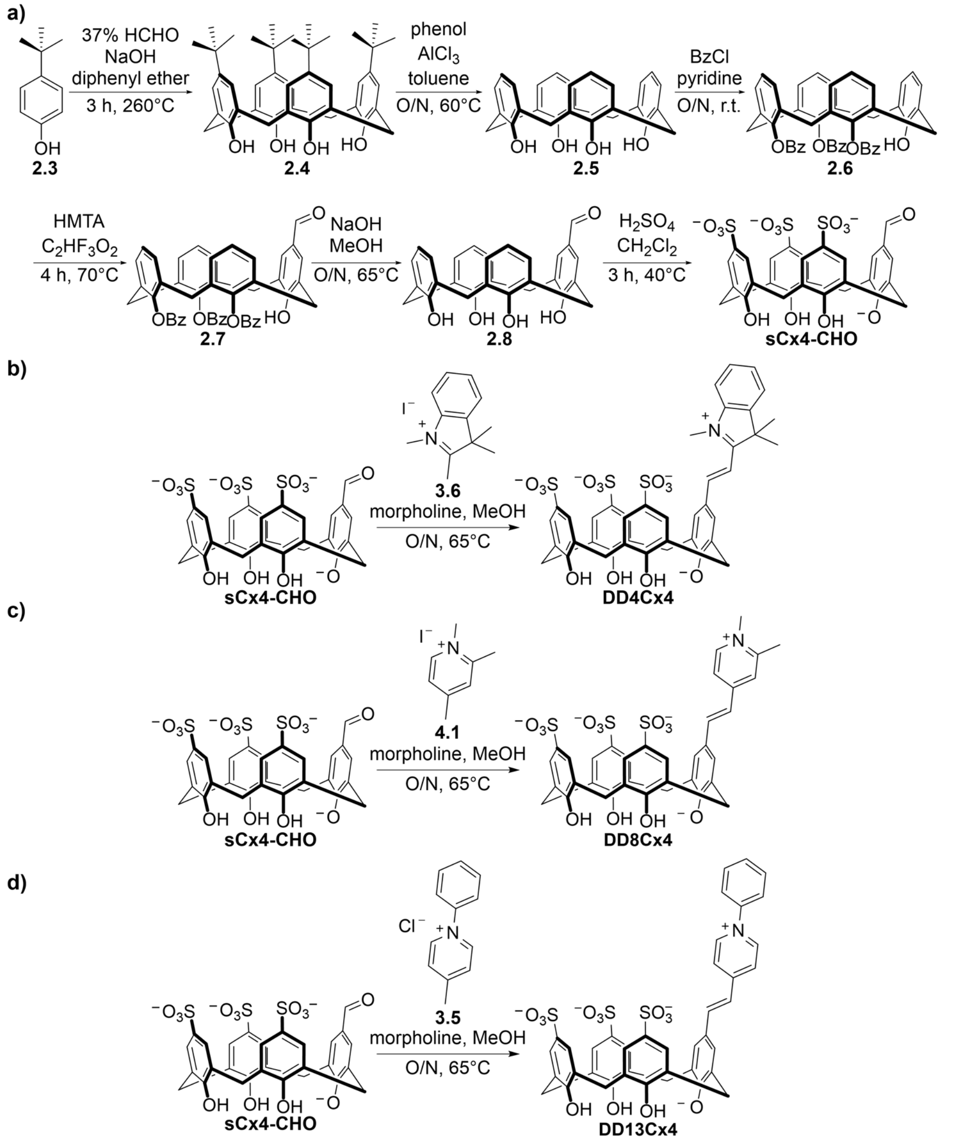

Scheme 4.1. Synthetic route of previously reported **a)** intermediate **sCx4-CHO** and DimerDyes, **b) DD4Cx4**, **c) DD8Cx4** and **d) DD13Cx4**.[54, 72]

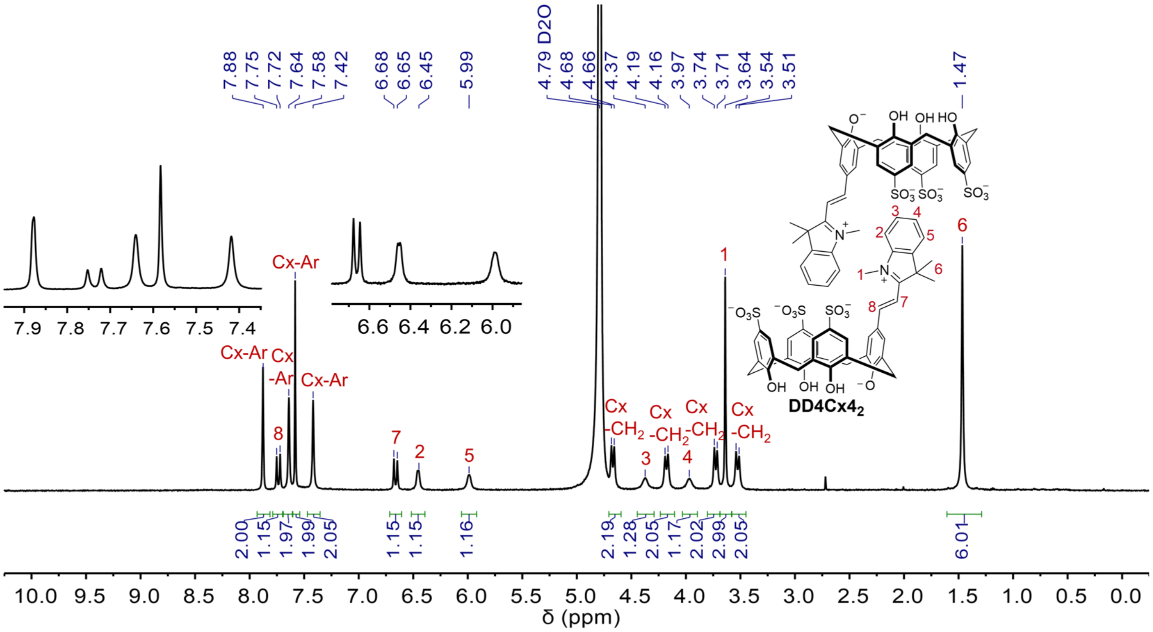

Figure 4.8. ^1H NMR spectrum of **DD4Cx4** in NaH_2PO_4/Na_2HPO_4 (50 mM, pD 7.4) in D_2O (500 MHz, 298 K) shows upfield-shifted pendant arm methyl and aromatic protons, supporting the existence of the molecule as a homodimer (**DD4Cx4$_2$**) in aqueous solution.

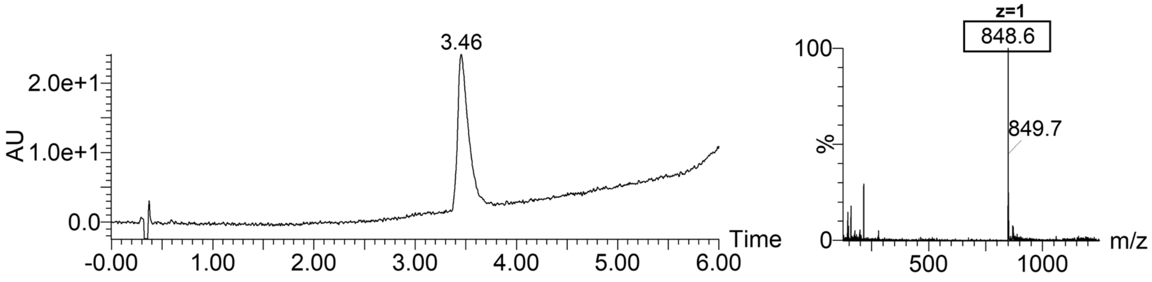

Figure 4.9. UPLC-MS (ES+) of **DD4Cx4**. Left = UV diode array detected chromatogram (190:400 nm). Right = positive ion mode ESI mass spectrum of the eluted peak.

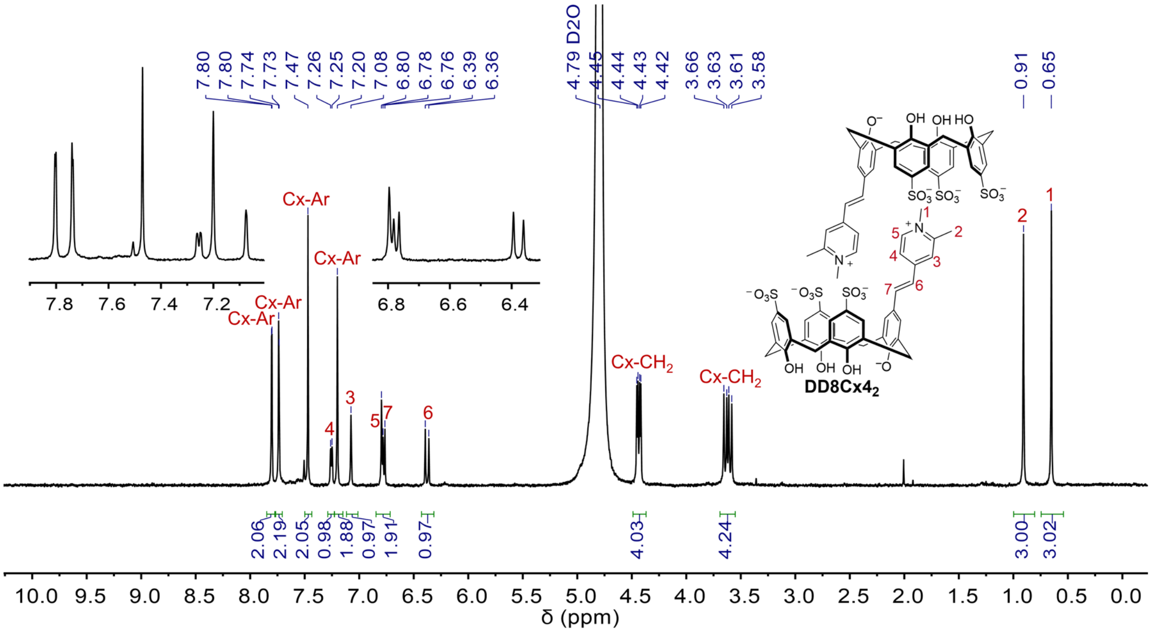

Figure 4.10. ^{1}H NMR spectrum of **DD8Cx4** in NaH_2PO_4/Na_2HPO_4 (50 mM, pD 7.4) in D_2O (500 MHz, 298 K) shows upfield-shifted pendant arm methyl and aromatic protons, supporting the existence of the molecule as a homodimer (**DD8Cx4$_2$**) in aqueous solution.

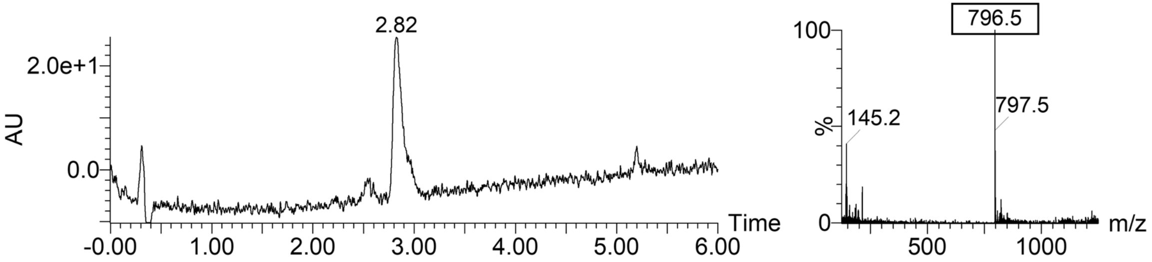

Figure 4.11. UPLC-MS (ES+) of **DD8Cx4**. Left = UV diode array detected chromatogram (190:800 nm). Right = positive ion mode ESI mass spectrum of the eluted peak.

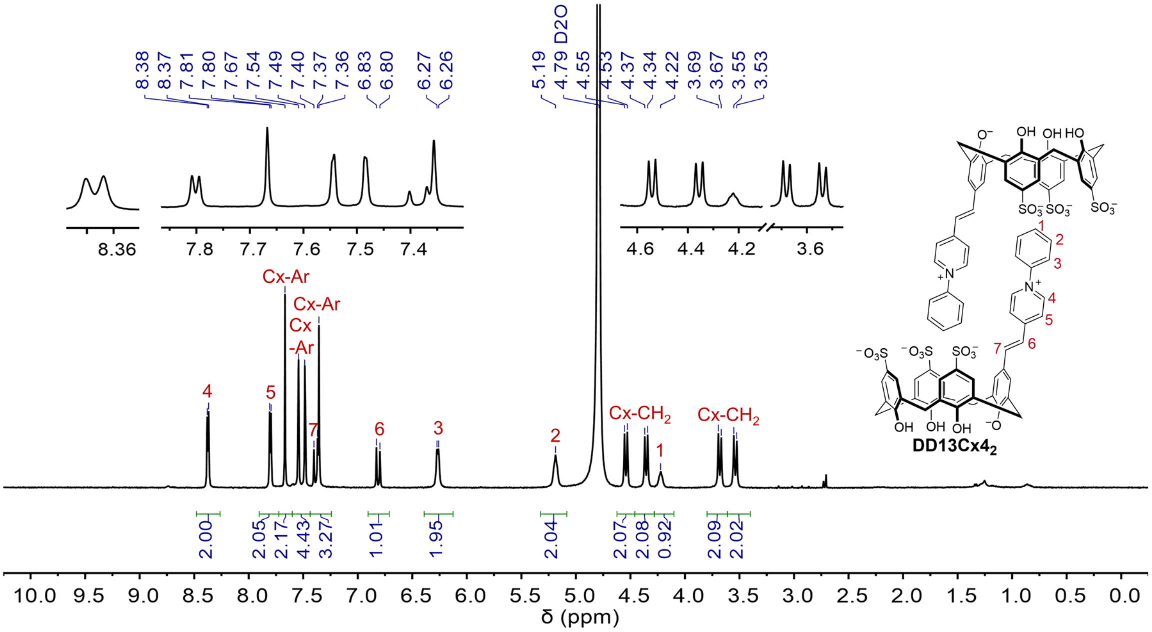

Figure 4.12. ^{1}H NMR spectrum of **DD13Cx4** in NaH_2PO_4/Na_2HPO_4 (50 mM, pD 7.4) in D_2O (500 MHz, 298 K) shows upfield-shifted pendant arm aromatic protons, supporting the existence of the molecule as a homodimer (**DD13Cx4$_2$**) in aqueous solution.

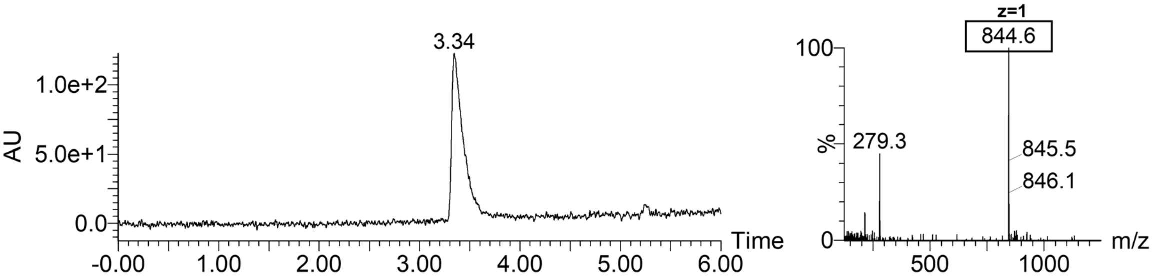

Figure 4.13. UPLC-MS (ES+) of **DD13Cx4**. Left = UV diode array detected chromatogram (190:800 nm). Right = positive ion mode ESI mass spectrum of the eluted peak.

Cucurbit[8]uril (**CB8**) was synthesized using literature methods.[203]

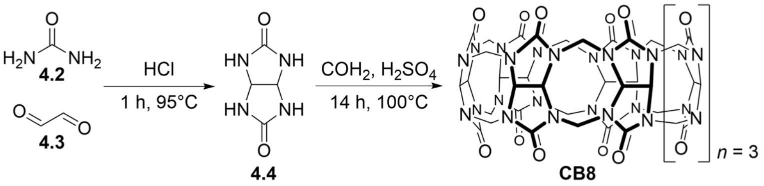

Scheme 4.2. Synthetic route of **CB8**.[203]

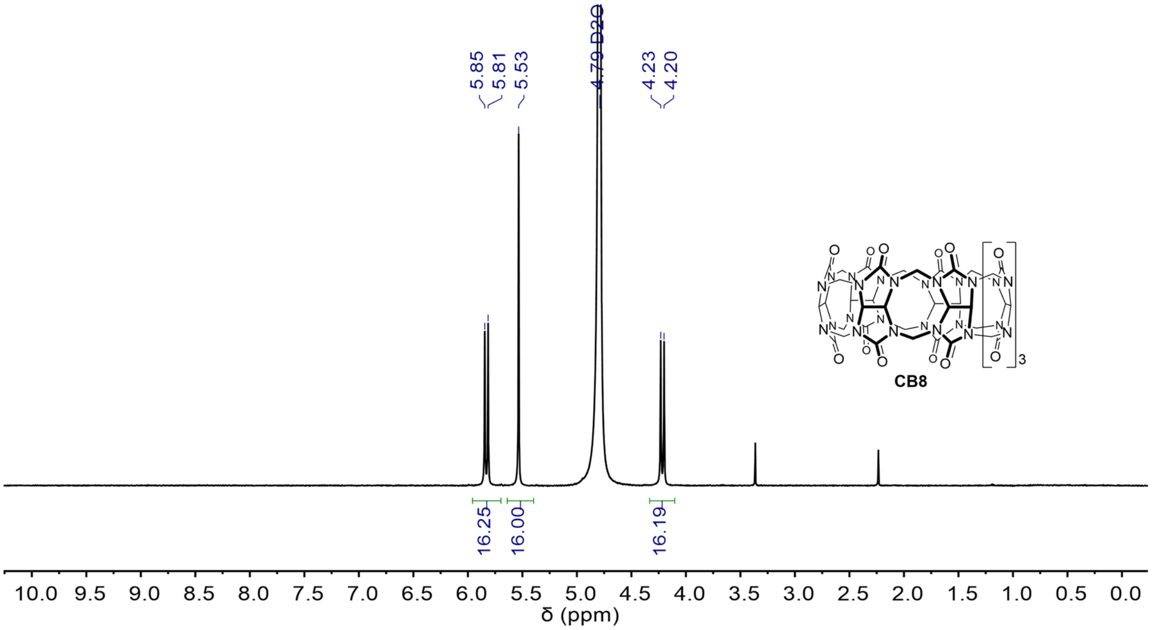

Figure 4.14. ^{1}H NMR spectrum of **CB8** in D_2O (500 MHz, 298 K).

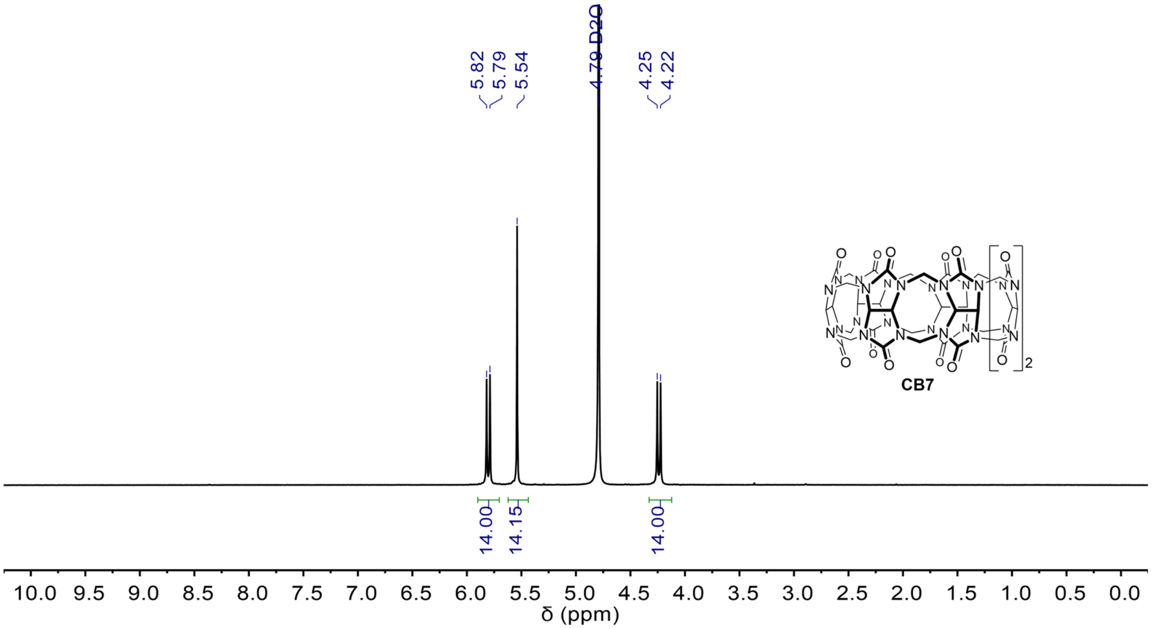

Figure 4.15. ^{1}H NMR spectrum of **CB7** in D_2O (500 MHz, 298 K).

4.5.3 Mixed host co-assembled DimerDye•cucurbit[*n*]uril sensors

4.5.3a Cucurbit[n]uril into DimerDye titrations – absorbance and fluorescence

Preliminary experiments of a panel of previously reported DimerDyes (**DD1Cx4**, **DD4Cx4**, **DD8Cx4**, **DD12Cx4** and **DD13Cx4**),[72] with **CB7** and **CB8** were conducted, data not shown. DimerDyes in this work were narrowed down to **DD4Cx4**, **DD8Cx4** and **DD13Cx4** that showed changes in absorbance and/or fluorescence upon addition of **CB7** or **CB8**.

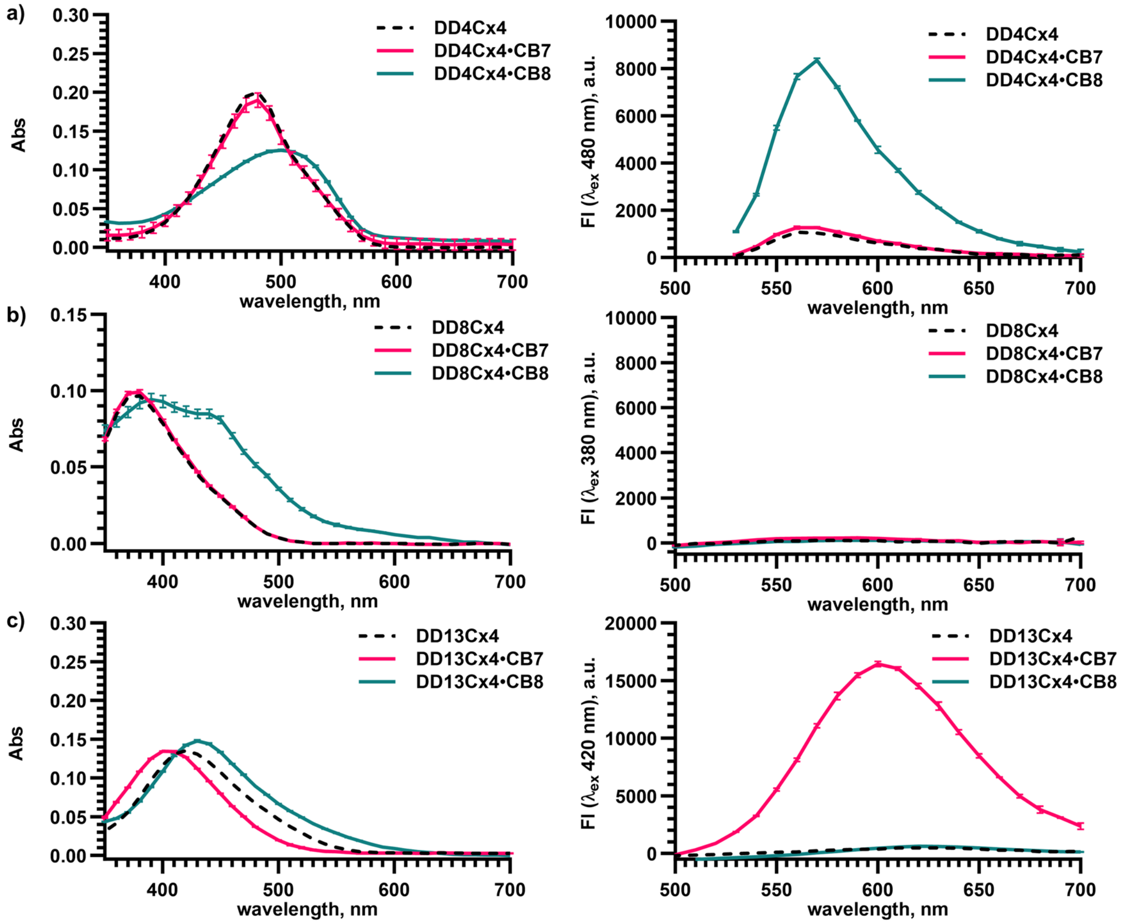

Figure 4.16. Select cucurbit[*n*]urils induce changes in DimerDye absorbance and fluorescence. **a) DD4Cx4** produces a red shift in absorbance and turn-on fluorescence response with **CB8**. No change in **DD4Cx4** absorbance or fluorescence is observed with **CB7**. **b) DD8Cx4** produces a red shift in absorbance with **CB8**. No change in **DD8Cx4** absorbance or fluorescence is observed with **CB7**. **c) DD13Cx4** produces a blue shift in absorbance and turn-on fluorescence response with **CB7** and a red shift in absorbance with **CB8**. Traces of DimerDyes (10.5 µM) alone are shown as black dashed lines. DimerDyes (10.5 µM) with **CB7** (21 µM) are shown as red lines. DimerDyes (10.5 µM) with **CB8** (21 µM) are shown as teal lines. All solutions in NaH_2PO_4/Na_2HPO_4 (10 mM, pH 7.4) in H_2O. Absorbance and fluorescence spectra are plotted as the mean of experiments done in triplicate with error bars corresponding to the standard deviation. Error bars are not visible in cases where the error is smaller than the depicted data point.

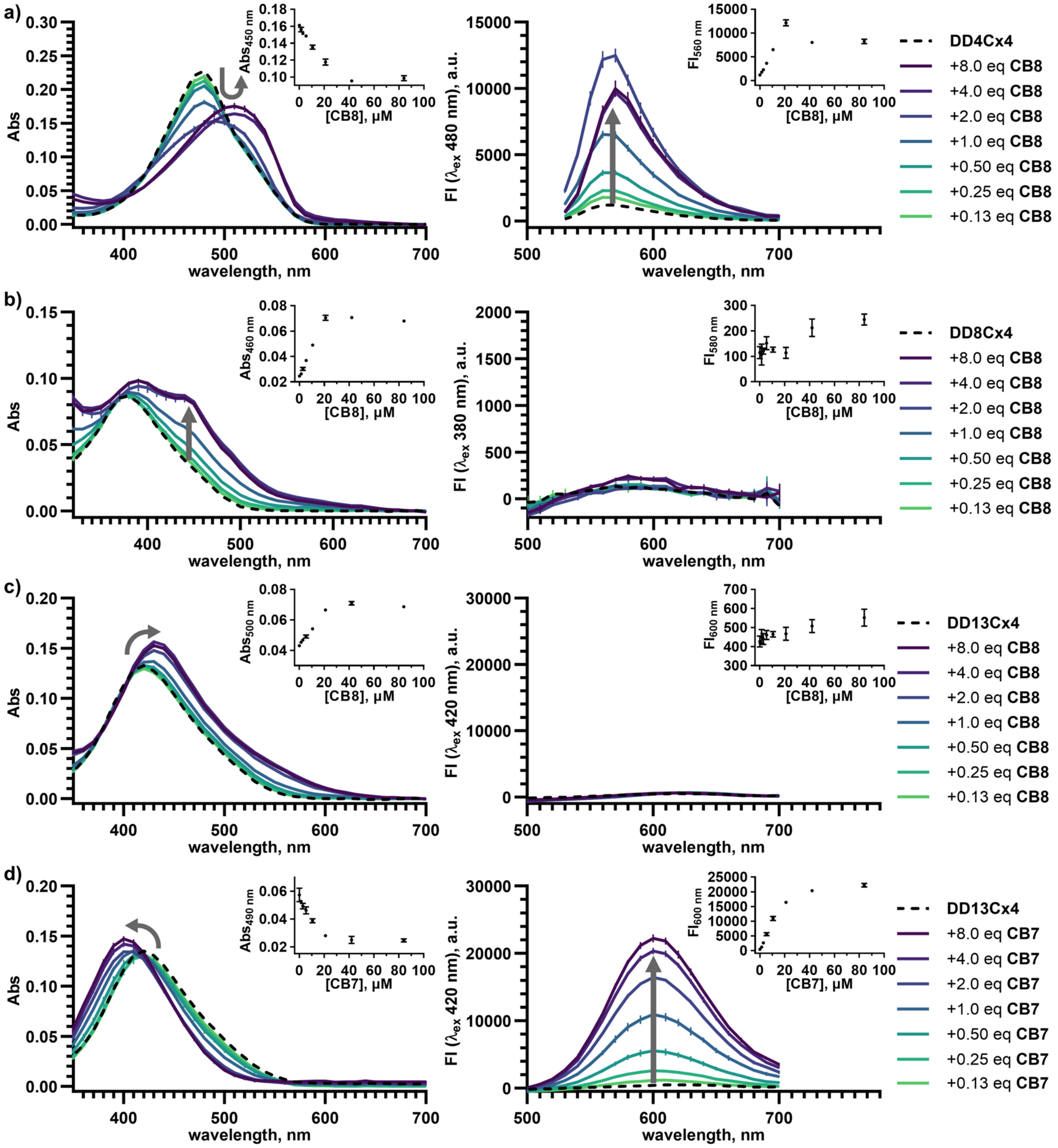

Figure 4.17. Titrations of cucurbit[*n*]uril into DimerDye induce red/blue shifts in absorbance and turn-on fluorescence responses. **CB8** titrations into **a) DD4Cx4** (10.5 μM), **b) DD8Cx4** (10.5 μM), and **c) DD13Cx4** (10.5 μM). **CB7** titration into **d) DD13Cx4** (10.5 μM). Titrations are monitored by absorbance (left) and fluorescence (right), where the darkest purple line represents the highest concentration of CB (84 μM) and the lightest green line represents the lowest concentration of CB (1.3 μM). Traces of DimerDyes (10.5 μM) alone are shown as black dashed lines. Insets show the binding isotherms. All solutions in NaH_2PO_4/Na_2HPO_4 (10 mM, pH 7.4) in H_2O. Absorbance and fluorescence spectra are plotted as the mean of experiments done in triplicate with error bars corresponding to the standard deviation. Error bars are not visible in cases where the error is smaller than the depicted data point.

Previous stopped-flow dimerization studies determined a dimer association constant (K_a) of $(1.6 \pm 0.9) \times 10^5$ M^{-1} for **DD1Cx4**.[126] Apparent dissociation constants ($K_{d,\,app}$) of DD•CB mixed host co-assemblies were determined using absorbance binding isotherms, plotting the change in DimerDye absorbance (Abs-Abs$_o$) as a function of cucurbit[*n*]ruil concentration. The data was fit in GraphPad Prism using a direct one site binding equation, constrained by the constant concentration of DimerDye (10.5 μM).

$$Y = A \times \frac{\left(DD + x + K_{d,\,app}\right) - \sqrt{(DD + x + K_{d,\,app})^2 - (4DDx)}}{2DD}$$

Where, A = amplitude of change in absorbance (Abs-Abs$_o$),

DD = concentration of DimerDye

x = amount titrated

$K_{d,\,app}$ = apparent dissociation constant

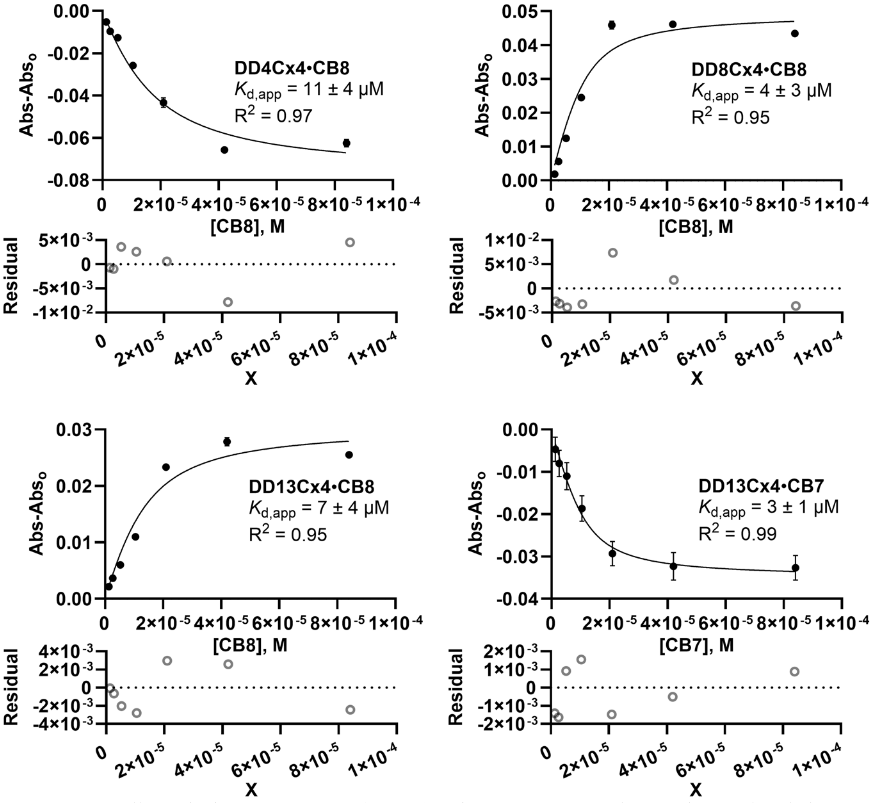

Figure 4.18. Apparent dissociation constants ($K_{d,\,app}$) of DD•CB complexes determined from a direct one site binding model. Triplicate data from direct titrations of **CB8** and **CB7** into DimerDyes **DD4Cx4** (10.5 μM), **DD8Cx4** (10.5 μM) and **DD13Cx4** (10.5 μM). Error bars were plotted for each triplicate but are not visible in cases where the error is smaller than the plotted point. All solutions in NaH_2PO_4/Na_2HPO_4 (10 mM, pH 7.4) in H_2O. Note: These fits do not account for the dissociation of the dimer and should only be considered as comparisons between related systems.

4.5.3b ^{1}H NMR investigation of mixed host co-assembled DD•CB complexes

^{1}H NMR experiments were conducted to further validate DD•CB complexation interactions. Studies were limited by the solubility restraints of DD•CB complexes at concentrations required for ^{1}H NMR studies. Therefore, only mixed host complexation interactions of **DD4Cx4•CB8** and **DD13Cx4•CB7** were investigated by ^{1}H NMR. The turn-off fluorescence sensing mechanism of **DD13Cx4•CB7** was further probed by ^{1}H NMR through the addition of a **CB7** selective guest (**$AdNH_3^+$**). Solubility limitations prevented further experimental investigation of the size of complexes formed by dynamic light scattering (DLS) or diffusion ordered spectroscopy (DOSY).

Stock solutions of cucurbit[*n*]uril hosts (**CB7** and **CB8**) were prepared in D_2O and concentrations were determined by titration experiments with known strong binding dyes (**MDAP** and **BC**, respectively) in H_2O.[211, 212] Stock solutions of DimerDyes (1 mM) were prepared by mass in NaH_2PO_4/Na_2HPO_4 (50 mM, pD 7.4) in D_2O. Final NMR solutions contained [DD] = 100 μM, [CB] = 100 μM in NaH_2PO_4/Na_2HPO_4 (10 mM, pD 7.4) in D_2O.

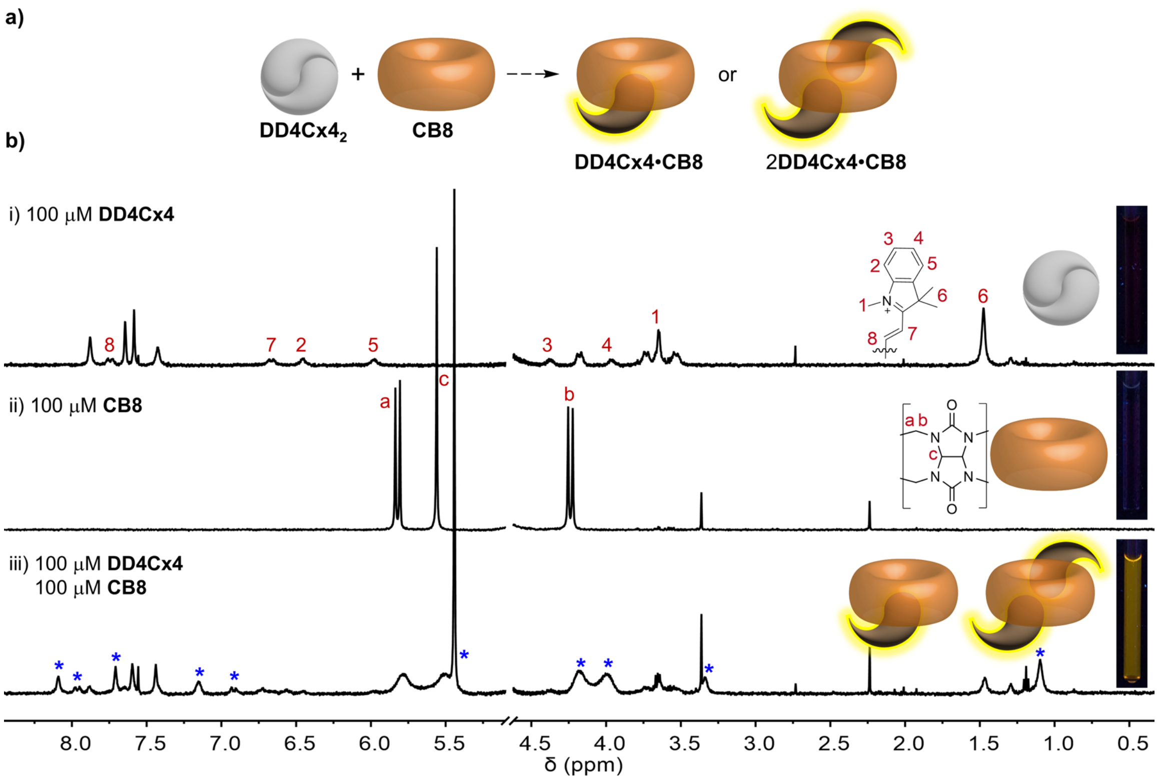

Figure 4.19. DD4Cx4 and **CB8** form a fluorescent mixed host sensor. **a)** Schematic of **DD4Cx4•CB8** co-assembly illustrating possible binary and ternary complexes that could form in the larger **CB8** cavity.[187-189] **b)** ^{1}H NMR of i) **DD4Cx4** (100 μM). Upfield-shifted aromatic peaks in fast exchange and non-fluorescent appearance support the existence of the homodimer **DD4Cx4₂** in aqueous solution. ii) **CB8** (100 μM). iii) **DD4Cx4** (100 μM) and **CB8** (100 μM) combined. Blue stars illustrate the appearance of new **DD4Cx4** and **CB8** resonances. The presence of new upfield-shifted and broadened aromatic peaks and upfield-shifted methyl peaks indicate **DD4Cx4•CB8** complexation. Fluorescent appearance of the NMR tube further supports the disassembly of the homodimer **DD4Cx4₂**. NMR tube irradiated with a hand-held UV lamp (λ_{ex} = 356 ± 20 nm). All samples in NaH_2PO_4/Na_2HPO_4 (10 mM, pD 7.4) in D_2O (500 MHz, 298 K).

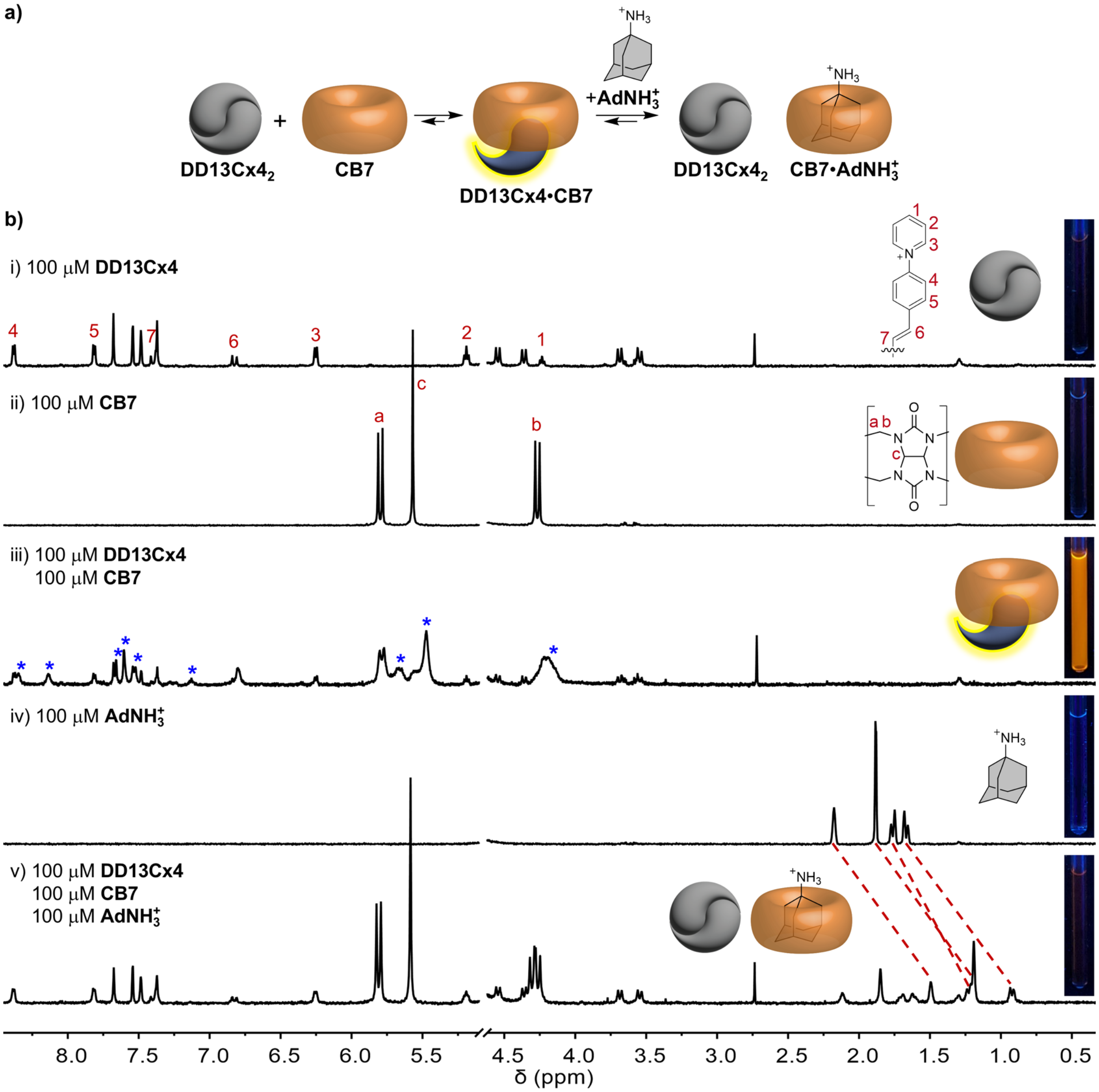

Figure 4.20. DD13Cx4•CB7 complex functions as a turn-off mixed host sensor for strong binding guests of **CB7**. **a)** Schematic of **DD13Cx4•CB7** formation and turn-off sensing mechanism upon analyte addition. **b)** ^{1}H NMR of i) **DD13Cx4** (100 µM) shows upfield-shifted aromatic peaks in fast exchange. Non-fluorescent appearance of the NMR tube supports the existence of homodimer **DD13Cx4$_2$** in aqueous solution. ii) **CB7** (100 µM). iii) **DD13Cx4** (100 µM) and **CB7** (100 µM) combined. Blue stars illustrate the appearance of new **DD13Cx4** and **CB7** resonances. The presence of new upfield-shifted and broadened aromatic peaks indicate **DD4Cx4•CB8** complexation. The fluorescent appearance of the NMR tube further supports the disassembly of the homodimer **DD13Cx4$_2$**. iv) **$AdNH_3^+$** (100 µM). v) **DD13Cx4** (100 µM), **CB7** (100 µM) and **$AdNH_3^+$** (100 µM) combined. Upfield-shifted **$AdNH_3^+$** peaks (red dashed lines) and the return of homodimer **DD13Cx4$_2$** peaks indicate a **CB7•$AdNH_3^+$** assembly forms. The non-fluorescent appearance of the NMR tube further supports the reformation of the homodimer **DD13Cx4$_2$**. NMR tube irradiated with a hand-held UV lamp (λ_{ex} 356 ± 20 nm). All samples in NaH_2PO_4/Na_2HPO_4 (10 mM, pD 7.4) in D_2O (500 MHz, 298 K).

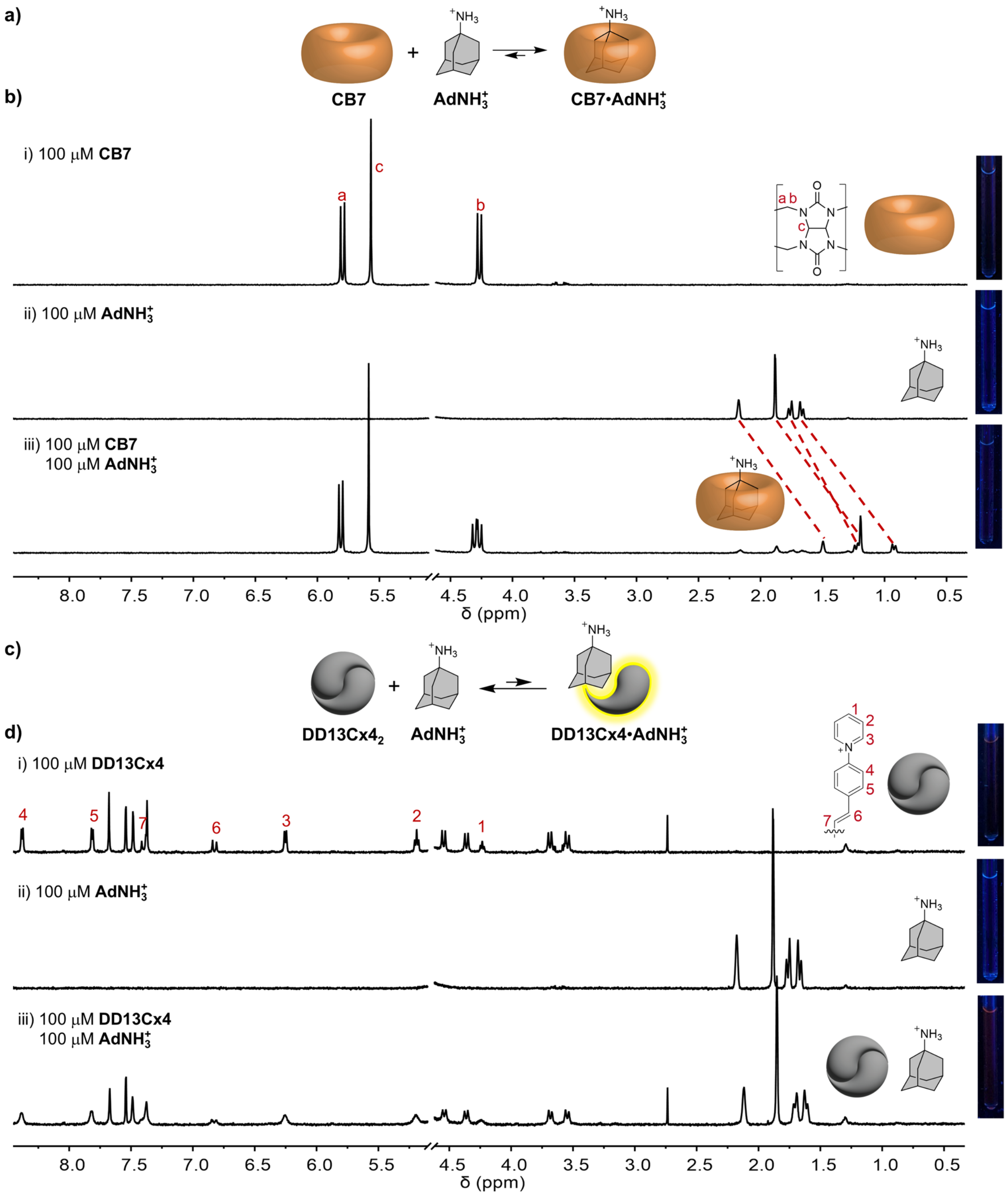

Figure 4.21. Control experiments demonstrate that the **DD13Cx4•CB7** mixed host complex is responsible for observed sensing responses. **a)** Schematic illustrating **CB7•AdNH$_3^+$** favoured complexation. **b)** ^{1}H NMR of i) **CB7** (100 µM), ii) **AdNH$_3^+$** (100 µM), and iii) **CB7** (100 µM) combined with **AdNH$_3^+$** (100 µM). Complexation of **AdNH$_3^+$** is observed by upfield-shifted resonances in slow exchange, shown as red dashed lines. All NMR tubes are non-fluorescent in appearance as **CB7** and **AdNH$_3^+$** are spectroscopically silent. **c)** Schematic illustrating the homodimer **DD13Cx4$_2$** is favoured over **DD13Cx4•AdNH$_3^+$** complexation. **d)** ^{1}H NMR of i) **DD13Cx4** (100 µM), upfield-shifted aromatic peaks in fast exchange and non-fluorescent appearance supports the existence of homodimer **DD13Cx4$_2$** in aqueous solution. ii) **AdNH$_3^+$** (100 µM). iii) **DD13Cx4** (100 µM) and **AdNH$_3^+$** (100 µM) combined. Minimal shifts observed in **AdNH$_3^+$** and **DD13Cx4$_2$** resonances indicate little disruption of the **DD13Cx4$_2$** homodimer. The non-fluorescent appearance of the NMR tube further supports the presence of **DD13Cx4$_2$** homodimer. NMR tube irradiated with a hand-held UV lamp (λ_{ex} = 356 ± 20 nm). All samples in NaH_2PO_4/Na_2HPO_4 (10 mM, pD 7.4) in D_2O (500 MHz, 298 K).

4.5.3c Molecular modeling of mixed host co-assembled DD13Cx4•CB7

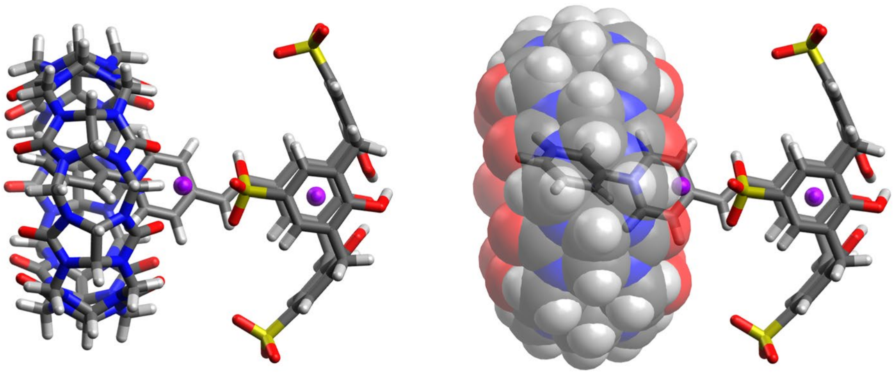

Figure 4.22. Molecular modeling using DFT (RWB97X-D/6-31G(D)) was performed with Spartan to illustrate a potential 1:1 binding geometry between **DD13Cx4** and **CB7**. To partially counterbalance the overall charge of the complex, two sodium ions were strategically placed: one within the **DD13Cx4** cavity, which is recognized for its Na^+ binding capability, and another adjacent to the **CB7** portals, known for their cation-binding affinity.[214] It is important to note that, in reality, a variety of conformers likely exist, differing in both the number and positions of bound counterions. Therefore, this molecular model should be viewed as a visual representation intended to provide insight into possible binding configurations, rather than a definitive structural depiction.

4.5.4 DimerDye and mixed host co-assembly titrations with cocaine – absorbance and fluorescence

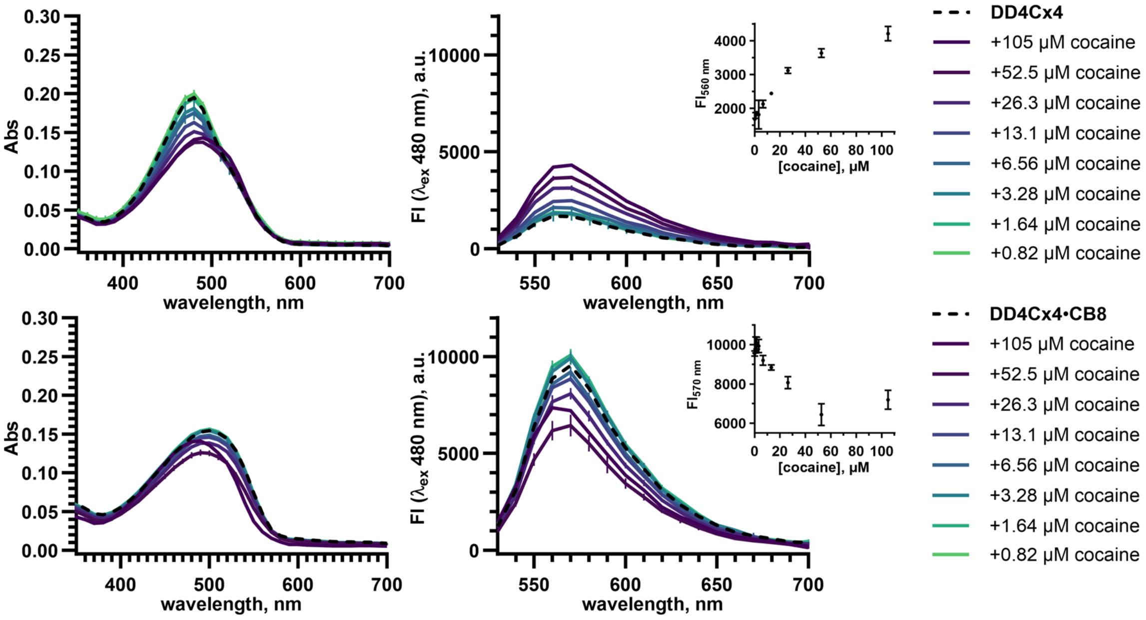

Figure 4.23. Titrations of cocaine into **DD4Cx4** (top) and cocaine into **DD4Cx4•CB8** (bottom). Titrations monitored by absorbance and fluorescence, where the darkest purple line represents the highest concentration of cocaine (105 μM), and the lightest green line represents the lowest concentration of cocaine (0.82 μM). Traces of DimerDye ([**DD4Cx4**] = 10.5 μM) or **DD4Cx4•CB8** ([**DD4Cx4**] = 10.5 μM, [**CB8**] = 21 μM) alone are shown as black dashed lines. Insets show the fluorescence binding isotherms. All solutions in NaH_2PO_4/Na_2HPO_4 (8.4 mM, pH 7.4) in H_2O with 2% MeOH. Absorbance and fluorescence spectra are plotted as the mean of experiments done in triplicate with error bars corresponding to the standard deviation. Error bars are not visible in cases where the error is smaller than the depicted data point.

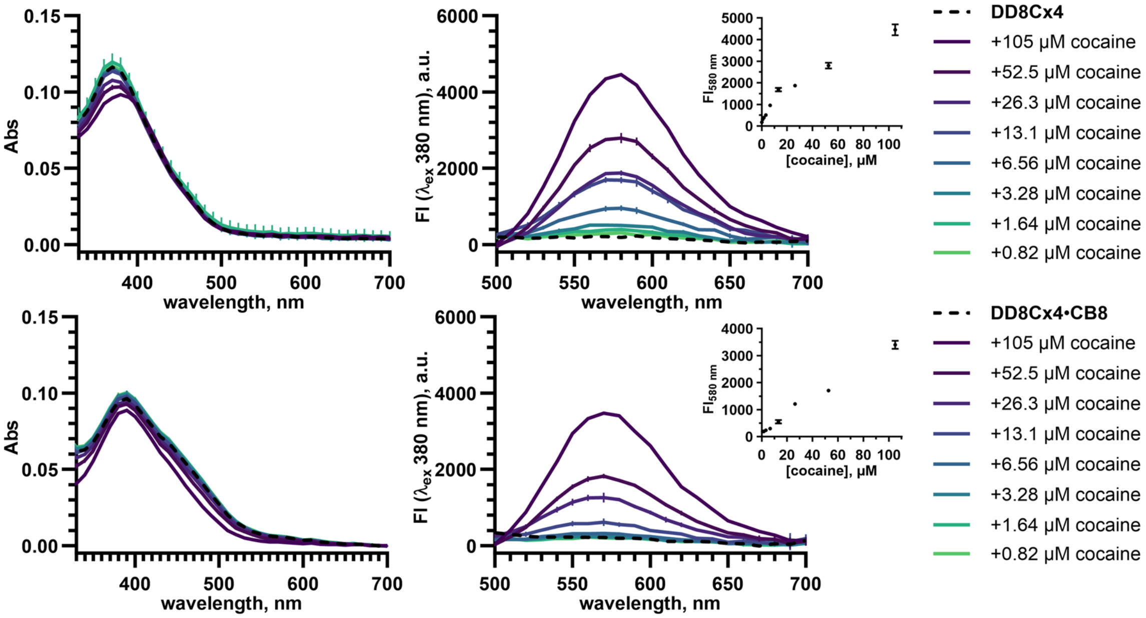

Figure 4.24. Titrations of cocaine into **DD8Cx4** (top) and cocaine into **DD8Cx4•CB8** (bottom). Titrations monitored by absorbance and fluorescence, where the darkest purple line represents the highest concentration of cocaine (105 µM) and the lightest green line represents the lowest concentration of cocaine (0.82 µM). Traces of DimerDye ([**DD8Cx4**] = 10.5 µM) or **DD8Cx4•CB8** ([**DD8Cx4**] = 10.5 µM, [**CB8**] = 21 µM) alone are shown as black dashed lines. Insets show the fluorescence binding isotherms. All solutions in NaH_2PO_4/Na_2HPO_4 (8.4 mM, pH 7.4) in H_2O with 2% MeOH. Absorbance and fluorescence spectra are plotted as the mean of experiments done in triplicate with error bars corresponding to the standard deviation. Error bars are not visible in cases where the error is smaller than the depicted data point.

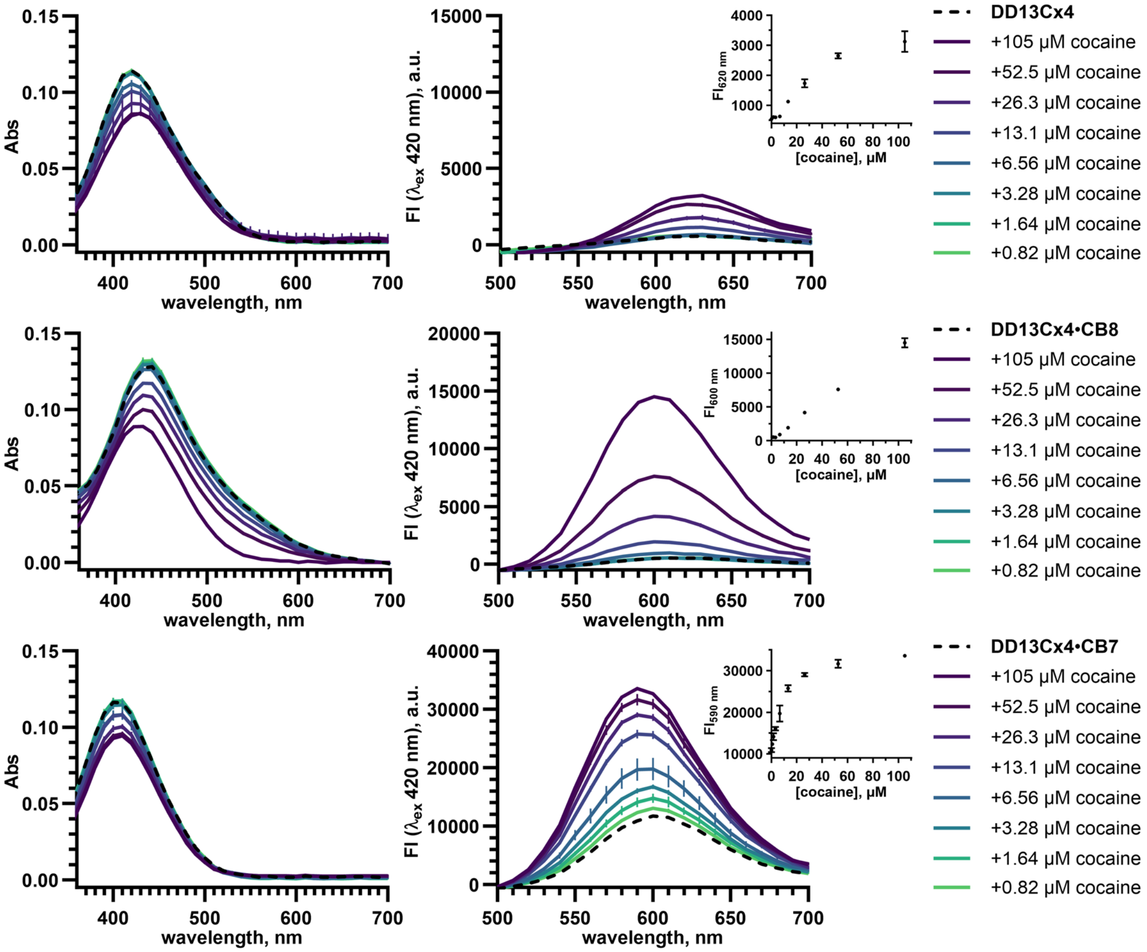

Figure 4.25. Titrations of cocaine into **DD13Cx4** (top), cocaine into **DD13Cx4•CB8** (middle) and cocaine into **DD13Cx4•CB7** (bottom). Titrations monitored by absorbance and fluorescence, where the darkest purple line represents the highest concentration of cocaine (105 µM) and the lightest green line represents the lowest concentration of cocaine (0.82 µM). Traces of DimerDye ([**DD13Cx4**] = 10.5 µM), **DD13Cx4•CB8** ([**DD13Cx4**] = 10.5 µM, [**CB8**] = 21 µM) and **DD13Cx4•CB7** ([**DD13Cx4**] = 10.5 µM, [**CB7**] = 21 µM) alone are shown as black dashed lines. Insets show the fluorescence binding isotherms. All solutions in NaH_2PO_4/Na_2HPO_4 (8.4 mM, pH 7.4) in H_2O with 2% MeOH. Absorbance and fluorescence spectra are plotted as the mean of experiments done in triplicate with error bars corresponding to the standard deviation. Error bars are not visible in cases where the error is smaller than the depicted data point.

Limits of detection (LODs) were determined by fitting a linear regression to the initial linear region of each cocaine titration curve and calculating $LOD = \frac{3.3\sigma}{m}$, where σ is the standard deviation of the y-intercept and m is the slope of the linear regression.[161]

Table 4.2. LODs of cocaine with DimerDye and mixed host co-assembled sensors in NaH_2PO_4/Na_2HPO_4 (8.4 mM, pH 7.4) in H_2O with 2% MeOH.

Sensor	σ	m	LOD (μM)
DD4Cx4	45.1	53.6	2.78
DD4Cx4•CB8	202	-184	3.62
DD8Cx4	17.9	114	0.51
DD8Cx4•CB8	24.7	30.9	2.64
DD13Cx4	25.7	41.5	2.05
DD13Cx4•CB8	66.1	136	1.60
DD13Cx4•CB7	340	1106	1.02

4.5.5 Principal component analysis – absorbance and fluorescence

PCA analysis was conducted using select absorbance and fluorescence wavelength responses. A covariance matrix was used in cases where only absorbance or only fluorescence measurements were compiled. In cases where absorbance and fluorescence measurements were combined, a correlation matrix was used. The general process for PCA analysis is described below. A detailed tutorial review providing methods on improving visual discrimination is reported by Anslyn and co-workers.[65]

- Spectral scans of sensor absorbance and fluorescence responses to different analytes were visually compared. Key individual wavelengths that provided separated patterns of response, different/unique patterns and large amplitudes in change were initially selected (e.g. absorbance and fluorescence maxima of each sensor and wavelengths that capture induced shifts in maxima).
- PCA analysis was done using the selected wavelength responses, producing loading plots that identify the vector contribution of each sensor wavelength.
- Loading plots were evaluated and sensor responses were narrowed down to provide the most discrimination. This was done through an iterative process of PCA and loading plot re-evaluation, eliminating sensor vectors with small or close to zero contribution, eliminating unnecessary overlapping vectors (sensors with redundant sensing patterns) and maximizing overall vector separation.

4.5.5a Identifying illicit drugs and adulterants

Discriminant analysis experiments of illicit drugs and adulterants were conducted in NUNC black-walled optical bottom 384-well plates, with 70 µL final well volumes. Final solutions contained [DD] = 10.5 µM, [CB] = 21 µM, and [drug] = 105 µM in NaH_2PO_4/Na_2HPO_4 (8.4 mM, pH 7.4) in H_2O with 2% MeOH. Mixed host sensor combinations of **DD4Cx4•CB8**, **DD8Cx4•CB8**, **DD13Cx4•CB8**, and **DD13Cx4•CB7** were tested for their responses to each individual illicit drug and adulterant. Absorbance and emission wavelengths were selected based on preliminary experimental results, using excitation wavelengths at the maxima of each DimerDye (**DD4Cx4** λ_{ex} = 480 nm, **DD8Cx4** λ_{ex} = 380 nm and **DD13Cx4** λ_{ex} = 420 nm) (Table 4.3). Cannabinoid sensing of DimerDyes alone was also tested using the same selected absorbance and fluorescence wavelengths (Table 4.4), this was done to validate the improved differentiation ability of the array of mixed host sensors. Absorbance and fluorescence end-point measurements of each DD•CB•drug combination were collected in 12 replicates, along with 2 solvent blank measurements. The raw data was pre-processed by subtracting the solvent blank from each DD•CB•drug measurement, then the two highest and two lowest data values were systematically excluded. Absorbance and fluorescence wavelengths that provided discrimination of drugs and adulterants were selected for PCA, while aiming to minimize the number of observations. PCA correlation plots with confidence ellipses (95%) and loading vectors were plotted on sample sets of 8 replicates using OriginPro 2022b Principal Component Analysis App (Version: 1.50, File Name: PCAC.opx).

Table 4.3. Mixed host sensor wavelengths used in PCA analysis for the identification of drugs and adulterants.

Mixed host sensor	Absorbance (nm)	Fluorescence (λ_{ex} (nm), λ_{em} (nm))
DD4Cx4•CB8	480	480, 570 480, 600
DD8Cx4•CB8	440	380, 570
DD13Cx4•CB8	400 430	420, 600
DD13Cx4•CB7	400 430	420, 600

Table 4.4. DimerDye sensor wavelengths used in PCA analysis for the identification of cannabinoids.

DimerDye	Absorbance (nm)	Fluorescence (λ_{ex} (nm), λ_{em} (nm))
DD4Cx4	480	480, 570 480, 600
DD8Cx4	440	380, 570
DD13Cx4	400 430	420, 600

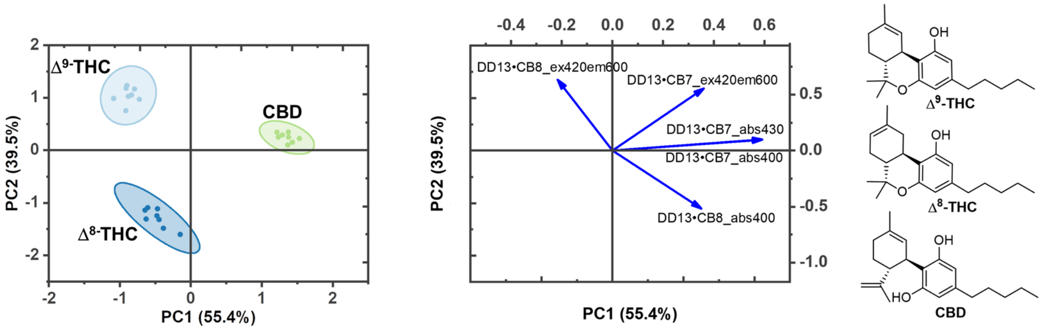

Figure 4.26. An array of mixed host sensors differentiates structurally similar neutral cannabinoids. Sensor array includes absorbance and fluorescence responses of mixed host sensors **DD13Cx4•CB7** and **DD13Cx4•CB8**. PCA (correlation) scores plot shows each sample set (n = 8) enclosed by 95% confidence ellipses with the respective loading plot of absorbance and fluorescence observations shown as blue arrows. Chemical structures are represented in the expected protonation forms under sensing conditions of pH 7.4. Samples contain [DD] = 10.5 µM, [CB] = 21 µM, and [drug] = 105 µM. All samples are in NaH_2PO_4/Na_2HPO_4 (8.4 mM, pH 7.4) in H_2O with 2% MeOH.

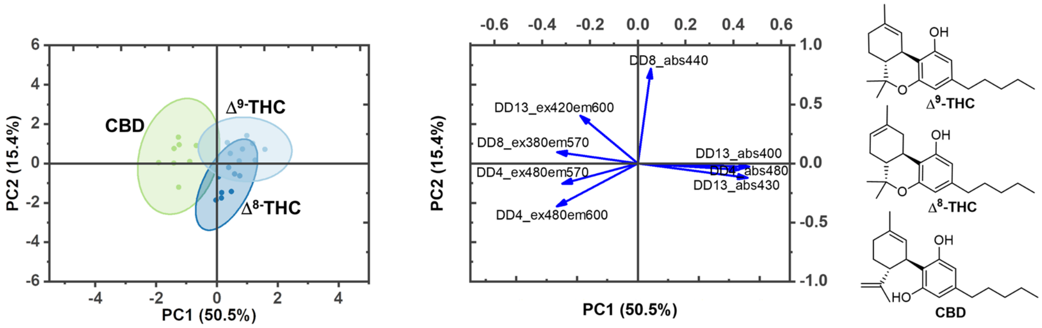

Figure 4.27. An array of DimerDye sensors does not differentiate structurally similar neutral cannabinoids. Sensor array includes absorbance and fluorescence responses of **DD4Cx4**, **DD8Cx4**, and **DD13Cx4**. PCA (correlation) scores plot shows each sample set (n = 8) enclosed by 95% confidence ellipses with the respective loading plot of absorbance and fluorescence observations shown as blue arrows. Chemical structures are represented in the expected protonation forms under sensing conditions of pH 7.4. Samples contain [DD] = 10.5 µM, and [drug] = 105 µM. All samples are in NaH_2PO_4/Na_2HPO_4 (8.4 mM, pH 7.4) in H_2O with 2% MeOH.

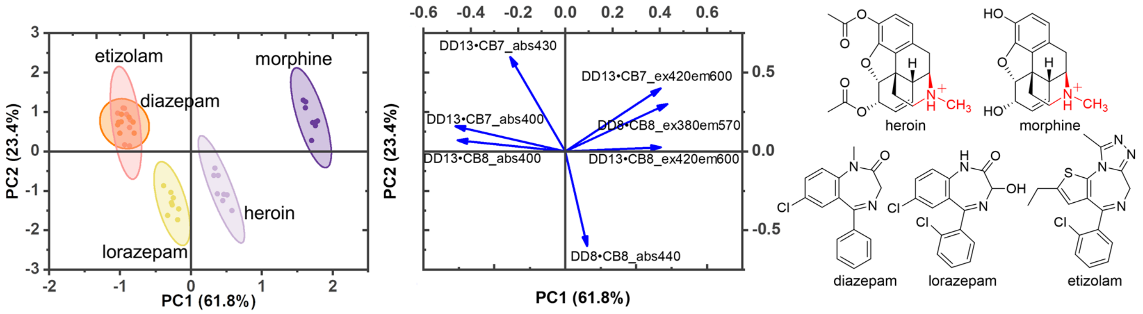

Figure 4.28. An array of mixed host sensors shows the differentiation of central nervous system depressant cationic opiates and neutral benzodiazepine analogs. Sensor array includes absorbance and fluorescence responses of mixed host sensors **DD8Cx4•CB8**, **DD13Cx4•CB8**, and **DD13Cx4•CB7**. PCA (correlation) scores plot shows each sample set (n = 8) enclosed by 95% confidence ellipses with the respective loading plot of absorbance and fluorescence observations shown as blue arrows. Chemical structures are represented in the expected protonation forms under sensing conditions of pH 7.4. Samples contain [DD] = 10.5 µM, [CB] = 21 µM, and [drug] = 105 µM. All samples are in NaH_2PO_4/Na_2HPO_4 (8.4 mM, pH 7.4) in H_2O with 2% MeOH.

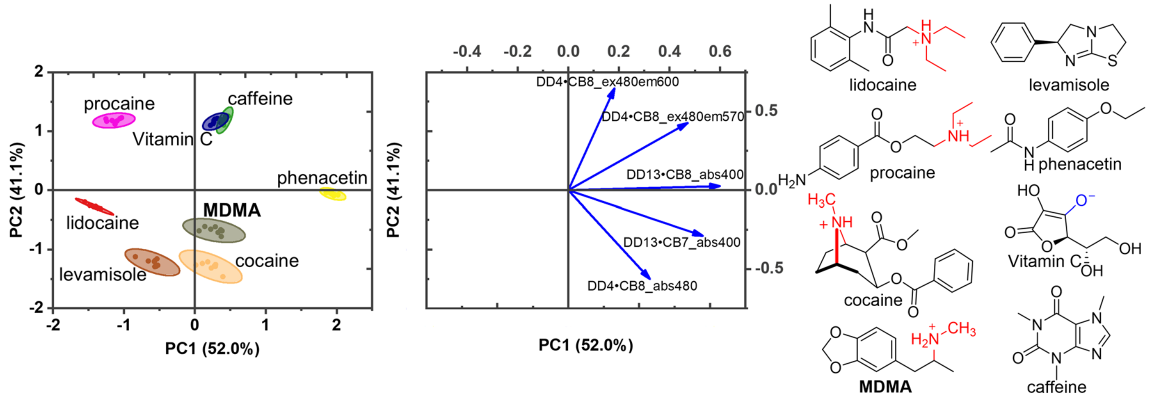

Figure 4.29. An array of mixed host sensors discriminates anesthetics and amphetamine from common adulterants. Sensor array includes absorbance and fluorescence responses of mixed host sensors **DD4Cx4•CB8**, **DD13Cx4•CB8**, and **DD13Cx4•CB7**. PCA (correlation) scores plot shows each sample set (n = 8) enclosed by 95% confidence ellipses with the respective loading plot of absorbance and fluorescence observations shown as blue arrows. Chemical structures are represented in the expected protonation forms under sensing conditions of pH 7.4. Samples contain [DD] = 10.5 µM, [CB] = 21 µM, and [drug] = 105 µM. All samples are in NaH_2PO_4/Na_2HPO_4 (8.4 mM, pH 7.4) in H_2O with 2% MeOH.

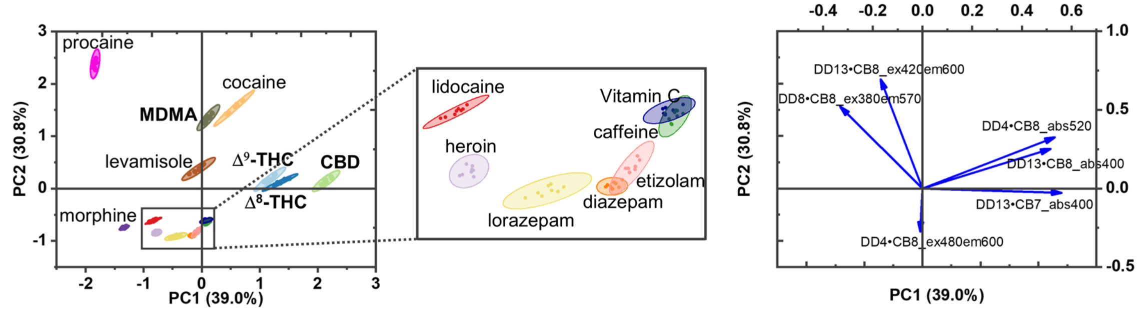

Figure 4.30. All drug and adulterant differentiation from an array of mixed host sensors. Sensor array includes absorbance and fluorescence responses from mixed host sensors **DD4Cx4•CB8**, **DD8Cx4•CB8**, **DD13Cx4•CB8**, and **DD13Cx4•CB7**. PCA (correlation) scores plot shows each sample set (n = 8) enclosed by 95% confidence ellipses with the respective loading plot of absorbance and fluorescence observations shown as blue arrows. Samples contain [DD] = 10.5 µM, [CB] = 21 µM, and [drug] = 105 µM. All samples are in NaH_2PO_4/Na_2HPO_4 (8.4 mM, pH 7.4) in H_2O with 2% MeOH.

4.5.5b Identifying multi-component street drug samples

Discriminant analysis experiments of multi-component street drug samples were conducted in NUNC black-walled optical bottom 384-well plates, with 50 μL final well volumes. Final solutions contained [DD] = 10.5 μM, [CB] = 21 μM, [street drug sample] = 0.03 mg/mL in NaH_2PO_4/Na_2HPO_4 (8.4 mM, pH 7.4) in H_2O with 2% MeOH. A blank of each multi-component street drug sample was measured to ensure no signal overlap in the DimerDye regions. Full absorbance and fluorescence spectral scans of each combination were collected in 12 replicates, along with 2 solvent blank measurements. Full spectral scans were collected to cover any binding induced changes in λ_{max} occurring in the multi-component mixtures (Figure 4.32 and Figure 4.33). Excitation wavelengths were selected at the maxima of each DimerDye (**DD4Cx4** λ_{ex} = 480 nm, **DD8Cx4** λ_{ex} = 380 nm, and **DD13Cx4** λ_{ex} = 420 nm). A second set of absorbance spectral scans was taken after the experiment was completed and compared to the measurements from the start of the experiment, this was done to ensure there were no changes in the spectra throughout the course of experimental measurements and a steady equilibrium was reached within the multi-component mixtures. Collected raw data was preprocessed by subtracting a buffer blank from absorbance and fluorescence readings. Absorbance and fluorescence wavelengths from the mixed host sensors that provided different responses to the multi-component street drug samples were selected for PCA discrimination, while aiming to use a minimal number of observations (Table 4.5). DimerDye sensors alone were also tested using the same selected absorbance and fluorescence wavelengths (Table 4.6) as a direct comparison of the DimerDye sensor array (Figure 4.35) to the array of DD•CB mixed host sensors (Figure 4.34). PCA correlation plots with confidence ellipses (95%) and loading vectors were plotted on sample sets of 8 replicates using OriginPro 2022b Principal Component Analysis App (Version: 1.50, File Name: PCAC.opx).

Table 4.5. Mixed host sensor wavelengths used in PCA analysis for the identification of multi-component street drug samples.

Mixed host sensor	Absorbance (nm)	Fluorescence ($\lambda_{ex.}$ (nm), $\lambda_{em.}$ (nm))
DD4Cx4•CB8	-	480, 570 480, 580
DD8Cx4•CB8	-	380, 580
DD13Cx4•CB8	430	420, 600
DD13Cx4•CB7	400	420, 600

Table 4.6. DimerDye sensor wavelengths used in PCA analysis for the identification of multi-component street drug samples.

DimerDye	Absorbance (nm)	Fluorescence ($\lambda_{ex.}$ (nm), $\lambda_{em.}$ (nm))
DD4Cx4	-	480, 570 480, 580
DD8Cx4	-	380, 580
DD13Cx4	400 430	420, 600

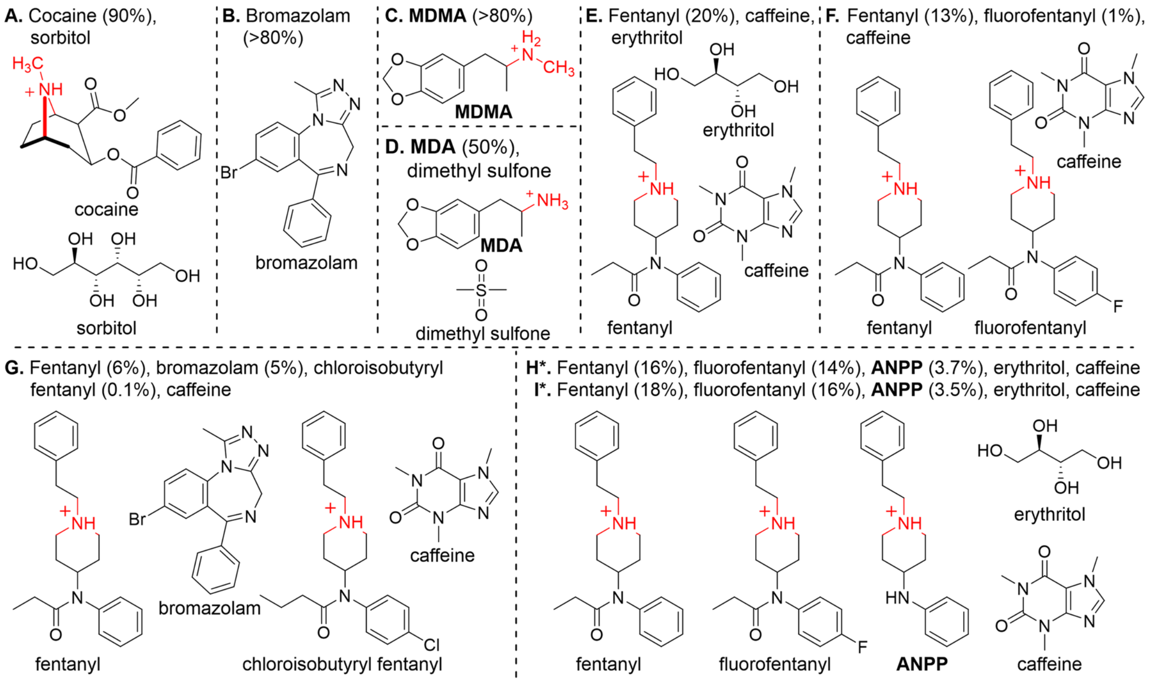

Figure 4.31. Composition and chemical structures of the multi-component street drug samples acquired through Substance, the Vancouver Island Drug Checking Project, located in Victoria, British Columbia, Canada.[206] *Samples H and I were provided by two different people reporting the same drug from the same batch and supplier. All chemical structures are represented in the expected protonation forms under sensing conditions of pH 7.4.

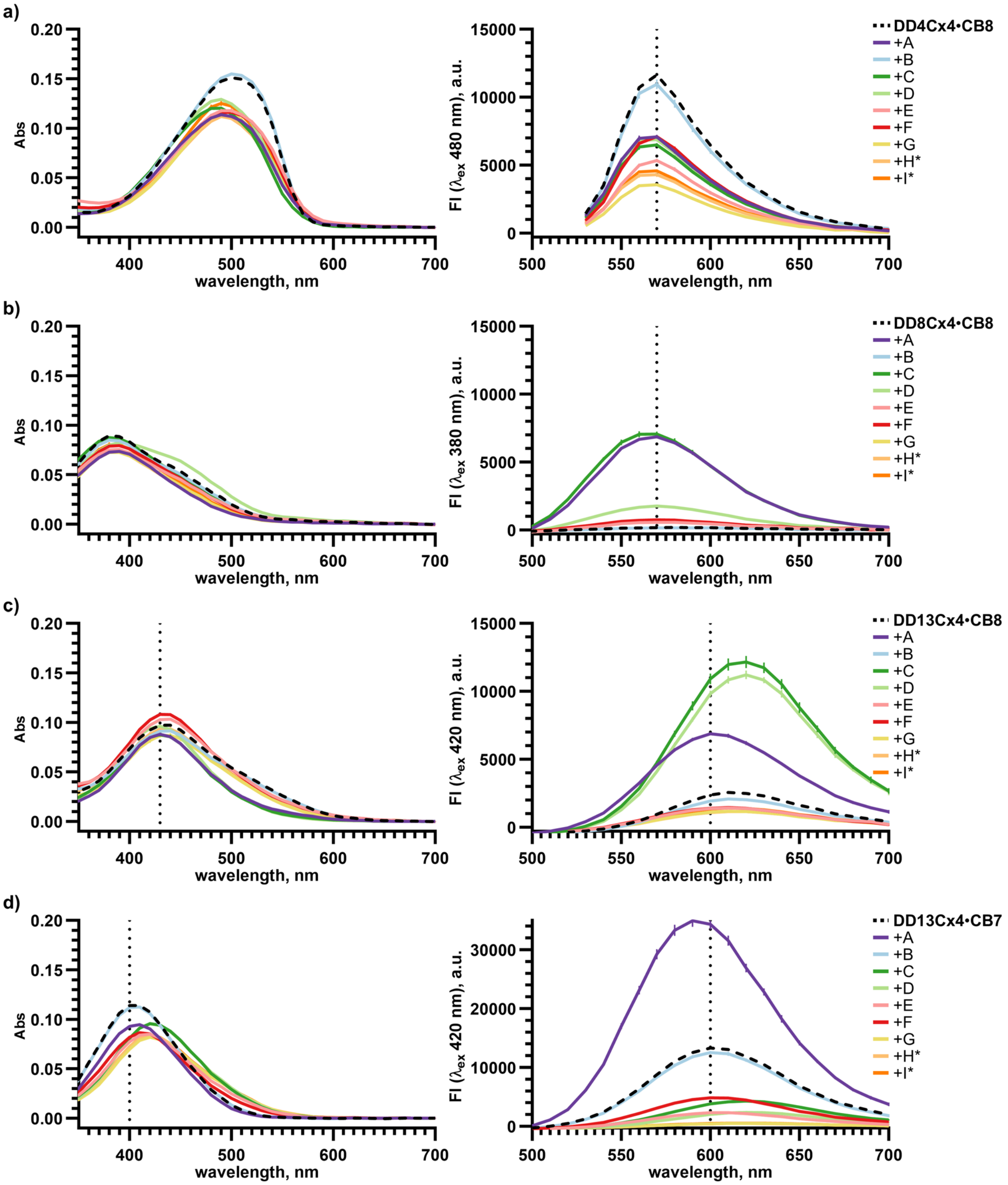

Figure 4.32. Mixed host sensor absorbance and fluorescence responses to multi-component street drug samples. Absorbance responses (left) and fluorescence responses (right) of mixed host sensors **a) DD4Cx4•CB8**, **b) DD8Cx4•CB8**, **c) DD13Cx4•CB8** and **d) DD13Cx4•CB7** to multi-component street drug samples A-I (Table 4.1 and Figure 4.31). The dotted lines in the spectra represent the selected wavelengths used in PCA analysis. Samples contain [DD] = 10.5 μM, [CB] = 21 μM, and [street drug sample] = 0.03 mg/mL. All samples are in NaH_2PO_4/Na_2HPO_4 (8.4 mM, pH 7.4) in H_2O with 2% MeOH.

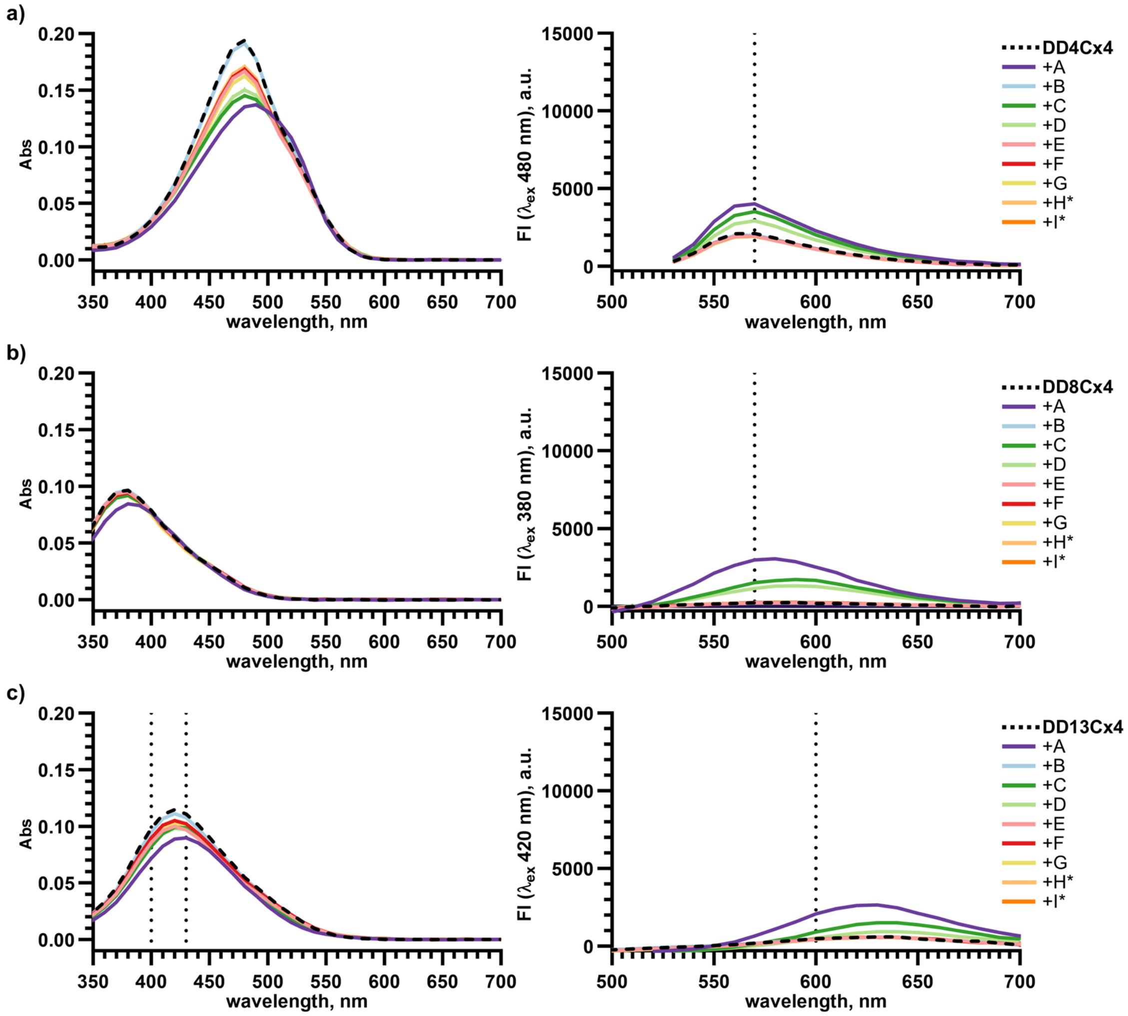

Figure 4.33. DimerDye absorbance and fluorescence responses to multi-component street drug samples. Absorbance responses (left) and fluorescence responses (right) of DimerDyes **a) DD4Cx4 b) DD8Cx4** and **c) DD13Cx4** to multi-component street drug samples A-I (Table 4.1 and Figure 4.31). The dotted lines in the spectra represent the selected wavelengths used in PCA analysis. Samples contain [DD] = 10.5 µM and [street drug sample] = 0.03 mg/mL. All samples are in NaH_2PO_4/Na_2HPO_4 (8.4 mM, pH 7.4) in H_2O with 2% MeOH.

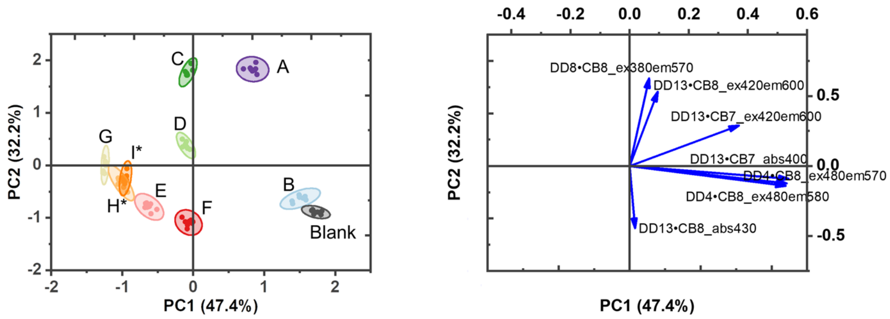

Figure 4.34. An array of mixed host sensors differentiates multi-component street drug samples. Sensor array includes absorbance and fluorescence responses from mixed host sensors **DD4Cx4•CB8**, **DD8Cx4•CB8**, **DD13Cx4•CB8**, and **DD13Cx4•CB7**. PCA (correlation) scores plot shows each sample set (n = 8) enclosed by 95% confidence ellipses with the respective loading plot of absorbance and fluorescence observations shown as blue arrows. Samples contain [DD] = 10.5 µM, [CB] = 21 µM, and [street drug sample] = 0.03 mg/mL. All samples are in NaH_2PO_4/Na_2HPO_4 (8.4 mM, pH 7.4) in H_2O with 2% MeOH.

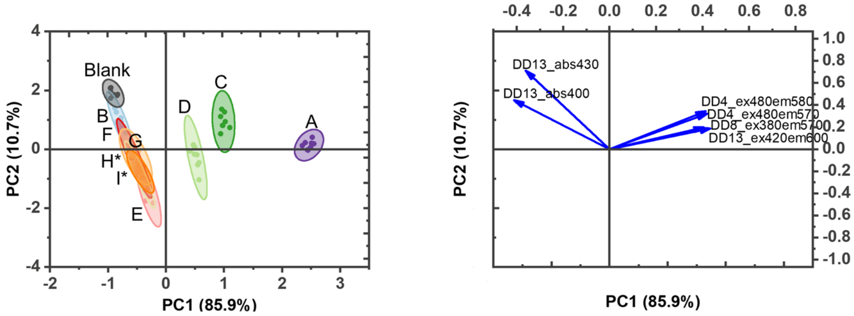

Figure 4.35. An array of DimerDye sensors does not differentiate multi-component street drug samples. Sensor array includes absorbance and fluorescence responses from DimerDye sensors **DD4Cx4**, **DD8Cx4**, and **DD13Cx4**. PCA (correlation) scores plot shows each samples set (n = 8) enclosed by 95% confidence ellipses with the respective loading plot of absorbance and fluorescence observations shown as blue arrows. Samples contain [DD] = 10.5 µM and [street drug sample] = 0.03 mg/mL. All samples are in NaH_2PO_4/Na_2HPO_4 (8.4 mM, pH 7.4) in H_2O with 2% MeOH.

Chapter 5: Conclusions and future directions

5.1 State of the field in host•guest sensing

At the onset of this dissertation, macrocyclic hosts were customarily studied as discrete pairwise host•guest interactions. There was a rapidly increasing number of reported hosts that bind small bioactive molecules in water, along with fewer, more recent examples that persist in the presence of salts and buffers. The biological application potential of supramolecular hosts spurred many researchers to emphasize designing sensing systems that function in more complex biological solutions.

Host-based sensing via noncovalent self-assembly of a reporter dye is the most studied (and easiest) route to sensing, with many reported host•dye combinations. Concentrations in indicator displacement assays (IDA) can be tuned towards competitive dye displacement, producing a photophysical response upon host•analyte complexation. Despite the relative ease of this approach, the presence of various salts are known to diminish photophysical outputs and perturb desired host binding events. At the beginning of this dissertation sensing systems that maintained their function in biorelevant conditions were underexplored.

Rational design strategies have advanced host-based sensing in the presence of competitive interferants. This progression represents the classical synthesis-oriented approach taken in the field. Typical strategies for improving molecular recognition include synthetic incorporation of additional non-covalent binding motifs, altering host cavity size, and modifying the upper and lower rim to introduce new functionality. In the case of host-based sensors, rational design has recently advanced salt tolerant systems through synthetic integration or tethering of a reporter dye to the host scaffold. Although time consuming, this approach can effectively enhance analyte sensitivity and inhibits dye dilution effects in salty solutions.

The application of host-based sensors in an array is an ongoing technique used to differentiate biorelevant small molecules, peptides and proteins. Initial examples of host-based sensor arrays were built around isolated sensor units detecting isolated analytes. These arrays often consisted of the same host scaffold paired with various dyes, applied to the differentiation of small molecules within the same class (e.g. differentiation of amino acid methylation states). In this platform the differentiation of highly similar chemical structures posed an ongoing challenge, as similar binding affinities result in indistinguishable response patterns. Another limitation within the field was the tendency to focus on a singular scaffold, which is inherently limited to a class of interacting molecules (eg. *p*-sulfonatocalix[*n*]arenes bind hydrophobic cationic analytes), with fewer examples of host-based sensing systems that detect a larger range of analytes. Throughout the duration of this dissertation, the field has shifted towards designing more information-rich systems, tackling more challenging sensing tasks, distinguishing highly similar analytes, biomacromolecules, and more complex biological mixtures.

5.2 Contributions and future directions in host-based systems design and sensing

This dissertation presented systems-oriented strategies that improve host synthesis (Chapter 2) and establish more powerful sensing tools (Chapters 3 and 4). Each Chapter incorporated a form of systems complexity, deriving function through linked equilibria.

In Chapter 2, we learned the value of combining noncovalent interactions and dynamic covalent chemistry to drive the formation of new host structures. Using a mixture of dynamic covalent building blocks and a target analyte, we formed a new synthetically challenging host via templated self-assembly. The use of reductive chemistry locked the linked dynamic covalent building blocks in place, allowing for easy isolation and purification. Furthermore, the selected aqueous buffer reaction conditions ensured favourable binding to the target analyte was maintained, for future studies in biorelevant conditions. Although template assisted self-assembly is not a novel concept, this work illustrates how it can be readily applied to the formation of new host structures. This general method can be extended into dynamic covalent libraries, as a means of developing selective hosts for a range of applications (e.g. supramolecular drug reversal, drug delivery and sensing). A mixture of building blocks containing reactive dynamic covalent handles can be combined in solution (e.g. aldehyde with amine or hydrazine, boric acid with catechol, and/or thiol groups) with an unreactive target analyte to encourage template assisted self-assembly and effectively amplify the most thermodynamically stable host species. Through this approach novel host structures can arise, while circumventing failures encountered in rational design and multi-step synthesis.

At the beginning of my graduate studies, I contributed to the study of salt tolerant host-based DimerDye sensors. This work transformed the well-known *p*-sulfonatocalix[4]arene scaffold into a unique disassembly-driven turn-on sensing system, resilient to high salt conditions known to perturb many host-based assemblies. Through parallel synthesis, integrating a panel of merocyanine dyes, an array of DimerDye sensors were readily formed. This allowed us to further explore array-based sensing platforms, discriminating cationic drugs in buffer and saliva,[72] providing important context for the subsequent work presented in this dissertation. I chose not to explicitly include the initial DimerDye sensor array studies as a Chapter in this dissertation, as a portion of the work was done while I was a research associate, prior to starting graduate studies.

The initial published works recognized several areas for DimerDye improvement. Although the reported sensitivity of DimerDyes towards small cationic drugs is good, operating at low µM concentrations, several properties of the system can be optimized. In mechanistic studies we found weaker DimerDye•analyte affinities were competing with stronger DimerDye dimerization, requiring relatively higher concentrations of analyte in sensing applications.[126] We also found that the sensitivity of the system was hindered by low apparent quantum yields of the integrated merocyanine fluorophore.[72] Both these areas provide opportunities for improvement through rational design of new DimerDye structures. Ideally, a DimerDye sensing system would provide stronger DimerDye•analyte binding affinity and integrate a brighter fluorophore, improving the overall sensitivity. This route is currently being pursued by other students in the group through the synthetic integration of diphenylacetylene derivatives. Lastly, initial differentiation studies with an array of isolated DimerDyes revealed limitations in the information output and range of detected analytes. This dissertation focused on addressing the latter challenges, expanding the sensing application of DimerDyes through systems chemistry. Although the presented DimerDye system is unique, the obstacles encountered in host sensing and how they were approached are applicable to the broader supramolecular sensing community.

Chapter 3 and 4 introduced new complex systems approaches towards information-rich sensing. In Chapter 3, a fundamental study was conducted, mixing multiple cross-reactive DimerDye building blocks, containing different integrated fluorophores. This work highlights the benefits of complex interconnected equilibria, allowing for adaptive information-rich outputs upon analyte perturbation of a host network. In these studies, we found that the network system gave rise to new and unexpected emergent properties, providing better discrimination from a single sensing solution compared to an array of isolated sensors. This increase in systems information supported my pursuit of more challenging sensing tasks, with the ability to discriminate amongst highly similar isolated proteins and profile complex protein mixtures. In Chapter 4, we established host co-assemblies as a new form of sensing with a broadened analyte scope. Through the co-assembly of two different host scaffolds via an integrated environmentally sensitive dye, we were able to expand sensing outputs towards hydrophobic, cationic and neutral species. To further build in complexity I applied co-assembled mixed host sensors towards profiling illicit street drug samples, containing multiple components of hydrophobic, neutral and cationic molecules.

The concepts explored in Chapter 3 and 4 can be expanded into building more powerful sensing tools from mixtures of three or more cross-reactive building blocks. This could include a range of accessible water-soluble macrocyclic hosts that differ in binding properties and affinities (e.g. *p*-sulfonatocalix[*n*]arene, cucurbit[*n*]uril, sulfo-pillar[*n*]arene, water-soluble calix[4]pyrroles, and cyclodextrins) and the incorporation of dyes that undergo diverse photophysical responses (e.g. dyes that undergo PET, charge transfer, FRET pairs, dyes that display solvatochromic behaviour or pH sensitivity). Most importantly the design of new complex systems must promote cross-reactivity amongst building blocks, in order to facilitate emergent properties and information-rich outputs. This can be achieved through systems comprised of general binding motifs that operate in equilibrium of one another (i.e. letting go of targeted selectivity and self-sorting) or the incorporation of additional components that facilitate co-complexation and/or higher-order self assemblies; examples thus far include metal ions or salts that co-complex with host assemblies, the incorporation of dynamic covalent building block interactions, host dimerization and micelle induced host aggregation.

Overall, this work illustrates that overcoming host-based sensing limitations requires us to diverge from a single host-class, single target outlook. Systems approaches to sensing provide the ability not only to distinguish highly similar analytes but also distinguish diverse classes of dissimilar analytes, giving rise to new properties that push differential sensing further. Although this body of work is far from complex systems that mimic nature, it ultimately demonstrates the value gained through increased complexity of multi-interacting systems, giving rise to new and better functions.

5.3 Future directions of the field in host-based sensing

The recent application of systems complexity in host-based sensing represents the forefront of the field. The development of multi-component macrocyclic systems from readily accessible building blocks has led to more advanced sensing functions, with rapid access to information-rich outputs. This development has begun to shift host-based differentiation towards much larger sensor arrays, via high throughput microplate screening of different readily mixed system components, ratios of co-assembled building blocks and solvent conditions. As larger data sets are produced, the community will adapt more data science strategies, including machine learning, to aid in determining the most valuable variables within a data set. This is comparable to the advances in data science that are currently being explored in other information-rich and/or data-rich disciplines, such as bioinformatics. The development of these tools will further enable the community to overcome challenging tasks of identify small changes in complex biological mixtures and work towards identifying multiple components within complex samples. As the field progresses, increasingly powerful sensing tools will arise from the combined benefits of rational synthetic design and systems chemistry, bringing us closer to mimicking the complex systems that govern biology.

Bibliography

1. Whitesides, G. M.; Ismagilov, R. F. Complexity in chemistry. *Science* **1999**, *284*, 89-92.
2. Ashkenasy, G.; Hermans, T. M.; Otto, S.; Taylor, A. F. Systems chemistry. *Chem. Soc. Rev.* **2017**, *46*, 2543-2554.
3. Lehn, J. M. From supramolecular chemistry towards constitutional dynamic chemistry and adaptive chemistry. *Chem. Soc. Rev.* **2007**, *36*, 151-160.
4. Krämer, J.; Kang, R.; Grimm, L. M.; De Cola, L.; Picchetti, P.; Biedermann, F. Molecular probes, chemosensors, and nanosensors for optical detection of biorelevant molecules and ions in aqueous media and biofluids. *Chem. Rev.* **2022**, *122*, 3459-3636.
5. Zhou, J.; Yu, G.; Huang, F. Supramolecular chemotherapy based on host-guest molecular recognition: a novel strategy in the battle against cancer with a bright future. *Chem. Soc. Rev.* **2017**, *46*, 7021-7053.
6. Braegelman, A. S.; Webber, M. J. Integrating stimuli-responsive properties in host-guest supramolecular drug delivery systems. *Theranostics* **2019**, *9*, 3017-3040.
7. Yin, H.; Zhang, X.; Wei, J.; Lu, S.; Bardelang, D.; Wang, R. Recent advances in supramolecular antidotes. *Theranostics* **2021**, *11*, 1513-1526.
8. Deng, C.-L.; Murkli, S. L.; Isaacs, L. D. Supramolecular hosts as *in vivo* sequestration agents for pharmaceuticals and toxins. *Chem. Soc. Rev.* **2020**, *49*, 7516-7532.
9. Daze, K.; Hof, F. Molecular interaction and recognition. In *Encyclopedia of physical organic chemistry*, Wang, Z., Wille, U., Juaristi, E. Eds.; Wiley, 2016; pp 1-51.
10. Otto, S.; Furlan, R. L. E.; Sanders, J. K. M. Dynamic combinatorial chemistry. *Drug Discov. Today* **2002**, *7*, 117-125.
11. Corbett, P. T.; Leclaire, J.; Vial, L.; West, K. R.; Wietor, J. L.; Sanders, J. K.; Otto, S. Dynamic combinatorial chemistry. *Chem. Rev.* **2006**, *106*, 3652-3711.
12. Kubik, S. *Supramolecular Chemistry in Water*; Wiley, 2019.
13. Frank, H. S.; Evans, M. W. Free volume and entropy in condensed systems III. Entropy in binary liquid mixtures; partial molal entropy in dilute solutions; structure and thermodynamics in aqueous electrolytes. *J. Chem. Phys.* **1945**, *13*, 507-532.
14. Tanford, C. Interfacial free energy and the hydrophobic effect. *Proc. Natl. Acad. Sci. U.S.A.* **1979**, *76*, 4175-4176.
15. Smithrud, D. B.; Sanford, E. M.; Chao, I.; Ferguson, S. B.; Carcanague, D. R.; Evanseck, J. D.; Houk, K. N.; Diederich, F. Solvent effects in molecular recognition. *Pure & Appl. Chem.* **1990**, *62*, 2227-2236.
16. Chandler, D. Interfaces and the driving force of hydrophobic assembly. *Nature* **2005**, *437*, 640-647.
17. Anslyn, E. V.; Dougherty, D. A. *Modern physical organic chemistry*; University Science, 2006.

18. Biedermann, F.; Nau, W. M.; Schneider, H. J. The hydrophobic effect revisited-studies with supramolecular complexes imply high-energy water as a noncovalent driving force. *Angew. Chem. Int. Ed.* **2014**, *53*, 11158-11171.
19. Kubik, S. When molecules meet in water-recent contributions of supramolecular chemistry to the understanding of molecular recognition processes in water. *ChemistryOpen* **2022**, *11*, e202200028.
20. Gokel, G. W.; Barbour, L.; Atwood, J. L. *Comprehensive supramolecular chemistry II*; Elsevier Science, 2017.
21. Rekharsky, M. V.; Inoue, Y. Complexation thermodynamics of cyclodextrins. *Chem. Rev.* **1998**, *98*, 1875-1918.
22. Houk, K. N.; Leach, A. G.; Kim, S. P.; Zhang, X. Binding affinities of host-guest, protein-ligand, and protein-transition-state complexes. *Angew. Chem. Int. Ed.* **2003**, *42*, 4872-4897.
23. Pan, Y.-C.; Tian, J.-H.; Guo, D.-S. Molecular recognition with macrocyclic receptors for application in precision medicine. *Acc. Chem. Res.* **2023**, *56*, 3626-3639.
24. Chen, F.-Y.; Geng, W.-C.; Cai, K.; Guo, D.-S. Molecular recognition of cyclophanes in water. *Chin. Chem. Lett.* **2024**, *35*.
25. Escobar, L.; Sun, Q.; Ballester, P. Aryl-extended and super aryl-extended calix[4]pyrroles: design, synthesis, and applications. *Acc. Chem. Res.* **2023**, *56*, 500-513.
26. Quílez-Pardo, J.; Solaz-Portolés, J. J. Students' and teachers' misapplication of Le Chatelier's principle: Implications for the teaching of chemical equilibrium. *J. Res. Sci. Teach.* **1995**, *32*, 939-957.
27. Jordan, J. H.; Ashbaugh, H. S.; Mague, J. T.; Gibb, B. C. Buffer and salt effects in aqueous host-guest systems: screening, competitive binding, or both? *J. Am. Chem. Soc.* **2021**, *143*, 18605-18616.
28. Selinger, A. J.; Macartney, D. H. Cucurbit[7]uril complexations of Good's buffers. *RSC Adv.* **2017**, *7*, 42513-42518.
29. Mattia, E.; Otto, S. Supramolecular systems chemistry. *Nat. Nanotechnol.* **2015**, *10*, 111-119.
30. Beatty, M. A.; Hof, F. Host–guest binding in water, salty water, and biofluids: general lessons for synthetic, bio-targeted molecular recognition. *Chem. Soc. Rev.* **2021**, *50*, 4812-4832.
31. Escobar, L.; Ballester, P. Molecular recognition in water using macrocyclic synthetic receptors. *Chem. Rev.* **2021**, *121*, 2445-2514.
32. Kim, J. S.; Quang, D. T. Calixarene-derived fluorescent probes. *Chem. Rev.* **2007**, *107*, 3780-3799.
33. De Silva, A. P.; Moody, T. S.; Wright, G. D. Fluorescent PET (Photoinduced Electron Transfer) sensors as potent analytical tools. *Analyst* **2009**, *134*, 2385-2393.
34. Valeur, B. Design principles of fluorescent molecular sensors for cation recognition. *Coord. Chem. Rev.* **2000**, *205*, 3-40.
35. Hestand, N. J.; Spano, F. C. Expanded theory of H- and J-molecular aggregates: the effects of vibronic coupling and intermolecular charge transfer. *Chem. Rev.* **2018**, *118*, 7069-7163.

36. Dsouza, R. N.; Pischel, U.; Nau, W. M. Fluorescent dyes and their supramolecular host/guest complexes with macrocycles in aqueous solution. *Chem. Rev.* **2011**, *111*, 7941-7980.
37. Wu, J.-R.; Wu, G.; Li, D.; Yang, Y.-W. Macrocycle-based crystalline supramolecular assemblies built with intermolecular charge-transfer interactions. *Angew. Chem. Int. Ed.* **2023**, *62*, e202218142.
38. Lou, X.-Y.; Song, N.; Yang, Y.-W. Fluorescence resonance energy transfer systems in supramolecular macrocyclic chemistry. *Molecules* **2017**, *22*.
39. Nguyen, B. T.; Anslyn, E. V. Indicator–displacement assays. *Coord. Chem. Rev.* **2006**, *250*, 3118-3127.
40. Sedgwick, A. C.; Brewster, J. T.; Wu, T.; Feng, X.; Bull, S. D.; Qian, X.; Sessler, J. L.; James, T. D.; Anslyn, E. V.; Sun, X. Indicator displacement assays (IDAs): the past, present and future. *Chem. Soc. Rev.* **2021**, *50*, 9-38.
41. Wiskur, S. L.; Ait-Haddou, H.; Lavigne, J. J.; Anslyn, E. V. Teaching old indicators new tricks. *Acc. Chem. Res.* **2001**, *34*, 963-972.
42. Guo, D.-S.; Uzunova, V. D.; Su, X.; Liu, Y.; Nau, W. M. Operational calixarene-based fluorescent sensing systems for choline and acetylcholine and their application to enzymatic reactions. *Chem. Sci.* **2011**, *2*, 1722-1734.
43. Sinn, S.; Krämer, J.; Biedermann, F. Teaching old indicators even more tricks: binding affinity measurements with the guest-displacement assay (GDA). *Chem. Commun.* **2020**, *56*, 6620-6623.
44. Ghale, G.; Lanctot, A. G.; Kreissl, H. T.; Jacob, M. H.; Weingart, H.; Winterhalter, M.; Nau, W. M. Chemosensing ensembles for monitoring biomembrane transport in real time. *Angew. Chem. Int. Ed.* **2014**, *53*, 2762-2765.
45. Pangeni, S.; Prajapati, J. D.; Bafna, J.; Nilam, M.; Nau, W. M.; Kleinekathofer, U.; Winterhalter, M. Large-peptide permeation through a membrane channel: understanding protamine translocation through CymA from *Klebsiella Oxytoca*. *Angew. Chem. Int. Ed.* **2021**, *60*, 8089-8094.
46. Nilam, M.; Karmacharya, S.; Nau, W. M.; Hennig, A. Proton-gradient-driven sensitivity enhancement of liposome-encapsulated supramolecular chemosensors. *Angew. Chem. Int. Ed.* **2022**, *61*, e202207950.
47. Krishnamurthy, V. M.; Semetey, V.; Bracher, P. J.; Shen, N.; Whitesides, G. M. Dependence of effective molarity on linker length for an intramolecular protein-ligand system. *J. Am. Chem. Soc.* **2007**, *129*, 1312-1320.
48. Hu, C.; Grimm, L.; Prabodh, A.; Baksi, A.; Siennicka, A.; Levkin, P. A.; Kappes, M. M.; Biedermann, F. Covalent cucurbit[7]uril-dye conjugates for sensing in aqueous saline media and biofluids. *Chem. Sci.* **2020**, *11*, 11142-11153.
49. Megyesi, M.; Biczók, L.; Jablonkai, I. Highly sensitive fluorescence response to inclusion complex formation of berberine alkaloid with cucurbit[7]uril. *J. Phys. Chem. C* **2008**, *112*, 3410-3416.
50. Thomas, S. S.; Tang, H.; Bohne, C. Noninnocent role of Na^+ ions in the binding of the *N*-phenyl-2-naphthylammonium cation as a ditopic guest with cucurbit[7]uril. *J. Am. Chem. Soc.* **2019**, *141*, 9645-9654.
51. Tang, H.; Fuentealba, D.; Ko, Y. H.; Selvapalam, N.; Kim, K.; Bohne, C. Guest binding dynamics with cucurbit[7]uril in the presence of cations. *J. Am. Chem. Soc.* **2011**, *133*, 20623-20633.

52. Buschmann, H.-J.; Cleve, E.; Jansen, K.; Wego, A.; Schollmeyer, E. Complex formation between cucurbit[*n*]urils and alkali, alkaline earth and ammonium ions in aqueous solution. *J. Incl. Phenom. Macrocycl. Chem.* **2001**, *40*, 117-120.
53. Bockus, A. T.; Smith, L. C.; Grice, A. G.; Ali, O. A.; Young, C. C.; Mobley, W.; Leek, A.; Roberts, J. L.; Vinciguerra, B.; Isaacs, L.; et al. Cucurbit[7]uril-tetramethylrhodamine conjugate for direct sensing and cellular imaging. *J. Am. Chem. Soc.* **2016**, *138*, 16549-16552.
54. Beatty, M. A.; Borges-González, J.; Sinclair, N. J.; Pye, A. T.; Hof, F. Analyte-driven disassembly and turn-on fluorescent sensing in competitive biological media. *J. Am. Chem. Soc.* **2018**, *140*, 3500-3504.
55. Garnett, G. A.; Daze, K. D.; Pena Diaz, J. A.; Fagen, N.; Shaurya, A.; Ma, M. C.; Collins, M. S.; Johnson, D. W.; Zakharov, L. N.; Hof, F. Attraction by repulsion: compounds with like charges undergo self-assembly in water that improves in high salt and persists in real biological fluids. *Chem. Commun.* **2016**, *52*, 2768-2771.
56. Krämer, J.; Grimm, L. M.; Zhong, C.; Hirtz, M.; Biedermann, F. A supramolecular cucurbit[8]uril-based rotaxane chemosensor for the optical tryptophan detection in human serum and urine. *Nat. Commun.* **2023**, *14*, 518.
57. Xu, Z.; Jia, S.; Wang, W.; Yuan, Z.; Jan Ravoo, B.; Guo, D.-S. Heteromultivalent peptide recognition by co-assembly of cyclodextrin and calixarene amphiphiles enables inhibition of amyloid fibrillation. *Nat. Chem.* **2019**, *11*, 86-93.
58. Zumbro, E.; Alexander-Katz, A. Influence of binding site affinity patterns on binding of multivalent polymers. *ACS Omega* **2020**, *5*, 10774-10781.
59. Behr, J.-P. *The Lock-and-Key Principle: The State of the Art-100 Years On*; Wiley, 1994.
60. Geng, Y.; Peveler, W. J.; Rotello, V. M. Array-based "chemical nose" sensing in diagnostics and drug discovery. *Angew. Chem. Int. Ed.* **2019**, *58*, 5190-5200.
61. Bushdid, C.; Magnasco, M. O.; Vosshall, L. B.; Keller, A. Humans can discriminate more than 1 trillion olfactory stimuli. *Science* **2014**, *343*, 1370-1372.
62. Mainland, J. D.; Li, Y. R.; Zhou, T.; Liu, W. L.; Matsunami, H. Human olfactory receptor responses to odorants. *Sci. Data* **2015**, *2*, 150002.
63. Wold, S.; Esbensen, K.; Geladi, P. Principal component analysis. *Chemom. Intell. Lab. Syst.* **1987**, *2*, 37-52.
64. Friedman, J. H. Regularized discriminant analysis. *J. Am. Stat. Assoc.* **1989**, *84*, 165–175.
65. Stewart, S.; Ivy, M. A.; Anslyn, E. V. The use of principal component analysis and discriminant analysis in differential sensing routines. *Chem. Soc. Rev.* **2014**, *43*, 70-84.
66. Cortes, C.; Vapnik, V. Support-vector networks. *Mach. Learn.* **1995**, *20*, 273-297.
67. Guyon, I.; Weston, J.; Barnhill, S.; Vapnik, V. Gene selection for cancer classification using support vector machines. *Mach. Learn.* **2002**, *46*, 389-422.
68. Brereton, R. G.; Lloyd, G. R. Support Vector Machines for classification and regression. *Analyst* **2010**, *135*, 230-267.
69. Chen, J.; Moreno, J. L.; Zhang, W.; Gibson-Elias, L. J.; Lian, R.; Najafi, S.; Zhang, H.; Zhong, W.; Hooley, R. J. Optical discrimination of terpenes in citrus peels with a host:guest sensing array. *Chem. Comm.* **2024**, *60*, 5598-5601.

70. Chen, J.; Gill, A. D.; Hickey, B. L.; Gao, Z.; Cui, X.; Hooley, R. J.; Zhong, W. Machine learning aids classification and discrimination of noncanonical DNA folding motifs by an arrayed host:guest sensing system. *J. Am. Chem. Soc.* **2021**, *143*, 12791-12799.
71. Minami, T.; Esipenko, N. A.; Zhang, B.; Kozelkova, M. E.; Isaacs, L.; Nishiyabu, R.; Kubo, Y.; Anzenbacher, P. Supramolecular sensor for cancer-associated nitrosamines. *J. Am. Chem. Soc.* **2012**, *134*, 20021-20024.
72. Beatty, M. A.; Selinger, A. J.; Li, Y.; Hof, F. Parallel synthesis and screening of supramolecular chemosensors that achieve fluorescent turn-on detection of drugs in saliva. *J. Am. Chem. Soc.* **2019**, *141*, 16763-16771.
73. Mei, Y.; Zhang, Q. W.; Gu, Q.; Liu, Z.; He, X.; Tian, Y. Pillar[5]arene-based fluorescent sensor array for biosensing of intracellular multi-neurotransmitters through host-guest recognitions. *J. Am. Chem. Soc.* **2022**, *144*, 2351-2359.
74. Das Saha, N.; Pradhan, S.; Sasmal, R.; Sarkar, A.; Berač, C. M.; Kölsch, J. C.; Pahwa, M.; Show, S.; Rozenholc, Y.; Topçu, Z.; et al. Cucurbit[7]uril macrocyclic sensors for optical fingerprinting: predicting protein structural changes to identifying disease-specific amyloid assemblies. *J. Am. Chem. Soc.* **2022**, *144*, 14363-14379.
75. Nitschke, J. R. Systems chemistry: Molecular networks come of age. *Nature* **2009**, *462*, 736-738.
76. Wiskur, S. L.; Floriano, P. N.; Anslyn, E. V.; McDevitt, J. T. A multicomponent sensing ensemble in solution: differentiation between structurally similar analytes. *Angew. Chem. Int. Ed.* **2003**, *42*, 2070-2072.
77. Buryak, A.; Severin, K. Dynamic combinatorial libraries of dye complexes as sensors. *Angew. Chem. Int. Ed.* **2005**, *44*, 7935-7938.
78. Hu, C.; Jochmann, T.; Chakraborty, P.; Neumaier, M.; Levkin, P. A.; Kappes, M. M.; Biedermann, F. Further dimensions for sensing in biofluids: distinguishing bioorganic analytes by the salt-induced adaptation of a cucurbit[7]uril-based chemosensor. *J. Am.Chem. Soc.* **2022**, *144*, 13084-13095.
79. Harrison, E. E.; Carpenter, B. A.; St. Louis, L. E.; Mullins, A. G.; Waters, M. L. Development of "imprint-and-report" dynamic combinatorial libraries for differential sensing applications. *J. Am. Chem. Soc.* **2021**, *143*, 14845-14854.
80. Harrison, E. E.; Waters, M. L. Application of an imprint-and-report sensor array for detection of the dietary metabolite trimethylamine N-oxide and its precursors in complex mixtures. *Angew. Chem. Int. Ed.* **2022**, *61*, e202205193.
81. Harrison, E. E.; Waters, M. L. Detection and differentiation of per- and polyfluoroalkyl substances (PFAS) in water using a fluorescent imprint-and-report sensor array. *Chem. Sci.* **2023**, *14*, 928-936.
82. Chen, J.; Hickey, B. L.; Wang, L.; Lee, J.; Gill, A. D.; Favero, A.; Pinalli, R.; Dalcanale, E.; Hooley, R. J.; Zhong, W. Selective discrimination and classification of G-quadruplex structures with a host–guest sensing array. *Nat. Chem.* **2021**, *13*, 488-495.
83. Chen, J.; Hickey, B. L.; Gao, Z.; Raz, A. A. P.; Hooley, R. J.; Zhong, W. Sensing base modifications in non-canonically folded DNA with an optimized host:guest sensing array. *ACS Sens.* **2022**, *7*, 2164-2169.

84. Tian, J.-H.; Hu, X.-Y.; Hu, Z.-Y.; Tian, H.-W.; Li, J.-J.; Pan, Y.-C.; Li, H.-B.; Guo, D.-S. A facile way to construct sensor array library via supramolecular chemistry for discriminating complex systems. *Nat. Commun.* **2022**, *13*, 4293.
85. Hu, X.-Y.; Hu, Z.-Y.; Tian, J.-H.; Shi, L.; Ding, F.; Li, H.-B.; Guo, D.-S. A heteromultivalent host-guest sensor array for cell recognition and discrimination. *Chem. Commun.* **2022**, *58*, 13198-13201.
86. Guo, D.-S.; Liu, Y. Supramolecular chemistry of *p*-sulfonatocalix[*n*]arenes and its biological applications. *Acc. Chem. Res.* **2014**, *47*, 1925-1934.
87. Gao, J.; Guo, D.-S. Supramolecular medicine of diverse calixarene derivatives. In *Handbook of macrocyclic supramolecular assembly*, Liu, Y., Chen, Y., Zhang, H.-Y. Eds.; Springer Singapore, 2020; pp 201-229.
88. Böhmer, V. Calixarenes, macrocycles with (almost) unlimited possibilities. *Angew. Chem. Int. Ed.* **1995**, *34*, 713-745.
89. Hunter, J. M. New neuromuscular blocking drugs. *N. Engl. J. Med.* **1995**, *332*, 1691-1699.
90. Appiah-Ankam, J.; Hunter, J. M. Pharmacology of neuromuscular blocking drugs. *BJA Educ.* **2004**, *4*, 2-7.
91. Lee, C. Conformation, action, and mechanism of action of neuromuscular blocking muscle relaxants. *Pharmacol. Ther.* **2003**, *98*, 143-169.
92. Bom, A.; Bradley, M.; Cameron, K.; Clark, J. K.; Van Egmond, J.; Feilden, H.; MacLean, E. J.; Muir, A. W.; Palin, R.; Rees, D. C.; et al. A novel concept of reversing neuromuscular block: chemical encapsulation of rocuronium bromide by a cyclodextrin-based synthetic host. *Angew. Chem. Int. Ed.* **2002**, *41*, 266-270.
93. Shields, M.; Giovannelli, M.; Mirakhur, R. K.; Moppett, I.; Adams, J.; Hermens, Y. Org 25969 (sugammadex), a selective relaxant binding agent for antagonism of prolonged rocuronium-induced neuromuscular block. *Br. J. Anaesth.* **2006**, *96*, 36-43.
94. de Boer, H. D.; van Egmond, J.; van de Pol, F.; Bom, A.; Booij, L. H. Sugammadex, a new reversal agent for neuromuscular block induced by rocuronium in the anaesthetized Rhesus monkey. *Br. J. Anaesth.* **2006**, *96*, 473-479.
95. Shurpik, D. N.; Mostovaya, O. A.; Sevastyanov, D. A.; Lenina, O. A.; Sapunova, A. S.; Voloshina, A. D.; Petrov, K. A.; Kovyazina, I. V.; Cragg, P. J.; Stoikov, II. Supramolecular neuromuscular blocker inhibition by a pillar[5]arene through aqueous inclusion of rocuronium bromide. *Org. Biomol. Chem.* **2019**, *17*, 9951-9959.
96. Zhang, X.; Cheng, Q.; Li, L.; Shangguan, L.; Li, C.; Li, S.; Huang, F.; Zhang, J.; Wang, R. Supramolecular therapeutics to treat the side effects induced by a depolarizing neuromuscular blocking agent. *Theranostics* **2019**, *9*, 3107-3121.
97. Xue, W.; Zavalij, P. Y.; Isaacs, L. Pillar[n]MaxQ: a new high affinity host family for sequestration in water. *Angew. Chem. Int. Ed.* **2020**, *59*, 13313-13319.
98. Ma, D.; Zhang, B.; Hoffmann, U.; Sundrup, M. G.; Eikermann, M.; Isaacs, L. Acyclic cucurbit[*n*]uril-type molecular containers bind neuromuscular blocking agents *in vitro* and reverse neuromuscular block *in vivo*. *Angew. Chem. Int. Ed.* **2012**, *51*, 11358-11362.

99. Guo, D.-S.; Wang, K.; Liu, Y. Selective binding behaviors of *p*-sulfonatocalixarenes in aqueous solution. *J. Incl. Phenom. Macrocycl. Chem.* **2008**, *62*, 1-21.
100. Gamal-Eldin, M. A.; Macartney, D. H. Cucurbit[7]uril host−guest complexations of steroidal neuromuscular blocking agents in aqueous solution. *Can. J. Chem.* **2014**, *92*, 243-249.
101. Coleman, A. W.; Jebors, S.; Cecillon, S.; Perret, P.; Garin, D.; Marti-Battle, D.; Moulin, M. Toxicity and biodistribution of *para*-sulfonato-calix[4]arene in mice. *New J. Chem.* **2008**, *32*, 780-782.
102. Ahuja, B. B.; Vigalok, A. Fluorescent calixarene scaffolds for NO detection in protic media. *Angew. Chem. Int. Ed.* **2019**, *58*, 2774-2778.
103. Zadmard, R.; Schrader, T. DNA recognition with large calixarene dimers. *Angew. Chem. Int. Ed.* **2006**, *45*, 2703-2706.
104. Wang, J.; Bodige, S. G.; Watson, W. H.; Gutsche, C. D. Complexation of fullerenes with 5,5'-biscalix[5]arene. *J. Org. Chem.* **2000**, *65*, 8260-8263.
105. Bottino, A.; Cunsolo, F.; Piattelli, M.; Garozzo, D.; Neri, P. Synthesis of 5,5'-bicalix[6]arene and 5,5'-bicalix[8]arene systems. *J. Org. Chem.* **1999**, *64*, 8018-8020.
106. Garozzo, D.; Gattuso, G.; Notti, A.; Pappalardo, A.; Pappalardo, S.; Parisi, M. F.; Perez, M.; Pisagatti, I. A calix[5]arene-based heterotetratopic host for molecular recognition of long-chain, ion-paired α,ω-alkanediyldiammonium salts. *Angew. Chem. Int. Ed.* **2005**, *44*, 4892-4896.
107. Brody, M. S.; Schalley, C. A.; Rudkevich, D. M.; Rebek, J. J. Synthesis and characterization of a unimolecular capsule. *Angew. Chem. Int. Ed.* **1999**, *38*, 1640-1644.
108. Podoprygorina, G.; Janke, M.; Janshoff, A.; Böhmer, V. Self-assembled polymers based on *bis*-tetra-urea calix[4]arenes connected via the wide rim. *Supramol. Chem.* **2008**, *20*, 59-69.
109. Evans, N. H.; Beer, P. D. Advances in anion supramolecular chemistry: from recognition to chemical applications. *Angew. Chem. Int. Ed.* **2014**, *53*, 11716-11754.
110. Gimeno, N.; Vilar, R. Anions as templates in coordination and supramolecular chemistry. *Coord. Chem. Rev.* **2006**, *250*, 3161-3189.
111. Kondratuk, D. V.; Sprafke, J. K.; O'Sullivan, M. C.; Perdigao, L. M. A.; Saywell, A.; Malfois, M.; O'Shea, J. N.; Beton, P. H.; Thompson, A. L.; Anderson, H. L. Vernier-templated synthesis, crystal structure, and supramolecular chemistry of a 12-porphyrin nanoring. *Chem. Eur. J.* **2014**, *20*, 12826-12834.
112. Cao, Y.; Yang, J.; Eichin, D.; Zhao, F.; Qi, D.; Kahari, L.; Jia, C.; Peurla, M.; Rosenholm, J. M.; Zhao, Z.; et al. Self-synthesizing nanorods from dynamic combinatorial libraries against drug resistant cancer. *Angew. Chem. Int. Ed.* **2021**, *133*, 3099-3107.
113. Chichak, K. S.; Cantrill, S. J.; Pease, A. R.; Chiu, S. H.; Cave, G. W.; Atwood, J. L.; Stoddart, J. F. Molecular borromean rings. *Science* **2004**, *304*, 1308-1312.
114. Połowiński, S. Template polymerisation and co-polymerisation. *Prog. Polym. Sci.* **2002**, *27*, 537-577.

115. Canal-Martín, A.; Pérez-Fernández, R. Protein-directed dynamic combinatorial chemistry: an efficient strategy in drug design. *ACS Omega* **2020**, *5*, 26307-26315.

116. Furlan, R. L. E.; Otto, S.; Sanders, J. K. M. Supramolecular templating in thermodynamically controlled synthesis. *Proc. Natl. Acad. Sci. U.S.A.* **2002**, *99*, 4801-4804.

117. Wang, K.; Guo, D.-S.; Zhang, H.-Q.; Li, D.; Zheng, X.-L.; Liu, Y. Highly effective binding of viologens by *p*-sulfonatocalixarenes for the treatment of viologen poisoning. *J. Med. Chem.* **2009**, *52*, 6402-6412.

118. Krezel, A.; Bal, W. A formula for correlating pK_a values determined in D_2O and H_2O. *J. Inorg. Biochem.* **2004**, *98*, 161-166.

119. Gutsche, C. D.; Iqbal, M. *p-tert*-butylcalix[4]arene. *Org. Synth.* **1990**, *68*.

120. Gutsche, C. D.; Lin, L.-G. Calixarenes 12: The synthesis of functionalized calixarenes. *Tetrahedron* **1986**, *42*, 1633-1640.

121. Stewart, D. R.; Gutsche, C. D. The one step synthesis of *p-tert*-butylcalix[5]arene. *Org. Prep. Proced. Int.* **1993**, *25*, 137-139.

122. Coruzzi, M.; Andreetti, G. D.; Bocchi, V.; Pochini, A.; Ungaro, R. Molecular inclusion in functionalized macrocycles. Part 5. The crystal and molecular structure of 25,26,27,28,29-pentahydroxycalix[5]arene–acetone (1:2) clathrate. *J. Chem. Soc., Perkin Trans. 2* **1982**, 1133-1138.

123. Thompson, J. W.; Kaiser, T. J.; Jorgenson, J. W. Viscosity measurements of methanol–water and acetonitrile–water mixtures at pressures up to 3500bar using a novel capillary time-of-flight viscometer. *J. Chromatogr. A* **2006**, *1134*, 201-209.

124. *ITC data analysis in Origin®, tutorial guide, using Origin® scientific plotting software to analyze calorimetric data from all MicroCal Isothermal Titration Calorimeters*.

125. Horváti, K.; Bacsa, B.; Mlinkó, T.; Szabó, N.; Hudecz, F.; Zsila, F.; Bősze, S. Comparative analysis of internalisation, haemolytic, cytotoxic and antibacterial effect of membrane-active cationic peptides: aspects of experimental setup. *Amino Acids* **2017**, *49*, 1053-1067.

126. Gallo, C.; Thomas, S. S.; Selinger, A. J.; Hof, F.; Bohne, C. Mechanism of a disassembly-driven sensing system studied by stopped-flow kinetics. *J. Org. Chem.* **2021**, *86*, 10782-10787.

127. Wehner, M.; Würthner, F. Supramolecular polymerization through kinetic pathway control and living chain growth. *Nat. Rev. Chem.* **2020**, *4*, 38-53.

128. Chen, H.; Huang, Z.; Wu, H.; Xu, J.-F.; Zhang, X. Supramolecular polymerization controlled through kinetic trapping. *Angew. Chem. Int. Ed.* **2017**, *56*, 16575-16578.

129. Liu, B.; Wu, J.; Geerts, M.; Markovitch, O.; Pappas, C. G.; Liu, K.; Otto, S. Out-of-equilibrium self-replication allows selection for dynamic kinetic stability in a system of competing replicators. *Angew. Chem. Int. Ed.* **2022**, *61*, e202117605.

130. Rieß, B.; Grötsch, R. K.; Boekhoven, J. The design of dissipative molecular assemblies driven by chemical reaction cycles. *Chem* **2020**, *6*, 552-578.

131. Fujita, D.; Ueda, Y.; Sato, S.; Mizuno, N.; Kumasaka, T.; Fujita, M. Self-assembly of tetravalent Goldberg polyhedra from 144 small components. *Nature* **2016**, *540*, 563-566.

132. Wei, B.; Dai, M.; Yin, P. Complex shapes self-assembled from single-stranded DNA tiles. *Nature* **2012**, *485*, 623-626.

133. Kingsmore, S. F. Multiplexed protein measurement: technologies and applications of protein and antibody arrays. *Nat. Rev. Drug. Discov.* **2006**, *5*, 310-321.
134. Fargher, H. A.; D'Oelsnitz, S.; Diaz, D. J.; Anslyn, E. V. Pushing differential sensing further: the next steps in design and analysis of bio-inspired cross-reactive arrays. *Anal. Sens.* **2023**, *3*, e202200095.
135. Rana, S.; Le, N. D. B.; Mout, R.; Saha, K.; Tonga, G. Y.; Bain, R. E. S.; Miranda, O. R.; Rotello, C. M.; Rotello, V. M. A multichannel nanosensor for instantaneous readout of cancer drug mechanisms. *Nat. Nanotechnol.* **2015**, *10*, 65-69.
136. Wu, A.; Isaacs, L. Self-sorting: the exception or the rule? *J. Am. Chem. Soc.* **2003**, *125*, 4831-4835.
137. Majorek, K. A.; Porebski, P. J.; Dayal, A.; Zimmerman, M. D.; Jablonska, K.; Stewart, A. J.; Chruszcz, M.; Minor, W. Structural and immunologic characterization of bovine, horse, and rabbit serum albumins. *Mol. Immunol.* **2012**, *52*, 174-182.
138. Mishra, V.; Heath, R. J. Structural and biochemical features of human serum albumin essential for eukaryotic cell culture. *Int. J. Mol. Sci.* **2021**, *22*, 8411.
139. Viegas, A.; Manso, J.; Nobrega, F. L.; Cabrita, E. J. Saturation-Transfer Difference (STD) NMR: a simple and fast method for ligand screening and characterization of protein binding. *J. Chem. Educ.* **2011**, *88*, 990-994.
140. Fielding, L.; Rutherford, S.; Fletcher, D. Determination of protein-ligand binding affinity by NMR: observations from serum albumin model systems. *Magn. Reson. Chem.* **2005**, *43*, 463-470.
141. Ji, Z.; Yao, Z.; Liu, M. Saturation transfer difference nuclear magnetic resonance study on the specific binding of ligand to protein. *Anal. Biochem.* **2009**, *385*, 380-382.
142. Sun, Q.; Zhai, Y.; Wang, W.; Gan, N.; Zhang, S.; Suo, Z.; Li, H. Molecular recognition patterns between Vitamin B12 and human serum albumin explored through STD-NMR and spectroscopic methods. *Spectrochim. Acta A Mol. Biomol. Spectrosc.* **2021**, *258*, 119828.
143. Sudlow, G.; Birkett, D. J.; Wade, D. N. The characterization of two specific drug binding sites on human serum albumin. *Mol. Pharmacol.* **1975**, *11*, 824-832.
144. Petitpas, I.; Bhattacharya, A. A.; Twine, S.; East, M.; Curry, S. Crystal structure analysis of warfarin binding to human serum albumin: anatomy of drug site I. *J. Biol. Chem.* **2001**, *276*, 22804-22809.
145. Kober, A.; Sjöholm, I. The binding sites on human serum albumin for some nonsteroidal antiinflammatory drugs. *Mol. Pharmacol.* **1980**, *18*, 421-426.
146. Memmi, L.; Lazar, A.; Brioude, A.; Ball, V.; Coleman, A. W. Protein-calixarene interactions: complexation of bovine serum albumin by sulfonatocalix[*n*]arenes. *Chem. Commun.* **2001**, 2474-2475.
147. McGovern, R. E.; Fernandes, H.; Khan, A. R.; Power, N. P.; Crowley, P. B. Protein camouflage in cytochrome *c*–calixarene complexes. *Nat. Chem.* **2012**, *4*, 527-533.
148. McGovern, R. E.; Snarr, B. D.; Lyons, J. A.; McFarlane, J.; Whiting, A. L.; Paci, I.; Hof, F.; Crowley, P. B. Structural study of a small molecule receptor bound to dimethyllysine in lysozyme. *Chem. Sci.* **2015**, *6*, 442-449.

149. Alex, J. M.; Rennie, M. L.; Engilberge, S.; Lehoczki, G.; Dorottya, H.; Fizil, A.; Batta, G.; Crowley, P. B. Calixarene-mediated assembly of a small antifungal protein. *IUCrJ* **2019**, *6*, 238-247.
150. Lynch, J. A.; Mestayer, J. J.; Blanda, M. T. Efficient syntheses of calix[4]arenes in the 1,2-alternate conformation via intramolecular benzoate ester migrations. *Supramol. Chem.* **2001**, *1*, 139-145.
151. Warmerdam, Z.; Kamba, B. E.; Shaurya, A.; Sun, X.; Maguire, M. K.; Hof, F. Calix[4]arene sulfonate hosts selectively modified on the upper rim: a study of nicotine binding strength and geometry. *Supramol. Chem.* **2021**, *33*, 88-96.
152. Selinger, A. J.; Cavallin, N. A.; Yanai, A.; Birol, I.; Hof, F. Template-directed synthesis of bivalent, broad-spectrum hosts for neuromuscular blocking agents. *Angew. Chem. Int. Ed.* **2022**, *61*, e202113235.
153. Rosania, G. R.; Lee, J. W.; Ding, L.; Yoon, H. S.; Chang, Y. T. Combinatorial approach to organelle-targeted fluorescent library based on the styryl scaffold. *J. Am. Chem. Soc.* **2003**, *125*, 1130-1131.
154. Coe, B. J.; Harris, J. A.; Asselberghs, I.; Clays, K.; Olbrechts, G.; Persoons, A.; Hupp, J. T.; Johnson, R. C.; Coles, S. J.; Hursthouse, M. B.; et al. Quadratic nonlinear optical properties of *N*-aryl stilbazolium dyes. *Adv. Funct. Mater.* **2002**, *12*, 110-116.
155. Song, X.; Bian, H.; Wang, C.; Hu, M.; Li, N.; Xiao, Y. Development and applications of a near-infrared dye-benzylguanine conjugate to specifically label SNAP-tagged proteins. *Org. Biomol. Chem.* **2017**, *15*, 8091-8101.
156. Gutsche, C. D.; Bauer, L. J. Calixarenes. 13. The conformational properties of calix[4]arenes, calix[6]arenes, calix[8]arenes, and oxacalixarenes. *J. Am. Chem. Soc.* **1985**, *107*, 6052-6059.
157. Strauss, A. W.; Bennett, C. A.; Donohue, A. M.; Rodkey, J. A.; Boime, I.; Alberts, A. W. Conversion of rat pre-proalbumin to proalbumin *in vitro* by ascites membranes. Demonstration by NH_2-terminal sequence analysis. *J. Biol. Chem.* **1978**, *253*, 6270-6274.
158. Brennan, S. O.; Carrell, R. W. A circulating variant of human proalbumin. *Nature* **1978**, *274*, 908-909.
159. Gasteiger, E.; Hoogland, C.; Gattiker, A.; Duvaud, S.; Wilkins, M. R.; Appel, R. D.; Bairoch, A. Protein identification and analysis tools on the expasy server. In *The proteomics protocols handbook*, Walker, J. M. Ed.; Humana Press, 2005; pp 571–607.
160. Madeira, F.; Pearce, M.; Tivey, A. R. N.; Basutkar, P.; Lee, J.; Edbali, O.; Madhusoodanan, N.; Kolesnikov, A.; Lopez, R. Search and sequence analysis tools services from EMBL-EBI in 2022. *Nucleic Acids Res.* **2022**, *50*, W276-W279.
161. Shrivastava, A. Methods for the determination of limit of detection and limit of quantitation of the analytical methods. *Chron. Young Sci.* **2011**, *2*, 21-25.
162. Mayer, M.; Meyer, B. Characterization of ligand binding by saturation transfer difference NMR spectroscopy. *Angew. Chem. Int. Ed.* **1999**, *38*, 1784-1788.
163. Hwang, T. L.; Shaka, A. J. Water suppression that works. Excitation sculpting using arbitrary wave-forms and pulsed-field gradients. *J. of Magn. Reson. Series A* **1995**, *112*, 275-279.

164. Nilam, M.; Hennig, A. Enzyme assays with supramolecular chemosensors - the label-free approach. *RSC Adv.* **2022**, *12*, 10725-10748.
165. Guerrini, L.; Garcia-Rico, E.; Pazos-Perez, N.; Alvarez-Puebla, R. A. Smelling, seeing, tasting—old senses for new sensing. *ACS Nano.* **2017**, *11*, 5217-5222.
166. Motiei, L.; Margulies, D. Molecules that generate fingerprints: a new class of fluorescent sensors for chemical biology, medical diagnosis, and cryptography. *Acc. Chem. Res.* **2023**, *56*, 1803-1814.
167. Rout, B.; Unger, L.; Armony, G.; Iron, M. A.; Margulies, D. Medication detection by a combinatorial fluorescent molecular sensor. *Angew. Chem. Int. Ed.* **2012**, *51*, 12477-12481.
168. Pode, Z.; Peri-Naor, R.; Georgeson, J. M.; Ilani, T.; Kiss, V.; Unger, T.; Markus, B.; Barr, H. M.; Motiei, L.; Margulies, D. Protein recognition by a pattern-generating fluorescent molecular probe. *Nat. Nanotechnol.* **2017**, *12*, 1161-1168.
169. De, M.; Rana, S.; Akpinar, H.; Miranda, O. R.; Arvizo, R. R.; Bunz, U. H. F.; Rotello, V. M. Sensing of proteins in human serum using conjugates of nanoparticles and green fluorescent protein. *Nat. Chem.* **2009**, *1*, 461-465.
170. Geng, Y.; Amante, J. J.; Goel, H. L.; Zhang, X.; Walker, M. R.; Luther, D. C.; Mercurio, A. M.; Rotello, V. M. Differentiation of cancer stem cells through nanoparticle surface engineering. *ACS Nano.* **2020**, *14*, 15276-15285.
171. Peri-Naor, R.; Pode, Z.; Lahav-Mankovski, N.; Rabinkov, A.; Motiei, L.; Margulies, D. Glycoform differentiation by a targeted, self-assembled, pattern-generating protein surface sensor. *J. Am. Chem. Soc.* **2020**, *142*, 15790-15798.
172. Chen, J.; Hooley, R. J.; Zhong, W. Applications of synthetic receptors in bioanalysis and drug transport. *Bioconjug. Chem.* **2022**, *33*, 2245-2253.
173. Pinalli, R.; Pedrini, A.; Dalcanale, E. Biochemical sensing with macrocyclic receptors. *Chem. Soc. Rev.* **2018**, *47*, 7006-7026.
174. Hickey, B. L.; Chen, J.; Zou, Y.; Gill, A. D.; Zhong, W.; Millar, J. G.; Hooley, R. J. Enantioselective sensing of insect pheromones in water. *Chem. Comm.* **2021**, *57*, 13341-13344.
175. Wang, B.; Han, J.; Bojanowski, N. M.; Bender, M.; Ma, C.; Seehafer, K.; Herrmann, A.; Bunz, U. H. F. An optimized sensor array identifies all natural amino acids. *ACS Sens.* **2018**, *3*, 1562-1568.
176. Selinger, A. J.; Hof, F. Adaptive supramolecular networks: emergent sensing from complex systems. *Angew. Chem. Int. Ed.* **2023**, *62*, e202312407.
177. Zhong, W.; Hooley, R. J. Combining excellent selectivity with broad target scope: biosensing with arrayed deep cavitand hosts. *Acc. Chem. Res.* **2022**, *55*, 1035-1046.
178. Barrow, S. J.; Kasera, S.; Rowland, M. J.; Del Barrio, J.; Scherman, O. A. Cucurbituril-based molecular recognition. *Chem. Rev.* **2015**, *115*, 12320-12406.
179. Sinn, S.; Biedermann, F. Chemical sensors based on cucurbit[*n*]uril macrocycles. *Isr. J. Chem.* **2018**, *58*, 357-412.
180. Assaf, K. I.; Nau, W. M. Cucurbiturils: from synthesis to high-affinity binding and catalysis. *Chem. Soc. Rev.* **2015**, *44*, 394-418.
181. Lazar, A. I.; Biedermann, F.; Mustafina, K. R.; Assaf, K. I.; Hennig, A.; Nau, W. M. Nanomolar binding of steroids to cucurbit[*n*]urils: Selectivity and applications. *J. Am. Chem. Soc.* **2016**, *138*, 13022-13029.

182. Murkli, S.; Klemm, J.; Brockett, A. T.; Shuster, M.; Briken, V.; Roesch, M. R.; Isaacs, L. *In vitro* and *in vivo* sequestration of phencyclidine by Me_4Cucurbit[8]uril. *Chem. Eur. J.* **2021**, *27*, 3098-3105.

183. Das, D.; Assaf, K. I.; Nau, W. M. Applications of cucurbiturils in medicinal chemistry and chemical biology. *Front. Chem.* **2019**, *7*, 619.

184. Huang, Y.; Gao, R.-H.; Liu, M.; Chen, L.-X.; Ni, X.-L.; Xiao, X.; Cong, H.; Zhu, Q.-J.; Chen, K.; Tao, Z. Cucurbit[*n*]uril-based supramolecular frameworks assembled through outer-surface interactions. *Angew. Chem. Int. Ed.* **2021**, *60*, 15166-15191.

185. Tian, X.; Chen, L. X.; Yao, Y. Q.; Chen, K.; Chen, M.-D.; Zeng, X.; Tao, Z. 4-Sulfocalix[4]arene/cucurbit[7]uril-based supramolecular assemblies through the outer surface interactions of cucurbit[*n*]uril. *ACS Omega* **2018**, *3*, 6665-6672.

186. Lin, R.-G.; Long, L.-S.; Huang, R.-B.; Zheng, L.-S. Directing role of hydrophobic−hydrophobic and hydrophilic−hydrophilic interactions in the self-assembly of calixarenes/cucurbiturils-based architectures. *Cryst. Growth Des.* **2008**, *8*, 791-794.

187. Liu, J.; Lambert, H.; Zhang, Y.-W.; Lee, T.-C. Rapid estimation of binding constants for cucurbit[8]uril ternary complexes using electrochemistry. *Anal. Chem.* **2021**, *93*, 4223-4230.

188. Biedermann, F.; Ross, I.; Scherman, O. A. Host–guest accelerated photodimerisation of anthracene-labeled macromolecules in water. *Polym. Chem.* **2014**, *5*, 5375-5382.

189. Sayed, M.; Biedermann, F.; Uzunova, V. D.; Assaf, K. I.; Bhasikuttan, A. C.; Pal, H.; Nau, W. M.; Mohanty, J. Triple emission from *p*-dimethylaminobenzonitrile-cucurbit[8]uril triggers the elusive excimer emission. *Chem. Eur. J.* **2015**, *21*, 691-696.

190. Liu, S.; Ruspic, C.; Mukhopadhyay, P.; Chakrabarti, S.; Zavalij, P. Y.; Isaacs, L. The cucurbit[*n*]uril family: prime components for self-sorting systems. *J. Am. Chem. Soc.* **2005**, *127*, 15959-15967.

191. Zhao, H.-X.; Guo, D.-S.; Wang, L.-H.; Qian, H.; Liu, Y. A novel supramolecular ternary polymer with two orthogonal host–guest interactions. *Chem. Commun.* **2012**, *48*, 11319-11321.

192. Belzak, L.; Halverson, J. Evidence synthesis - the opioid crisis in Canada: a national perspective. *Health Promot. Chronic Dis. Prev. Can.* **2018**, *38*, 224-233.

193. Gill, A. D.; Hickey, B. L.; Zhong, W.; Hooley, R. J. Selective sensing of THC and related metabolites in biofluids by host:guest arrays. *Chem. Comm.* **2020**, *56*, 4352-4355.

194. Du, X.; Hao, H.; Qin, A.; Tang, B. Z. Highly sensitive chemosensor for detection of methamphetamine by the combination of AIE luminogen and cucurbit[7]uril. *Dyes Pigm.* **2020**, *180*, 108413.

195. Cole, C.; Jones, L.; McVeigh, J.; Kicman, A.; Syed, Q.; Bellis, M. Adulterants in illicit drugs: a review of empirical evidence. *Drug Test Anal.* **2011**, *3*, 89-96.

196. C. Cole; L. Jones; J. McVeigh; A. Kicman; Q. Syed; Bellis, M. A. *CUT: a guide to adulterants, bulking agents and other contaminants found in illicit drugs.*; Liverpool John Moores University, Liverpool, 2010.

197. Halifax, J. C.; Lim, L.; Ciccarone, D.; Lynch, K. L. Testing the test strips: laboratory performance of fentanyl test strips. *Harm Reduct. J.* **2024**, *21*, 14.
198. Ivsins, A.; Boyd, J.; Beletsky, L.; McNeil, R. Tackling the overdose crisis: the role of safe supply. *Int. J. Drug Policy* **2020**, *80*, 102769.
199. Gozdzialski, L.; Wallace, B.; Hore, D. Point-of-care community drug checking technologies: an insider look at the scientific principles and practical considerations. *Harm Reduct. J.* **2023**, *20*, 39.
200. Wallace, B.; Hills, R.; Rothwell, J.; Kumar, D.; Garber, I.; Van Roode, T.; Larnder, A.; Pagan, F.; Aasen, J.; Weatherston, J.; et al. Implementing an integrated multi-technology platform for drug checking: social, scientific, and technological considerations. *Drug Test Anal.* **2021**, *13*, 734-746.
201. Wallace, B.; Gozdzialski, L.; Qbaich, A.; Shafiul, A.; Burek, P.; Hutchison, A.; Teal, T.; Louw, R.; Kielty, C.; Robinson, D.; et al. A distributed model to expand the reach of drug checking. *Drugs Habits Soc. Pol.* **2022**, *23*, 220-231.
202. Borden, S. A.; Saatchi, A.; Vandergrift, G. W.; Palaty, J.; Lysyshyn, M.; Gill, C. G. A new quantitative drug checking technology for harm reduction: pilot study in Vancouver, Canada using paper spray mass spectrometry. *Drug Alcohol Rev.* **2022**, *41*, 410-418.
203. Kim, J.; Jung, I.-S.; Kim, S.-Y.; Lee, E.; Kang, J.-K.; Sakamoto, S.; Yamaguchi, K.; Kim, K. New cucurbituril homologues: syntheses, isolation, characterization, and X-ray crystal structures of cucurbit[*n*]uril (*n* = 5, 7, and 8). *J. Am. Chem. Soc.* **2000**, *122*, 540-541.
204. Jiao, D.; Scherman, O. A. Isolation of cucurbit[*n*]uril homologues with imidazolium salts in a recyclable manner. *Green Chem.* **2012**, *14*, 2445-2449.
205. Blacker, A. J.; Jazwinski, J.; Lehn, J.-M. Molecular anion binding and substrate photooxidation in visible light by 2,7-diazapyrenium cations. *Helv. Chim. Acta.* **1987**, *70*, 1-12.
206. *Substance: Vancouver Island Drug Checking Project*. https://substance.uvic.ca.
207. Gozdzialski, L.; Hutchison, A.; Wallace, B.; Gill, C.; Hore, D. Toward automated infrared spectral analysis in community drug checking. *Drug Test Anal.* **2023**, *16*, 83-92.
208. Borden, S. A.; Saatchi, A.; Krogh, E. T.; Gill, C. G. Rapid and quantitative determination of fentanyls and pharmaceuticals from powdered drug samples by paper spray mass spectrometry. *Anal. Sci. Adv.* **2020**, *1*, 97-108.
209. Gozdzialski, L.; Rowley, A.; Borden, S. A.; Saatchi, A.; Gill, C. G.; Wallace, B.; Hore, D. K. Rapid and accurate etizolam detection using surface-enhanced Raman spectroscopy for community drug checking. *Int. J. Drug Policy* **2022**, *102*, 103611.
210. *Paper Spray Mass Spectrometry Target List by Category*. https://substance.uvic.ca/paperspray.
211. Prabodh, A.; Bauer, D.; Kubik, S.; Rebmann, P.; Klärner, F. G.; Schrader, T.; Delarue Bizzini, L.; Mayor, M.; Biedermann, F. Chirality sensing of terpenes, steroids, amino acids, peptides and drugs with acyclic cucurbit[*n*]urils and molecular tweezers. *Chem. Commun.* **2020**, *56*, 4652-4655.
212. Prabodh, A.; Sinn, S.; Biedermann, F. Analyte sensing with unselectively binding synthetic receptors: virtues of time-resolved supramolecular assays. *Chem. Commun.* **2022**, *58*, 13947-13950.

213. Swinehart, D. F. The Beer-Lambert law. *J. Chem. Educ.* **1962**, *39*, 333.

214. Zhang, S.; Grimm, L.; Miskolczy, Z.; Biczók, L.; Biedermann, F.; Nau, W. M. Binding affinities of cucurbit[*n*]urils with cations. *Chem. Commun.* **2019**, *55*, 14131-14134.